41st Symposium on Chemical Kinetics and Dynamics Book of Abstracts

第 41 回化学反応討論会 講演要旨集

June 2 (Tue.) – 4 (Thu.), 2026

Suzuki Akira Hall, Hokkaido University

Hosted by

ICReDD-Hokkaido University

Local Organizing Committee of SCKD41

Cooperated by

The Chemical Society of Japan
The Spectroscopical Society of Japan
Japan Society of Theoretical Chemistry
Japan Society for Molecular Science
The Atomic Collision Society of Japan

winmostar

Winmostar は、MO、DFT、MD などのシミュレーション環境を提供する統合 GUI ソフトウェアです。
20 年以上の歴史を持ち、現在もなお進化を続けています。

主な機能

1. **様々な原子・分子構造の作成**
   分子、錯体、液体、アモルファス、
   ポリマー、結晶、表面、界面など
2. **シンプルかつ柔軟な計算条件の設定**
   GAMESS、Gaussian、LAMMPS、
   Gromacs、Quantum ESPRESSO などに対応
3. **様々な計算リソースのシームレスな切り替え**
4. **膨大なファイル・プロセスの自動管理**
5. **シミュレーションデータの変換**
6. **計算結果の解析・可視化、各種物性算出**
   45 種類以上の物性に対応

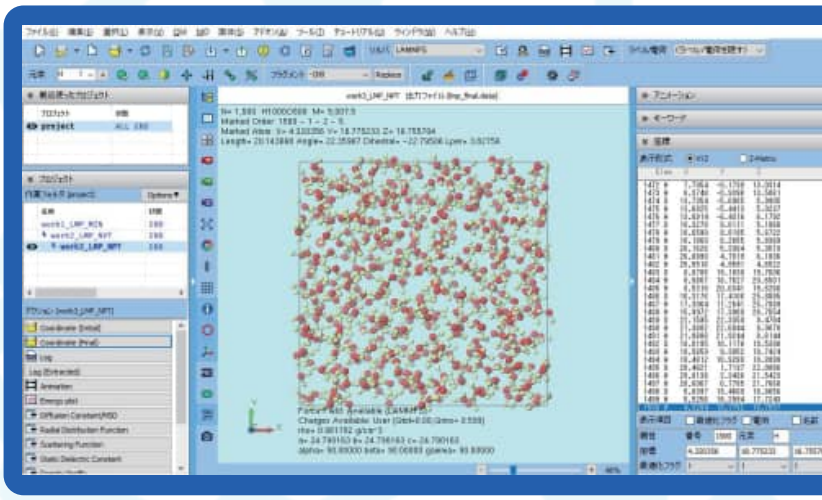

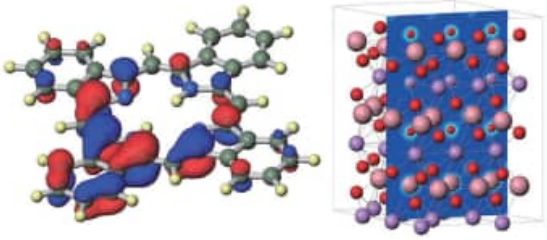

特徴

- 主要なシミュレーション手法を Winmostar だけで網羅
- 基礎原理の学習から受託計算まで充実したサポートで初心者でも安心
- 長年の開発・サポート実績を活用し高いコストパフォーマンス
- 実用的な入力ファイルを生成するのでソルバの学習に有用

導入実績 (2022 年 10 月 4 日現在)

・メーカー 160 社、研究機関 26 機関、教育機関 105 機関で導入
・93 本の学術論文と 13 社の特許で引用
・74 の大学で授業・実習に利用、公的機関の講習会で採用

弊社リサーチフェローが執筆した
『LAMMPS による分子動力学シミュレーション』
が出版されました。

LAMMPS の実践的な利用方法に特化した解説書となります。
化学工業日報　8,800 円 (税込)

料金プラン (税別)

特定ユーザライセンス	民間企業 官公庁	¥ 360,000 ~
	教育機関	¥ 120,000 ~
サイトライセンス	¥ 1,440,000 ~	

全機能を 1 ヶ月間利用可能な無料トライアルと、
機能を限定した学生版および無償版を
Web から無料でダウンロードできます。

各ライセンスの詳細、ダウンロード、注文見積もりも Web にてご確認ください

winmostar　GET STARTED

株式会社クロスアビリティ　東京都文京区本郷4-1-5 石渡ビル3階
https://x-ability.co.jp/

株式会社ハイブリッジ
HyBridge Co.,Ltd.

表面・界面反応速度論研究用 Si–P 成膜用 真空成膜システム

【 主 な 特 長 】

Si–P 系成膜装置の設計・製作を通じて培った真空・熱・反応場制御技術により、気相―表面―界面における化学反応の初期過程および動力学研究に適した高再現性の実験環境を提供します。

■ 高純度 UHV 環境による反応場形成

超高真空多ポートチャンバーにより不純物を排除し、清浄な反応環境を実現します。

■ 加熱成膜セルによる Si–P 同時／反応温度・時間・組成を独立制御可能

加熱成膜セルで成膜温度や供給フラックス、反応時間を独立制御可能です。

■ 励起・緩和過程解析を想定した拡張モジュール設計

分析チャンバーや照射系追加可能なモジュール設計で実験の拡張が容易です。

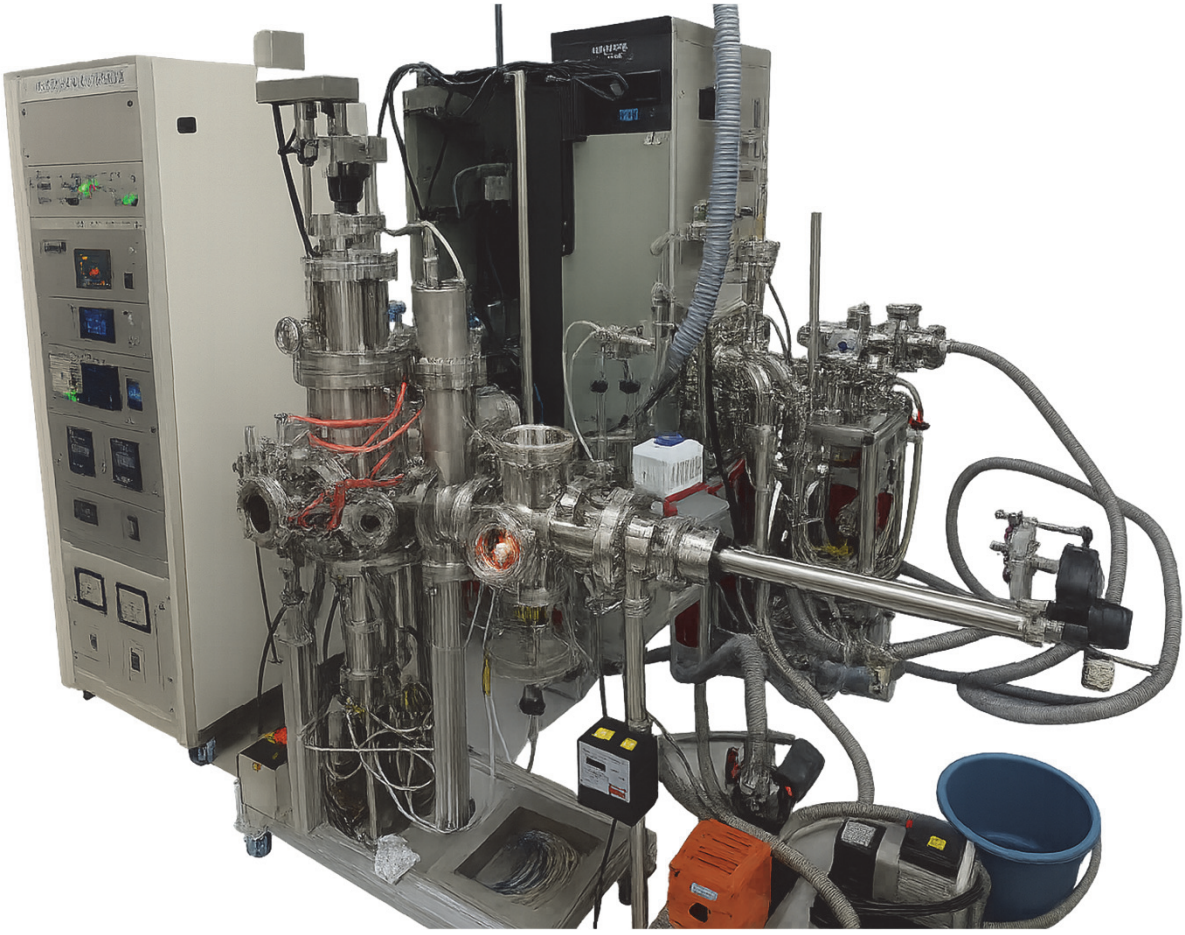

＊仕様変更対応します。お気軽にご相談下さい。

株式会社 ハイブリッジ
札幌本社
〒065-0021　札幌市東区北21条東3丁目2番7号
TEL：011-769-9170　FAX：011-769-9172

E-mail sales@hybridge.co.jp http://www.hybridge.co.jp/
東京営業所
〒190-1201　東京都西多摩郡瑞穂町二本木457-4
TEL：042-513-9250　FAX：042-513-9251

導入事例　HPEサーバー＆ストレージ

量子化学計算とデータサイエンスの融合により、革新的な触媒開発への道を拓く知見を創出

Your Trusted,
technology and solution advisor.

SOLUTION Report

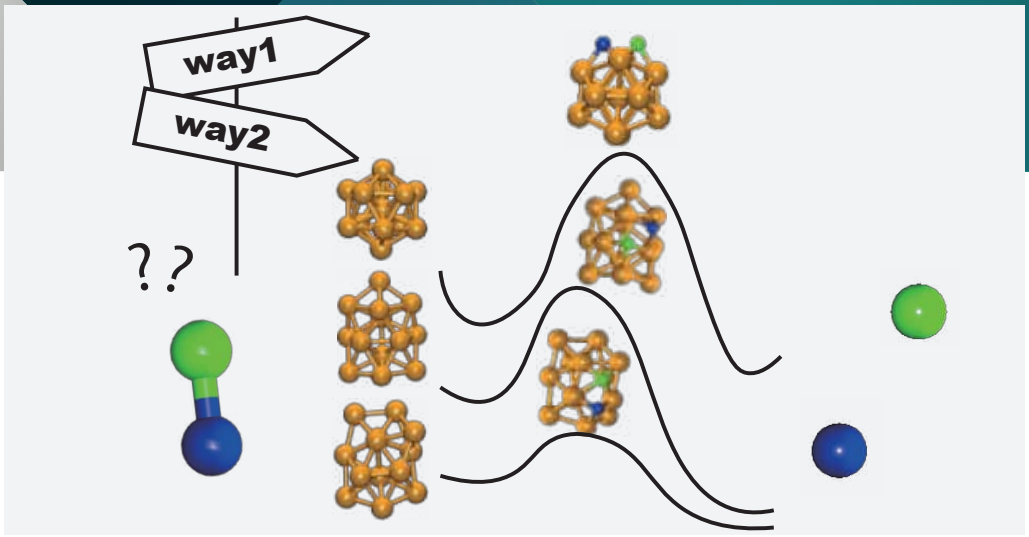

北海道大学
HOKKAIDO UNIVERSITY

ICReDD
Institute for Chemical Reaction Design and Discovery
北海道大学 化学反応創成研究拠点

北海道大学　化学反応創成研究拠点（ICReDD）

北海道大学 化学反応創成研究拠点（ICReDD）は、文部科学省が主導する「世界トップレベル研究拠点プログラム（WPI）」の一環として2018年10月に設立された。計算科学を中心に、情報科学、実験科学の3分野を融合し、「化学反応創成学」というひとつの研究領域を確立することを目指しており、触媒や材料に代表される革新的な化学物質を高速かつ効率的に開発する技術が世界から注目されている。北海道大学 大学院理学研究院 化学部門 准教授でありICReDDに参画している小林正人氏は、量子化学計算に「ハイスループット化」の手法を適用し、これに「データサイエンス」を融合させる独自のアプローチで触媒開発の困難な課題を着実に解決へ導こうとしている。

- POINT 01 ● 社会を変えるような革新的な触媒の高速開発
- POINT 02 ● 量子化学計算のトレンドは「ハイスループット化」へ
- POINT 03 ● 金属ナノクラスター触媒の活性化エネルギー回帰
- POINT 04 ● 表面吸着モデル計算データベースの構築とその不均一触媒活性予測への応用
- POINT 05 ● インテル® Xeon® スケーラブル・プロセッサー搭載サーバーを100台導入

●お問合せ・お見積りは下記までお願い致します。
Email：pr@synnex.co.jp

TD SYNNEX　TD SYNNEX株式会社

NEW

Controlling the Ion Particles Electronics

ADCAP *Alliance with* CGC INSTRUMENTS

ELECTRODYNAMIC TRAPS

Our company lends a hand and supplies custom-made hardware for ion traps, mass spectrometers and electron and ion optics. Our range of instrumentation extends to RF generators for ion traps and ultra-precision amplifiers for precise mass measurements in micro-particle traps.
We also offer preamplifiers and ion counters for detection, as well as signal filters for cooling trapped particles.

Areas of expertise:
- Mass and Optical Spectroscopy, Laser technology
- Electron, Ion, and light optics
- Ultra-High Vacuum and Cryogenic technology

Production Line

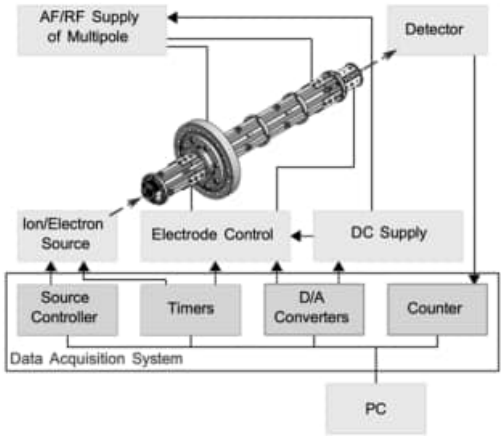

~ Custom-made Electronics ~

- **Power or signal switch** that also functions as pulse generator (modular design up to 24 channels)
- **AF and RF supply** for ion trap (guide) such as multipoles, 3D-QIT, funnel, etc.
- Precise and stable **bipolar (four-quadrant) DC voltage source** without any switching devices (modular design up to 12 lines)
- **Signal amplifier** including **bipolar picoammeter** and **D/A converter** (modular design up to 8 meters)
- Modular data acquisition system including timer, logic array, and counter

Soft Ionization and Deposition/Detection

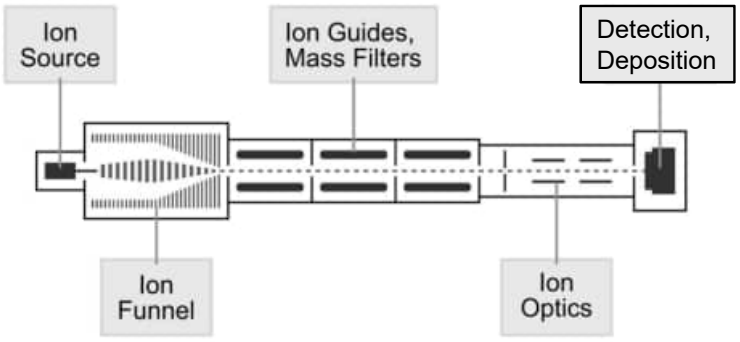

(1) Beam generation and focusing, e.g., ESI source and ion funnel
→ Power Switch *19AMX* in combination with Power Supply Unit *19PSU*

(2) Mass selection, e.g., multipoles as ion trap (guide) or mass filter, and aperture
→ RF Generator *RFG50* and Modular (Compact) Switch *AMXR (AMXT)*

(3) Ion optics, e.g., ToF analyzer
→ Modular Bipolar Power Supply System *AMPR*

(4) Detection and/or deposition, e.g., EM coupled with conversion dynode, MCP delay line detector, and Daly detector
→ Signal Amplifier *HV-AMP* including bipolar picoammeter, customized power supply and counting module for EM, MCP, and PMT available

<19AMX>

- Output power: >100 W per channel (*19AMX*)
- Trilevel switching available
- Operating voltage: <1.5 kV
- Pulse rates: <5 MHz (*19AMX*), <1 MHz (*AMXR*)
- Switching slope: ~35 ns (*19AMX*), ~15 ns (*AMXR*)
- Jitter: <1 ns
- Combination with *AMPR* available for *AMXR*

<AMXR>

<RFG50>

- Output RF power: <50 W
- Output voltage amplitude: <1 kV
- Frequency: auto tuned to designed value (fixed)
- Supported frequency: 100 kHz to 10 MHz

<AMPR>

- Continuous bipolar (four-quadrant) output without polarity switching
- Voltage rating: ±1 kV, ±500 V, etc.
- Output current: ±1 mA
- True 16-bit voltage resolution
- Low output noise: about 2 $ppm_{p\text{-}p}$

<HV-AMP>

- Output voltage: several 100 V
- Ultra-low temperature coefficients and noise
- High dynamic range
- Current measurement range: 10 nA, 1 μA, 100 μA
- Current noise: 30 fA_{RMS}, 100 fA_{pp} at best

ADCAP

ADCAP VACUUM TECHNOLOGY Co., Ltd.

#201 Sunport Bldg., 87 Iwai-cho, Hodogaya-ku,
Yokohama, Kanagawa, 240-0023, Japan
TEL: +81-45-720-1123, URL= http://www.adcap-vacuum.com

あなたの計算が世界の化学を加速する

計算化学はあらゆる化学の課題を解決する可能性を持っています。
しかし化学全体を見渡すと、計算を本格的に使っている研究はまだわずか 2 割程度。
あなたの経験と知見は、化学の未来を変える力になります。
私たちと一緒に、もっと多くの分野に計算化学を届けませんか。

インターン募集

対象

- 一般的な化学・物理分野での大学学部卒の資格を持つこと
- 量子化学計算・機械学習等、何らかの計算化学を用いた研究に携わった経験があること望ましい

就業体験地

京都または東京 ※遠隔地の方もご相談に応じます

会社概要

会社名：HPC システムズ株式会社
所在地：〒108-0022 東京都港区海岸 3-9-15 LOOP-X 8 階
株　式：東京証券取引所 グロース市場上場
資本金：2 億 3,151 万円
社員数：136 名

募集人数

募集枠には限りがあり、応募状況によってはお断りさせていただく場合がございます。

お問い合わせ先

〒108-0022 東京都港区海岸 3-9-15 LOOP-X 8 階
HPC システムズ株式会社
採用担当 米澤／青木

ＴＥＬ：03-5446-5530
メール：hpcs_hr@hpc.co.jp

HPC SYSTEMS

信頼と実績のあるフェムト秒

LIGHT CONVERSION

PHAROS最大エネルギー 5 mJモデル
最大5 mJ励起のORPHEUS-HE-5mJ/ ORPHEUS-ONE-HE-5mJが新登場

NEW テラヘルツ発生・X線発生・高次高調波発生、過渡吸収・時間分解・蛍光分析、LITG ・SFG ・TR-ARPES ・CARS ・SRS 用途に適したマーケットリーディング製品!

PHAROS

1030 ± 10 nm
5 mJ @ 4 kHz
< 100fs @ 1 mJ

高エネルギーYb フェムト秒レーザ

特徴

NEW

- 最大平均出力: 10 ～ 20 W
- **最大パルスエネルギー: 0.2 ～ 5 mJ**
- パルス幅: 100 fs ～ 10 ps (最大20 ps) PC 制御
- 繰返し周波数: Single shot ～ 1 MHz (最大)
- 高調波出力オプション: 515/343/257/206 nm
- BiBurst オプション: GHz/MHz バーストパルス発生
- キャリアエンベロープ位相(CEP) 安定化オプション
- 繰返し周波数ロックオプション
- 高熱安定性・密閉デザイン

CARBIDE

1030 ± 10 nm
120 W (50W UV)
Single shot ～ 10 MHz (Max)

高平均出力Yb フェムト秒レーザ

特徴

- 最大平均出力 : 4 ～ 6 W (空冷) 20 ～ 120 W (水冷)
- 最大パルスエネルギー: ～100 μJ (空冷) 0.2 ～ 2 mJ (水冷)
- パルス幅: 190 fs ～ 20 ps PC 制御
- 繰返し周波数: Single shot ～ 10 MHz (最大)
- 高調波出力オプション: 515/343/257 nm / 50W UV モデル
- BiBurst オプション: GHz/MHz バーストパルス発生
- キャリアエンベロープ位相 (CEP) 安定化オプション
- 繰返し周波数ロックオプション
- 小型・ 高安定性の産業グレードデザイン

FLINT

Yb フェムト秒
オシレータ

特徴

- 高繰返しモデルFL1 : 8 W@60 ～ 90 MHz, 1035 nm±10 nm
- 高出力高エネルギーモデルFL2 : 20 W @ 40, 80 MHz, 1030 nm±10 nm
- ショートパルスモデルFL2-SP : <50 fs, 4 W @ 10 MHz, 1030 nm±10 nm
- 高出力安定性: <0.5 % rms
- パルスエネルギー: 6 nJ ～ 0.5 μJ
- CEP 安定化オプション
- HG FLINT 内蔵オプション(FL2)
- 外部信号同期オプション

ORPHEUS

NEW

フェムト秒
光パラメトリック増幅器

特徴

- PC 制御波長可変 : 190 ～ 16000 nm
- **最大入力パルスエネルギー: 5 mJ (-HE)** NEW
- 最大入力平均出力 : 80 W
- 中赤外MID-IR OPA (-ONE) (1350 ～ 16000 nm)
- 自動GDD 制御近赤外短パルス (-F) (55 ～ 100 fs)
- 中赤外広帯域OPA (-MIR) (<100 fs, 2500 ～ 15000 nm)
- ノンコリニアOPA (-N) (<30 fs, 530 ～ 900 nm)
- 狭帯域ピコ秒型 (-PS) (800 fs ～ 3 ps, < 20 cm^{-1})
- 次世代型高安定OPA (-NEO or -NEO-ONE)

PHOTO TECHNICA
https://www.phototechnica.co.jp
フォトテクニカ株式会社
〒336-0017 埼玉県さいたま市南区南浦和2-18-2
TEL : 048-871-0067 FAX : 048-871-0068
e-mail : voc@phototechnica.co.jp

Timetable for SCKD41 in Sapporo

	Day 1 June 2 (Tue.)	Day 2 June 3 (Wed.)	Day3 June 4 (Thu.)
9:00	9:05–9:10 Opening Remarks		
	9:10–10:25 Chair: Nanbu, Shinkoh **1A1** Suzuki, Toshinori **1A2** Nakagawa, Shoto	9:30–10:50 Chair: Hasegawa, Jun-ya **IL3** Zhu, Chaoyuan **IL4** Takahashi, Satoshi	9:30–11:00 Chair: Ishibashi, Atsuki **IL6** Kawai, Akio **3A1** Majima, Takuya **3A2** Sie, Ni-En
10:00	**1A3** Wada, Satoi		
	10:25–10:40 Coffee/Tea Break	10:50–11:05 Coffee/Tea Break	
	10:40–12:00 Chair: Sekikawa, Taro **IL1** Hishikawa, Akiyoshi **IL2** Tiwari, Ashwani K.	11:05–11:55 Chair: Sumiya, Yosuke **2A1** Nagahata, Yutaka **2A2** Tsuoka, Kazuki	11:00–11:15 Coffee/Tea Break 11:15–12:05 Chair: Hamada, Morihiko **3A3** Nakajima, Atsushi **3A4** Ohta, Nobuhiro
11:00			
12:00	12:00–13:30 Lunch Break	11:55–14:00 Lunch Break	12:05–13:30 **Group Photo** Lunch Break
13:00	13:30–14:45 Chair: Horio, Takuya **1A4** Yamada, Kana **1A5** Fushitani, Mizuho **1A6** Kumagai, Yoshiaki		13:30–15:00 **Poster Session 3**
14:00	14:45–15:00 Break	14:00–15:30 **Poster Session 2**	
15:00	15:00–16:30 **Poster Session 1**	15:30–15:45 Break	15:00–15:10 Break 15:10–16:40 Chair: Komatsuzaki, Tamiki **IL7** Ishizaki, Akihito **3A5** Tsubouchi, Masaaki **3A6** Minato, Taketoshi
16:00	16:30–16:45 Break	15:45–17:15 Chair: Kumagai, Yoshiaki **IL5** Sims, Ian **2A3** Ardelia, Mellisa **2A4** Minemoto, Shinichiro	16:40–17:00 Poster Award Ceremony
17:00	16:45–17:35 Chair: Murakami, Tatsuhiro **1A7** Zhou, Zhiyi **1A8** Lu, Bateer	**17:30- Banquet**	17:00–17:10 Closing

41st Symposium on Chemical Kinetics and Dynamics

Invited Lectures:

IL1 "Tunnel-Electron Momentum Imaging of Gas-Phase Molecules in Intense Laser Fields"
Hishikawa, Akiyoshi (Nagoya University)
June 2, 10:40 - 11:20

IL2 "Dynamics of atoms and molecules under the influence of intense laser pulses"
Tiwari, Ashwani K. (Indian Institute of Science Education and Research, Kolkata)
June 2, 11:20 - 12:00

IL3 "Nuclear quantum effects in semiclassical and mixed quantum-classical nonadiabatic molecular dynamics"
Zhu, Chaoyuan (National Yang Ming Chiao Tung University)
June 3, 9:30 - 10:10

IL4 "Numerical analysis of the pathway selection in fully reversible chemical reaction networks"
Takahashi, Satoshi (The University of Tokyo)
June 3, 10:10 - 10:50

IL5 "Absolute rate constants and branching fractions for low temperature reactions and inelastic collisions of astrophysical interest"
Sims, Ian (University of Rennes)
June 3, 15:45 - 16:25

IL6 "Elementary reaction rate constants of organic free radicals in liquid phase as measured by the laser synchronized pulsed ESR method"
Kawai, Akio (Kanagawa University)
June 4, 9:30 - 10:10

IL7 "Exploring dynamics in molecular systems using quantum science and technology"
Ishizaki, Akihito (The University of Tokyo)
June 4, 15:10 - 15:50

Day 1: June 2 (Tue.)

9:05–9:10 Opening Remarks

9:10–10:25 Oral Presentations (Chair: Nanbu, Shinkoh)

1A1

Impact of C5 Methylation on Nonadiabatic Transition and Photohydration Damage of Nucleosides

Ghosh, Srijon[1]; Obara, Yuki[1]; Jaiswal, Vishal Kumar[2]; Taddei, Mario[2]; Nenov, Artur[2]; Conti, Irene[2]; Garavelli, Marco[2]; Suzuki, Toshinori[1]
([1]Kyoto University, [2]Universita degli Studi Bologna)

1A2

Solvent Effects on Ambimodal Diels-Alder/Dipolar Cycloadditions: Classical and Ring-Polymer Molecular Dynamics with Explicit Solvation

Nakagawa, Shoto[1]; Matsubuchi, Hayato[1]; Ota, Haruki[1]; Takayanagi, Toshiyuki[1]; Murakami, Tatsuhiro[2]
([1]Saitama University, [2]Tokyo Metropolitan University)

1A3

Solvent effects on the photoreaction dynamics of cis-stilbene: A QM/MM nonadiabatic molecular dynamics study

Wada, Satoi[1]; Minegishi, Yusuke[1]; Tsutsumi, Takuro[1]; Taketsugu, Tetsuya[1]
([1]Hokkaido University)

10:25–10:40 Coffee/Tea Break

10:40–12:00 Oral Presentations (Chair: Sekikawa, Taro)

IL1

Tunnel-Electron Momentum Imaging of Gas-Phase Molecules in Intense Laser Fields

Hishikawa, Akiyoshi
(Nagoya University)

IL2

Dynamics of atoms and molecules under the influence of intense laser pulses

Tiwari, Ashwani K.
(Indian Institute of Science Education and Research, Kolkata)

12:00–13:30 Lunch Break

13:30–14:45 Oral Presentations (Chair: Horio, Takuya)

1A4

Ultrafast state-selective dynamics of electronically excited N_2^+ by pump-probe measurements using few-cycle near-infrared laser pulses and high-order harmonics

Yamada, Kana[1]; Ando, Toshiaki[1]; Iwasaki, Atsushi[1]; Yamanouchi, Kaoru[1]
([1]The University of Tokyo)

1A5

Formation of I 4d double-core-hole states of CH_3I in strong EUV-FEL fields studied by electron-ion coincidence spectroscopy

Fushitani, Mizuho[1,2]; Hikosaka, Yasumasa[2,3]; Owada, Shigeki[2,4]; Hishikawa, Akiyoshi[1,2,5]
([1]Nagoya Univ., [2]RIKEN SPring-8 Center, [3]Univ. of Toyama, [4]JASRI, [5]RCMS, Nagoya Univ.)

1A6

Ultraviolet photodynamics in iodopropane isomers studied by time-resolved momentum imaging with extreme ultraviolet photoionization

Kumagai, Yoshiaki[1,2]; Allum, Felix[3,4,5]; Nagaya, Kiyonobu[6]; Harries, James R.[7]; Iwayama, Hiroshi[8,9]; Britton, Mathew[5]; H. Bucksbaum, Philip[4]; Burt, Michael[10,11]; Brouard, Mark[10]; Downes-Ward, Briony[12]; Driver, Taran[5]; Heathcote, David[10]; Hockett, Paul[13]; J. Howard, Andrew[4]; W. L. Lee, Jason[3]; Liu, Yusong[4]; Kukk, Edwin[14]; W. McManus, Joseph[10]; Miléšević, Dennis[10]; S. Minns, Russell[12]; Niozu, Akinobu[15]; Niskanen, Johannes[14]; J. Orr-Ewing, Andrew[16]; Owada, Shigeki[17,18]; Robertson, Patrick[10,19]; Rolles, Daniel[20]; Rudenko, Artem[20]; Ueda, Kiyoshi[21]; Unwin, James[10]; Vallance, Claire[10]; Walmsley, Tiffany[10]; N. R. Ashfold, Michael[16]; Forbes, Ruaridh[5,22]
([1]Nara Women's University, [2]Tokyo University of Agriculture and Technology, [3]Deutsches Elektronen-Synchrotron (DESY), [4]Stanford PULSE Institute, SLAC, [5]Linac Coherent Light Source, SLAC, [6]Kyoto University, [7]QST, [8]Institute for Molecular Science, [9]Sokendai, [10]University of Oxford, [11]Trent University, [12]University of Southampton, [13]National Research Council of Canada, [14]University of Turku, [15]Hiroshima University, [16]University of Bristol, [17]RIKEN SPring-8 Center, [18]Japan Synchrotron Radiation Research Institute, [19]University of Nottingham, [20]Kansas State University, [21] Tohoku University, [22] University of California, Davis)

14:45–15:00 Break (Proceed to the Poster Session Venue)

15:00–16:30 Poster Session 1

16:30–16:45 Break (Return to the Oral Session Venue)

16:45–17:35 Oral Presentations (Chair: Murakami, Tatsuhiro)

1A7

Ring-opening via conical intersections in thiophene revealed by extreme ultraviolet time-resolved photoelectron spectroscopy

Zhou, Zhiyi[1]; Wada, Satoi[2]; Arai, Yuto[1]; Kambara, Ryuto[3]; Taketsugu, Tetsuya[2,4]; Sekikawa, Taro[1]
([1]Dept. of Applied Physics, Fac. of Eng., Hokkaido Univ., [2]WPI-ICReDD, Hokkaido Univ., [3]Grad. Sch. of Chem. Sci. & Eng., Hokkaido Univ., [4]Dept. of Chemistry, Fac. of Sci., Hokkaido Univ.)

1A8

First observation of sequential photochemical and thermal ring-opening dynamics in 1,3-cyclohexadiene

Lu, Bateer[1]; Sekikawa, Taro[1]
([1]Hokkaido University)

Day 2: June 3 (Wed.)

9:30–10:50 Oral Presentations (Chair: Hasegawa, Jun-ya)

IL3

Nuclear quantum effects in semiclassical and mixed quantum-classical nonadiabatic molecular dynamics

Zhu, Chaoyuan
(National Yang Ming Chiao Tung University)

IL4

Numerical analysis of the pathway selection in fully reversible chemical reaction networks

Takahashi, Satoshi
(The University of Tokyo)

10:50–11:05 Coffee/Tea Break

11:05–11:55 Oral Presentations (Chair: Sumiya, Yosuke)

2A1

An efficient approximation of the timescale hierarchies in a large-scale first-order kinetics

Nagahata, Yutaka[1]; Toda, Mikito[1,2,3]; Komatsuzaki,Tamiki[1,4,5,6]
([1]RIES, Hokkaido University, [2]Research Institute for Engineering, Kanagawa University, [3]Graduate School of Information Science, University of Hyogo, [4]WPI-ICReDD, Hokkaido University, [5]Department of Chemistry, Faculty of Science, Hokkaido University, [6]OTRI, Osaka University)

2A2

Exploration of chemical reaction pathways by quantum walk

Tsuoka, Kazuki[1]; Nishi, Takanori[1,2]; Kaoru, Yamanouchi[1,2]
([1]School of Science, The Univ. of Tokyo, [2]Institute for Attosecond Laser Facility, The Univ. of Tokyo)

11:55–14:00 Lunch Break

14:00–15:30 Poster Session 2

15:45–17:15 Oral Presentations (Chair: Kumagai, Yoshiaki)

IL5

Absolute rate constants and branching fractions for low temperature reactions and inelastic collisions of astrophysical interest

Sims, Ian
(University of Rennes)

2A3

Observation of Rabi oscillation between the inversion splitting doubling in ammonia

Ardelia, Mellisa[1]; Ueno, Kazuki[1]; Saida, Ryota[1]; Nakamura, Masaaki[1]; Ohshima, Yasuhiro[1]
([1]Graduate School of Science, Institute of Science Tokyo)

2A4

Hydrogen momentum spectroscopy of small hydrocarbon molecules

Minemoto, Shinichirou[1]; Kanaya, Satoru[1]; Sugai, Takuma[1]; Jones, Darryl[2]; Takahashi, Masahiko[1]
([1]IMRAM, Tohoku University, [2]Flinders University)

17:30– Banquet

Day 3: June 4 (Thu.)

9:30–11:00 Oral Presentations (Chair: Ishibashi, Atsuki)

IL6

Elementary reaction rate constants of organic free radicals in liquid phase as measured by the laser synchronized pulsed ESR method
Kawai, Akio
(Kanagawa University)

3A1

Combined experimental and computational study of ionization-induced reactions on propanol ice surfaces
Majima, Takuya[1]; Otsuka, Sota[1]; Jifuku, Shuntaro[1]; Murakami, Tatsuhiro[2]; Tsuchida, Hidetsugu[1]; Saito, Manabu[1]
([1]Kyoto University, [2]Tokyo Metropolitan University)

3A2

Photodesorption of hydroxyl radical on ice induced by visible light
Sie, Ni-En[1]; Tsuge, Masashi[1,2]; Nakai, Yoichi[3]; Watanabe, Naoki[1]
([1]Hokkaido University, [2]Hiroshima University, [3]RIKEN Nishina Center for Accelerator-based Science)

11:00–11:15 Coffee/Tea Break

11:15–12:05 Oral Presentations (Chair: Hamada, Morihiko)

3A3

Oxygen reactivity of surface-supported pure and boron-doped aluminum superatoms
Inoue, Tomoya[1]; Nakajima, Atsushi[1]
([1]Keio University)

3A4

Effects of nanosecond pulsed electric field on brain and pancreatic cells and fluorescence microscopy with particular attention to the difference between cancerous and normal cells
Ohta, Nobuhiro[1]; Awasthi, Kamlesh[1]; Bai, Dong-Jie[1]; Wei, Chun-Yen[1]; Hsu, Hsin-Yun[1]
([1]National Yang Ming Chiao Tung University (NYCU))

12:05–13:30 Lunch Break

13:30–15:00 Poster Session 3

15:10–16:40 Oral Presentations (Chair: Komatsuzaki, Tamiki)

IL7

Exploring dynamics in molecular systems using quantum science and technology
Ishizaki, Akihito
(The University of Tokyo)

3A5

Two-dimensional electronic spectroscopy of light-harvesting phycobiliproteins synthesized by recombinant DNA techniques
Tsubouchi, Masaaki[1,2]; Fujita, Takatoshi[2]; Adachi, Motoyasu[2]; Itakura, Ryuji[1]
([1]Kansai Institute for Photon Science, QST, [2]Institute for Quantum Life Science, QST)

3A6

Reaction of fluoride ions at the electrode–electrolyte interface for high energy density batteries
Minato, Taketoshi[1,2]; Tabtimtong, Nicha[1,3]; Kaisook, Pattanapon[1,3]; Tenaillon Johan, 1[4]; Athikaphan Pakpoom[5,1]; Imai, Yumiko[1]; Ueda, Tadashi[1]; Nakamoto, Kei-ichi[1,6]; Neramittagapong, Arthit[3]; Neramittagapong, Sutasinee[3]
([1]Institute for Molecular Science, [2]Spin-L, [3]Khon Kaen Univ., [4]Chimie-ParisTech ENSCP, [5]National Institutes of Natural Science, [6]NAIST)

16:40–17:00 Poster Award Ceremony

17:00–17:10 Closing Remarks

Poster Presentations

(*Candidates for the Best Poster Prize)

Session 1 (June 2, 15:00–16:30)

1P01*

Floquet-theory-based nonadiabatic ab initio molecular dynamics for analyzing chemical reactions in strong laser fields

Kambara, Ryuto[1]; Tsutsumi, Takuro[1]; Taketsugu, Tetsuya[1]
([1]Hokkaido University)

1P02

Femtosecond laser filament reaction in gaseous hexane studied by time-of-flight mass spectrometry with velocity screening

Matsuda, Akitaka[1]; Okumura, Yuya[1]; Hashigaya, Kasumi[1]; Hishikawa, Akiyoshi[1]
([1]Nagoya University)

1P03*

Nonadiabatic internal conversion of S_2 and isomerization dynamics of silabenzene

Sato, Hazuki[1]; Kimura, Mizuki[1]; Nanbu, Shinkoh[2]
([1]Graduate School of Science and Technology, Sophia University, [2]Faculty of Science and Technology, Sophia University)

1P04

Photofragment imaging of oriented methyl/ethyl bromide (CH_3Br, C_2H_5Br) for the assessment of their transition dipole moments

Kawamata, Hiroshi[1]; Nakamura, Masaaki[2]; Che, Dock-Chil[3]
([1]Hokkaido University, [2]Institute of Science Tokyo, [3]Osaka University)

1P05*

Suppression of twisted intermediate formation in uracil by C6 methylation

Aki, Yoshino[1]; Ghosh, Srijon[1]; Obara, Yuki[1]; Suzuki, Toshinori[1]
([1]Kyoto University)

1P06*

Theoretical study on C5 substituent effects on the excited-state relaxation dynamics of pyrimidine bases

Kobayashi, Yuto[1]; Kambara, Ryuto[1]; Minegishi, Yusuke[1]; Wada, Satoi[1]; Taketsugu, Tetsuya[1]
([1]Hokkaido University)

1P07

Observations of vibrational wavepackets of N_2 and N_2^+ generated in air plasma

Endo, Tomoyuki[1]; Mashiko, Hiroki[2]; Sako, Tokuei[3]; Oguri, Katsuya[2]; Itakura, Ryuji[1]
([1]QST, KPSI, [2]NTT BRL, [3]Nihon University)

1P08*

Photoelectron circular dichroism of epichlorohydrin in near-infrared intense laser fields studied by electron-ion coincidence momentum imaging

Ogawa, Kazumi[1]; Kuroda, Runa[1]; Matsuda, Akitaka[1]; Hishikawa, Akiyoshi[1,2]
([1]Grad. Sc. Sci, Nagoya U., [2]RCMS, Nagoya U.)

1P09*

Multimodal Energy Landscape Underlying Adhesive Interface Peeling

Kubo, Koki[1]; Sumiya, Yosuke[1]
([1]Yamaguchi University)

1P10*

Predicting Product Branching in Post-Transition State Bifurcation Reactions via Molecular Dynamics Simulations

Okamoto, Daichi[1]; Yamaki, Keita[1]; Hayashi, Daiki[1]; Nakagawa, Shota[1]; Matsubuchi, Hayato[1]; Sasaki, Yuki[1]; Takayanagi, Toshiyuki[1]; Murakami, Tatsuhiro[2]
([1]Saitama University, [2]Tokyo Metropolitan University)

1P11

Robust High-Order Derivative Evaluation for Phase-Space Reaction Dynamics Using Chebyshev Polynomial-Based Spectral Differentiation

Umer, Umair[1]; Li, Jizhou[2]; Komatsuzaki, Tamki[1,2]; Staub, Ruben[1]; Taketsugu, Tetsuya[1]; Yagi, Kiyoshi[3]
([1]ICReDD, Hokkaido University, [2]RIES, Hokkaido University, [3]Department of Chemistry, University of Tsukuba)

1P12*

Development of a fluctuation-assisted molecular dynamics method for the efficient sampling of chemical reactions

Tsukamura, Sei[1]; Nishimura, Yoshifumi[2]; Nakai, Hiromi[1,2]
([1]Grad. Sch. Adv. Sci. Eng., Waseda University, [2]WISE, Waseda University)

1P13*

Dynamical Effects Beyond Kinetic Analysis Based on Reaction Path Networks: An Ab Initio Molecular Dynamics Study

Takizawa, Soei[1]; Tsutsumi, Takuro[1]; Ono, Yuriko[1]; Sada, Kazuki[1]; Taketsugu, Tetsuya[1]
([1]Hokkaido University)

1P14

A Reusable Explicit Chemical Ontology-Based Method to Expedite Reaction Path Searches

Nath, Pinku[1]; ([1]WPI-ICReDD, Hokkaido University)

1P15*

Analysis of the Product Branching Boundary Determining Reaction-Path Bifurcation

Suzuki, Jidai[1]; Nakanishi, Tatsuhiro[1]; Kambara, Ryuto[1]; Ono, Yuriko[2,3]; Taketsugu, Tetsuya[2,4]
([1]Grad. School Chem. Sci. Eng., Hokkaido Univ., [2]Fac. Sci., Hokkaido Univ., [3]Institute for Quantum Chemical Exploration, [4]WPI-ICReDD, Hokkaido Univ.)

1P16

Merged-beam experiment on a low-energy ion-neutral reaction study

Dhongade, Siddhant[1],; Tamaru, Hiroya[1]; Ota, Rin[1]; Bllantyne, Lucius Thaine[1]; Matsuzaki, Taichi[1]; Yabuki, Sorato[1]; Nakayama, Akifumi[2]; Nakano, Yuji[1]
([1]Department of Physics, Rikkyo University, [2]Earth-Life Science Institute, Institute of Science Tokyo)

1P17*

Entropic advantage and induction-mediated polarization in the adsorption of cyclic oligomers on fullerene surfaces

Arima, Sota[1]; Yamamoto, Takuya[2]; Sato, Shin-ichiro[2]
([1]Grad. School Chem. Sci. Eng., Hokkaido Univ., [2]Div. Appl. Chem., Fac. Eng., Hokkaido Univ.)

1P18

Surface reactions of sulfur-bearing molecules with hydrogen atoms on amor-phous solid water

Nguyen, Thanh[1,2]; Oba, Yasuhiro[1]; Sameera, W. M. C.[1,3]; Molpeceres, German[4]; Watanabe, Naoki[1]
([1]Hokkaido University, [2]Present address: Leiden University, [3]University of Gothenburg, [4]Institute de Fisica Fundamental (IFF-CSIC))

1P19*

Towards the Observation of Gas-Phase Vibrational Polaritons via Cavity Transmission Spectroscopy

Miyashita, Kaichi[1]; Mitsukawa, Eiyu[1]; Matsumoto, Yoshiteru[2]
([1]Grad. Sch. Integr. Sci. Technol., Shizuoka Univ., [2]Dept. Chem., Fac. Sci., Shizuoka Univ.)

1P20

Physical Adsorption and Conformational Changes of Figure-Eight Poly(ethylene glycol) on Gold Nanosheet Surfaces: A Molecular Dynamics Study

Kobayashi, Takuto[1]; Arima, Souta[1]; Yamamoto, Takuya[1]; Sato, Shin-ichiro[1]
([1]Hokkaido University)

1P21*

Molecular Dynamics Simulation of the Rotational Relaxation Time of an Aptamer-Based Fluorescent Molecular Sensor in Aqueous Solution

Hashimoto, Kohei[1]; Arima, Sota[1]; Tokeshi, Manabu[1]; Yamamoto, Takuya[1]; Sato, Shinichiro[1]
([1]Hokkaido University)

1P23*

Theoretical prediction of atomic diffusion energy at the ice surface under cryogenic conditions using the kinetic MC method.

Taniguchi, Riko[1]; Nakatani, Naoki[1]; Nakatani, Kaho[1]
([1]Tokyo Metropolitan University)

1P24

Conformational Constraints in Ni Complexes for Tuning H_2 Production and Oxidation: A DFT-Based Ligand Design Study

Hadsadee, S.[1]; Ratanasak, M.[1]; Naweephattana, P.[1]; Morita, S.[1]; Miyazaki, R.[1]; Iida, K.[1]; Nakayama, A.[1]; Jungsuttiwong, S.[2]; Hasegawa, J.[1]
([1]Hokkaido University, [2]Ubonrachatani University)

1P25*

Electron Momentum Spectroscopy Study of the Intramolecular Hydrogen Bond in Acetylacetone

Mohri, Fumiya[1]; Sato, Takumi[1]; Takahashi, Masahiko[2]; Ohshima, Yasuhiro[1]; Yamazaki, Masakazu[1;3]
([1]Institute of Science Tokyo, [2]Tohoku University, [3]Keio University)

1P26

Electrochemical Behavior of BiF_3-Based Electrodes in Liquid Electrolyte for Fluoride Shuttle Batteries

Athikaphan, Pakpoom[1]; Tabtimtong, Nicha[2]; Kaisook, Pattanapon[2]; Imai, Yumiko[1]; Ueda, Tadashi[1]; Neramittagapong, Arthit[2,3]; Sutasinee Neramittagapong, 2[3]; Minato, Taketoshi[1,4]

([1]Institute for Molecular Science, National Institutes of Natural Sciences, [2]Department of Chemical Engineering, Faculty of Engineering, Khon Kaen University, [3]Research Center for Environmental and Hazardous Substance Management, Khon Kaen University, [4]Core for Spin Life Sciences, Okazaki Collaborative Platform, National Institutes of Natural Sciences)

1P27*

Polar-molecule trajectory simulations for cluster isolation using a Stark deflector

Miwa, Yutaro[1]; Ardelia, Mellisa[1]; Nakamura, Masaaki[1]; Ohshima, Yasuhiro[1]

([1]Institute of Science Tokyo)

1P28

Photochemical Reaction of Methylene Blue and Ascorbic Acid

Suzuki, Takahiro[1]; Ie, Kanon[1]; Kimura, Takayoshi[1]; Inoue, Masayuki[1]

([1]Tokyo University of Science)

Session 2 (June 3, 14:00–15:30)

2P01*

Photodissociation dynamics of *N*,*N*-dimethylformamide: Generation of highly vibrational excited HCO

Karino, Momiji[1]; Shinohara, Ryo[1]; Inoue, Kosuke[1]; Yamasaki, Katsuyoshi[1]; Kohguchi, Hiroshi[1]
([1]Hiroshima University)

2P02

High-Resolution Laser Spectroscopy of the $S_1 \leftarrow S_0$ transition of Fluorene: Perturbation analysis in the S_1 sate

Kasahara, Shunji[1]; Minik, Luke[1]; Kuroda, Shinji[1]
([1]Kobe University)

2P03*

Photoelectron Circular Dichroism in chiral molecules using 21.7eV HHG light

Matano, Shuhei[1]; Oshima, Ryunosuke[1]; Minemoto, Shinichiro[2]; Sekikawa, Taro[1]
([1]Department of Applied Physics, Hokkaido University, [2]IMRAM, Tohoku University)

2P04

Unimolecular decomposition of highly excited C_2H_4: Trajectory calculations of product branching

Matsugi, Akira[1]; Matsui, Hiroyuki[2]
([1]AIST, [2]NYCU)

2P05*

Simulation of post-ionization population inversion in CO_2^+ in an ultrashort intense laser pulse

Huang, Siwei[1]; Lötstedt, Erik[1,2]; Yamanouchi, Kaoru[1,3]
([1]School of Science, The University of Tokyo, [2]iTHEMS, RIKEN, [3]I-ALFA, The University of Tokyo)

2P06

Relaxation dynamics via the S_1 state of Ag_3^- probed by time-resolved photoelectron imaging

Kusaba, Yuri[1]; Aoki, Yuma[1]; Suzuki, Yuta[1]; Ushiki, Yuta[1]; Shimizu, Misaki[1]; Toyama, Yuki[1]; Terasaki, Akira[1]; Horio, Takuya[1]
([1]Kyushu University)

2P07*

Microsolvation effects on photodissociation dynamics of the hemibonded $(H_2S)_2^+$ ioncore

Shioura, Mitsuaki[1]; Koshiba, Takumi[1]; Kanno, Manabu[1]; Misaizu, Fuminori[1]; Fujii, Asuka[1]
([1]Tohoku University)

2P08

High-resolution laser spectroscopy of the A-X transition of $^{14}NO_2$ radical

Tada, Kohei[1]; Misono, Masatoshi[1]; Yoshizawa, Takumi[2]; Kishigami, Ko[2]; Kasahara, Shunji[3]
([1]Faculty of Science, Fukuoka University, [2]Faculty of Science, Kobe University, [3]Center for Life Photonic Innovation, Kobe University)

2P09*

An analysis of charge migration in the McLafferty rearrangement utilizing natural reaction orbital method

Nakanishi, Tatsuhiro[1]; Takayama, Mitsuo[2]; Taketsugu, Tetsuya[3,4]
([1]Grad. Sch. Chem. Sci. Eng., Hokkaido Univ., [2]Grad. Nanobio., Yokohama City Univ., [3]Dep. Chem., Fac. Sci., Hokkaido Univ., [4]WPI-ICReDD, Hokkaido Univ.)

2P10*

Theoretical Design of Unactivated Arene Conversion Reactions Using Triazene Compounds

Nagano, Ayana[1]; Kokubu, Shusuke[2]; Yamakawa, Kazuhito[2]; Haraguchi, Ryosuke[2]; Sumiya, Yosuke[1]
([1]Yamaguchi University, [2]Chiba Institute of Technology)

2P11

Theoretical study on the thermal dissociation reaction of 3-methylaminopropylamine

Kanno, Nozomu[1]
([1]Meijo University)

2P12*

What Underlies the Woodward-Hoffmann rules? A Reaction Analysis Based on Orbital Energies

Tsuruta, Masaya[1]; Mita, Tsuyoshi[2]; Taketsugu, Tetsuya[2,3]; Tsuneda, Takao[2,4]
([1]Grad. Sch. Chem. Sci. Eng., Hokkaido Univ., [2]WPI-ICReDD, Hokkaido Univ., [3]Fac. Sci., Hokkaido Univ., [4]Grad. Sch. System Informatics, Kobe Univ.)

2P13*

Quantifying the Contribution of Nonreactive Modes to Reaction Dynamics in Phase Space: Analytical Prediction of the Passage Time τ near a Saddle Point

Kurahashi, Ryo[1]; Li, Jizhou[1]; Tanaka, Ryoichi[1]; Umer, Umair[1]; Nagahata, Yutaka[1]; Mizuno, Yuta[2]; Komatsuzaki, Tamiki[1]
([1]Hokkaido University, [2]AIST)

2P14*

Development of a quadratic convergence two-point search algorithm using the Dynamical NEB method

Kanazawa, Ryosuke[1]; Nakatani, Naoki[1]; Nakatani, Kaho[1]
([1]Tokyo Metropolitan University)

2P15*

Electronic Driving Factors in Outer-Sphere Electron Transfer Reactions: A Reactive Orbital Energy Theory Analysis

Yamada, Daisuke[1]; Tsuruta, Masaya[1]; Taketsugu, Tetsuya[2,3]; Tsuneda, Takao[3,4]
([1]Grad. School Chem. Sci. Eng., Hokkaido Univ., [2]Fac. Sci., Hokkaido Univ., [3]WPI-ICReDD, Hokkaido Univ., [4]Grad School of System Informatics, Kobe Univ.)

2P16

Heavy atom tunneling reactions on interstellar icy grain analogs

Tsuge, Masashi[1,2]; Molpeceres, Germán[3]; Sie, Ni-En[1]; Watanabe, Naoki[1]
([1]Hokkaido University, [2]Hiroshima University, [3]IFF CSIC)

2P17*

Molecular orbital signatures in photoelectron circular dichroism of oxirane derivatives studied by a tunnel ionization theory

Kuroda, Runa[1]; Ogawa, Kazumi[1]; Uchida, Tomohide[1]; Nishimura, Koya[1]; Matsuda, Akitaka[1]; Hishikawa, Akiyoshi[1,2]
([1]Grad. Sc. Sci, Nagoya U., [2]RCMS, Nagoya U.)

2P18*

Experimental determination of N-atom surface diffusion activation energy based on the decay of surface number density due to diffusive recombination reactions

Endo, Tamaki[1,2]; Tsuge, Masashi[2,3]; Watanabe, Naoki[2]
([1]Cosmosciences-Graduate School of Science, Hokkaido Univ., [2]Institute of Low Temperature Science, Hokkaido Univ., [3]ADSE, Hiroshima University)

2P19

Dynamical electronic structure change of metal oxide surface with oxygen defects under electric current revealed by first-principles computational method

Toyama, Shunsuke[1]; Iida, Kenji[1]; Hasegawa, Jun-ya[1]
([1]Institute for Catalysis, Hokkaido University)

2P20*

Comparison of HCl dissociation behaviors on hexagonal (I_h) and amorphous ice clusters accounting for nuclear quantum effects

Sasaki, Yuki[1]; Ueno, Hinami[1]; Takayanagi, Toshiyuki[1]; Murakami, Tatsuhiro[2]
([1]Saitama University, [2]Tokyo Metropolitan University)

2P21

Reactions between low-energy CH_3^+ ions and a methanol solid surface at low temperatures

Nakai, Yoichi[1]; Hidaka, Hiroshi[2]; Watanabe, Naoki[2]
([1]RIKEN Nishina Center, [2]ILTS, Hokkaido University)

2P22*

Development of a new apparatus for atomic momentum spectroscopy at the world's highest incident electron energy

Kanaya, Satoru[1]; Minemoto, Shinichirou[1]; Jagutzki, Ottmar[2,3]; Takahashi, Masahiko[1]
([1]IMRAM, Tohoku university, [2]Institut für Kernphysik, Universität Frankfurt, [3]RoentDek Handels GmbH)

2P23

Methanol formation via CH_3 + OH reactions with transient diffusion on amorphous solid water at low temperatures

Hidaka, Hiroshi[1]; Iguchi, Arisa[2]; Ishibashi, Atsuki[3]; Tsuge, Masashi[4]; Oba, Yasuhiro[1]; Watanabe, Naoki[1]
([1]Hokkaido University, [2]The University of Electro-Communications, [3]The University of Tokyo, [4]Hiroshima University)

2P24*

Kinetic analysis of luminol chemiluminescence in dimethyl sulfoxide driven by dissolved oxygen under a nitrogen atmosphere

Ie, Kanon[1]; Suzuki, Takahiro[2]; Inoue, Masayuki[2]
([1]Graduate School of Science, Tokyo University of Science, [2]Tokyo University of Science)

2P25

Development and Application of a Conformational Analysis Method Combining MD Simulation and Ion Mobility Mass Spectrometry

Tashiro, Keisuke[1]; Ide, Yuki[2]; Taketsugu, Tetsuya[1,2]; Ohara, Kazuaki[3]; Yamaguchi, Kentaro[3]; Kobayashi, Masato[1,2]; Inokuma, Yasuhide[2,4]
([1]Fac. Sci., Hokkaido Univ., [2]WPI-ICReDD, Hokkaido Univ., [3]Fac. Pharm. Sci., Tokushima Bunri Univ., [4]Fac. Eng., Hokkaido Univ.)

2P26*

Development of Fourier Transform Three-Color Excitation Action Spectroscopy for Model-Free Analysis of Photo-Stationary States

Yamashita, Sayaka[1]; Inoue, Rinka[1]; Fukuda, Kai[1]; Wada, Akihide[1]
([1]Kobe University)

2P27

Vibrational states and transition intensities based on variational vibrational theory

Sunaga, Ayaki[1,2]
([1]Hokkaido University, [2]Eötvös Loránd University)

Session 3 (June 4, 13:30–15:00)

3P01*

Substituent Effects on Electrocyclic Reactions: Ultrafast Ring-Opening of α-Phellandrene Stimulated by Impulsively Excited Molecular Vibrations

Zhou, Zhiyi[1]; Saita, Kenichiro[2]; Minegishi, Yusuke[3]; Taketsugu, Tetsuya[4,5]; Sekikawa, Taro[1]

([1]Appl. Phys., Eng., Hokkaido Univ., [2]Nanobiosci., Yokohama City Univ., [3]Chem. Sci. Eng., Hokkaido Univ., [4]Chem., Sci., Hokkaido Univ., [5]WPI-ICReDD, Hokkaido Univ.)

3P02

Photochemical reaction of pyrene with CCl_4 in alcohols

Watanabe, Akihiro[1]; Kanemura, Sakura[1]; Naruo, Nanami[1]

([1]Kobe City College of Technology)

3P03*

Ion pair dissociation of carbon dioxide following absorption of a vacuum ultraviolet photon

Oda, Akiko[1]; Suzuki, Isao H.[1]; Odagiri, Takeshi[1]

([1]Sophia University)

3P04

Rotational excitation of NO in an intense femtosecond laser field carrying orbital angular momentum

Fukahori, Shinichi[1,2]; Hasegawa, Hirokazu[1,2]

([1]Graduate School of Arts and Sciences, The Univ. of Tokyo, [2]Komaba Institute for Science, The Univ. of Tokyo)

3P05*

Photodissociation pathways of O_4^+ leading to singlet oxygen $O_2(a\ ^1\Delta_g)$ and $O_2(b\ ^1\Sigma_g^+)$ studied by mass-analyzed ion imaging

Watabe, Yu[1]; Koshiba, Takumi[1]; Ito, Yuri[1]; Kanno, Manabu[1]; Ohshimo, Keijiro[2]; Misaizu, Fuminori[1]

([1]Graduate School of Science, Tohoku Univ., [2]Hokkaido University of Education)

3P06

Mechanism of the delayed fragmentation of ethanol molecules upon VUV photoionization

Nakao, Tomohiko[1]; Kaneyasu, Tatsuo[2,3]; Yanagawaya, Takuma[1]; Iwayama, Hiroshi[2]; Majima, Takuya[1]

([1]Kyoto University, [2]Institute for Molecular Science, [3]Sokendai)

3P07*

The relationship between photon energy and two translational energy components of the CH_3 fragment in photodissociation of $Zn(CH_3)_2$

Morimoto, Takumi[1]; Okuda, Yuuka[1]; Haze, Misato[1]; Kohguchi, Hiroshi[1]
([1]Hiroshima University)

3P08

Solvent effects on the ground and first excited states of aniline

Ohashi, Kazuhiko[1]
([1]Kyushu University)

3P09*

Mechanochemical Reaction Path Analysis of Polymer Chain Cleavage

Mori, Itsuki[1]; Sumiya, Yosuke[1]
([1]Yamaguchi Univ.)

3P10

Elucidation of the Mechanism of Bifurcation Control in Enzymatic Reactions Based on the Reaction Space Projector Method

Qu, Lihao[1]; Tsutsumi, Takuro[1]; Ono, Yuriko[1]; Taketsugu, Tetsuya[1]
([1]Hokkaido University)

3P11*

Accelerating the Mechanistic Study of Triarylborane Catalysts through Virtual Borane

Hirose, Ken[1]; Maeda, Satoshi[1,2]; Matsuoka, Wataru[1,2]
([1]Hokkaido University, [2]WPI-ICReDD)

3P12*

Mechanistic Study on the Degradation of Aliphatic Amines for CO2 Capture Using Systematic Reaction Path Exploration

Toma, Shunta[1]; Sumiya, Yosuke[1]
([1]Yamaguchi Univ)

3P13*

Machine-learning extraction of reaction coordinates and transition states in phase space

Noda, Takuto[1]; Md. Al Mehedi, Hasan[2]; Li, Jizhou[2]; Komatsuzaki, Tamiki[1,2,3]
([1]CSE, Hokkaido University, [2]RIES, Hokkaido University, [3]WPI-ICReDD, Hokkaido University)

3P14*

Exploring Valley-Ridge Inflection Regions in Post-Transition State Bifurcation Reactions

Yamaki, Keita[1]; Okamoto, Daichi[1]; Hayashi, Daiki[1]; Nakagawa, Shoto[1]; Matsubuchi, Hayato[1]; Sasaki, Yuki[1]; Takayanagi, Toshiyuki[1]; Murakami, Tatsuhiro[2]
([1]Saitama University, [2]Tokyo Metropolitan University)

3P15*

Machine Learning-based Multi-objective Optimization of reaction condition of ^{211}At Astatination Reactions

Kitano, Tomoyuki[1]; Hashiba, Shunnichi[1]; Ando, Masaya[1]; Iida, Keita[1]; Mukaimine, Akari[1]; Mizuno, Yuta[2,1]; Tabata, Koji[1]; Nakajima, Kohei[1]; Komatsuzaki, Tamiki[1]; Ogawa, Mikako[1]
([1]Hokkaido University, [2]AIST)

3P16*

Can Reactive Species Be Spontaneously Formed at the Air－Water Interface of Microdroplets? A Spray Ionization Mass Spectrometry Investigation

Kurokawa, Kei[1]; Enami, Shinichi[1]; Numadate, Naoki[1]
([1]Tsukuba University)

3P17

Transient diffusion of radicals induced by surface reactions at 10 K

Ishibashi, Atsuki[1,2]; Hidaka, Hiroshi[2]; Iguchi, Arisa[2]; Watanabe, Naoki[2]
([1]The University of Tokyo, [2]Hokkaido University)

3P18*

Theoretical investigation of the structure and electronic properties of N_2O adsorbed on an Ir_{20} cluster.

Uchiyama, Nino[1]; Taketsugu, Tetsuya[1]; Hinokuma, Satoshi[2]; Iwasa, Takeshi[1]
([1]Hokkaido University, [2]AIST)

3P19

A near-edge x-ray absorption fine structure study of products in ice film by monochromic soft x-ray irradiation

Nakagawa, Seiko[1]; Obata, Yui[2]; Baba, Yuji[3]; Yokoya, Akinari[2,4]
([1]Tokyo Metropolitan Industrial Technology Research Institute, [2]Ibaraki University, [3]Japan Atomic Energy Agency, [4]National Institutes for Quantum Science and Technology)

3P20*

Nonlinear photocurrent generation in SiO_2 device by ω-2ω asymmetric strong laser fields

Kinoshita, Hiroshi[1]; Matsumoto, Ryutaro[1]; Fushitani, Mizuho[1]; Hishikawa, Akiyoshi[1]
([1]Nagoya University)

3P21

Syntheses and evaluation of photocatalytic activities of the composites of antimony halide perovskites and graphitic carbon nitride

Akiyama, Sogo[1]; Iitaka, Fumiaki[1]; Kadota, Yusuke[1]; Mitsuke, Koichiro[1,2]; Ogata, Hironori[1,2]
([1]Hosei University, [2]Hosei Univ. Res. Cntr. Micro-Nano Technol.)

3P22*

Electron momentum spectroscopy of aniline: Towards molecular orbital imaging of the excited triplet state

Sato, Takumi[1]; Mori, Yutori[1]; Takahashi, Masahiko[2]; Ohshima, Yasuhiro[1]; Yamazaki, Masakazu[1.3]
([1]Institute of Science Tokyo, [2]Tohoku University, [3]Keio University)

3P23

Toward Time-Resolved Core-Level Spectroscopy Beyond Oxygen K-edge Using an Ultrashort Soft X-ray Light Source

Ishii, Nobuhisa[1]; Sun, Hung-Wei[1]; Maruyama, Momoko[1]; Itakura, Ryuji[1]
([1]Kansai Institute for Photon Science, QST)

3P24*

Distribution of ions at the air-water interface investigated by spray ionization mass spectrometry

Kosugi, Kento[1]; Numadate, Naoki[1]; Enami, Shinichi[1]
([1]University of Tsukuba)

3P25

Synthesis and Optical Property of Eu doped Carbon Dots

Hamada, Morihiko[1]; Tanaka, Misaki[1]; Fuki, Masaaki[2]; Kobori, Yasuhiro[2]
([1]Kobe City College of Technology, [2]Kobe University)

3P26*

A Systematic Exploration of Nonradiative Decay Paths in Carbo[n]Helicenes(n=5-12): Role of Cyclization Paths

Kondo, Itsuki[1]; Harabuchi, Yu[2,3]; Akiyama, Seiji[4]; Nagata, Yuuya[2,3,5]; Maeda, Satoshi[2,3,6]

([1]Graduate School of Chemical Sciences and Engineering, Hokkaido University, [2]WPI-ICReDD, Hokkaido University, [3]JST, ERATO, [4]RIKEN, [5]NIMS, [6]Graduate School of Science, Hokkaido University)

3P27

The rate rules for the reactions of Alkenes with OH

Fushimi, Ryota[1,2]; Oguchi, Tatsuo[1]

([1]Toyohashi University of Technology, [2]National Institute of Technology, Hakodate College)

Invited Lectures

IL1 Tunnel-Electron Momentum Imaging of Gas-Phase Molecules in Intense Laser Fields

([1]RCMS Nagoya U, [2]Graduate School of Science, Nagoya U) Akiyoshi HISHIKAWA[1, 2]

Quantum tunneling, a key manifestation of the wave nature of matter, plays a central role in modern science and technology. The scanning tunneling microscope (STM), for example, exploits electron tunneling to probe the properties of individual molecules on surfaces, including the energies and symmetries of molecular orbitals. Electron tunneling also plays a pivotal role in atomic and molecular dynamics in intense laser fields (~10^{14} W/cm^2), including high-order harmonic generation, laser-induced electron diffraction, and Coulomb explosion. These phenomena have become indispensable tools in ultrafast spectroscopy on the atto- and femtosecond timescales.

In circularly polarized laser fields, a tunnel electron forms a torus- (or donut-) like structure in momentum space (Fig. 1(a)). The angular distribution along the major circle reflects the dependence of the ionization yield on the direction of the instantaneous electric field relative to the molecule, providing information on the symmetry of the ionizing molecular orbital. In contrast, the cross section of the torus represents the photoelectron momentum distribution perpendicular to the instantaneous laser electric field at the moment of tunneling. This transverse momentum distribution (TMD) encodes target properties such as the ionization potential, dipole moment, polarizability, and molecular-orbital shape. Here, we present our recent studies on gas-phase molecules to demonstrate how rich information can be extracted by three-dimensional tunnel-electron momentum imaging.

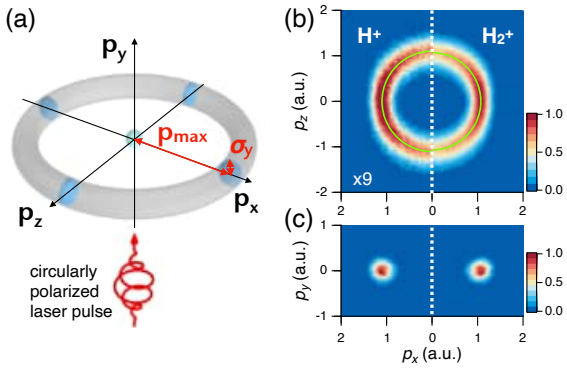

Fig.1 (a) Schematic of photoelectron momentum distributions (PEMDs) for tunneling ionization in circularly polarized intense laser fields. Laboratory-frame PEMDs of H_2, recorded in coincidence with H^+ (left) and H_2^+ (right) (b) in the p_x - p_z plane and (c) in the $p_x - p_y$ plane [1].

[Quantitative decoding of intense-field ionization] Using H_2 as a benchmark system, we proposed a method to determine the effective laser-field amplitude (F) and the effective ionization potential (I_p) from the photoelectron momentum torus formed by tunnel ionization in an intense circularly polarized laser field. Based on state-of-the-art tunnel-ionization theory, we derived expressions for the parameters characterizing the torus shape, namely the torus radius (p_{max}) and the width of the transverse momentum distribution (σ_y). By analyzing these expressions as simultaneous equations for the torus parameters obtained from three-dimensional tunnel-electron–ion coincidence measurements in Fig.1(b), we determined F and I_p simultaneously (Fig. 2). For the H_2^+ ionization channel, the obtained I_p was found to be smaller than the vertical ionization potential of H_2, in agreement with theoretical predictions of tunnel ionization theory that incorporate the effect of nuclear motion.

Furthermore, for the H^+ ionization channel, an ionization potential different from that for H_2^+ was obtained. This difference is interpreted as reflecting the post-ionization time evolution of the nuclear wavepacket and the dissociation selectivity induced by interaction with the laser field. These results represent an important advance toward establishing ultrafast tunnel-electron spectroscopy as a basis for the quantitative characterization of molecules in laser fields.

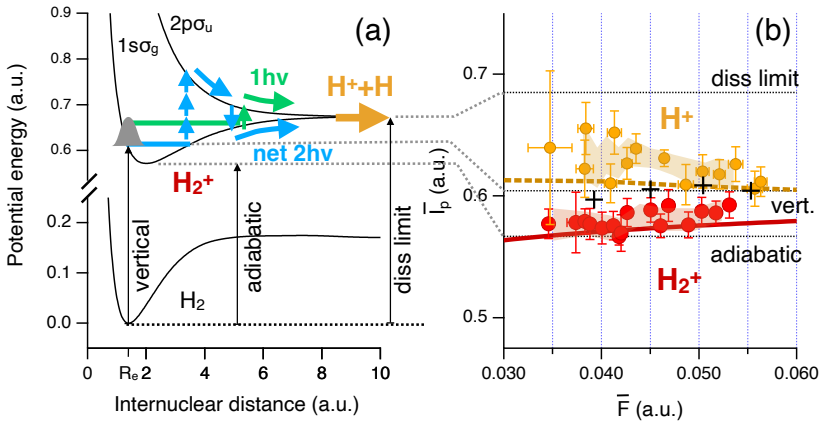

Fig. 2. (a) Potential energy curves of H_2 and H_2^+. (b) Ionization potential I_p plotted against the field amplitude F for H_2^+ (red) and H^+ (orange). Solid line shows the theoretical I_p incorporating the nuclear motion effect. Results from the wavepacket calculation for H^+ are also shown (dashed line). Results of TDSE calculation are also shown (cross).

[Spin-orbit-state-resolved RFPAD] The recoil-frame photoelectron angular distribution (RFPAD) of methyl iodide (CH_3I) was measured using an auxiliary dissociation pulse. The spin-orbit-state-resolved tunnel ionization channels to CH_3I^+ ($X^2E_{3/2}$, $X^2E_{1/2}$) exhibit clear differences in their RFPADs. Calculations of tunnel ionization rates based on the corresponding Dyson orbitals reproduce the characteristic features of the measured RFPADs, highlighting the importance of multielectron effects in laser-induced tunnel ionization.

[Tunnel-electron circular dichroism] Photoelectron circular dichroism (PECD) in tunnel ionization of the chiral molecule methyloxirane (MOX) was investigated. The TMD exhibits a clear PECD effect, namely a forward–backward asymmetry along the laser propagation direction, with a sign reversal as a function of p_{max}. The underlying mechanism was examined through comparison with model calculations based on tunnel-ionization theory, demonstrating the importance of the chirality of the ionizing molecular orbital.

Acknowledgements A.H. thanks D. Ikeya, K. Yasui, H. Hasegawa, R. Kuroda, J. Yazawa, A. Matsuda, M. Fushitani (Nagoya U), T. Morishita (UEC), O. I. Tolstikhin (MIPT) for their contributions, and JSPS KAKENHI (JP16H04029, JP19H00887, JP21K18929, JP22H00313, JP26H02267).

[References]

[1] D. Ikeya, H. Fujise, M. Takahashi, K. Yasui, A. Matsuda, M. Fushitani, H. Matsui, H. Hasegawa, O. I. Tolstikhin, T. Morishita, and A. Hishikawa, Phys. Rev. Res. 7 (2025) L032059.

IL2 Dynamics of Atoms and Molecules under the Influence of Intense Laser Pulses

Ashawani Kumar Tiwari

Department of Chemical Sciences, Indian Institute of Science Education and Research Kolkata, Mohanpur 741246, Email: ashwani@iiserkol.ac.in

Atoms and Molecules show many exotic behaviours under the influence of strong laser pulses. In the recent experiments, it has been shown that electronic and nuclear dynamics strongly depends on the Carrier Envelop Phase (CEP) of the few femto second pulses. In my talk, I will discuss origin Of the CEP dependent dynamics for the certain prototype atoms and molecules.

References:

1. Intense 2-cycle laser pulses induced time-dependent bond hardening in a polyatomic molecule; K. Dota, M. Garg, **A. K. Tiwari**, J.A. Dharmadhikari, A.K. Dharmadhikari and D. Mathur, ***Phys. Rev. Lett.* 108,** 073602 (2012).
2. Controlling Electron Dynamics with Carrier Envelope Phases of a Laser Pulse ; D. Dey, D. Ray and **A. K. Tiwari *J. Phys. Chem. A.,* 123,** 4702-4707 (2019).
3. Controlling the ultrafast dynamics of HD^+ by the carrier-envelope phases of an ultrashort laser pulse: A quasi-classical dynamics study; G. Pandey, D. Dey and **A. K. Tiwari *J. Phys. Chem. A.,* 124,** 9710-9720 (2020)
4. Attosecond coupled electron-nuclear dynamics of H_2 molecule under intense laser fields; G. Pandey, and **A. K. Tiwari *Eur. Phys. J. D,* 76,** 75 (2022).
5. Dissociative ionization of H_2 molecule under strong elliptically polarized laser field: Carrier-envelope phase and orientation effect; G. Pandey, Sandip Ghosh and **A. K. Tiwari *Phys. Chem. Chem. Phys.,* 24,** 24582-24592 (2022)

IL3 Nuclear quantum effects in semiclassical and mixed quantum-classical nonadiabatic molecular dynamics

Chaoyuan Zhu

Department of Applied Chemistry, National Yang Ming Chiao Tung University, Taiwan

[Abstract]

Nonadiabatic switching probabilities play a central role in on-the-fly trajectory surface-hopping molecular dynamical simulations. Within mixed quantum–classical nonadiabatic frameworks, where nuclear operators are neglected, both the analytical Landau–Zener formula and the numerical Tully fewest-switches algorithm are generally regarded as nearly exact. In contrast, within semiclassical nonadiabatic theories that explicitly include nuclear operators, the Zhu–Nakamura approach and modified versions of Tully's fewest-switches method are considered to be similarly accurate descriptions. Numerical examples can further illustrate how nuclear quantum effects influence nonadiabatic transition probabilities.

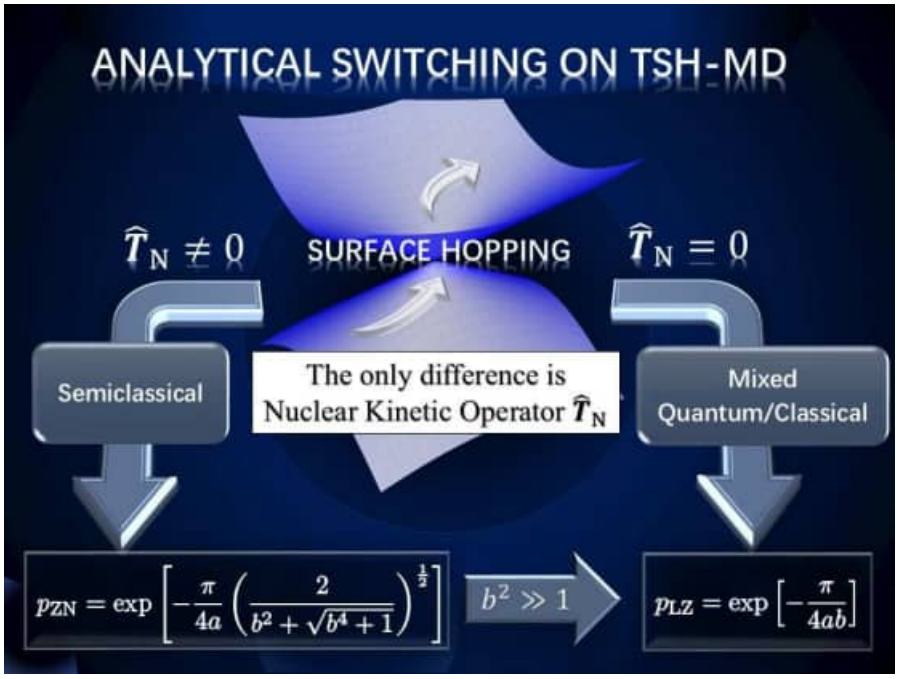

IL4 Numerical analysis of the pathway selection in fully reversible chemical reaction networks

(The University of Tokyo) Satoshi Takahashi

Over the past 10 years, we have pioneered a computational method that treats real chemical reactions as transitions on complex reaction networks composed of expected intermediates and stable structures. By analyzing the transition dynamics among these elements, we have been able to numerically track the self-assembly processes of supramolecular systems and elucidate reaction mechanisms, thereby demonstrating the effectiveness of this approach [1]. In this talk, two topics are mainly presented, both of which are related to different types of the M_6L_4 self-assembly complex (M: metal center with two coordination sites, L: tritopic ligands).

[Emergence of quasi-irreversibility and pathway selection]

Chemical reactions represented with the network composed solely of reversible elementary reactions are governed by thermodynamics, and thus, kinetics and pathway selection have not been discussed well. However, as seen in protein folding and molecular self-assembly, unexpected metastable species called kinetic traps can be obtained in nature. Their formation processes have been mainly explained by the kinetic stability, but in the cases with reversible elementary reactions alone, the direction to which each reaction preferentially proceeds is determined via adaptation to the surrounding environment, and the general idea of what principle is used to select the reaction pathway has not yet been established. In this study, we have clarified that the emergence of quasi-irreversibility is the key to the pathway selection in fully reversible chemical reaction networks.

We performed numerical simulations in the network for M_6L_4 truncated tetrahedron complex (**TT**), whose self-assembly pathways can be broadly classified into two groups. Pathway analysis revealed the main pathway, showing an appearance of quasi-irreversibility in spite of almost the same rate constants for forward and backward processes ($k_+ \simeq k_-$). The elementary reaction on the other pathway with the same parameters k_+ and k_- behaved reversibly, with the direction reversed over time. It was found that the behavior of each elementary reaction is determined not only by the rate constant but also by the network structure [2].

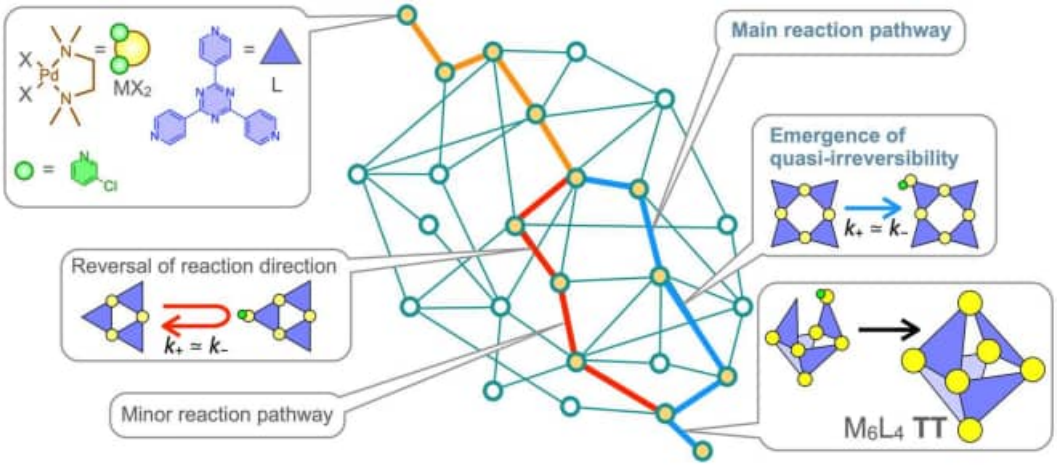

Fig. 1. Schematic illustration for the self-assembly of an M_6L_4 truncated tetrahedron (**TT**).

[Hybridization of reversibility and irreversibility]

Based on experimental results showing that the yield of an M_6L_4 square-based pyramid complex (**SP**) largely increases when the coexisting anion ReO_4^- acts as a catalyst, we performed numerical simulations and analysis using a mathematical model in which the chemical reaction network is composed of reversible elementary reactions.

When ReO_4^- is absent, triangular intermediate species (M_3L_3 and M_4L_3X) were trapped, and their conversions afterward were prevented. ReO_4^- indirectly promoted the subsequent elementary reactions by significantly accelerating the final steps in the self-assembly, though the direct increase in the rate constant was small for the most difficult reaction step to reach **SP**. This uneven acceleration behavior is due to the fact that the acceleration trend depends on the coordination ability of L. To investigate this heterogeneous effect, which was corroborated in experiments with a mononuclear model system by the finding that the accelerating effect of ReO_4^- is greater for ligands with weaker coordinating ability, we numerically determined the ligand exchange rate constants using those model complexes and confirmed that tendency. On the other hand, the metastable state biased to **SP** was maintained by reversible reaction loops involving **SP**. Such an appropriate co-creation of global irreversibility and local reversibility promoted by the catalytic action of the anion was found to increase the product yield and accelerate the global self-assembly reaction [3].

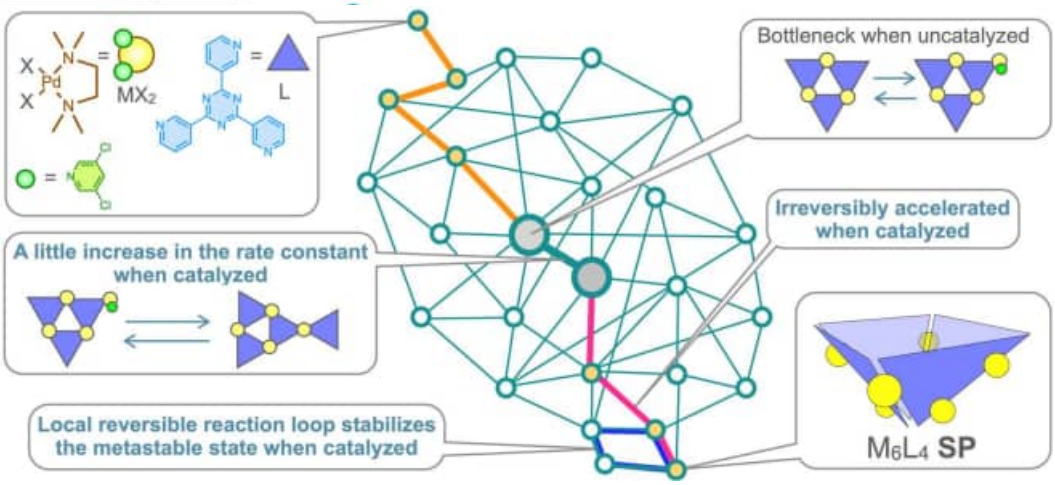

Fig. 2. Schematic illustration for the self-assembly of an M_6L_4 square-based pyramid (**SP**).

Acknowledgments: The researches related to molecular self-assembly, including those presented here, were conducted at the Laboratory of Prof. Shuichi Hiraoka at the Graduate School of Arts and Sciences, The University of Tokyo, and was carried out in collaboration with Prof. Hirofumi Sato at the Graduate School of Engineering, Kyoto University. I would like to express my gratitude to the co-authors of the papers related to these studies.

[1] S. Takahashi, S. Iuchi, S. Hiraoka, and H. Sato, *Phys. Chem. Chem. Phys.* **25**, 14659–14671 (2023). 10.1039/D3CP00082F.

[2] S. Takahashi, T. Abe, H. Sato, S. Hiraoka, *Chem* **9**, 2971–2982 (2023). 10.1016/j.chempr.2023.06.015.

[3] T. Abe, S. Takahashi, R. Chai, H. Sato, S. Hiraoka, *Chem* **12**, 102741 (2026). 10.1016/j.chempr.2025.102741.

IL5 Absolute rate constants and branching fractions for low temperature reactions and inelastic collisions of astrophysical interest

(Univ Rennes, CNRS, IPR (Institut de Physique de Rennes) - UMR 6251, F-35000 Rennes, France) I.R. Sims and the CRESUCHIRP team

Outside of artificially created laboratory environments, the coldest places in the Universe are to be found in dense interstellar clouds, and in particular pre-stellar cores, with temperatures as low as 5.5 K [1]. Observations reveal a rich inventory of molecules, evidence of a surprisingly active chemistry occurring under these extreme conditions. State-of-the-art astrochemical models often fail to predict accurately the observed abundances of these gas-phase (mainly) organic molecules, sometimes by many orders of magnitude. This is in part due to a lack of knowledge of important chemical kinetics input parameters – the rate coefficients and in particular product branching ratios for formation and destruction reactions of these species, especially at low temperatures. Furthermore, transformation of radioastronomical detections into absolute abundances requires knowledge not only of radiative transitions but also collisional (de-) excitation by the most abundant species in these environments (hydrogen, helium, ..).

The CRESU technique (Cinétique de Réaction en Ecoulement Supersonique Uniforme or reaction kinetics in uniform supersonic flow) [2] employs carefully controlled expansions through Laval nozzles to recreate gas phase environments at such low temperatures. Using ultraviolet photolysis or infrared pumping combined with probes such as laser-induced fluorescence or chirped pulse Fourier transform millimeter wave spectroscopy, we can measure absolute cross sections or rate constants for a variety of reactive [2-4] and inelastic [5-7] molecular collisions to provide essential data for astrochemical models and astronomical observations. I will describe our latest measurements, including a focus on new measurements on collisional excitation and the determination of absolute rate constants for the formation of weakly bound complexes, the first stage in homogeneous nucleation, the key link between the gas-phase and condensed phases.

References

[1] A. Crapsi, P. Caselli, M.C. Walmsley, and M. Tafalla, 2007, A&A 470, 221.
[2] I. R. Cooke and I. R. Sims, 2019, ACS Earth Space Chem. 3, 1109.
[3] I. R. Cooke, D. Gupta, J. P. Messinger, and I. R. Sims, *Astrophys. J. Lett*. 891, L41 (2020).
[4] T. Guillaume, B. M. Hays, D. Gupta, I. R. Cooke, O. Abdelkader Khedaoui, T. S. Hearne, M. Drissi, and I. R. Sims, 2024, *J. Chem. Phys.* 160, 16, 204201.
[5] I. R. Cooke, I. R. Sims, in *Uniform Supersonic Flows in Chemical Physics: Chemistry Close to Absolute Zero Studied Using the CRESU Method*, A. Canosa, D. E. Heard, B. R. Rowe, Eds. (World Scientific, 2022), chap. 7, pp. 393-434.
[6] H. Labiad, M. Fournier, L. A. Mertens, A. Faure, D. Carty, T. Stoecklin, P. Jankowski, K. Szalewicz, S. D. Le Picard, and I. R. Sims, 2022, *Phys. Rev. A* 105, 6, L020802; H. Labiad, A. Faure, and I. R. Sims, *Phys. Rev. A* 112, 062816 (2025).
[7] B. M. Hays, D. Gupta, T. Guillaume, O. Abdelkader Khedaoui, I. R. Cooke, F. Thibault, F. Lique, and I. R. Sims, 2022, *Nature Chemistry* 14, 811.

IL6 Elementary reaction rate constants of organic free radicals in liquid phase as measured by the laser synchronized pulsed ESR method

([1]Grad. Sch. of Sci., Kanagawa Univ.; [2]Inst. Quant. Life Sci., Natl. Inst. Quant. Sci. Tech.; [3]Fac. Mol. Chem. Eng., Kyoto Inst. Tech.) Akio Kawai[1,2], Ikuo Nakanishi[2], Yusuke Miyake[3], Masatoshi Kato[1]

Introduction

Free radicals are important intermediate species controlling various fast and complex reactions. To understand the free radical reaction mechanisms, kinetic studies based on the elementary reaction rate constants are of significance. To determine the rate constants, transient absorption methods are widely used for short-lived free radicals. Although electronic absorption spectroscopy is very sensitive and its time-resolution is high enough to probe time-evolution of short-lived intermediates, many radicals have no or weak absorption in UV/VIS wavelength regions except the ones with conjugated π-orbitals. Therefore, the transient absorption method is not always applicable for measurements of free radicals. ESR spectroscopy is another important tool to monitor free radicals in solution chemistry and assignment of radicals by the hyperfine structure is quite reliable. Nowadays, time-resolved (TR-)ESR detection is possible for many reaction systems with sub-microsecond time resolution. However, TR-ESR signal intensity depends on various factors and in general, it does not reflect the concentration of free radical. Because of this complicated character, determination of kinetic parameters of free radical reactions is not straightforward by TR-ESR.

In early 21st century, a new method was proposed to determine radical reaction rate constants by using pulsed ESR synchronized with pulsed laser excitation [1]. This method includes two important frameworks : (1) Free radicals were generated by photo-dissociation of aromaticketones. This process creates spin-polarized free radicals, whose ESR signals are largely enhanced. (2) Electron spin echo (ESE) signal of the spin-polarized radical was generated by a pulsed microwave irradiation, which enables us to measure ESE decay rate. In general, this rate gives transverse spin relaxation time, but in the presence of radical scavengers, echo decay rate becomes faster than the rate without scavenging reaction. This discrepancy originates from the radical reaction process. We have been applying this method for various reactions of alkyl type radicals and determined the rate constants of addition reactions and hydrogen abstraction reactions [2-6]. Here, we overview these results of laser-synchronized pulsed ESR spectroscopic studies for radical chemistry.

Experimental

TR- and pulsed-ESR measurements were made by an X-band ESR spectrometers (Bruker, ELEXIS). The light sources were a Nd^{3+}: YAG laser (Continuum, Surelite I-10, 7 mJ/pulse, 10 Hz) or a diode pumped laser (EKSPLA, NT200, 1 mJ/pulse, 50Hz). For Pulsed-ESR, a dielectric resonator cavity was used. Sample solutions were flowed through the quartz cell in the ESR cavity at 295 K.

Results and Discussion

Organic free radicals were produced by the Type I photodissociation under the 355 nm laser photolysis of aromaticketones. Fig. 1 shows an example of the photodissociation reaction scheme for the generation of hydroxycyclohexyl (Hy-CyH) radical from IRG184. The rapid dissociation gives rise to the electron spin-polarized radicals with α-spin enriched population through the triplet mechanism that is well-studied spin polarization generation mechanism. We have examined a few different substituted alkyl radicals as models to learn free radical reactions.

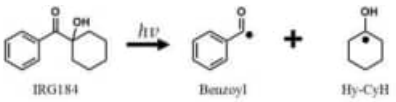

Fig.1 Photodissociation scheme of IRG184

Fig. 2(a) shows TR-ESR spectrum of IRG184 in solution recorded at 0.5-1.0 μs after laser shot. The spectrum shows a quintet splitting due to four equivalent hydrogens of Hy-CyH along with a singlet peak of benzoyl type radical near the center. These peaks were observed with microwave emission due to the strong electron spin polarization. Fig. 2(b) shows TR-ESR spectrum measured with tri-*tert*-butyl-phenol (TTBP). Hy-CyH intensity was weakened and the phenoxy type radical was observed near the benzoyl peak [6]. The expanded view shows the triplet peak with 1.8 G splitting for phenoxy. This value agrees with the literature, which is attributed to the aromatic protons. This result indicates Hy-CyH undergoes hydrogen abstraction with TTBP.

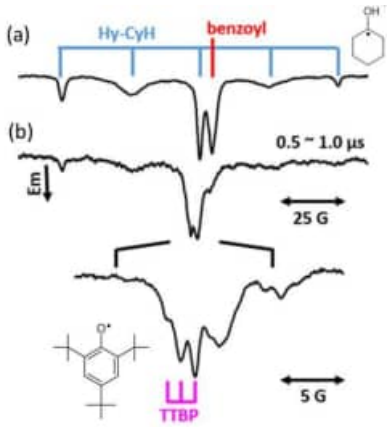

Fig.2 TR-ESR spectra for Hy-CyH and TTBP system

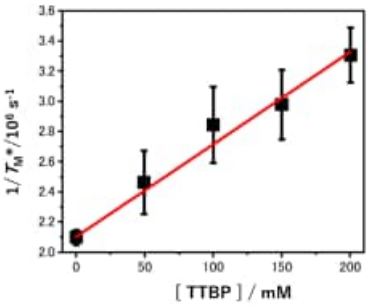

Fig.3 Stern-Volmer plot for ESE decay rate of Hy-CyH vs. [TTBP]

Then, reaction rate constants were determined by monitoring ESE decays. Fig. 3 shows Stern-Volmer plot of the ESE decay rate. The linear fitting for the slope gives rate constant of Hy-CyH with TTBP. Similar analysis for the rate constants of elementary reaction processes was made for various radical scavengers such as olefines monomers, phenols, fullerenes and RAFT agents. Based on the results, radical reaction mechanism will be argued in the view-point of enthalpy effect and charge transfer interaction. Advantageous points of the pulsed ESR method will also be discussed.

References

[1] M. Weber, N. J. Turro, *J. Phys. Chem. A* **2003**, *107*, 3326.

[2] H. Takahashi, Y. Marushima, K. Tsuji, K. Shibuya, A. Kawai, *J.Phys.Chem.A* **2015**, *119*, 8261.

[3] H. Takahashi, H. Hirano, K. Nomura, K. Hagiwara, A. Kawai, *Chem.Phys.Lett.*, **2021**, *763*, 138205.

[4] H. Hirano, H. Takahashi, A. Kawai, *J. Phys. Chem. B*, **2022**(126), 6074-6082.

[5] H. Takahashi, H.Hirano, A. Kawai, *J. Photochem. Photobiol. A: Chemistry*, **2023**(763), 114690- 114697.

[6] H. Hirano, A. Nagata, K. Marumo, H. Takahashi, I. Nakanishi, A. Kawai, *J.Chem.Phys.*, **2025**(162), 124707.

IL7 Exploring Dynamics in Molecular Systems using Quantum Science and Technology

(U. Tokyo) Akihito Ishizaki, Yuta Fujihashi

Quantum light, such as entangled photons, is a fundamental resource for advancing cutting-edge quantum technology. A primary application aims to improve the precision of optical measurements via non-classical photon correlations; consequently, quantum metrology has rapidly gained widespread attention for its capacity to make measurements with sensitivity and resolution beyond classical limits. Accordingly, it is anticipated that quantum light will also open new avenues for optical spectroscopy by leveraging the unique properties of quantum states [1].

In this presentation, we discuss spectroscopy using entangled photon pairs to probe exciton and charge dynamics in complex molecules. Specifically, we address the transmission measurement of frequency-entangled broadband photon pairs generated via parametric down-conversion with a monochromatic laser. We observe that state-to-state dynamics in the system under study can be temporally resolved by adjusting the path difference between the entangled twin beams, provided that the entanglement time is sufficiently short. Such non-classical photon correlations enable time-resolved spectroscopy using monochromatic pumping instead of a pulsed laser. We further demonstrate that the signal corresponds to the spectral information along the anti-diagonal lines of, for example, two-dimensional Fourier-transformed photon echo spectra [2]. This correspondence suggests that more elaborately engineered photon states could significantly broaden the applicability of quantum light spectroscopy.

However, it should be noted that the resulting signals are typically too weak for practical time-resolved experiments. To address this challenge, we propose two-dimensional time-resolved fluorescence spectroscopy that exploits these correlations and operates with current single-photon detectors. The method offers two key advantages over conventional 2D electronic spectroscopy: (i) it yields 2D spectra without phase-stable multi-pulse control, relying instead on heralded twin-photon correlations; and (ii) it simplifies spectra by isolating the contribution spectroscopically equivalent to stimulated emission, thereby suppressing ground-state bleaching and excited-state absorption. Numerical calculations for a natural pigment-protein complex–inspired trimer demonstrate that this pathway selectivity enables the extraction of rich information on energy transfer dynamics [3]. These results indicate a feasible route to the real-time observation of molecular dynamics using entangled photon pairs.

[1] S. Mukamel, “Roadmap on quantum light spectroscopy,” *J. Phys. B: At. Mol. Opt. Phys.* **53**, 072002 (2020).

[2] A. Ishizaki, “Probing excited-state dynamics with quantum entangled photons: Correspondence to coherent multidimensional spectroscopy,” *J. Chem Phys.* **153**, 051102 (2020).

[3] Y. Fujihashi, O. Iso, R. Shimizu, A. Ishizaki, “Two-dimensional fluorescence spectroscopy with entangled photons and time- and frequency-resolved two-photon coincidence detection,” *Sci. Adv.* **12**, eaed7026 (2026).

Oral Presentations

1A1 Impact of C5 Methylation on Nonadiabatic Transition and Photohydration Damage of Nucleosides

(Kyoto U.[1] and U. Bologna[2]) Srijon Ghosh,[1]Yuki Obara,[1] Vishal Kumar Jaiswal,[2] Mario Taddei,[2] Artur Nenov, [2] Irene Conti,[2] Marco Garavelli,[2] ○Toshinori Suzuki[1]

Recently, it has been found that ultrafast internal conversion of UV-excited pyrimidine nucleosides and nucleotides in aqueous solution generates a twisted intermediate (TI) in the ground state (S_0). Here, we report a combined experimental and theoretical study on the ultrafast internal conversion, the subsequent photohydration process of these molecules, and the pronounced effects of C5 methylation on their dynamics.

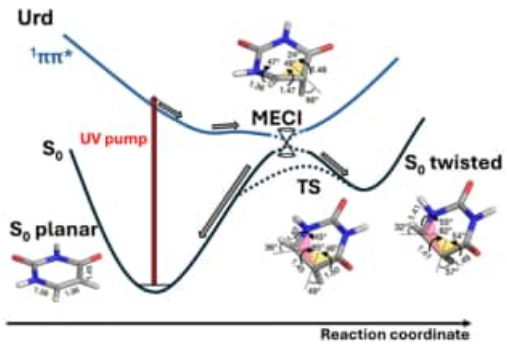

Figures 1(a) and 1(b) respectively show a 2D map of infrared transient absorption (IR-TA) spectra of uridine in phosphate buffer in D_2O and lineouts at selected time delays. Figure 1(c) shows the static IR spectrum of unexcited uridine in S_0. The IR-TA spectra display negative (blue) ground-state bleach (GSB) signals at 1656 and 1692 cm^{-1}, corresponding to out-of-phase and in-phase C=O stretching vibrations, respectively. The positive C=O stretching bands (red), which are shifted to higher wavenumbers compared to the pre-photoexcitation values, serve as fingerprints of the TI, as discussed previously. Weak positive bands extending beyond 1 ns are attributed to the triplet state.

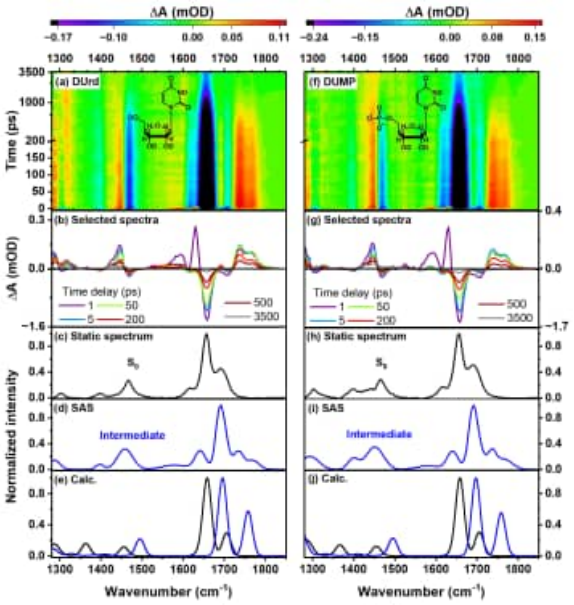

Figure 1 Infrared transient absorption spectra and calculated spectra for uridine and uridine monophosphate in D2O solution.

Figure 1(d) is the spectrum (SAS) of the TI extracted by global fitting of the IR-TA data beyond 10 ps. The assignment was confirmed by harmonic frequency calculations at the B3LYP/def2-TZVP level with PCM (D_2O) solvation [Figure 1(e)]: the blue and black correspond to the TI and planar structures in S_0. From the analysis of these spectra, we estimated the quantum yield (Φ_{TI}) and lifetime (τ_{TI}) of TI for structurally distinct nucleosides and nucleotides.

Nucleobases and their derivatives are known to undergo photodegradation via the addition of water across the C5=C6 double bond. Figures 2(a) and 2(b) show the photodegradation of uridine and thymidine, respectively, measured as a function of irradiation time of continuous 267 nm laser light. Uridine exhibits a rapid decay in absorption intensity, whereas thymidine shows only a minor change. These results demonstrate a strong influence of C5 methylation on the hydration reaction.

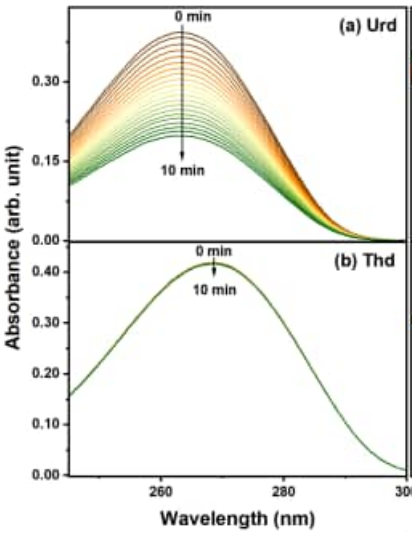

Figure 2 Reduction of UV absorption intensities of uridine and thymidine by photohydration reaction upon irradiation of 267 nm light.

We observed clear correlation between photohydration rates (k_{hyd}) and the product of a quantum yield and the lifetime of TI ($\Phi_{TI} \cdot \tau_{TI}$), indicating that the thermalized TI mediates the hydration reaction. The C5–methylated derivatives reduce k_{hyd} for two reasons. First, C5-methylated molecules experience strong steric hindrance from the hydration shell around the methyl group, which prevents pyramidalization at C5 and promotes vibrational energy randomization. This reduces the momentum along the TI-forming reaction coordinate, dissipating the initially directed momentum and causing the dynamics to be governed by the topography of the potential energy surface at the conical intersection. Consequently, thymidine exhibits the lowest Φ_{TI}. Second, C5 methylation attenuates the electric polarization of the C5=C6 bond, thereby reducing hydration reactivity. We also found that the reactivity strongly depends on the structural framework (cytosine, uracil, or thymine) of the pyrimidine nucleobases.

In conclusion, we elucidate the mechanistic details of non-adiabatic transitions and hydration reactions in nucleobases and their derivatives in aqueous solution and reveal a clear C5 methylation effect. This study was supported by the Japan Society for the Promotion of Science (JSPS) KAKENHI Grant No. 21H04970.

References

1. Miura et al. *J. Am. Chem. Soc.* **2023,** *145* (6), 3369-3381.

2. Orimo et al. *J. Phys. Chem. Lett.* **2023,** *14* (11), 2758-2763.

3. Obara et al. *J. Am. Chem. Soc.* **2025,** *147* (18), 15077-15087.

4. Obara et al. *J. Am. Chem. Soc.* **2025,** *147* (45), 41284-41296.

5. Ghosh et al. *J. Am. Chem. Soc.* **2026**, *in press*.

1A2 Solvent Effects on Ambimodal Diels–Alder/Dipolar Cycloadditions: Classical and Ring-Polymer Molecular Dynamics with Explicit Solvation

([1]*Saitama University*, [2]*Tokyo Metropolitan University*) Nakagawa Shoto[1], Matsubuchi Hayato[1], Ota Haruki[1], Takayanagi Toshiyuki[1], Murakami Tatsuhiro[2]

1. Introduction

Recent computational studies have revealed the existence of post-transition state bifurcation (PTSB), a phenomenon in which multiple products are formed from a single transition state (TS) without intervening intermediates [1–3]. Conventional chemical reactions yield a single product corresponding to the transition state structure along the intrinsic reaction coordinate (IRC), which usually connects one reactant to one product. In PTSB reactions, additional products are formed along a pathway that diverges from the IRC (red dashed line in Fig. 1). These branching processes are typically characterized by a valley-ridge inflection (VRI) point, where the potential energy surface (PES) transforms from a valley into a ridge as it descends toward the products [1, 2]. Product selectivity in such regions is therefore governed by dynamic effects.

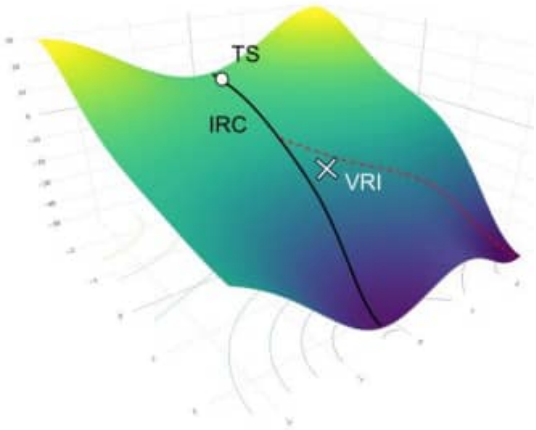

Figure 1. Schematic 2-dimensional potential energy surface exhibiting PTSB phenomena.

Solvation is a crucial factor that significantly influences chemical reactivity, including that of PTSB reactions. Previous computational studies have demonstrated that different major products are obtained from the PTSB reaction of 1,3-butadiene + 2-aminoacrolein between the gas phase and aqueous solution when a PCM-based implicit solvation model is used [4, 5]. Although implicit solvation models are highly effective for characterizing the key features of the potential energy landscape, they lack detailed atomistic information on solvent dynamics during the reaction.

In this study, we conducted molecular dynamics (MD) simulations of this system using explicit solvation models containing 5–45 water molecules. The reaction bifurcates into two distinct pathways: the Diels–Alder reaction (Fig. 2, upper the path) and the 1,3-dipolar cycloaddition (Fig. 2, the lower path). In addition, formation of the (4+3) product involves proton-transfer processes that convert the zwitterionic (4+3) intermediate into the final neutral product. We also employed ring-polymer MD (RPMD) to quantitatively evaluate the influence of nuclear quantum effects on these proton-transfer pathways, providing a more comprehensive understanding of their contribution to the reaction dynamics.

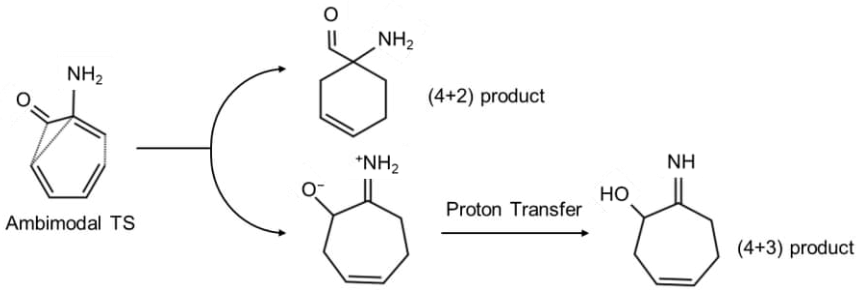

Figure 2. The Reaction Scheme for 1,3-butadiene and 2-aminoacrolein.

2. Method

Dynamical simulations were conducted for cluster reaction systems consisting of 2-aminoacrolein and 1,3-butadiene with three different cluster sizes, namely $(H_2O)_5$, $(H_2O)_{15}$, and $(H_2O)_{45}$. The parameter-optimized GFN2-xTB [6] model, which reproduces the energies and gradients obtained at the DFT-B3LYP(D3)/6-31+G(d,p) level, was used for the entire system, including the solvent water molecules. The MD calculations were initiated from configurations near the TS region; the corresponding initial coordinates and momenta were obtained from path-integral molecular dynamics simulations at 300 K. For each cluster size, 1000 trajectories were propagated with a time step of 0.1 fs for a total simulation time of 500 fs.

3. Results and Discussion

The branching fractions between the (4+2) and (4+3) products listed in Table 1 show an increasing contribution of the (4+3) channel with increasing cluster size, in both classical MD and RPMD. RPMD predicts a (4+3) fraction that is 4–9% lower than classical MD, since the inclusion of zero-point energy can promote the formation of products that deviate from the dominant IRC pathway.

Analysis of the temporal evolution of the populations reveals that the population of the (4+3) intermediate first rises to a maximum and then decreases, while that of the (4+3) product increases correspondingly. Moreover, the decay of the (4+3) intermediate is faster in RPMD than in classical MD across all cluster sizes, and proton-transfer events occur more frequently in RPMD than in classical MD, indicating that proton tunneling plays a significant role in the proton-transfer process even at 300 K. In our cluster systems, the water-mediated proton-transfer process involves a single water molecule acting as a proton shuttle. The RPMD results reveal that approximately half of the proton-transfer events proceed via this indirect mechanism, which cannot be captured by implicit solvation models or classical nuclear dynamics approaches.

Table 1. Branching fractions leading to the (4+2) and (4+3) species obtained from classical MD and RPMD

	Classical MD		RPMD	
	(4+2)	(4+3)	(4+2)	(4+3)
Gas[5]	0.996	0.004	0.993	0.007
Implicit (water)[5]	0.369	0.631	0.387	0.613
$(H_2O)_5$	0.371	0.629	0.419	0.581
$(H_2O)_{15}$	0.229	0.771	0.270	0.730
$(H_2O)_{45}$	0.044	0.956	0.143	0.857

Reference

[1] Ess, D. H., Houk, K N. *et al. Angew. Chem. Int. Ed*. **2008**, 47, 7592–7601.
[2] Hare, S. R., Tantillo, D. J. *Pure Appl. Chem.* **2017**, 89, 679–698.
[3] Rehbein, J., Carpenter, B. K. *Phys. Chem. Chem. Phys.* **2011**, 13, 20906–20922.
[4] Chen, S., Yu, P., Houk, K. N. *J. Am. Chem. Soc*. **2018**, 140, 18124–18131.
[5] Murakami, T., Takayanagi, T. *et al. J. Phys. Org. Chem*. **2024**, 37, e4611.
[6] Bannwarth, C., Grimme S. *et al. WIREs Comput Mol. Sci*. **2021**, 11, e1493.

1A3 Solvent effects on the photoreaction dynamics of *cis*-stilbene: A QM/MM nonadiabatic molecular dynamics study

(Hokkaido University) Satoi Wada, Yusuke Minegishi, Takuro Tsutsumi, Tetsuya Taketsugu

Stilbene is a prototypical photoswitch that undergoes photoisomerization of its olefin moiety. Upon photoexcitation, *cis*-stilbene exhibits ultrafast nonradiative decay dynamics through conical intersections, resulting in photoisomerization to *trans*-stilbene and photocyclization to 4,4-dihydrophenanthrene (DHP), along with ground-state recovery of the *cis* form. This branching dynamics is known to be dependent on solvent polarity (**Figure 1**) and has been often discussed in experimental literature [1,2]. Our group has long studied excited-state reaction pathways and dynamics of the isolated stilbene and its derivatives, providing molecular level understanding of stilbene photochemistry [3-5]. However, there is no further detailed insight into *cis*-stilbene photoreaction in solution. In this study, we perform QM/MM nonadiabatic molecular dynamics (NAMD) simulations that explicitly account for nonpolar and polar solvents to investigate how solvent influences ultrafast nonradiative decay dynamics of *cis*-stilbene in solution.

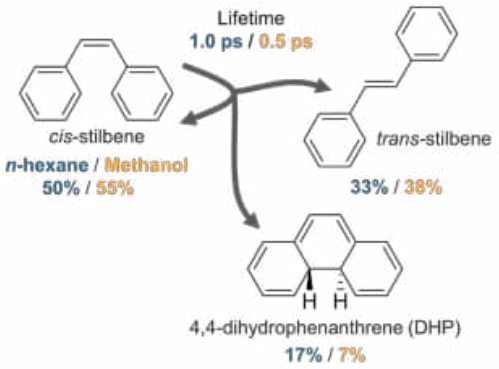

Figure. 1 Photoreactions of *cis*-stilbene: photoisomerization to *trans*-stilbene and photocyclization to 4,4-dihydrophenanthrene (DHP). Lifetime and quantum yield in *n*-hexane and methanol [2] are shown.

Method The solvated *cis*-stilbene system was modeled with a QM/MM scheme, where the centered *cis*-stilbene was computed at mixed-reference spin-flip time-dependent density functional theory (MRSF-TDDFT) and all surrounding solvent molecules were treated by general amber force field (GAFF) with restrained electrostatic potential (RESP) charges. To prepare initial conditions for QM/MM-NAMD simulations, the system was first modeled in a periodic box and equilibrated under NVT (300 K) followed by NPT (1 atm) conditions using GROMACS. From the equilibrated trajectory, fifty snapshots were collected and truncated into spherical droplets with a radius of 20 Å centered on *cis*-stilbene (**Figure 2a**). These cluster models were further equilibrated by 1-ps QM/MM-MD simulations in the ground state, where solvents in an outer shell region (15-20 Å) were fixed to maintain a spherical boundary condition. $S_1 \rightarrow S_0$ internal conversions were accounted for using Zhu-Nakamura global switching algorithm. QM/MM-MD simulations were performed using the SPPR program [6] interfaced to GAMESS (US) program.

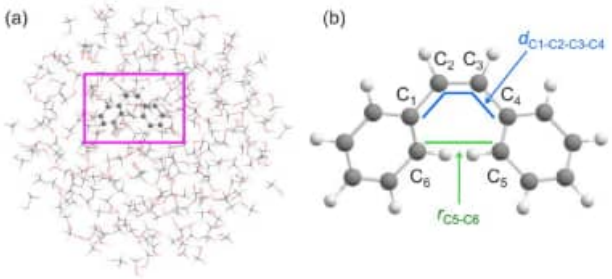

Figure. 2 (a) QM/MM cluster model of cis-stilbene in methanol and (b) the centered cis-stilbene structure with the atomic numbering and the key internal coordinates.

Results and discussion QM/MM-NAMD simulations were performed to investigate the photoreaction of *cis*-stilbene in *n*-hexane and methanol, respectively. **Figure 3** presents the time evolution of the S_1 population. The population begins to decay within 0.1 ps in each solvent environment; however, it decays faster in methanol than in *n*-hexane with excited-state lifetimes of 1.35 ps in *n*-hexane and 0.61 ps in methanol. Calculated branching ratios of DHP:*trans* are 0.23:0.30 in *n*-hexane and 0.08: 0.43 in methanol. These results are quantitively in good agreement with the experimental values [2]. Thus, our simulations successfully capture the solvent-dependent excited-state dynamics. **Figure 4** represents a projection of trajectory snapshots in (a) *n*-hexane and (b) methanol onto a two-dimensional coordinate space defined by the C-C bond length $r_{C5\text{-}C6}$ and the torsion angle $d_{C1\text{-}C2\text{-}C3\text{-}C4}$ (see Figure 2b). In both solvent environments, the system rapidly exits from the *cis* region and move around intermediate space between DHP and *twist* region. However, nonadiabatic transitions in methanol occur in a wider range of the coordinate space than in *n*-hexane, which indicates that the solvent-polarity promotes nonradiative transition. A detailed analysis to clarify the microscopic origin of the solvent-dependent dynamics will be discussed at the presentation.

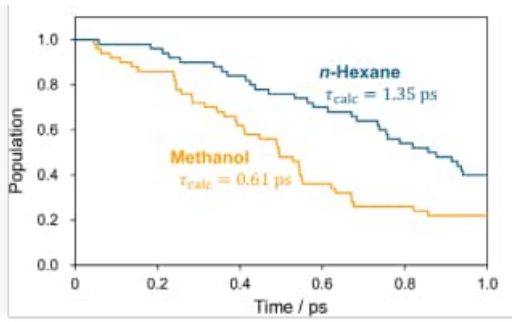

Figure 3. Time evolution of S_1 populations in *n*-hexane (purple) and methanol (orange).

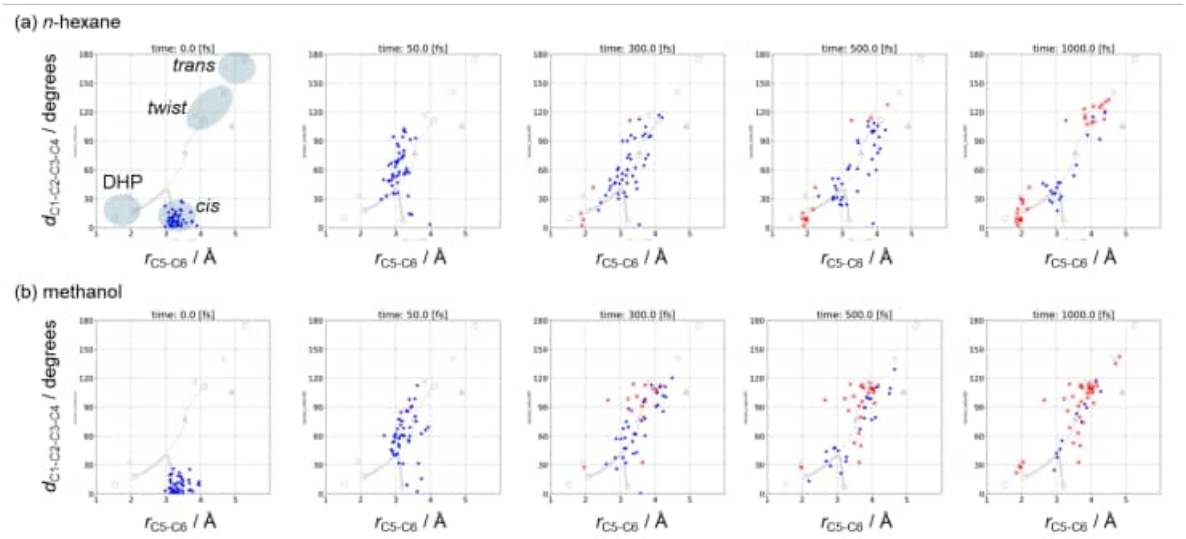

Figure 4. Projection of trajectory snapshots in (a) *n*-hexane and (b) methanol onto a two-dimensional coordinate space defined by the C–C bond length $r_{C5\text{-}C6}$ and the torsion angle $d_{C1\text{-}C2\text{-}C3\text{-}C4}$. The blue dot represents each trajectory, and the red cross represents a geometry where internal conversion occurs.

[1] J. K. Rice *et al. J. Phys. Chem.*, **96**, 3359–3366 (1992); [2] J. M. Rodier *et al. J. Am. Chem. Soc.*, **115**, 10791–10795 (1993); [3] Y. Harabuchi *et al. J. Phys. Chem. A*, **118**, 11987–11998 (2014); [4] Y. Harabuchi *et al. J. Phys. Chem. A*, **120**, 8804–8812 (2016); [5] T. Tsutsumi *et al. Chem. Phys.*, **515**, 564–571 (2018); [6] T. Tsutsumi *et al.* SPPR (a developmental version), 2026, Hokkaido University, Sapporo, Japan.

1A4 Ultrafast state-selective dynamics of electronically excited N_2^+ by pump-probe measurements using few-cycle near-infrared laser pulses and high-order harmonics

(The University of Tokyo[1]) Kana Yamada[1], Toshiaki Ando[1], Atsushi Iwasaki[1], Kaoru Yamanouchi[1]

1. Introduction

When molecules are ionized by extreme ultraviolet (XUV) light pulses, molecular ions are created in both ground and electronically highly excited states. Owing to differences in the shapes of the potential energy curves (PECs), molecules prepared in these states exhibit a wide variety of different nuclear dynamics in the time domain. As demonstrated in our recent study on O_2^+ [1], such characteristic dynamics of molecular ions in the electronically excited states can be elucidated by pump-probe measurements using high-order harmonics (HHs) of femtosecond near-IR (NIR) laser pulses for ionization and the NIR laser pulses for probing. For N_2^+, nuclear dynamics in the electronically excited states were investigated by pump-probe measurements using HHs and NIR pulses [2−4], but the early-stage dynamics of N_2^+ in the short time delay range below ~75 fs has not been explored in detail except for that in the $F^2\Sigma_g^+$ state [5]. In the present study, we investigate the early-stage nuclear dynamics of N_2^+ in the $C^2\Sigma_u^+$ and $D^2\Pi_g$ states (Fig. 1(a)) by the HHs pump and NIR probe scheme.

2. Experimental and theoretical methods

We focus NIR laser pulses (780 nm, 6 fs, 5 kHz, 0.14 mJ) into a Xe-filled gas cell to generate HHs covering the photon energy range of 20–35 eV. The HHs in the XUV range are focused onto an N_2 molecular beam in the interaction region of a velocity map imaging spectrometer to produce N_2^+ ions in the electronically excited states. After the time delay τ (τ = −31–78 fs), the NIR laser pulses are focused on the same spatial position as the HHs. By varying the time delay, we record the time-delay-dependent kinetic energy distribution of the resulting N^+ fragment ions.

To numerically simulate the time-delay-dependent kinetic energy distribution of N^+, we first calculate the potential energy curves (PECs) of ten lowest electronic states of N_2^+ for each one of $^2\Sigma_g^+$, $^2\Sigma_u^+$, $^2\Pi_g$, and $^2\Pi_u$ symmetries (Fig. 1(a)) and the transition dipole moments using Molpro [6]. By solving the time-dependent Schrödinger equation, we simulate the temporal evolution of vibrational wave packets of N_2^+ in the respective electronic states for the time-delay range of τ = 0–100 fs until the influence of the NIR laser field becomes negligibly small. Then, we project the resulting wave packets onto the continuum of the higher-lying electronic states and covert the temporal evolution of the relative populations of the vibrational eigenstates in the continuum to the kinetic energy distributions of N^+.

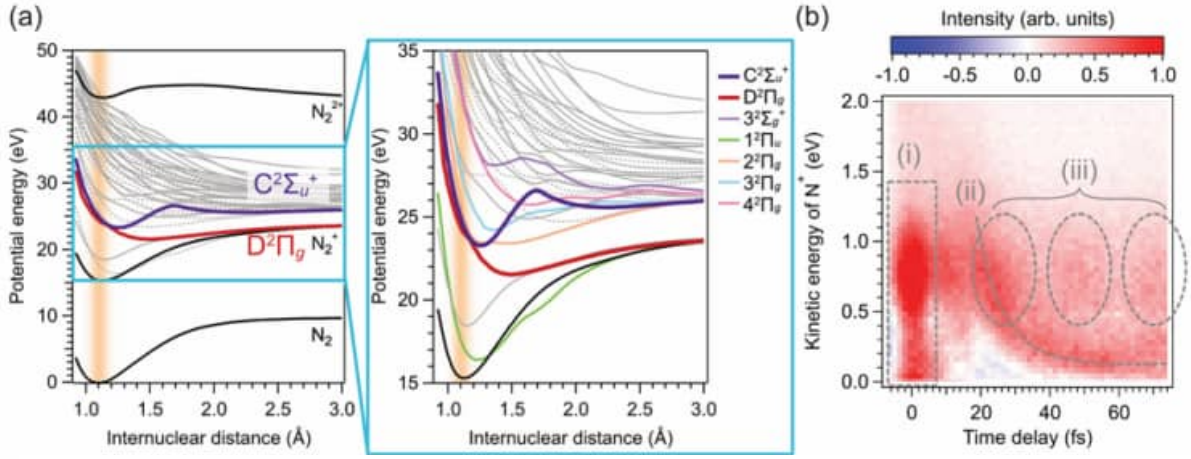

Fig. 1. (a) Theoretical potential energy curves of N_2^+ calculated by Molpro [6]. The potential energy curves of the electronic ground states of N_2 and N_2^{2+} [2] are also shown. (b) Time-delay dependent kinetic energy distribution of N^+ fragments obtained after subtracting the background signals independent of the time-delay.

3. Results and Discussion

The time-delay dependent kinetic energy distribution of N^+ fragments (Fig. 1(b)) shows (i) an enhanced N^+ yield around $\tau = 0$ fs, (ii) a curvilinear structure with a negative slope emerging after $\tau \sim 20$ fs, and (iii) periodic broad distributions appearing around τ = 30, 50, and 70 fs. The feature (i) is attributed to the simultaneous absorption of XUV and NIR photons, producing mainly the $F^2\Sigma_g^+$ state, which cannot be prepared by one-photon XUV ionization.

To interpret the curvilinear structure of feature (ii), we calculate the internuclear-distance dependence of the transition probabilities from the $D^2\Pi_g$ state. As shown in Fig. 2, N_2^+ in the $D^2\Pi_g$ state can efficiently be excited to the $1^2\Pi_u$ state by one-photon transition and to the $2^2\Pi_g$, $3^2\Pi_g$, and $4^2\Pi_g$ states by two-photon transitions.

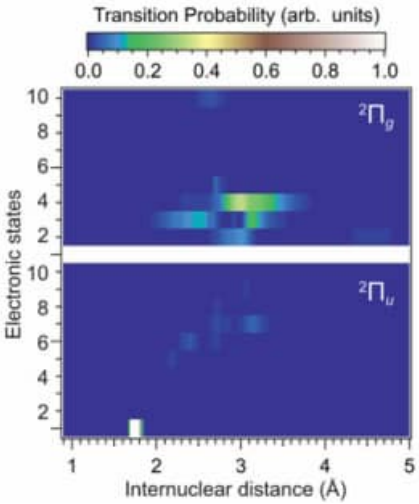

Fig. 2 The internuclear-distance dependence of the transition probabilities of N_2^+ in the $D^2\Pi_g$ state to the $1–10^2\Pi_g$ and $1–10^2\Pi_u$ states.

We then simulate the time-delay dependence of the kinetic energy distributions of N^+ produced by the dissociation of N_2^+ in the $1^2\Pi_u$, $2^2\Pi_g$, $3^2\Pi_g$, and $4^2\Pi_g$ states as shown in Fig. 3(a). The sum of the distributions shown in Fig. 3(b) is in good agreement with the experimentally observed feature (ii) in Fig. 1(a). A comparison between Fig. 3(a) and Fig. 3(b) shows that the dissociation of N_2^+ via the $4^2\Pi_g$ state has the dominant contribution to the feature (ii). The time-delay dependent decrease in the N^+ kinetic energy reflects the decrease in the potential energy difference between the $D^2\Pi_g$ and $4^2\Pi_g$ states as the internuclear distance increases.

The time evolution of the kinetic energy distribution of N^+ is also simulated assuming that N_2^+ is prepared first in the $C^2\Sigma_u^+$ state by the XUV pulse. The results of the simulation show that N_2^+ in the $C^2\Sigma_u^+$ state is dominantly excited to the $3^2\Sigma_g^+$ state by one photon and the resultant N^+ fragment ions are created at τ = 30, 51, and 72 fs. This periodical production of N^+ reflects the period (~21 fs) of the oscillation of the vibrational wave packet in the $C^2\Sigma_u^+$ state of N_2^+, which is consistent with the periodical signals forming the feature (iii) in Fig. 1(c).

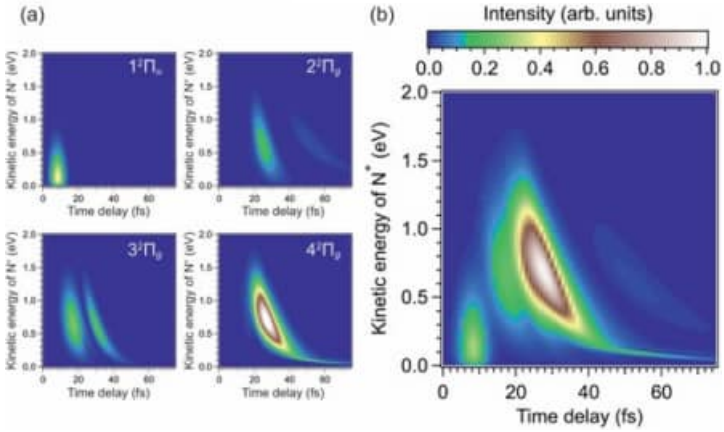

Fig. 3 (a) Calculated time-delay dependent kinetic energy distributions of N^+ produced by the dissociation of N_2^+ in the $1^2\Pi_u$, $2^2\Pi_g$, $3^2\Pi_g$, and $4^2\Pi_g$ states excited from the $D^2\Pi_g$ state. (b) The sum of the distributions in Fig. 3(a).

By combining the time-domain measurements using ultrashort XUV and NIR pulses with the theoretical simulations, we have elucidated previously unresolved ultrafast nuclear dynamics of N_2^+ in the $D^2\Pi_g$ and $C^2\Sigma_u^+$ states.

References

[1] K. Yamada et al., *Phys. Rev. A* **112**, 063117-1–10 (2025). [2] E. Gagnon et al., *Science* **317**, 1374–1378 (2007). [3] M. Lucchini et al., *Phys. Rev. A* **86**, 043404-1–4 (2012). [4] M. Eckstein et al., *J. Phys. Chem. Lett.* **6**, 419–425 (2015). [5] A. Trabattoni et al., *Phys. Rev. X* **5**, 041053-1–11 (2015). [6] H. -J. Werner, et al., *J. Chem. Phys.* **152**, 144107-1–24 (2020).

1A5 Formation of I 4d double-core-hole states of CH_3I in strong EUV-FEL fields studied by electron-ion coincidence spectroscopy

([1]Nagoya Univ., [2]RIKEN SPring-8 Center, [3]Univ. of Toyama, [4]JASRI, [5]RCMS, Nagoya Univ.) M. Fushitani[1,2], Y. Hikosaka[2,3], S. Owada[3,4], and A. Hishikawa[1,2,5]

[Introduction] Double-core-hole (DCH) states are highly exited states where two vacancies are created in inner-shell levels. Auger electrons emitted in DCH decays carry energies that sensitively reflect chemical environment around atomic sites with the vacancies so that electron spectroscopy on DCH states has drawn attention as a new method on chemical analysis [1,2]. Ultrashort and intense free-electron laser (FEL) is a suitable light source that enables efficient DCH formations by sequential two-photon absorption processes as it can create the second core-hole before the initial core-hole decays [3]. In our previous study on Xe 4d DCH states [4], we have demonstrated that electron-ion coincidence spectroscopy is a powerful method to observe electron signals related to the DCH states even though they are spectrally overlapped with dominant photoelectron and/or Auger electron signals generated from one-photon processes. In this work, we aimed to extend the method to molecular systems and performed electron-ion coincidence measurements on nonlinear ionization of iodomethane (CH_3I) to observe two-photon formation of I 4d DCH states.

[Experimental] Experiments were carried out at the soft X-ray beamline (BL1) of SACLA at RIKEN Harima site, Japan. Ultrashort extreme ultraviolet (EUV) FEL pulses (111 eV, 30 fs) were focused by a Kirkpatrick-Baez mirror to an effusive CH_3I molecular beam introduced into a magnetic bottle type multielectron-ion coincidence spectrometer [4]. Electrons generated in the interaction region were guided by strong inhomogeneous and weak homogeneous magnetic fields to a time-of-flight (TOF) tube (1.5 m length) and detected by a microchannel plate (MCP) detector. The counterpart ions were pushed into the TOF tube by applying pulsed voltages to ion collection electrodes ~1.5 μs after the laser irradiation and detected by the same MCP detector. The electron energy was calibrated with Xe 4d [5] and Kr 3d [6] Auger spectra.

[Results and discussion] Figure 1(b) shows normalized electron spectra for I 4d photoionization of CH_3I by using EUV-FEL fields with a pulse energy of 0.24 μJ (gray) and 1.26 μJ (red), respectively. A doublet peak seen at 52.7 and 54.3 eV in both spectra are attributed to I $4d_{3/2, 5/2}$ photoelectron peaks: (i) $CH_3I + h\nu \rightarrow CH_3I^+ (I\ 4d_{3/2, 5/2}^{-1}) + e^-(P1)$ (see Fig. 1(a)). On the other hand, electron signals in the 30-40 eV energy region show the larger yield in the case of stronger FEL. FEL intensity dependence reveals that the electron yield increases quadratically as a function of FEL intensity, suggesting that the electron signals are formed by two-photon processes. Considering energy levels, there may be two pathways after the initial ionization to generate electrons in the energy region of interest. One is a pathway via I 4d Auger decays,

(ii-1) $CH_3I^+(I\ 4d^{-1}) \rightarrow CH_3I^{2+} + e^-(A1)$, (ii-2) $CH_3I^{2+} + h\nu \rightarrow CH_3I^{3+}(I\ 4d^{-1}(2e)^{-2}) + e^-(P3)$.

The other pathway involves I 4d DCH states,

(iii-1) $CH_3I^+(I\ 4d^{-1}) + h\nu \rightarrow CH_3I^{2+}(I\ 4d^{-2}) + e^-(P2)$

(iii-2) $CH_3I^{2+}(I\ 4d^{-2}) \rightarrow CH_3I^{3+}(\ I\ 4d^{-1}\ (2e)^{-2}) + e^{-}(A2)$.

In both pathways, the second photoionization could produce photoelectrons distributed in the energy range of 30-40 eV. Although the two-photon signals (P2&P3) are difficult to be observed for each pathway due to their spectral overlapping, their contributions can be identified by correlating them with Auger electrons in (ii-1) and (iii-2) as well as ion species.

Figure 1(c) shows an electron correlation map obtained in coincidence with I^{2+} ions. The two-photon signals are found to be correlated with electrons distributed in the 10-20 eV and 20-30 eV regions. The distribution is similar to that for an I 4d Auger electron spectrum (A1) associated with P1 photoelectrons, indicating a large contribution of the I 4d Auger decay pathway (ii). On the other hand, a closer inspection reveals that electron signals in the 22-26 eV region are more generated compared to the A1 spectrum. The signals can be attributed to Auger electrons formed by the I 4d DCH decay process (iii-2), and their energies are expected to be in the 20-28 eV region. These results strongly suggest the two-photon formation of I 4d DCH states through pathway (iii), competing with I4d core-hole decays of CH_3I^{+} during the second photoabsorption.

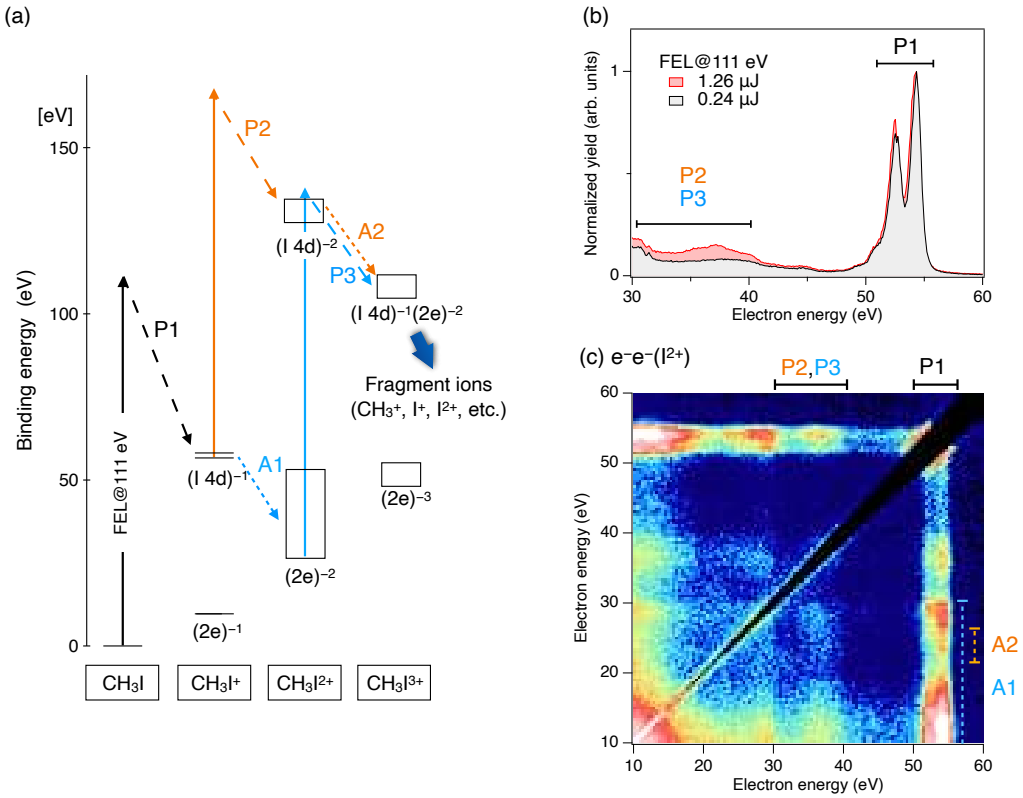

Figure 1. (a) Energy levels of CH_3I relevant to the present study. (b) Normalized electron spectra of CH_3I in intense EUV-FEL fields (111 eV, 30 fs). Red: 1.26 μJ, Gray: 0.24 μJ.(Red). (c) Electron correlation map obtained in coincidence with I^{2+} ions.

References [1] M. Tashiro *et al., J. Chem. Phys.* **132** 184302 (2010). [2] N. Berrah *et al., Proc. Natl. Acad. Sci. USA* **108** 16912 (2011). [3] P. Salén *et al., Phys. Rev. Lett.* **108** 153003 (2012). [4] M. Fushitani *et al., Phys. Rev. Lett.* **124** 193201 (2020). [5] T. X. Carroll *et al., J. Electron Spectrosc. Relat. Phenom.* **125** 127 (2002). [6] J. Palaudoux *et al., Phys. Rev. A* **82** 043419 (2010).

1A6 Ultraviolet photodynamics in iodopropane isomers studied by time-resolved momentum imaging with extreme ultraviolet photoionization

Kumagai, Yoshiaki[1,2], Allum, Felix[3,4,5], Nagaya, Kiyonobu[6], Harries, James R.[7], Iwayama, Hiroshi[8, 9], Britton, Mathew[5], Bucksbaum, Philip H.[4], Burt, Michael[10,11], Brouard, Mark[10], Downes-Ward, Briony[12], Driver, Taran[5], Heathcote, David[10], Hockett, Paul[13], Howard, Andrew J.[4], Lee, Jason W. L.[3], Liu, Yusong[4], Kukk, Edwin[14], McManus, Joseph W.[10], Milěsević, Dennis1[0], S. Minns, Russell[12], Niozu, Akinobu[15], Niskanen, Johannes[14], Orr-Ewing, Andrew J.[16] , Owada, Shigeki[17, 18], Robertson, Patrick[10, 19], Rolles, Daniel[20], Rudenko, Artem[20], Ueda, Kiyoshi[21], Unwin, James[10], Vallance, Claire[10], Walmsley, Tiffany[10], Ashfold, Michael N. R. [16], Forbes, Ruaridh [5, 22]
([1]NWU, [2]TUAT, [3]DESY, [4]Stanford PULSE Institute, [5]LCLS, [6]Kyoto Univ., [7]QST, [8]IMS, [9]Sokendai, [10]Univ. of Oxford, [11]Trent Univ., [12]Univ. of Southampton, [13]NRC of Canada, [14]Univ. of Turku, [15]Hiroshima Univ., [16]Univ. of Bristol, [17]RIKEN, [18]JASRI, [19]Univ. of Nottingham, [20]Kansas State Univ., [21]Tohoku Univ., [22]Univ. of California, Davis)

Methyl iodide has been extensively studied in gas-phase chemical physics as a prototypical system for photodissociation dynamics in polyatomic molecules. More complex alkyl iodides have garnered less attention; however, a number of studies have highlighted how increased structural complexity and the consequent increase in the number of nuclear degrees of freedom lead to rich photodissociation dynamics. In particular, structural isomers such as 1- and 2-iodopropane (C_3H_7I) exhibit distinct reaction pathways induced ultraviolet (UV) light, with previous work reporting efficient ultrafast HI elimination in 2-iodopropane but not in 1-iodopropane, attributed to differences in the nuclear motion of the recoiling fragments [1].

Recently, we observed high kinetic energy ions produced through charge transfer (CT) in UV-excited 2-iodopropane by employing femtosecond extreme ultraviolet (XUV) laser pulses, yielding significant insights into CT probabilities as a function of internuclear distance [2]. In the present study, we investigatethe UV-induced photodissociation dynamics of the structural isomers 1- and 2-iodopropane using a time-resolved scheme incorporating site-selective XUV ionization [3].

The experiments were conducted at the XUV beamline (BL1) at the free-electron laser facility SACLA in Japan [4]. 1- and 2- iodopropane were introduced into a veclocity map imaging (VMI) spectrometer by expansion of their room-temperature vapor pressure [5]. In the interaction region, molecules were photoexcited by a femtosecond UV (267 nm) laser pulse prior to ionization at a variable time delay by the XUV laser pulse produced by the FEL. To induce multiple ionization selectively at the iodine site, the XUV photon energy was tuned to 95 eV, approximately in the center of the I 4*d* giant dipole resonance [6]. The ions were accelerated by a set of ion optics to a position- and time-sensitive detector, allowing reconstruction of full three-dimentional momenta of each detected event. The single-shot jitter of the UV and XUV pulses was recorded using an arrival time monitor [7].

Time-resolved momentum distributions of multiply charged iodine ions reveal three delay-dependent features associated with UV-induced C-I bond fission: (I) site-selective XUV

multiple ionization of the dissociating iodine atom followed by charge transfer (CT) to the neutral propyl cofragment, leading to Coulomb repulsion between the resulting ions; (II) site-selective XUV ionization of the departing iodine atom without subsequent CT, producing low-momentum multiply charged iodine ions that reflect the neutral photodissociation dynamics; and (III) XUV ionization of both separating fragments, resulting in Coulomb explosion with ion momenta that decrease with increasing internuclear separation.

A key observation is that the delay-dependent momentum of feature II differs between the two isomers: in 1-iodopropane, the iodine ion momentum increases over the first few hundred femtoseconds, whereas in 2-iodopropane it remains largely constant. The pump-probe delay affects the measured ion momenta by projecting the system from neutral to ionic potential energy surfaces before the fragments reach their asymptotic velocities, such that earlier ionization leads to lower final momentum if the ionic potentials are shallower, which may explain the stronger delay dependence observed in 1-iodopropane.

The delay-dependent ion yields show that the onset of charge transfer shifts to longer pump-probe delays for higher charge states in both isomers, consistent with charge transfer occurring at larger internuclear distances. This shift is generally larger in 1-iodopropane than in 2-iodopropane, indicating deviations from simple over-the-barrier model predictions, which treat the system as structureless. These differences likely arise from distinct nuclear dynamics of the propyl radicals, suggesting that rotational and vibrational motion may influence the charge transfer process.

Previous studies reported ultrafast HI elimination from UV-excited 2-iodopropane, evidenced by strongly anisotropic recoil indicating dissociation before significant molecular rotation, whereas no such channel was observed in 1-iodopropane [1]. The HI products were found to have kinetic energy distributions similar to those of ground-state iodine atoms from C–I bond cleavage. In the present study, the ratio of singly charged iodine ion yields at high and low momentum shows no clear delay dependence in 1-iodopropane, while in 2-iodopropane it exhibits a step-like enhancement of the low-momentum contribution when the UV pulse precedes the XUV pulse near time-zero. This behavior is consistent with ultrafast HI elimination occurring on a sub-picosecond timescale, predominantly in 2-iodopropane.

[1] M. A. Todt *et al*., *Phys. Chem. Chem. Phys.*, **22** (2020) 27338
[2] F. Allum *et al*., *Phys. Rev.* A, **108** (2023) 043113
[3] F. Allum *et al*., *Phys. Chem. Chem. Phys*., **27** (2025) 20602
[4] S. Owada *et al.*, *J. Synchrotron Radiat.*, **25** (2018) 282
[5] H. Fukuzawa *et al*., *Nucl. Instruments Methods Phys. Res. Sect.* A, **907** (2018) 116
[6] N. Saito *et al.*, *Int. J. Mass Spectruom. Ion Processes*, **115** (1992) 12725
[7] S. Owada *et al.*, *J. Synchrotron Radiat.*, **26** (2019) 887

1A7 Ring-opening via conical intersections in thiophene revealed by extreme ultraviolet time-resolved photoelectron spectroscopy

Zhiyi Zhou[1], Satoi Wada[2], Yuto Arai[1], Ryuto Kambara[3], Tetsuya Taketsugu[2,4], Taro Sekikawa[1]
([1]Department of Applied Physics, Faculty of Engineering, Hokkaido University, [2]WPI-ICReDD, Hokkaido University, [3]Graduate School of Chemical Sciences and Engineering, Hokkaido University, [4]Department of Chemistry, Faculty of Science, Hokkaido University.)

Introduction

Five-membered aromatic heterocycles with π-conjugated rings are pivotal in organic photochemistry and optoelectronic materials, motivating investigations of their photoinduced reaction dynamics to establish structure–function relationships in photoactive systems. Among them, furan and thiophene (**Fig. 1**) have served as prototypical models owing to their simple molecular structures, making them ideal systems for investigating photoinduced reaction dynamics. Unlike furan, where most excited molecules return to the ground state via nonadiabatic transitions dominated by ring puckering (RP) [1,2], excited-state deactivation in sulfur-containing thiophene has been suggested to proceed preferentially governed by a ring-opening (RO) pathway involving S–C bond cleavage [3-6]. However, existing ultraviolet (UV)-based studies are limited by their available probe photon energies, restricting detection primarily to low-binding-energy features from low-lying neutral excited states and the outermost molecular orbitals (MOs) [3,4]. This narrow spectral window obscures access to deeper-lying MOs associated with bond rearrangement, thereby hindering direct observation of post-excitation nonadiabatic dynamics mediated by conical intersections (CIs).

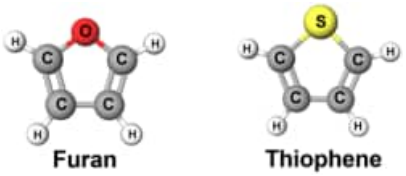

Figure 1. Molecular structures of representative heterocyclic molecules: furan (left) and thiophene (right).

In this study, extreme ultraviolet (EUV)-based time-resolved photoelectron spectroscopy (TRPES), with high sensitivity to electronic redistribution induced by pronounced molecular structural distortions, captures the ballistic nuclear wavepacket motion of thiophene along the RO pathway, from the initially excited S_2 ($\pi\pi^*$) state to the ground state via CIs over an extended energy window. Distinct changes in spectral intensity and line shape from lower-lying MOs provide previously inaccessible insight into RO in thiophene and enable the timing of nuclear wavepacket passage through a CI to be directly resolved.

Experimental

A Ti: sapphire laser system generated femtosecond pulses centered at 800 nm (1.55 eV). Naturally evaporated gaseous thiophene was predominantly excited to S_2 ($\pi\pi^*$) state via two-photon absorption of the second harmonic (3.1 eV), and subsequently probed by the 19th harmonic (29.4 eV) generated in Kr gas. The EUV probe pulse enables direct time-resolved tracking of lower-lying MOs over an extended energy window, providing rich electronic-state information beyond the frontier orbitals and enhanced sensitivity to molecular structural variation. The pump-probe delay was controlled by a computer-driven delay stage, giving a cross-correlation temporal width of ~80 fs. Photoelectron spectra were recorded by a magnetic-bottle photoelectron spectrometer. Combined with quantum chemical calculations, these measurements allow the relaxation pathway through the CIs and subsequent isomerization dynamics to be comprehensively characterized.

Results and Discussion

Advanced quantum chemical calculations by Wada *et al.* [7] provide the theoretical framework for understanding the ultrafast photoinduced dynamics of thiophene and for assigning the observed spectroscopic signatures. Following S_2 photoexcitation, the theoretical results suggest a nearly barrierless downhill evolution on the excited-state potential energy surfaces, in which C–S bond cleavage occurs prior to reaching the S_1/S_0 CI, after which the nuclear wavepacket branches toward

either ring reclosure (**Fig. 2A**, structure **I**) or further isomerization (**Fig. 2A**, structure **III**). Guided by this framework, the difference photoelectron spectrogram (**Fig. 2C**) reveals rich dynamics.

Figure 2C was generated by subtracting the ground-state contribution (**Fig. 2B**) from the raw spectrogram, thereby highlighting transient changes and improving visualization of the evolving spectral features. Initially, two excited-state signals are observed at around 3 and 6 eV. These signals, decaying with time constants of 26 ± 8 fs and 24 ± 2 fs, are assigned to ionization predominantly from the S_2 state to D_0 (2.89 eV) / D_1 (3.21 eV) and D_2 (6.05 eV) / D_3 (6.24 eV) cationic states, respectively. The short-lived peaks at 8.3 and 9.0 eV observed at 20 fs in **Fig. 2D**, assigned to the $S_2 \rightarrow D_6/D_7$ of thiophene, indicate rapid wavepacket departure from the Franck–Condon region. Notably, peaks attributed to structure **II** ($S_1 \rightarrow D_2$: 8.42 eV; $S_1 \rightarrow D_4$: 9.53 eV) are already discernible at 100 fs in **Fig. 2D** before full recovery of the ground-state bleach, in strong agreement with the prediction that the wavepacket develops RO character on S_1 prior to reaching the S_1/S_0 CI.

The 125 fs and 150 fs spectra exhibit pronounced broadening of the 8–10 eV bands (**Fig. 2D**), indicating passage through an unstable transition region associated with CI traversal accompanied by continuous, disordered, and large-amplitude structural evolution. This broad structural dispersion effectively "washes out" the spectral features, giving rise to the smooth spectral profile. With continued relaxation, thiophene either recovers to its original cyclic structure from the incipient ring-opened intermediate (**Fig. 2A**, structure **II**) or forms ring-opened isomers via C–C bond rotation. This localized structural rearrangement, rather than the global conformational reorganization, restores spectral band narrowing and the re-emergence of characteristic peaks at longer delay times. Specifically, the dashed circles in the 510 fs transient spectrum in **Fig. 2D** indicate features at 8.55 eV, 9.55 eV, and 9.91 eV, corresponding to the $S_0 \rightarrow D_2$, $S_0 \rightarrow D_4$, and $S_0 \rightarrow D_5$ ionization channels of structure **III**, respectively. The re-emergent peak of thiophene near 9.0 eV in the 510 fs spectrum (**Fig. 2D,** red triangle) provides direct experimental evidence supporting the theoretical prediction that a fraction of molecules undergo ring reclosure following C–S bond cleavage (**Fig. 2A**, structure **II → I**).

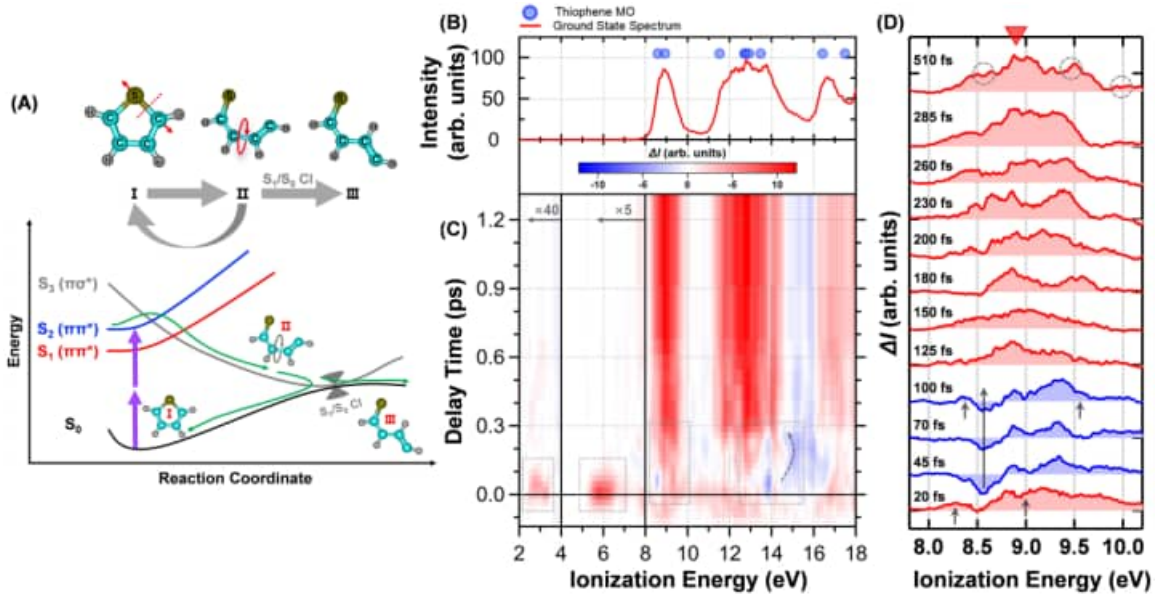

Figure 2. (A) Schematic potential-energy profiles and energetically favored structural evolution along the RO pathway of thiophene. (B) Ground-state photoelectron spectrum of thiophene, with the absolute values of MO energies plotted. (C) Difference photoelectron spectrogram of thiophene with signal intensities below 8.0 and 4.0 eV amplified by factors of 5 and 40, respectively. (D) Temporal evolution of difference spectra extracted at selected delay times.

Reference

[1] R. Uenishi *et al.*, *J. Phys. Chem. Lett.*, **15**, 2222−2227 (2024). [2] S. Adachi *et al.*, *Phys. Chem. Chem. Phys.*, **21**, 13902–13905 (2019). [3] O. Schalk *et al.*, *J. Phys. Chem. A*, **122**, 8809–8818 (2018). [4] R. Weinkauf *et al.*, *Phys. Chem. Chem. Phys.*, **10**, 393–404 (2008). [5] X. F. Wu *et al.*, *J. Chem. Phys.*, **133**, 134507 (2010).
[6] A. Prlj *et al.*, *Phys. Chem. Chem. Phys.*, **17**, 14719–14730 (2015). [7] S. Wada *et al.*, in preparation.

1A8 First observation of sequential photochemical and thermal ring-opening dynamics in 1,3-cyclohexadiene

(Hokkaido University) Bateer Lu, Taro Sekikawa

1. Introduction

The photoinduced ring-opening of 1,3-cyclohexadiene (CHD) is a prototypical electrocyclic reaction and has long served as a benchmark for understanding nonadiabatic dynamics governed by the Woodward–Hoffmann rules [1]. Upon excitation to the 1B state, CHD undergoes ultrafast relaxation through a conical intersection (CI), leading to conrotatory ring opening and the formation of 1,3,5-hexatriene (HT) on a sub-100-fs timescale [2].

While the excited-state dynamics of CHD have been well characterized, the subsequent fate of the system after CI passage remains less understood. In particular, molecules returning to the ground state are expected to be highly vibrationally excited, and their potential to undergo further chemical transformations has not been directly observed. This limitation arises primarily from the restricted probing window of conventional ultrafast spectroscopies, which are less sensitive to ground-state structural evolution.

In this study, we employ time-resolved photoelectron spectroscopy (TRPES) using extreme ultraviolet (EUV) probe pulses to directly monitor orbital-resolved electronic structure changes. We demonstrate that the ring opening in CHD proceeds not only via the well-known photochemical pathway in the excited state but also through a delayed process originating from vibrationally excited ground-state molecules. This enables a direct temporal separation of sequential reaction pathways and provides new insights into chemical dynamics beyond the CI.

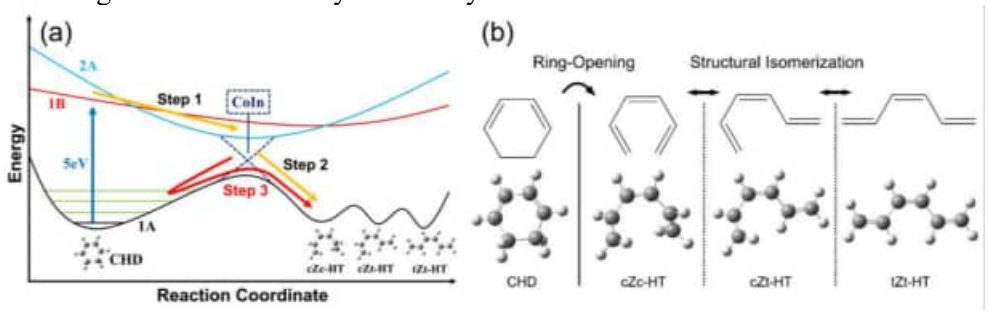

Fig. 1. (a) Schematic illustration of the photoinduced ring-opening pathway. (b) Structures of CHD and HT isomers.

2. Experimental and Computational Methods

The ring-opening dynamics of CHD were investigated by TRPES using high-harmonic-generated EUV pulses (29.5 eV) as the probe. The system was excited to the 1B state by ultraviolet pump pulses (4.65 eV, 266 nm) derived from a Ti:sapphire femtosecond laser system. The EUV probe pulses were spectrally selected using a time-delay-compensated monochromator, providing a pump–probe cross-correlation time width of 130 fs.

Photoelectron spectra were recorded as a function of delay time, and differential spectra were obtained by subtracting the ground-state signal. Molecular orbital (MO) energies of CHD and major HT isomers were calculated using density functional theory (DFT) at the ωB97X-D level.

3. Results and Discussion

Figure 2(b) shows the calculated MO energy levels of ground-state CHD and major HT isomers, while Fig. 2(c) presents the differential photoelectron spectra. Based on the comparison between experiment and theory, three regions are defined: the excited-state region, region I corresponding to the highest occupied molecular orbital (HOMO), and region II corresponding to the deeper-lying orbital (10a).

The excited-state signal appears from −150 to 150 fs and decays on a ~64 fs timescale, consistent with previous reports [2]. This defines the timescale of the primary photochemical ring-opening process following 1B excitation.

In region I (HOMO), a rapid depletion of the CHD signal is observed within ~200 fs,

accompanied by the emergence of a higher-energy feature assigned to cZc-HT. This behavior corresponds to the well-established photochemical ring-opening process. Notably, a similar spectral shift reappears on a delayed timescale (~700–1100 fs), indicating a second transformation involving additional CHD depletion and HT formation.

To verify this assignment, we examined region II corresponding to the 10a orbital of CHD (~12.7 eV), where no corresponding HT orbital exists. A decrease in spectral intensity at this energy is therefore expected upon ring opening. As shown in Fig. 2(e), such intensity reductions occur in two distinct delay windows (~0–400 fs and ~770–1050 fs), consistent with the dynamics in region I.

The recurrence of these spectral signatures in both orbital regions demonstrates that ring opening occurs in two temporally distinct regimes. The initial process corresponds to the primary photochemical ring opening following CI-mediated relaxation, whereas the delayed process is attributed to a secondary pathway originating from vibrationally excited CHD molecules in the ground state. These molecules retain sufficient internal energy to overcome the barrier for ring opening, leading to a thermally activated transformation.

This interpretation is supported by previous time-resolved high-harmonic spectroscopy, which reported ground-state structural evolution on a similar timescale (~650 fs) [3]. The agreement between independent techniques reinforces the assignment of the delayed process to ground-state dynamics.

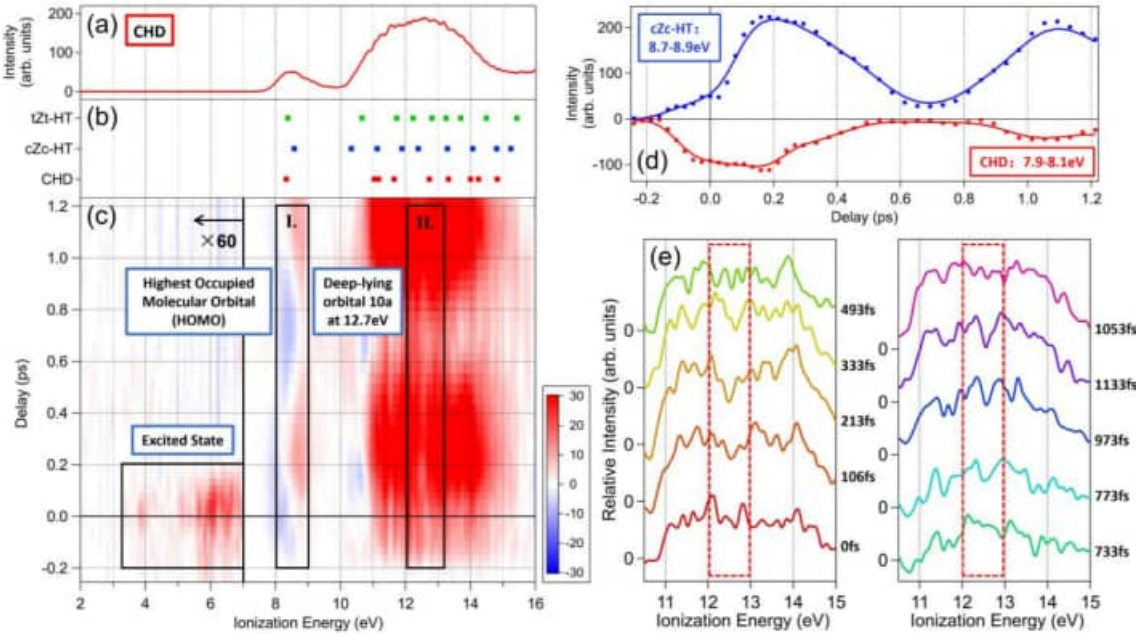

Fig. 2. (a) Photoelectron spectrum of ground-state CHD (pump off). (b) Calculated MO energy levels of CHD and HT isomers. (c) Differential photoelectron spectra and corresponding characteristic regions. (d) CHD and HT orbital signal intensities in region I. (e) Temporal evolution of the differential signal in region II.

4. Conclusion

We have demonstrated that the ring opening of CHD proceeds via two distinct pathways that are temporally separated and spectroscopically distinguishable. In addition to the well-known photochemical process occurring within ~200 fs, a delayed ring-opening pathway emerges on a sub-picosecond timescale, originating from vibrationally excited ground-state molecules.

These results reveal that chemical reactivity continues beyond the CI and can proceed via multiple pathways even after nonadiabatic relaxation. The present study highlights the capability of EUV-TRPES to provide orbital-resolved insights into both excited- and ground-state dynamics, offering a more complete picture of reaction mechanisms in prototypical electrocyclic systems.

5. References

[1] Q. Zhou et al., *The Journal of Organic Chemistry*, 89(2), pp. 1018–1034 (2024).
[2] S. Karashima et al., *Journal of the American Chemical Society*, 143(21), pp. 8034–8045 (2021).
[3] K. Kaneshima et al., *Journal of the Optical Society of America B*, 38(2), pp. 441–447 (2021).

2A1 An Efficient Approximation of the Timescale Hierarchies in a Large-Scale First-Order Kinetics

([1]ICReDD, Hokkaido University, [2]RIES, Hokkaido University, [3]Faculty of Science, Hokkaido University, [4]Faculty Division of Natural Sciences, Nara Women's University, [5]Graduate School of Information Science, University of Hyogo, [6]OTRI, Osaka University, [7]SANKEN, Osaka University) Yutaka Nagahata[2], Masato Kobayashi[1,2,3], Mikito Toda[2,4,5], Satoshi Maeda[1,3], Tetsuya Taketsugu[1,3], Tamiki Komatsuzaki[1,2,6,7]

Introduction

To uncover the physical essence of complex systems, approximation theories are frequently employed to isolate slow timescales from fast noise. In chemical kinetics, this involves the first-order rate equation:

$$\frac{\mathrm{d}\boldsymbol{x}}{\mathrm{d}t} = \boldsymbol{K}\boldsymbol{x}, \tag{1}$$

where, $x \coloneqq ([\mathrm{X}_1] \cdots [\mathrm{X}_n])^\top$ is the concentration vector of n chemical species and $[\mathrm{X}_i]$ denotes the concentration of chemical species X_i, $\boldsymbol{K}$ is the rate constant matrix, with its elements $(\boldsymbol{K})_{i,j} = k_{i,j}$ for $i \neq j$ and $(\boldsymbol{K})_{i,i} = -\sum_j k_{j,i}$ where $k_{i,j}$ represents the rate constant for the reaction $\mathrm{X}_j \to \mathrm{X}_i$. In these systems, fast reactions (e.g., side-chain rotations) are often less relevant to the overarching mechanism than slow structural changes (e.g., bond rearrangements). To extract physical insights from a network with massive reactions covering a wide range of fast and slow reactions, it is essential to develop lightweight analytical frameworks that provide a hierarchical overview, facilitating deeper investigation into the system's core dynamics.

Approximation methods rely on the assumption that subsystems reach equilibrium before a reaction occurs. These methods often fail when partial equilibrium is not clearly established. In the context of Markov State Models (MSMs), Perron-Cluster Cluster Analysis (PCCA) [1] is frequently employed as a coarse-graining criterion of Markov State Models (MSMs). This method examines the properties of eigenvectors within uncoupled Markov chains (a system with isolated subsystems). When these properties hold approximately, the coarse-grained rate constants are determined using the generalized pre-equilibrium approximation (GPE) [2].

To address this, we previously proposed the Exact Lumping (EL) and Indistinguishability Diagram (ID) as the EL-ID analysis framework [3]. Unlike subsystem-equilibration based methods, EL —which utilizes the Exact Lumping condition [4]—provides a mathematically rigorous, error-free projection theory that does not require an assumption of partial equilibrium. The ID, proposed in conjunction with EL to determine the projection targets, represents variables that become effectively indistinguishable as the observational time resolution decreases.

Despite its accuracy, EL-ID analysis, as well as PCCA-GPE, requires the diagonalization of the rate constant matrix $\boldsymbol{K}$. Reaction networks based on first-principles calculations, such as those obtained via reaction path search methods, are typically huge and encompass an extremely broad range of time scales. For large-scale networks with multiple precision arithmetic, this creates a significant computational overhead. This study addresses two critical questions to bypass this bottleneck:

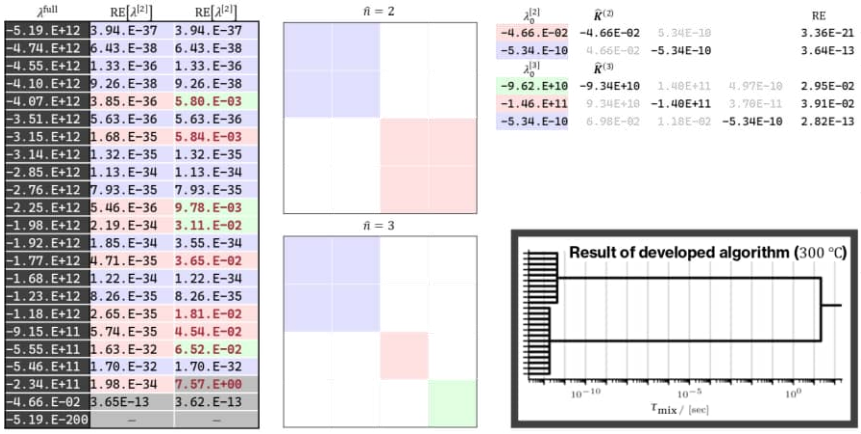

Fig. 1 [Left] Relative errors (RE) between the full eigenvalues of the Claisen rearrangement of allyl vinyl ether and the eigenvalues derived from the ID-identified two-state (red, blue) and three-state (red, blue, green) block-diagonal matrices, as well as those obtained via the GPE (gray). [Upper right] RE between the slowest eigenvalue of each sub matrix and the diagonal elements of the lumped matrix using the EL method. [Bottom right] A diagram of the subsystem mixing time obtained by the developed algorithm.

- Divide-and-Conquer Validity: Can stochastic processes within a Perron-Cluster be accurately approximated using the corresponding submatrix of $\boldsymbol{K}$?
- Algorithm Efficiency: Is there a more lightweight algorithm capable of identifying these Perron-Clusters without full-matrix diagonalization?

The former concerns the validity of a divide-and-conquer approach as a prerequisite for the latter, while the latter pertains to the efficiency of the preliminary analysis for the former. Resolving both issues should significantly reduce the required computational overhead and substantially broaden the applicability of the EL-ID analysis framework.

Methods and Results

Our findings confirm that the "divide-and-conquer" approach is valid for subsystems definitively classified as Perron-Clusters. As shown in Fig. 1, full eigenvalues can be predicted with high precision in two-state systems with clear timescale separation, though accuracy decreases in three-state systems where separation is less distinct. Fig. 1 presents a comparison between the eigenvalues of the full rate constant matrix and those of the coarse-grained matrix, derived via the GPE approximation, and the block-diagonal submatrices corresponding to indistinguishable subsystems (where two-state system $\lambda^{[2]}$ and three-state system $\lambda^{[3]}$) identified by the ID. These results demonstrate that the former premise holds for subsystems that can be definitively classified as Perron-Clusters.

Based on these insights, we developed a computationally efficient algorithm for identifying Perron-Clusters that bypasses the need for high-precision calculations and full-matrix diagonalization. Specifically, we developed an online algorithm for enumerating strongly connected components; by incorporating several physical constraints, such as the verification of time-scale separation, we successfully achieved the high-speed, hierarchical extraction of Perron-Clusters. Further details will be discussed during the presentation.

Reference
[1] P. Deuflhard, et al., *Linear Algebra Appl.* **315**, 39 (2000).
[2] M. Rae and M. N. Berberan-Santos, *J. Chem. Educ.*, **81**, 436 (2004).
[3] Y. Nagahata, et al., *PNAS* **121**, e2317781121 (2024).
[4] J. Wei and J. C. W. Kuo, *Ind. Eng. Chem. Fundam.* **8**, 114 (1969).

2A2 Exploration of chemical reaction pathways by quantum walk

([1]School of Science, The Univ. of Tokyo; [2]Institute for Attosecond Laser Facility, The Univ. of Tokyo)
Kazuki Tsuoka[1], Takanori Nishi[2], Kaoru Yamanouchi[1,2]

I. Introduction

To explore chemical reaction pathways by quantum chemical calculations, knowledge of the positions of local minima representing reactants and products, and of the transition states on the potential energy surface (PES) is a prerequisite. It has been shown that possible reaction pathways on the PES can be efficiently obtained by the global reaction route mapping program [1] by systematically searching for other local minima. However, as the number of atoms in reactants increases, the number of possible products increases exponentially, and consequently, a search for possible reaction pathways becomes unrealistically difficult. In order to overcome this difficulty, we adopt an approach called a discrete-time quantum walk (DTQW) to be implemented in quantum computing.

II. Methods

We adapt a quantum maze-solving algorithm [2] to explore chemical reaction pathways by a quantum walk process. We discretize each coordinate axis in an M-dimensional coordinate space, in which a PES is prepared, into N grid points, so that we have a total of N^M possible grid points. A state of the quantum walker is represented in a composite Hilbert space $\mathcal{H}_P \otimes \mathcal{H}_C$, where $\mathcal{H}_P$ is the position space and $\mathcal{H}_C$ is the coin space. The position coordinates are encoded into $n = \lceil M \log_2 N \rceil$ qubit state using binary encoding, where $\lceil \cdot \rceil$ is the ceiling function. For example, a two-dimensional space with $2^{10} = 1024$ grid points for each axis requires $2 \times \log_2 2^{10} = 20$ qubits. The time evolution operator of DTQW on PES is defined as $U = S(I \otimes C)\left(e^{iV} \otimes I\right)$, where C is a coin operator that changes the state of the coin register, I is an identity operator, and S is a shift operator that shifts the position of quantum walkers backwards when the state of the coin register is zero and forwards when the state of the coin register is one. The potential energy V must be calculated at each step of the quantum walk and applied to the qubits as a phase shift e^{iV} before applying the coin and shift operator (Fig. 1) [2].

In DTQW, the spatial spread of the probability distribution grows linearly with the number of steps, allowing the walker to scan N grid points along an axis in $O(N)$ time. In contrast, the width of the probability distribution of a classical random walk scales with the square root of the number of steps. Consequently, these classical methods require $O(N^2)$ steps to cover the same spatial distance. This fundamental difference in scaling ensures that DTQW can explore the PES landscape more quickly than a classical random walk. It is also important to emphasize that the spreading speed of the walker is independent of the time scale of the chemical reaction. The time complexity of the evolution-based quantum algorithm increases when the evolution time becomes longer, or a higher accuracy is required for the final state.

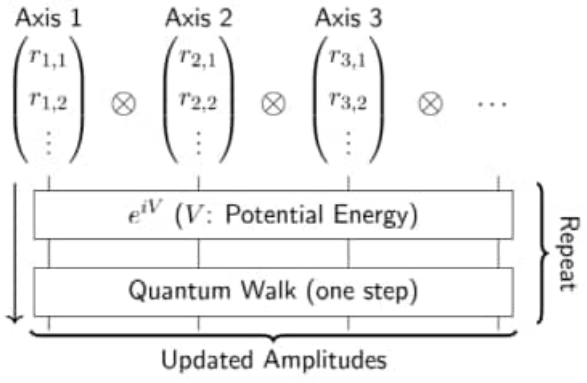

Fig. 1 Schematic illustration of a quantum algorithm for a DTQW on a PES. The walker's spatial coordinates are mapped to qubit states using binary encoding, and a phase shift corresponding to the potential energy is applied to each state. Subsequently, a quantum walk operator is applied to update the walker's probability distribution. Repeating this cycle realizes a DTQW on the PES. The coin register is omitted in this figure.

III. Results and discussion

We performed the quantum walk on a two-dimensional Müller-Brown potential with three minima (A, B, and C in Fig. 2(a)) and two first-

order saddle points (P and Q in Fig. 2(a)), which is defined as

$$V(x,y) = \sum_{i=1}^{4} A_i \exp[a_i(x-\bar{x}_i)^2 + b_i(x-\bar{x}_i)(y-\bar{y}_i) + c_i(y-\bar{y}_i)^2],$$

Where $\{A_i\}, \{a_i\}, \{b_i\}, \{c_i\}, \{\bar{x}_i\}$, and $\{\bar{y}_i\}$ $(i = 1, \ldots, 4)$ are constants given by [3]. The initial positions of the quantum walkers were are set at minimum A (Fig. 2(a)). To make the quantum walk possible, we modified the MB potential to $V'(\boldsymbol{x})$ given by

$$V'(\boldsymbol{x}) = \begin{cases} V(\boldsymbol{x}), & V(\boldsymbol{x}) \geq E \\ V(\boldsymbol{x}) + \dfrac{\left(E - V(\boldsymbol{x})\right)^2}{\alpha + E - V(\boldsymbol{x})}, & V(\boldsymbol{x}) < E \end{cases}$$

where E is the threshold energy and α is a tuning parameter, so that the potential energy at the minima is effectively raised by adding the second term called a boost potential to $V(x)$ when $V(x) < E$. At the beginning of the time evolution at t = 120 (Fig. 2(c)), the walker moved rapidly along the PES, and at t = 360 (Fig. 2(d)), the probability distribution peaked at the newly discovered minima B and C. At t = 480 and t = 600, the probability distribution oscillates while keeping the peaks around the three minima A, B, and C. This result demonstrates that DTQW on a PES can effectively explore another local minimum.

In the present study, we have demonstrated the DTQW approach using a two-dimensional PES. In the case of chemical reactions having a higher dimension, we may need to restrict the number of samplings, and consequently, we have to increase the number of measurements L, so that the statistical uncertainty becomes smaller whose scaling is $O\left(1/\sqrt{L}\right)$.

References

[1] K. Ohno and S. Maeda, *Mol. Sci.* **5**, A0042 (2011). [2] G. D. Varsamis et al., *Eur. Phys. J. Plus* **138**, 1–10 (2023). [3] K. Müller and L. D. Brown, *Theoret. Chim. Acta* **53**, 75 (1979).

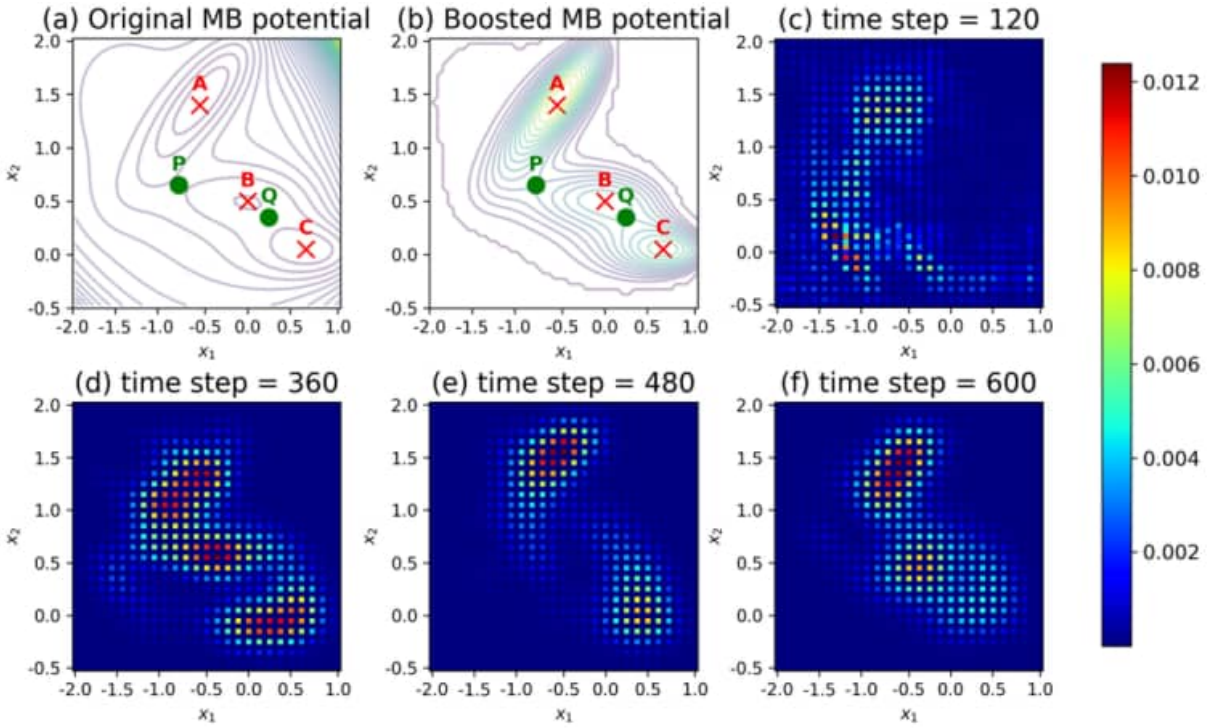

Fig. 2 The contour plot of the (a) Müller-Brown potential and (b) boosted Müller-Brown potential, and the cross marks and the filled circles on the plot represent the local minima and the saddle points, respectively. The probability distribution of quantum walkers on a boosted Müller-Brown potential at time step (c) t = 120, (d) t = 360, (e) t = 480, and (f) t = 600 obtained by a simulator. The number of grid points for each dimension is 51, E = 0.3, and α = 0.1.

2A3 Observation of Rabi Oscillation Between the Inversion Splitting Doubling in Ammonia

(Institute of Science Tokyo) M. Ardelia, K. Ueno, R. Saida, M. Nakamura, Y. Ohshima

The ammonia molecule has two most stable configurations equal in energy: the $|U\rangle$ ($|D\rangle$) form where the nitrogen atom is located above (below) the hydrogen plane (Fig. 1). The potential barrier between the two configurations is low enough to allow quantum mechanical tunnelling, resulting in the molecule's pyramidal form being inverted and each rovibronic level to be split into doublets with opposite symmetry (Fig. 1): $|v_2 \pm\rangle = \frac{|U\rangle \pm |D\rangle}{\sqrt{2}}$. Our work aims to capture this motion via real-time imaging, for which the creation of a vibrational wave packet leading to a population distribution of $|v_2 +\rangle : |v_2 -\rangle = 0.5 : 0.5$ is necessary, and this is achievable through irradiation of a microwave field resonant to the energy difference between the involved doublet. For the lowest level $|v_2 \pm\rangle = |0 \pm\rangle$, the energy difference between the split states is 0.8 cm^{-1} = 23.695 GHz. Previous attempts [1] showed that a higher degree of spatial coherence and field strength are required of the microwave field involved. In the present study, we have successfully fulfilled these conditions through the implementation of a Fabry-Pérot cavity (FPC).

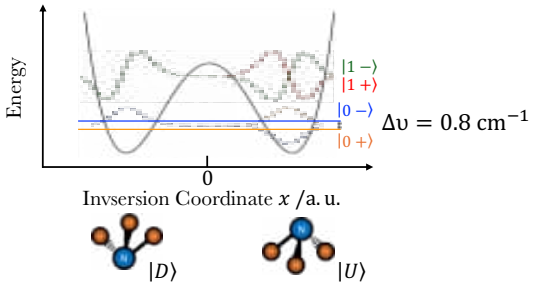

Fig. 1. Inversion motion in the umbrella molecule.

The experimental setup used in the present study is schematically shown in Fig. 2. 10% ammonia seeded in argon gas was adiabatically expanded into vacuum (~0.2 mPa static pressure) through a pulsed valve with stagnation pressure 0.60 MPa, resulting in a sample temperature of ≤10 K. The pulsed gases were then collimated into molecular beams by passing through two skimmers, set 88 mm and 237 mm downstream from the valve. The molecular beam was then introduced into a Stark deflector (SD), where an inhomogeneous electric field was applied, as shown in the upper inset, causing each molecule's trajectory to undergo changes according to the rovibrational state it resides in. Of the states of interest in this study, $|v_2 \pm, J, |KM|\rangle = |0+,1,1\rangle$ ($|0-,1,1\rangle$) stabilizes at high (low) electric fields, corresponding to an upward (downward) trajectory change in the described setup, as shown in the lower inset. The molecules thus enter the FPC with a spatial distribution corresponding to their state.

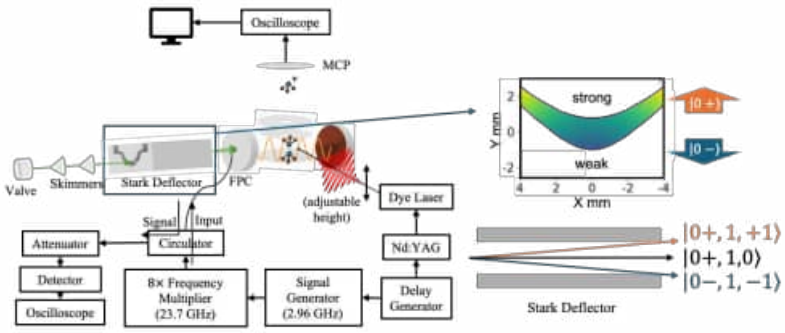

Fig. 2. Experimental Setup

The FPC is composed of two Cu coated mirrors of 40 mm radius and 158 mm radius of curvature, set 148 mm apart in what is known as the near-confocal arrangement, where the cavity is stable and has low dissipation losses. Microwave field is fed into the cavity through a monopole antenna with insertion depth and length of 3.1 mm each. With ion optics for time-of-flight mass spectroscopy (TOF-MS), the cavity has a loaded quality factor Q_L of 1.3×10^3, calculated from $Q_L = \frac{\nu}{\delta\nu}$, where ν is the resonance

frequency and $\delta\nu$ its full width at half maximum. This value can be used to calculate the field strength inside the cavity, from which a theoretical value for the Rabi frequency can be derived.

The rotational state population of the deflected beam is then characterized by (2+1) resonance enhanced multi-photon ionization (REMPI) via the $\widetilde{C'} \leftarrow \tilde{X}$ transition. By varying the height of the focal position of the probe laser (doubled output of ~300 nm from a Nd:YAG pumped dye laser, frequency resolution 0.2 cm^{-1}), we can select a particular state as the system's sole initial state. For the present work, we have chosen $|0-,1,1\rangle$.

When a microwave pulse is introduced into the FPC, the electric field forms a standing wave pattern of alternating nodes, where the field strength is near zero, and antinodes, where the field is strong. The ammonia molecules interact with this field, and population transfer occurs between the $|0-,1,1\rangle$ and $|0+,1,1\rangle$ states. The transfer efficiency is directly proportional to the field strength; areas inside the FPC with stronger field strength facilitate a more efficient population transfer. Figure 3 (a) shows REMPI signals, directly proportional to the population of the $|0-,1,1\rangle$ state, after it has interacted with a resonant microwave field for a fixed duration of 160 ns, while the timing at which the microwave is introduced was varied relative to ionization timing ($t = 0$). Points with weaker (stronger) signals thus indicate antinodes (nodes) in the FPC electric field pattern. A clear pattern of 11 nodes and antinodes each appear, which agrees with the expected field pattern in the current geometry.

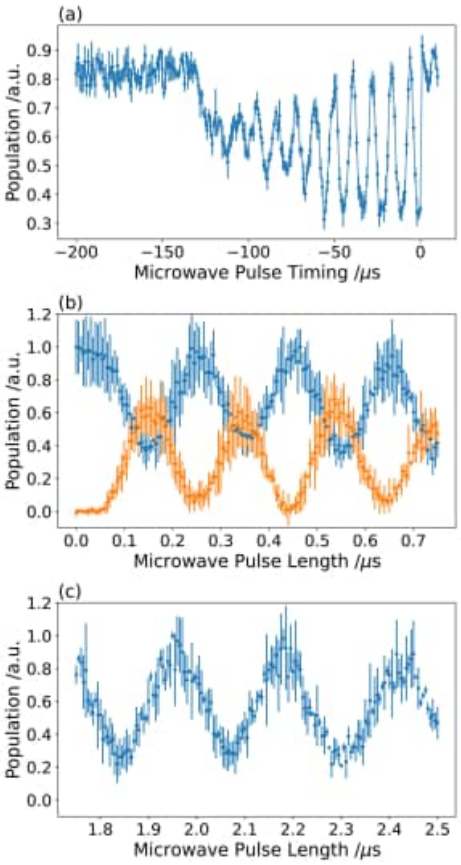

Fig. 3. (a) $|0-,1,1\rangle$ population, measured with varied microwave pulse timings. $t = 0$ corresponds to ionization. (b) Populations of $|0-,1,1\rangle$ (navy) and $|0+,1,1\rangle$ (orange) with varied microwave interaction time. (c) $|0-,1,1\rangle$ population with extended microwave interaction time.

Figure 3 (b) shows the $|0-,1,1\rangle$ (navy line) and $|0+,1,1\rangle$ (orange line) states' populations as a function of microwave interaction time. $|0-,1,1\rangle$ ($|0+,1,1\rangle$)'s population reached a minimum (maximum) of 30% (70%) before returning to 100% (0%), with a period of 220 ns or frequency of 4.5 MHz. This is in excellent agreement with the theoretical value of 7.5 MHz, calculated from $\omega_R = \frac{\mu E}{\hbar}$, where $E = \sqrt{\frac{Q_L P_{in}}{\epsilon_0 V \pi \upsilon}}$, with $P_{in} = 0.5$ mW, V the mode volume of the FPC, and υ the resonance frequency. Figure 3 (c) shows the $|0-,1,1\rangle$ state signals with significantly longer microwave interaction times. A similar pattern was observed, indicating that the incomplete population transfer was not due to radiative damping. The absence of radiative damping proves that the FPC successfully realized a higher degree of spatial coherence and field strength. The 30% not participating in the population transfer is likely due to randomization between the $M = 0, \pm 1$ states in a field free area between the SD and the FPC, with $M = 0$ states not having any allowed transitions to the $|0+\rangle$ state and therefore staying in the $|0-\rangle$ state. Further experiments are needed to verify this hypothesis.

[1] K. Ueno, K. Mizuse, Y. Ohshima, "Spatial Separation of Ammonia Inversion-Tunneling Levels by Using a Stark Deflector", the 14th Annual Meeting of JSMolSci, Osaka, Japan, Sept. 14-17, 2020.

2A4 Hydrogen momentum spectroscopy of small hydrocarbon molecules

([1]IMRAM, Tohoku Univ., [2]Flinders Univ.) Shinichirou Minemoto[1], Satoru Kanaya[1], Takuma Sugai[1], Darryl Jones[2], and Masahiko Takahashi[1]

The arrangement and interaction of atoms in a molecular environment are the fundamental properties that govern the reactivity and functionality of the molecule. The arrangement of atoms in the molecule or the molecular structure has intensively been studied by spectroscopy and diffraction techniques. On the other hand, atomic motion has been mostly investigated in terms of collective motions, i.e., normal modes of molecular vibration by vibrational spectroscopy, though the motion of one specific atom is often the key to understand the molecular reactivity and functionality. For this reason, atomic momentum spectroscopy (AMS) was proposed a quarter of a century ago [1], which aims to directly measure momenta of each constituent nucleus in a molecule by using electron-nucleus Compton scattering. To employ AMS as a molecular spectroscopy technique, we have recently constructed a highly sensitive AMS apparatus [2], developed a data analysis protocol [3], and built quantum chemistry-based AMS (QC-AMS) theory [3,4] to predict Compton profile due only to intramolecular motion of each atom. We have then started to study how intramolecular atomic motion of the same nuclear species depends upon the difference in the molecular environment [5]. Along this line, in the present study, we experimentally measured the hydrogen momentum distributions in small hydrocarbon molecules, C_2H_2, C_2H_4 and C_2H_6, and compared those with predictions of the QC-AMS theory.

AMS is an experimental method that measures kinetic energy distributions of quasi-elastically backscattered electrons from a gaseous molecule, and it is characterized as a binary collision of the incident electron with one constituent nucleus of the molecule [6]. In the present work, energy loss spectra of C_2H_2, C_2H_4 and C_2H_6 have been measured at an incident electron energy of 2 keV and at a scattering angle of 135° by using our AMS apparatus [2]. As an example of the experimental results, we show in Fig. 1 the electron energy loss spectrum measured for the C_2H_6 molecule. One can see from the figure that there are two bands centered at around 0.3 and 3.7 eV.

It is known [6] that the energy loss E_{loss} in AMS is expressed as

$$E_{loss} = \frac{q^2}{2M_i} + \frac{\boldsymbol{P}_i \cdot \boldsymbol{q}}{M_i}, \quad (1)$$

where M_i is the mass of the target nuclei having an initial momentum $\boldsymbol{P}_i$, and $\boldsymbol{q} \equiv \boldsymbol{p}_0 - \boldsymbol{p}_1$ is the momentum transferred from the incident electron to the scattering nuclei with $\boldsymbol{p}_0$ and $\boldsymbol{p}_1$ being the momenta of the incident and backscattered electrons, respectively. The first term on the right-hand side of Eq.

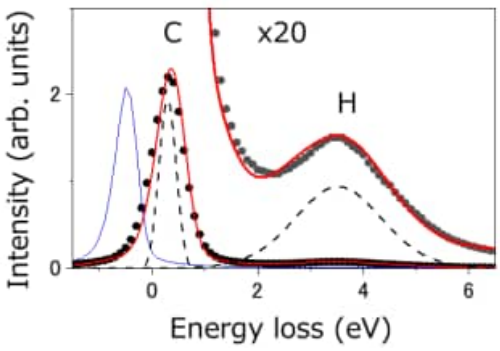

Fig. 1: An electron energy loss spectrum of the C_2H_6 molecule. The red curve is an associated theoretical spectrum, which is created by summing up convolutions of predictions of the QC-AMS theory (the dashed blue curves) and the instrumental response function (the solid blue curve) for the C and H atoms.

(1) represents the mean recoil energy, which corresponds to the recoil with the scattering nucleus being stationary ($\boldsymbol{P}_i = 0$). The observed band positions of 0.3 and 3.7 eV are in good agreement with the mean recoil energies of 0.3 and 3.7 eV calculated for the C and H atoms, and thus the former band is assigned to the C band and the latter to the H band. The second term on the right-hand side of Eq. (1) represents Doppler broadening due to motion of the scattering nuclei before the electron collision.

Also included in Fig. 1 is a theoretical electron energy loss spectrum of the C_2H_6 molecule, shown as the red curve. While the initial momentum $\boldsymbol{P}_i$ of the scattering atom is composed of those due to the molecular vibration and rotation and the center-of-mass translational motion, however, the effect of the translational motion can be dropped off in this case. This is because the Doppler broadening due to the translational motion is calculated to be ~0.01 eV and this value is much smaller than the intrinsic response function of about 0.4 eV FWHM, estimated by an energy loss spectrum of a much heavier nucleus, Kr (M_{Kr}~ 84), shown as the solid blue curve. We have thus created the theoretical electron energy loss spectrum by summing up convolutions of predictions of the QC-AMS theory (the dashed blue curves) and the instrumental response function for the C and H atoms, with a weight of 36 : 1 for the C and H bands estimated using the Rutherford cross section formula. It can be seen from Fig. 1 that the theoretical spectrum reasonably reproduces the experimental results, but there is noticeable small difference between the experimental and theory. The same is true with the results for other two molecules, C_2H_2 and C_2H_4, so we have obtained experimental momentum distributions of the H atom in C_2H_2, C_2H_4 and C_2H_6 by a curve fitting procedure while the predictions of the QC-AMS theory were used as trial functions.

For ease of catching outline of the main features of the hydrogen momentum distributions, we show in Fig. 2 those calculated for the C_2H_2, C_2H_4, and C_2H_6 molecules by using the QC-AMS theory. Interestingly, the FWHM values of the distributions for the C_2H_4 and C_2H_6 are similar to each other, but that for the C_2H_2 is narrower. In this contribution, the experimental hydrogen momentum distributions are presented to discuss the similarity and dissimilarity of the intramolecular atomic motion of the H atom in the three molecules.

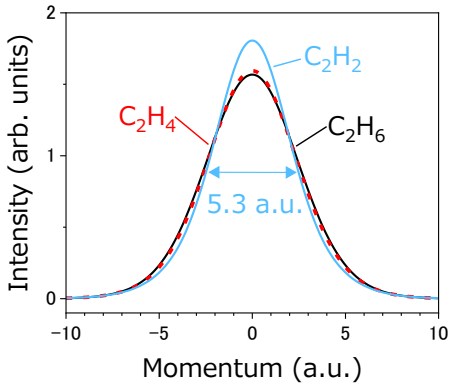

Fig.2: Comparison of the hydrogen momentum distributions calculated for the C_2H_2, C_2H_4, and C_2H_6 molecules by using the QC-AMS theory.

References

[1] M. Voss, *Phys. Rev. A* **65** 012703 (2001).

[2] M. Yamazaki, M. Hosono, Y. Tang, and M. Takahashi, *Rev. Sci. Instrum.* **88** 063103 (2017).

[3] Y. Tachibana, Y. Onitsuka, H. Kono, and M. Takahashi, *Phys. Rev. A* **105** 052813 (2022).

[4] S. Kanaya, Y. Onitsuka, N. Watanabe, H. Kono, and M. Takahashi, *Phys. Chem. Chem. Phys.* **27** 2453 (2025).

[5] D. B. Jones S. Kanaya, Y. Onitsuka, and M. Takahashi, *J. Phys. Chem. Lett.*, **17** 166 (2025).

[6] S. Kanaya, Y. Onitsuka, S. Houamer, O. Chuluunbaatar, Yu. V. Popov, D. Fursa, I. Bray, and M. Takahashi, *J. Phys. B*, in press.

3A1 Combined experimental and computational study of ionization-induced reactions on propanol ice surfaces

([1]Kyoto University, [2]Tokyo Metropolitan University) T. Majima[1]; S. Otsuka[1], S. Jifuku[1], T. Murakami[2], H. Tsuchida[1], M. Saito[1]

Ion–molecule reactions play a central role in the chemistry initiated by ionizing radiation. In condensed phases, however, many of these reactions remain poorly characterized (for example, on the negative-ion side) because they occur in a dense and complex reactive environment that is difficult to probe directly. We have recently used mass spectrometry to study the positive and negative secondary ions emitted from microdroplet surfaces under MeV heavy-ion impact, obtaining systematic and comprehensive data on these condensed-phase reactions [1,2]. The mass spectra contain many newly identified fragment and reaction-product ions, offering a rich basis for understanding the underlying chemistry. To examine how molecular structure affects ionization-induced reactions in the condensed phase, we use the smallest pair of structural isomers, 1-propanol (1-PrOH) and 2-propanol (2-PrOH), as a model case. Here we report secondary-ion mass spectra from 1-PrOH and 2-PrOH ice surfaces under MeV heavy-ion impact, interpreted using global reaction route mapping (GRRM) calculations on the ground-state potential energy surface (PES) of the protonated parents.

1-PrOH and 2-PrOH ices, prepared on a substrate cooled with liquid nitrogen, were irradiated with 1.5 MeV C^+ ions from the Kyoto University 2.5 MV Van de Graaff accelerator, and positive and negative secondary ions were analyzed by time-of-flight (TOF) mass spectrometry using a beam-chopping technique. Selectively deuterated isomers, 1-PrOH(d1) and 2-PrOH(d8), establish the chemical composition of each peak. GRRM calculations on the protonated parents were performed at MP2/cc-pVDZ with CCSD(T)/cc-pVTZ refinements at key stationary points; the C–O dissociation channel was characterized separately by scanning the C–O distance. The spectra obtained from droplets with 4 MeV C^{3+} were essentially indistinguishable from the ice spectra, as we previously observed for methanol.

Figure 1 shows the positive and negative TOF mass spectra (low-mass region) from 1-PrOH and 2-PrOH ice surfaces. In the gas-phase electron-impact mass spectrum of the isolated parent, α-cleavage of the radical cation $PrOH^+$ gives the base peak at m/z = 31 (CH_2OH^+) for 1-PrOH and m/z = 45 ($CH_3CH{=}OH^+$) for 2-PrOH. In the condensed-phase ice spectra, these α-cleavage fragments are strongly suppressed; the dominant features are instead the protonated parent $PrOH_2^+$ (m/z = 61), an extensive series of protonated cluster ions $[(PrOH)_n + H]^+$, and various fragment ions, the strongest of which is at m/z = 43. This is consistent with our previous findings for methanol and ethanol [1,2], in which the radical cation is rapidly converted into the protonated parent by an exothermic proton-transfer reaction with a neighboring molecule, $ROH^+ + ROH \rightarrow ROH_2^+ + RO$, driven by the high proton affinity of the alcohol; the dominant secondary cations therefore originate from $PrOH_2^+$ rather than from $PrOH^+$.

This fragment ion at m/z = 43 is identified by the d1/d8 substitutions as $C_3H_7^+$ from the dehydration

$PrOH_2^+ \rightarrow C_3H_7^+ + H_2O$. Consistent with the gas-phase mass spectrometric observations [3], the $C_3H_7^+$ signal was more abundant from 1-PrOH than from 2-PrOH. The GRRM search did not return this dissociation channel. A separate scan along the C–O coordinate of the protonated parent showed that the energy rises monotonically toward the dissociation limit, with no transition state along the path, and that both isomers rearrange to a common isopropyl-cation product. Single-point CCSD(T)/cc-pVTZ calculations showed that protonated 1-PrOH is 0.28 eV (6.42 kcal/mol) higher in energy than protonated 2-PrOH. Since the dissociation end state is common, the energy required for the dehydration $PrOH_2^+ \rightarrow C_3H_7^+ + H_2O$ is correspondingly lower for 1-PrOH (1.10 eV) than for 2-PrOH (1.38 eV). This energetic offset could account for the higher $C_3H_7^+$ yield observed from 1-PrOH than from 2-PrOH.

Several additional ions show clear structural-isomer dependence, and their mechanistic interpretation is still under investigation. (i) The Zundel cation $H_5O_2^+$ (m/z = 37) is observed only in 2-PrOH ice (its formula confirmed by d8 substitution). (ii) The negative-ion spectra are dominated by the deprotonated parent $C_3H_7O^-$ (m/z = 59) and a $[(PrOH)_n - H]^-$ cluster series; the strongest isomer dependence appears at m/z = 41 and 43 (C_2HO^- and $C_2H_3O^-$, both stronger from 2-PrOH). (iii) A high-mass m/z = 89 ion, and a cluster series at $m/z = 90 + 60n$ ($n \geq 1$), are observed exclusively from 1-PrOH ice. These observations will be presented together with the current status of our analysis.

[1] T. Majima et al., J. Chem. Phys. 153, 224201 (2020).

[2] T. Majima et al., J. Phys. Chem. A 126, 8988 (2022).

[3] Z. Karpas et al., Int. J. Mass Spectrom. Ion Process. 133, 47 (1994).

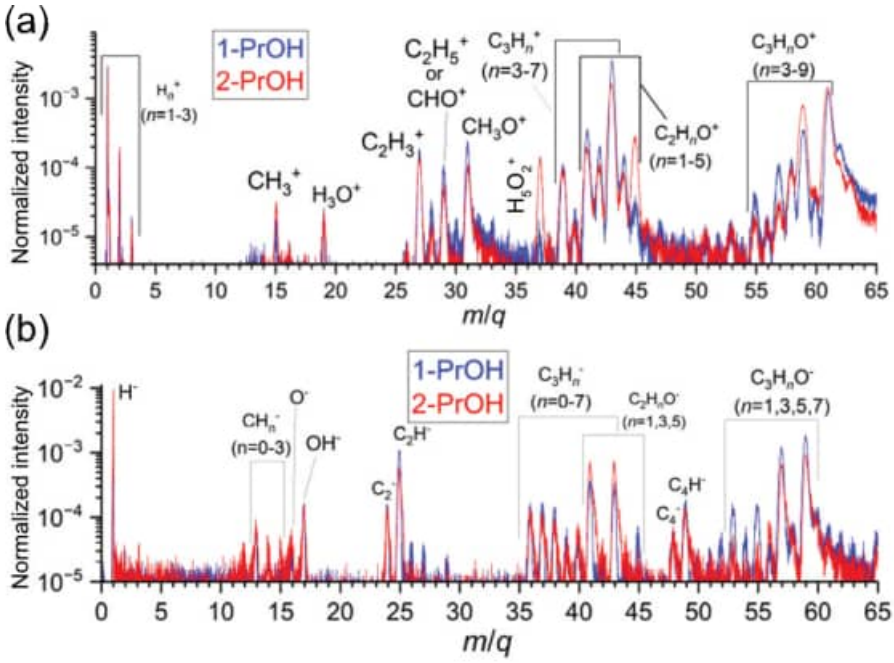

Figure 1. Positive (a) and negative (b) TOF mass spectra (low-mass region) from 1-PrOH and 2-PrOH ice surfaces under 1.5 MeV C^+ irradiation.

3A2 Photodesorption of hydroxyl radical on ice induced by visible light

([1]Hokkaido University, [2]Hiroshima University, [3]RIKEN Nishina Center for Accelerator-based Science)
Sie, Ni-En[1]; Tsuge, Masashi[1,2]; Nakai, Yoichi[3]; Watanabe, Naoki[1]

Hydroxyl (OH) radicals play a vital role in the chemical evolution of various environments, such as planetary atmospheres and cold interstellar regions. While photodesorption of OH induced by ultraviolet (UV) and X-ray irradiation has been investigated, the effect of visible light has not been widely considered in the past, since both isolated water molecules and OH radicals are transparent in the visible range. In addition, the in-situ detection of adsorbed OH radicals is challenging with the conventional techniques, including Raman, infrared spectroscopies, and mass spectrometries. Recently, the photodesorption of OH radicals at visible 532 nm photons was successfully observed by a newly developed PSD-REMPI method, a combination of photostimulated desorption (PSD) and resonance-enhanced multiphoton ionization (REMPI).[1] This method has also been applied to detect H and C atoms on water ice.[2, 3] For an isolated OH radical, transition from the ground state to the first doublet excited state was reported to occur at around 308 nm.[4] However, the quantum chemical calculations suggested that the excitation wavelength can extend to 600 nm when an OH radical has strong hydrogen bonds with water molecules[5], implying that the absorption efficiency is sensitive to the photon wavelength and adsorption sites on the water ice surface. To further investigate the relationship between photoabsorption and the population of OH adsorption sites on water ice, in this study, a wide range of wavelengths from 310–700 nm, including UV and visible photons, was used to induce the photodesorption of OH radicals adsorbed on amorphous solid water (ASW). The wavelength dependence of the photodesorption efficiency in the visible range is reported for the first time.

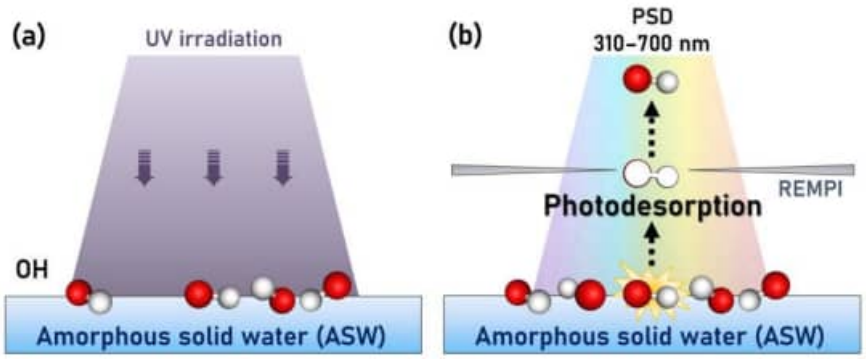

Figure 1. (a) The OH preparation on water ice by UV irradiation. (b) The photodesorption process.

The OH radicals were produced by the vacuum ultraviolet (VUV) irradiation of water molecules at 50 K, as shown in Fig.1 (a). The surface coverage of OH radicals on ASW was approximately 0.01. The OH radicals are photodesorbed by weak nano-second PSD laser pulses with the power of 0.2 mJ/pulse at the spot size of 3mm^2 and analyzed by a 2+1 REMPI process with a time-of-flight mass

spectrometer, as illustrated in Fig.1 (b). The PSD-REMPI signal intensities were measured by varying the wavelength of the PSD laser radiation. We define the photodesorption efficiency, Y_{pd}, as the absolute signal intensity divided by the photon number. The Y_{pd} values as a function of PSD wavelength are shown in Fig.2, which are strongly dependent on wavelength with a maximum near 370 nm. The results are consistent with quantum chemical calculations predicting that the majority of adsorbed OH radicals absorb photons within 300–400 nm range.

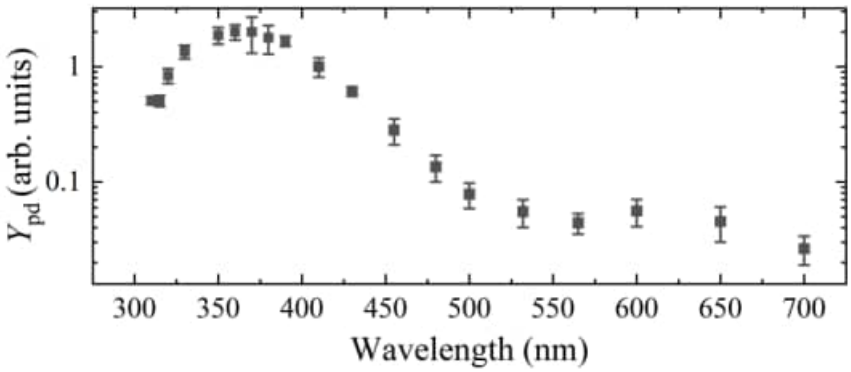

Figure 2. The photodesorption efficiency (Y_{pd}) as a function of wavelength from UV to visible light.

The photodesorption efficiency is determined by two factors: (1) the population of the OH adsorption site where excitation happens, (2) the photodesorption cross section, which depends on the adsorption sites. By monitoring the attenuation of the OH radical intensities by PSD laser irradiation at different wavelengths, the photodesorption cross sections were determined. We found that in the longer wavelength region (≥480 nm), the attenuation can be expressed by a single-exponential decay with one cross section, whereas in the shorter wavelength region (≤455 nm), an additional exponential component with a different cross section is required, resulting in a two-component exponential decay. The quantum calculations indicate that long-wavelength photons can be absorbed by OH radicals trapped at strong binding sites (binding energies above 0.45 eV) on the ice surface, while the short-wavelength photons can be absorbed by those at both strong and weak binding sites. Accordingly, we assign the cross sections obtained at longer wavelengths for the desorption from the strong binding site, while the two cross sections reflect the contributions from both strong and weak binding sites. From further analysis of the fittings, the populations of strong and weak binding sites were found to be comparable.

Reference

[1] Miyazaki, A., et al. 2020, *Physical Review A*, **102**, 052822
[2] Watanabe, N., & Tsuge, M. 2020, *Journal of the Physical Society of Japan*, **89**, 051015
[3] Tsuge, M., Molpeceres, G., Aikawa, Y., & Watanabe, N. 2023, *Nature Astronomy*, **7**, 1351
[4] Crawford, T. D., Abrams, M. L., King, R. A., Lane, J. R., Schofield, D. P., & Kjaergaard, H. G. 2006, *The Journal of chemical physics*, **125**, 204302
[5] Sameera, W., Senevirathne, B., Andersson, S., Maseras, F., & Nyman, G. 2017, *The Journal of Physical Chemistry C*, **121**, 15223

3A3 Oxygen reactivity of surface-supported pure and boron-doped aluminum superatoms

(Keio University) Inoue, Tomoya; Nakajima, Atsushi

Introduction

Superatoms (SAs) exhibit atom-like electronic shell structures and provide a promising platform for constructing functional materials from atomically precise building blocks. Among them, the 13-atom aluminum nanocluster (NC) anion, Al_{13}^-, is exceptionally stable in the gas phase due to its closed-shell 40-electron configuration filling the 1F superatomic orbital, combined with an icosahedral structure (Fig. 1a).[1,2] This stability is reflected in unusually low reactivity toward O_2 compared to other Al_n NCs.

Heteroatom substitution significantly modifies this system. For example, replacing one Al atom with Si leads to an endohedral $Si@Al_{12}$ binary cage superatom (BCSA), where structural distortion is relaxed and the electronic state is neutralized by valence electron adjustment. Similar stabilization is expected for boron (B), which is smaller than Al. Mass spectrometric studies of $Al_nB_m^-$ NCs show pronounced stability at compositions corresponding to Al_{13}^- and $B@Al_{12}^-$ (Fig. 1a), whereas further substitution destabilizes the icosahedral cage. These results indicate that a single dopant atom can be encapsulated within an Al_{12} cage, while additional substitution disrupts the icosahedral structure.

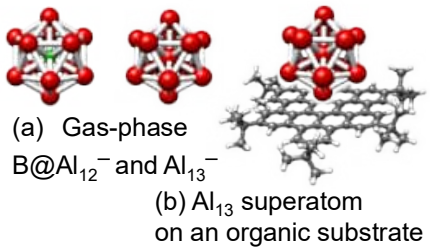

Fig. 1 (a) $B@Al_{12}^-/Al_{13}^-$ superatom and (b) Al_{13} superatom on HB-HBC substrate.

More generally, $X@Al_{12}$ systems (X = B, Si, phosphorus (P)) follow several key principles:[3,4] (i) stability is governed by electron shell closure (40 electrons), (ii) dopant size and position determine whether endohedral or exohedral structures form, (iii) closed-shell configurations exhibit low chemical reactivity, and (iv) superatomic chemical analogies emerge, with different dopants imparting element-like behavior.

Extending such superatomic properties to condensed-phase systems is essential for practical applications. While size-dependent trends in reactivity are qualitatively similar between gas-phase and surface-supported Al_n^- NCs, direct comparison remains difficult due to differences in experimental observables.

In this study, a unified framework for evaluating surface reactivity is presented by determining the activation energy for the oxidation of Al_{13}^- on an organic substrate, hexa-*tert*-butyl-hexa-*peri*-hexabenzocoronene (HB-HBC). Mass-selected Al_{13}^- SAs were soft-landed onto HB-HBC films prepared on HOPG substrates (Fig. 1b). The activation barrier was evaluated by temperature-dependence of reaction rate constants over the range of 250–450 K using Arrhenius analysis, providing a quantitative bridge between gas-phase and surface chemistry of SAs.

Experimental

Anionic Al_{13}^- SAs were generated using a magnetron sputtering source (Ayabo Corp., nanojima-NAP-01),[1,2] in which an Al target was sputtered with Ar^+ ions in a liquid N_2-cooled

aggregation cell. The resulting NC ions were transferred to a chamber equipped with a quadrupole ion bender and mass filter, enabling selection of ions with the desired mass and polarity. The mass-selected NCs were deposited onto conductive substrates, where the NCs were thermalized through collisions with cooled He gas, preventing fragmentation and implantation upon deposition.

Prior to soft-landing, HB-HBC films (~5 ML) were prepared on cleaned highly oriented pyrolytic graphite (HOPG). For a 6 mm diameter deposition area and a NC size of 0.8 nm, ~3.0×10^{13} NCs correspond to a coverage of ~0.6 ML. X-ray photoelectron spectroscopy (XPS) was used to evaluate NC coverage and electronic state using an Mg Kα source (hν = 1253.6 eV) and a hemispherical analyzer at a 45° emission angle. Spectra were processed with Shirley background subtraction and peak fitting including instrumental broadening. Oxidative reactivity was investigated by exposing Al_{13}/HB-HBC to O_2 at various substrate temperatures (250–450 K). The exposure was quantified in Langmuir units (1 L = 1.33×10^{-4} Pa·s). After each exposure step, XPS spectra were recorded to monitor changes in spectral features and evaluate oxidation behavior.

Results and Discussion

XPS measurements reveal that Al_{13} forms a charge-transfer complex with HB-HBC, evidenced by a shift of the C 1s peak to higher binding energy, indicating partial electron transfer (Al_{13}^-–HB-HBC$^+$). With O_2 exposure (Fig. 2), the Al 2p peak shifts to higher binding energy, confirming oxidation. However, the oxidation proceeds much more slowly than for bulk Al, demonstrating the preserved stability of the superatomic state.

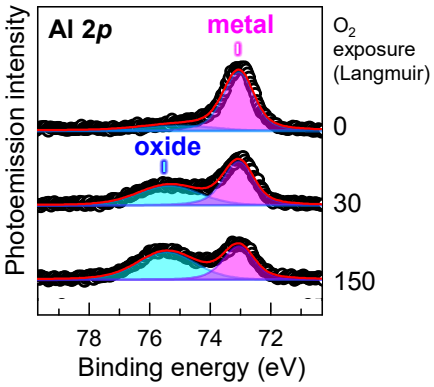

Fig. 2 XPS spectra of Al 2p core levels for the 0.6-ML Al_{13} SAs deposited on the HB-HBC substrate before O_2 exposure (top) and after 30 and 150 Langmuir O_2 exposures.

The oxidation kinetics were quantified by monitoring the decay of non-oxidized Al 2p components as a function of O_2 exposure. Importantly, the size dependence of oxidative rates on the size of Al_n NCs (n = 7 – 24) deposited on a HB-HBC substrate exhibits a local minimum at n = 13,[1,2] reflecting the superatomic nature of Al_{13}^-. From temperature-dependent measurements (250–450 K), furthermore, activation energy for the oxidation of Al_{13} SAs was extracted using Arrhenius plot. Notably, the activation barrier on the surface is several times lower than that in the gas phase (17 kJ mol^{-1}),[5] highlighting the influence of the interfacial environment.

By using activation energy as a common metric, we directly compare reactivity in gas-phase and surface-supported systems. The results show that the intrinsic stability of Al_{13}^- is largely preserved upon deposition, while interfacial effects modulate its reactivity. This work provides a quantitative bridge between gas-phase and surface chemistry of SAs and establishes activation energy as a universal descriptor for their stability in functional environments.

References [1] M. Shibuta, *et al.*, *Nat. Commun.* 13, 1336 (2022). [2] T. Inoue, *et al.*, *J. Am. Chem. Soc.* 145, 23088 (2023). [3] M. Akutsu, *et al.*, *Phys. Chem. Chem. Phys.* 19, 20401 (2017). [4] M. Akutsu, *et al.*, *J. Phys. Chem. A.* 128, 6648 (2024). [5] B.C.Sweeny, *et al.*, *J. Phys. Chem. Lett.* 11, 217 (2020).

3A4 Effects of nanosecond pulsed electric field on brain and pancreatic cells and fluorescence microscopy with particular attention to the difference between cancerous and normal cells

(NYCU, Taiwan) N. Ohta, K. Awasthi, D.-J. Bai, C.-Y. Wei, H.-Y. Hsu

Electric field effects on dynamics and function of biological systems may depend on the cell membrane capacitance and on the pulse duration of the applied field, which enables selective applications of pulsed electric field in specific organelles and specific live cells.

As we have reported [1-6], application of nanosecond pulsed electric field having a pulse-width of 50 ns and a strength of 20 kV/cm (nsPEF) induces apoptosis efficiently in lung and breast cancerous cells, whereas such field effect was less or not induced in normal cells, indicating that cancerous and normal cells show different field effects from each other. Such difference in electric field effect between cancerous and normal cells is very important from the clinical point of view because the damage of the healthy cells limits the effectiveness of the cancer treatment. However, it is not clear whether the effect of nsPEF on human cancerous cells differ from that on normal cells in any types of cells. In the present study, therefore, we have examined the effects of nsPEF on human brain and pancreatic cells, with particular attention to the difference between cancerous and normal cells. In the experiments, comb-type microelectrodes fabricated by electron lithography and covered by gold were used [7-9]. Fluorescence imaging of exogenous fluorophores and bright field imaging were done.

The representative bright field images of brain cancerous cells (DBTRG-0.5MG) and pancreatic cancerous cells (Panc-1) observed before and after application of nsPEF with a frequency of 1 kHz are shown in Fig. 1(upper), which shows a significant field-induced changes in morphology of cancerous cells, as evidenced by membrane blebbing. In contrast, the change in morphology was not detected in brain normal cells (HA) and pancreatic normal cells (HPaSteC) (see Fig.1(lower)).

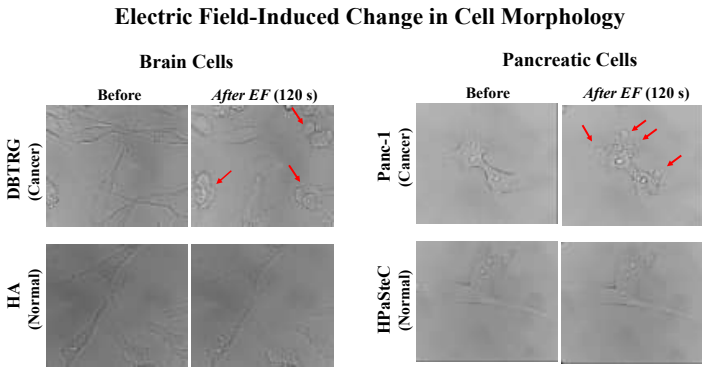

Fig. 1. Morphology observed before and after application of nsPEF for 120 s in cancerous cells (upper) and normal cells (lower) in brain cells (left) and pancreatic cells (right). Red arrows show blebbing induced by application of nsPEF.

The breakdown of the membrane integrity in cancerous cells was confirmed with a live/dead viability assay (Fig. 2). Calcein-AM is a cell-permeant dye that emits green fluorescence upon hydrolysis by intracellular esterase in live cells, as can be seen in all cells before applying nsPEF, indicating cell viability. In contrast, ethidium homodimer-1 (EthD-1), which emits red fluorescence, cannot penetrate intact cell membranes in live cells and only enter in dead cells with compromised membrane integrity. As shown for DBTRG-

0.5MG and Panc-1 in Fig. 2, the intensity of green fluorescence emitted from Calcein-AM decreased after applying nsPEF; at the same time, the red fluorescence from EthD-1, which was absent before nsPEF application, increased, whereas red fluorescence was not observed in normal cells, HA and HPaSteC, after the application of nsPEF. The field-induced cell death in cancerous cells was also confirmed by the propidium iodide (PI) fluorescence imaging (Fig. 3). By application of nsPEF, brain and pancreatic cancerous cells exhibited red fluorescence of PI, indicating a cell death. Conversely, normal cells showed no red fluorescence even after the nsPEF treatment, reaffirming their high resilience to the application of nsPEF.

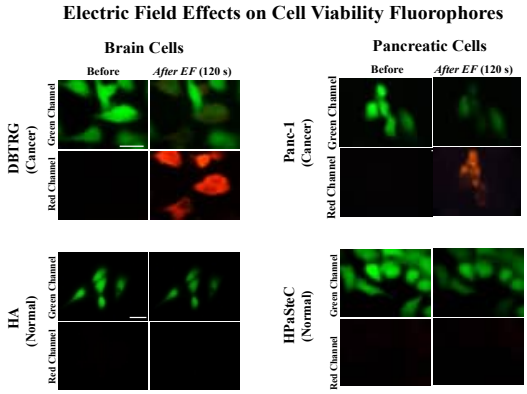

Fig. 2. Live/Death viability in brain (left) and pancreatic (right) cancerous and normal cells, observed before and after application of nsPEF for 120 s. The green fluorescence images represent Calcein-AM staining, while the red fluorescence images represent EthD-1 staining.

Cell morphology, live/dead viability assay, and PI imaging revealed an efficient field-induced cell death in both cancerous cells, whereas the normal cells are very insensitive to application of nsPEF. Thus, the effect of nsPEF on cell viability is very different between cancerous and normal cells in lung, breast, brain and pancreatic cells.

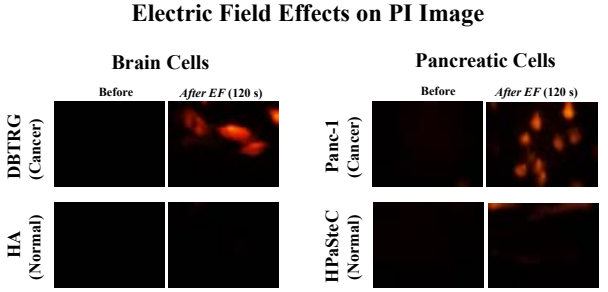

Fig. 3. PI imaging in brain (left) and pancreatic (right) cancerous (upper) and normal cells (lower) observed before and after application of nsPEF for 120 s.

Based on these results, we strongly believe that electric field effects play an important role in "cell-competition" to eliminate transformed cancerous cells from surrounding normal cells and in "photodynamic action" to kill cancerous cells, which is a root of photodynamic therapy and photoimmuno-therapy, though the attention was not paid [10-13].

【References】

[1] K. Awasthi, F.-L. Chang, H.-Y. Hsu, N. Ohta, *Sens. Actuators B: Chem.* **347**, 130635 (2021).
[2] K. Awasthi, F.-L. Chang, T.-E. Wu, H.-Y. Hsu, N. Ohta, *Sens. Actuators B: Chem.* **369**, 132848 (2022).
[3] K. Awasthi, T.-E. Wu, H.-Y. Hsu, N. Ohta, *J. Phys. Chem. B.* **127**, 5566 (2023).
[4] K. Awasthi, S.-P. Li, C.-Y. Zhu, H.-Y. Hsu, N. Ohta, *Sens. Actuators B: Chem.* **378**, 133199 (2023).
[5] K. Awasthi, W.-C. Huang, C.-Y. Wei, H.-Y. Hsu, N. Ohta, *Biosens. Bioelectron.* **272**, 117129 (2025).
[6] K. Awasthi, W.-C. Huang, H.-Y. Hsu, N. Ohta, *Scientific Reports* **16**, 2268 (2026)
[7] K. Awasthi, T. Nakabayashi, N. Ohta, *J. Phys. Chem. B* 116, 11159 (2012).
[8] K. Awasthi, T. Nakabayashi, N. Ohta, *ACS Omega* 1, 396 (2016).
[9] K. Awasthi, T. Nakabayashi, L. Li, N. Ohta, *ACS Omega* 2, 2916 (2017).
[10] S. Kon, K. Ishibashi, H. Katoh, M. Fujita, et al., *Nat. Cell Biol.* **19**, 530 (2017)
[11] C. S. Foote, *Science* **162**, 963 (1968).
[12] T. Takemura, N. Ohta, S. Nakajima, I. Sakata, *Photochem. Photobiol.* **50**, 339 (1989)
[13] M. Mitsunaga, M. Ogawa, H. Kobayashi, et al,. *Nature Medicine* **17**, 1685 (2011).

3A5 Two-dimensional electronic spectroscopy of light-harvesting phycobiliproteins synthesized by recombinant DNA techniques

(QST) Masaaki Tsubouchi1, Takatoshi Fujita, Motoyasu Adachi, Ryuji Itakura

Phycobilisomes, the light-harvesting antennae of cyanobacteria and red algae, achieve remarkably efficient unidirectional energy transfer through arrays of phycobiliproteins whose pigment–protein interactions remain only partially understood despite advances in cryo-electron microscopy (cryo-EM) and ultrafast spectroscopy. In particular, the roles of pigment number, spatial arrangement, and local protein environments in shaping the excited-state potential energy surfaces and ultrafast photoexcitation dynamics have yet to be fully clarified. In this study, we investigate these factors using artificially synthesized phycobiliproteins—allophycocyanin (APC) and C-phycocyanin (CPC)—produced through an *E. coli* expression system designed to replicate the pigment composition and trimeric assembly of the native proteins of *Thermosynechococcus elongatus BP-1*.

As shown in Figs. 1(a) and (b), APC and CPC share homologous αβ heterodimer structures with a pair of the pigments, α84 and β84 phycocyanobilins (PCBs), yet differ in that CPC contains a third pigment, β153 PCB, whose excited-state energy lies above the excitonic pair formed by the α84 and β84 PCBs. Although β153 PCB is electronically decoupled from the exciton pair, previous ultrafast measurements revealed unexpectedly large differences in relaxation pathways and coherence behavior between APC and CPC. To probe this systematically, we synthesized a mutant CPC lacking β153 PCB via Cys153→Tyr substitution, thereby producing a trimer with pigment number and arrangement nearly identical to APC (Fig. 1(c)). If pigment spatial arrangement were the dominant factor of photoexcitation dynamics, the β153-deficient CPC would be expected to exhibit APC-like spectral and temporal behavior.

The absorption and fluorescence spectra are shown in Fig. 1(d). While the absorption spectrum of APC exhibits a pronounced peak at 650 nm with a shoulder at 615 nm corresponding to its lower and higher excitonic states, that of wild-type CPC shows a single peak at 620 nm without a significant shoulder. Remarkably, the mutant CPC spectrum resembles that of wild-type CPC rather than APC, despite their similar pigment number and geometries. Fluorescence spectra likewise show that the mutant CPC maintains CPC-like Stokes shifts and emission profiles, supporting the conclusion that pigment spatial arrangement does not primarily factor the excited-state energy structure. Removal of β153 PCB simply eliminates its absorption contribution without altering properties of the exciton pair.

To examine relaxation kinetics and coherent vibrational motion, we performed time-resolved two-dimensional electronic spectroscopy (2D-ES). The 2D-ES setup has been reported in our previous papers [1,2]. Figure 2 shows the transient absorption spectra obtained at the specific excitation energies. Wild-type APC shows rapid vibrational relaxation to the bottom of the potential energy surface within 1 ps. Coherent analysis reveals a well-defined vibrational wave packet with a dominant beat frequency at 202 cm^{-1}, and decoherence times of 140~370 fs. The wild-type CPC displays markedly different behavior. The wild-type CPC exhibits broad positive signals even at T = 1 ps, demonstrating that excited vibronic states persist far longer than in APC. Coherent beating signal is weak and short lived. The β153-deficient CPC behaves nearly identically to wild-type CPC in both its

relaxation kinetics and its absence of long-lived coherence. These similarities, contrasted against those clear differences from APC, strongly indicate that pigment spatial arrangement and pigment number are not the primary factors of ultrafast relaxation or coherence.

Structural analysis provides a compelling explanation: although the β84 PCBs in APC and CPC share similar geometries, the α84 PCB is planar in APC but bent in CPC. The bending of PCB in CPC reduces π-conjugation, alters electronic coupling and vibronic structure, and reshapes the excited-state potential energy surface, leading to the different relaxation and coherence properties of CPC relative to APC. These results demonstrate that local pigment–protein interactions and subtle structural distortions, rather than pigment arrangement alone, govern the ultrafast photoinduced dynamics of phycobiliproteins.

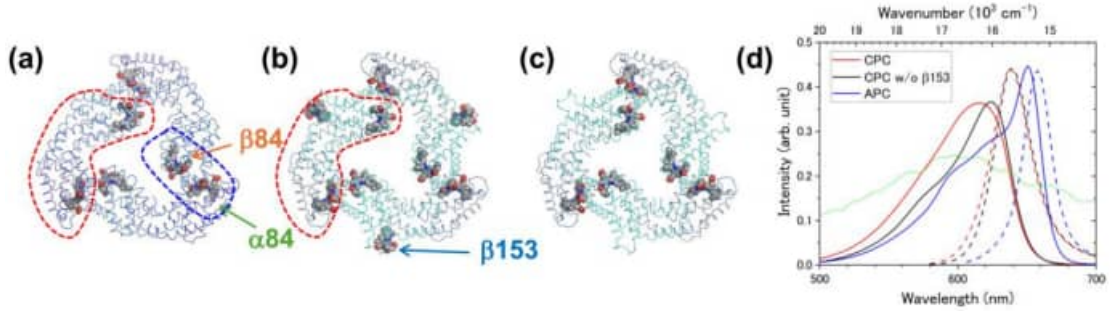

Fig. 1. Trimers structures of (a) wild-type APC, (b) wild-type CPC, and (c) β153-deficient CPC. PCB pigments are shown using a van der Waals representation. The red dashed lines indicate a monomer boundary. The blue dashed line surrounds a pair of pigments that form excitonic states. (d) Absorption and fluorescence spectra. The solid lines show the absorption spectra of APC (blue), CPC (red), and the β153-deficient CPC (black). The fluorescence spectra shown as dashed lines were measured by the excitation light with the wavelength of 600 nm for APC and 570 nm for the wild-type and the mutant CPCs. The thin green line represents the laser spectrum.

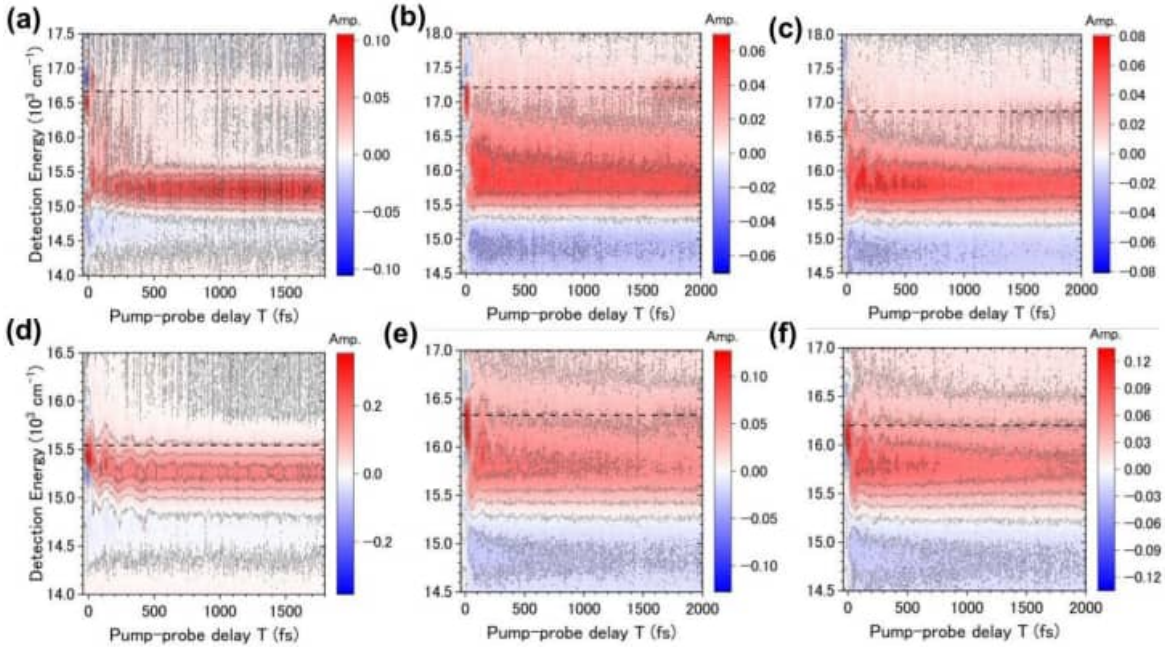

Fig. 2. Transient absorption spectra obtained at the specific excitation energies. Panels (a, d), (b, e), and (c, f) are the spectra for wild-type APC, wild-type CPC, and the mutant CPC, respectively. Panels (a-c) and (d-f) show the case of the excitation to higher and lower excitonic states, respectively.

[1] M. Tsubouchi, N. Ishii, T. Fujita, M. Adachi, and R. Itakura, J. Chem. Phys. 162, 145102 (2025).
[2] M. Tsubouchi, *et al*., Opt. Express 31, 6890-6906 (2023).

3A6 Reaction of Fluoride Ions at the Electrode/Electrolyte Interface for High Energy Density Batteries

(1. Institute for Molecular Science, 2. Spin-L, 3. Khon Kaen Univ., 4. Chimie-ParisTech ENSCP, 5. National Institutes of Natural Science, 6. NAIST)

Taketoshi Minato[1, 2], Nicha Tabtimtong[1, 3], Pattanapon Kaisook[1, 3], Johan Tenaillon[1, 4], Pakpoom Athikaphan[1, 5], Yumiko Imai[1], Tadashi Ueda[1], Kei-ichi Nakamoto[1, 6], Arthit Neramittagapong[3], Sutasinee Neramittagapong[3]

Energy is central to modern society, and the demand for more efficient energy utilization and storage continues to grow. We have investigated energy-conversion reactions at interfaces by using scanning probe microscopy, which enables nanoscale analysis of surface morphology and local interfacial processes[1–4]. While lithium-ion batteries are currently the dominant charge-storage devices[1], their practical energy densities are approaching limits for some applications. Fluoride shuttle batteries (Fig. 1, FSBs) have therefore attracted increasing attention as next-generation systems, owing to their exceptionally high theoretical energy densities derived from multi-electron redox reactions of metal fluorides[5-8]. However, realizing this potential requires precise control of reactions at electrode/electrolyte interfaces, where fluoride-ion transport and electron-transfer processes are strongly coupled.

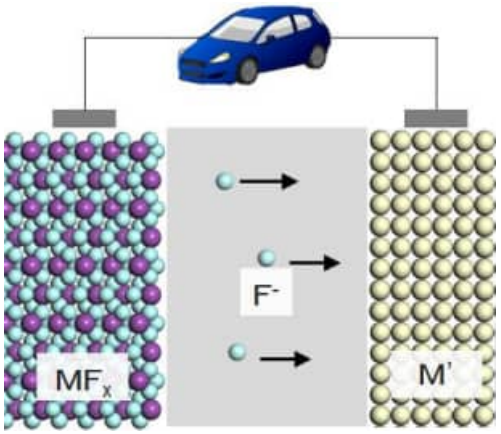

Fig. 1 The principle of fluoride shuttle battery systems.

In this study, we investigate key challenges limiting the development of FSBs, focusing on intrinsic issues related to electrode–electrolyte interfaces. A major bottleneck in FSB operation is the difficulty of the fluorination process, which often induces parasitic interfacial reactions, incomplete conversion, and degradation of battery performance[5-8]. To address this problem, we examine the effects of electrolyte on promoting efficient fluorination reactions[6–9]. Particular attention is paid to how electrolyte modify the chemical state and reactivity of fluoride ions and the local reaction environment near the interface. In addition, we analyze the reaction mechanisms occurring at the electrode–electrolyte interfaces using electrochemical scanning probe microscopy (Fig. 2). The results clarify how fluorination proceeds, how surface species evolve, and why selected electrolyte conditions facilitate the

desired conversion reaction more effectively. These findings provide detailed insights into interfacial reaction dynamics during fluoride-ion transfer and energy conversion processes. They also offer guidelines for the rational design of electrolytes and interfaces, contributing to the advancement of high-energy-density battery systems and next-generation energy technologies.

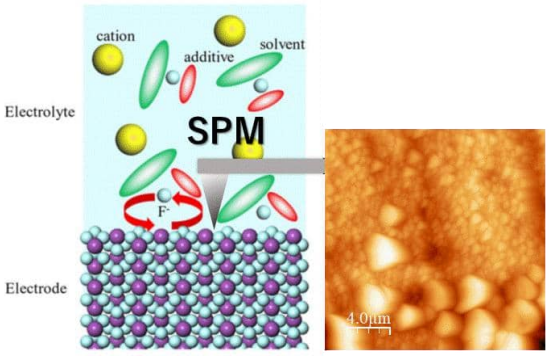

Fig. 2. A schematic illustration of the analysis of the electrolyte/electrode interface using scanning probe microscopy, along with an example image of a metal surface after fluorination.

References

[1] Taketoshi Minato and Takeshi Abe, *Prog. Surf. Sci.* **92**, 240–280 (2017).
[2] Hiroki Aizawa *et al*., *Nature Comm*. **14**, 4530 (2023).
[3] Jun Nishida *et al*., *Nano Lett.* **24**, 836–843 (2024).
[4] Jun Nishida *et al*., *Science Adv.* **11**, eadv9584 (2025).
[5] M. Anji Reddy and M. Fichtner, *J. Mater. Chem. 21*, 17059–17062, (2011).
[6] Hiroaki Konishi, Taketoshi Minato, Takeshi Abe, Zempachi Ogumi, *J. Appl. Electrochem. 48*, 1205–1211 (2018).
[7] Hiroaki Konishi *et al*., *J. Phys. Chem. C 123*, 10246–10252 (2019).
[8] Keiji Shimoda *et al.*, *J. Electroanal. Chem.* **895**, 115508 (2021).
[9] Nicha Tabtimtong *et al.*, *ACS Appl. Energy Mater.* **9**, 3690−3696 (2026).

Acknowledgements

The thank Shinako Iki and Kaho Hirano (Institute for Molecular Science) for experimental support. This research was supported by the grant of OML Project by the National Institutes of Natural Sciences (NINS program No, OML032301). A part of this work was conducted at the Institute for Molecular Science, supported by the Advanced Research Infrastructure for Materials and Nanotechnology in Japan (JPMXP1224MS0014, JPMXP1224MS1061, JPMXP1224MS1064, JPMXP1225MS1021, JPMXP1225MS0005, JPMXP1225MS3005) of the Ministry of Education, Culture, Sports, Science and Technology (MEXT), Japan.

Poster Presentations

1P01 Floquet-theory-based nonadiabatic ab initio molecular dynamics for analyzing chemical reactions in strong laser fields

(Hokkaido Univ.) Ryuto Kambara, Takuro Tsutsumi, and Tetsuya Taketsugu

[Introduction] When a molecule is exposed to an intense laser field comparable in strength to the Coulomb field acting on bound electrons, its potential energy surfaces (PESs) can be significantly modified, leading to chemical reactivity markedly different from that under field-free conditions. Surface-hopping *ab initio* molecular dynamics (SH-AIMD) has served as a powerful tool for analyzing excited-state reaction dynamics, but explicit treatment of strong light–molecule interactions remains challenging. Floquet theory, which provides eigenstates for time-periodic Hamiltonians, describing photon absorption and emission processes as well as laser-induced modifications of PESs. In this study, we combine Floquet theory with static PES analysis and SH-AIMD-based dynamics simulations to investigate electron–nuclear dynamics in molecules driven by string laser fields.

[Method] For a system under a time-periodic external field, the Floquet Hamiltonian H^F is constructed from the electronic Hamiltonian H^{elec}, the time-derivative operator, and the light–molecule interaction term:

$$H^{\mathrm{F}} = H^{\mathrm{elec}} - i\hbar\frac{\partial}{\partial t} - \hat{\boldsymbol{\mu}} \cdot \mathbf{F} \cos \omega t$$

Here, $\hat{\boldsymbol{\mu}}$ is the molecular dipole operator, $\mathbf{F}$ is the amplitude of the laser electric field, and ω is the frequency of the external field. By solving the Floquet eigenvalue problem at each molecular geometry, we obtain Floquet potential energy surfaces (Floquet-PESs) and the corresponding Floquet wavefunctions (Floquet-WFs). These quantities provide a basis for describing coupled electron-nuclear dynamics under laser irradiation, including field-induced changes in PES topology and nonadiabatic transitions between Floquet states.

[Results and Discussion] **Figure 1** shows the Floquet-PESs of H_2^+. The character of the Floquet state indicated by the thick black line changes from a field-dressed bound-state character to a dissociative one across a pseudo-crossing at a bond distance of approximately 2.3 Å. If the nuclear wavepacket passes this pseudo-crossing adiabatically, dissociation is promoted. This behavior corresponds to the well-known bond softening mechanism in H_2^+ [2]. We also analyzed how the Floquet-PESs and Floquet nonadiabatic couplings depend on laser intensity and photon number. In the presentation, we will discuss strong laser field–induced chemical reaction dynamics, including photon absorption and emission processes, on the basis of SH-AIMD trajectories propagated on the Floquet-PESs.

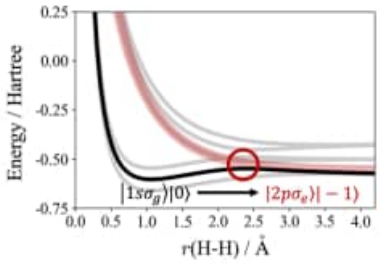

Fig. 1. Floquet-PESs of H_2^+.

[References]

[1] T. Fiedlschuster *et al.*, *PRA*, **93**, 053409 (2016); Z. Zhou *et al.*, *JCTC*, **16**, 821 (2020).

[2] P. H. Bucksbaum *et al.*, *PRL*., **64**, 1883 (1990).

1P02 Femtosecond laser filament reaction in gaseous hexane studied by time-of-flight mass spectrometry with velocity screening

(Nagoya Univ.) Akitaka Matsuda, Yuya Okumura, Kasumi Hashigaya, Akiyoshi Hishikawa

Ion mass spectrometry offers a powerful method to identify molecular species in a sample. On the other hand, since dissociation often takes place upon ionization, the obtained mass spectrum does not reflect directly the distribution of the constituent molecular species. In order to suppress extensive fragmentation upon ionization, soft ionization techniques such as ESI and MALDI have been developed and applied to liquid and solid samples. In this study, velocity screening time-of-flight mass spectrometry is introduced, in which the difference in the initial velocity distribution between the parent and fragment ions formed upon ionization is utilized for discrimination. The method is applied to identify laser-filament reaction products of gaseous hexane (C_6H_{14}) [1].

The output from a Ti:sapphire laser amplifier system (800 nm, 50 fs) was split into two by a beam splitter. The main pulse was focused by a plano-convex lens (f = 200 mm) into the reaction gas cell to generate a laser filament. The remaining pulse was focused into the Wiley-McLaren type time-of-flight mass spectrometer using a plano-convex lens (f = 200 mm) which serves as the ionization probe for the mass analysis of the filament products. Hexane was continuously supplied to the reaction gas cell using Ar as a carrier gas. Product molecules generated by the interaction with the laser filament were directly sampled into the mass spectrometer via a differential pumping stage.

Typical mass spectra obtained without the laser filament is shown in Fig. 1(a). Apart from the parent ion ($C_6H_{14}^+$) observed at m/z 86, the spectrum shows many prominent peaks in the lower m/z region, which are assigned to fragment ions generated by the dissociative ionization of the parent molecule by the ionization pulse. Fig. 1(b) shows the full width half maximum (FWHM) w_v of the velocity distributions obtained for each peak observed in Fig. 1(a). Significant difference is seen even in the width of the parent ion (w_v^0) and the largest fragment ion, $C_5H_{11}^+$ (w_v^c). This is due to translational energy released as a result of molecular dissociation, which shows that the velocity width can be used to discriminate the nascent filament products from the probe products. Fig. 1(c) shows the difference spectrum between that with and without the laser filament. Emergence of new peaks in mass range m/z 10 - 150 is clearly observed. The relative yields of the species observed in the difference spectrum obtained after ionization efficiency correction is shown in Fig. 1(d). Velocity screening reveals that hydrogen-capped polyynes C_nH_2 (n = 4, 6, 8) are the major products, with smaller contribution from other hydrocarbon molecules.

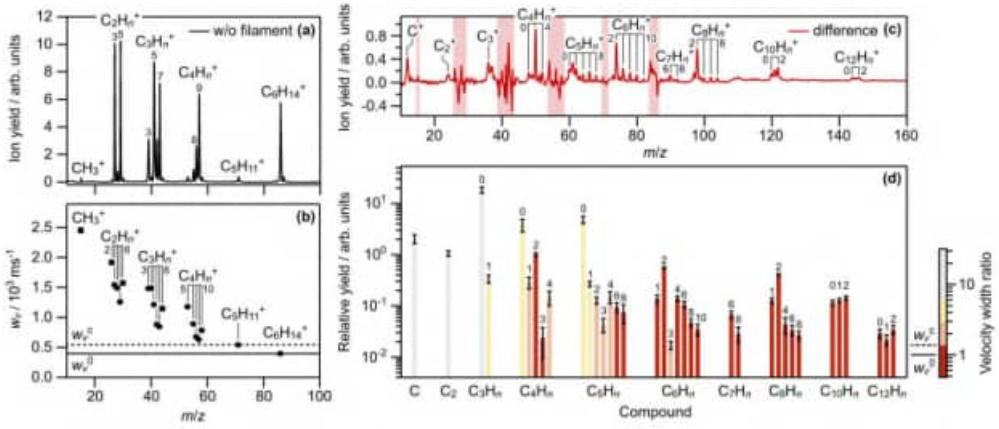

Fig. 1 (a) Representative time-of-flight mass spectrum of C_6H_{14} obtained without the laser filament. The field intensity of the ionization laser is estimated to be 8.2×10^{13} W/cm^2. (b) FWHM of the velocity distribution w_v for the peaks observed in (a). Reference width w_v^0 (solid) and w_v^c (dashed) are indicated. (c) Difference spectrum obtained by subtracting the spectrum without the laser filament from that with the laser filament (480 μJ/pulse, 500 Hz). The hatched areas indicate the spectral region where the fragment ions generated in the dissociative ionization of the parent C_6H_{14} molecule are observed. (d) Relative yields of the products obtained after tunnel ionization efficiency correction. The colors indicate the velocity width ratio $r_v = w_v/w_v^0$ of each peak.

[1] A. Matsuda *et al.*, *Phys. Chem. Chem. Phys.* **2026**, *28*, 2976.

1P03 Nonadiabatic internal conversion of S_2 and isomerization dynamics of silabenzene

([1]Graduate School of Science and Technology, Sophia University, [2]Faculty of Science and Technology, Sophia University) [1]Hazuki Sato, [1]Mizuki Kimura, [2]Shinkoh Nanbu

Silabenzene (SLB) is of interest in fundamental chemistry due to its unique electronic structure. In 1978, Schlegel *et al.* [1] suggested that SLB has a planar structure based on the geometry optimization at the Hartree-Fock/STO-3G level. Since the 1980s, the photochemistry of SLB has been the subject of extensive study. Specifically, in 1984, Maier *et al.* [2] reported the isomerization to Dewar-type under 320 nm irradiation in an Ar matrix. Meanwhile, in 2000, Wakita *et al.* [3] synthesized a stable SLB bearing a protecting group and reported the isomerization to benzvalene-type under 290-350 nm irradiation in C_6D_6 solution. Based on these findings, Su [4] theoretically investigated the photoisomerization mechanism of SLB in 2014 and proposed five reaction pathways, leading to two Dewar-type and three benzvalene-type products. However, to date, the complete photoisomerization pathway of SLB has not been investigated dynamically. Therefore, the aim of this study is to elucidate the complete photoisomerization of SLB in the gas phase using nonadiabatic molecular dynamics simulations.

Nonadiabatic *ab initio* MD simulations were performed using MOLPRO 2024.3 and 2024.1 [5]. The XMS-Complete Active Space (CAS) second-order perturbation (PT2) method with the ANO-RCC-VDZP basis set was employed. Geometry optimization and frequency analysis were performed on SLB in the S_0 electronic ground state. Based on the stable optimized structure, 247 initial structures were generated using the Wigner distribution method. The simulations were initiated by vertically exciting of the sampled structures to the S_2 electronic excited state based on the Franck-Condon principle. The potential energy and its gradient were calculated on-the-fly at the XMS-CASPT2 level, with a time step of 0.25 fs. The nuclear motions evolved over time using the velocity Verlet integration, while the nonadiabatic transitions were treated with the trajectory surface hopping (TSH) approach of Zhu-Nakamura formula.

Table 1 summarizes the vertical excitation energies and the squared values of the transition dipole moment (TDM) from the S_0 state. At the XMS-CASPT2 level, the S_1 and S_2 states were found to be lying at 4.6487 eV and 5.3074 eV, respectively. Furthermore, TDMs indicate that the $S_2 \leftarrow S_0$ transition is the most probable. Nonadiabatic *ab initio* MD simulations were performed to investigate the photoisomerization dynamics of SLB via the S_2 state. The main reaction pathways were identified as Dewar-type isomerization and a silabenzene retention.

Table 1. Vertical excitation energy and the squared values of TDM

	Vertical Excitation Energy / eV			TDM^2 / a_o^2	
Electronic state	XMS-CASPT2/ ANO-RCC-VDZP	SAC-CI/ aug-cc-pVDZ	Exp.	XMS-CASPT2/ ANO-RCC-VDZP	SAC-CI/ aug-cc-pVDZ
S_1	4.6487	4.2245	3.88(320 nm)	0.7340	0.8151
S_2	5.3074	4.8013	4.56(272 nm)	1.5622	2.0928
S_3		5.2093			0.2066

References

[1] H. B. Schlegel, B. Coleman and M. Jones, Jr., *J. Am. Chem. Soc.***100**, 6499-6501 (1978)
[2] G. Maier, G. Mihm *et al.*, *Chem. Ber* .**117**, 2337-2350 (1984)
[3] K. Wakita, N. Tokitoh *et al.*, *J. Am. Chem. Soc.* **122**, 5648-5649 (2000)
[4] M.D. Su, *Organometallics* **33**, 5231-5237 (2014)
[5] H.-J. Werner *et al.*, MOLPRO2024.3/2024.1, a package of *ab initio* programs, URL, https://www.molpro.net.

1P04 Photofragment imaging of oriented methyl/ethyl bromide (CH_3Br, C_2H_5Br) for the assessment of their transition dipole moments

([1]Hokkaido Univ., [2]Institute of Science Tokyo., [3]Univ. of Osaka)
KAWAMATA, Hiroshi[1]; NAKAMURA, Masaaki[2]; CHE, Dock-Chil[3]

Photofragment imaging of oriented methyl/ethyl bromide (CH_3Br, C_2H_5Br) was performed at UV irradiation ~234 nm. Both bromides with large dipole moment 1.82/ 2.03 D were focused through our hexapole state-selector (12 kV/cm, 1 m length), oriented to the imaging TOF (time-of-flight) axis under the succeeding guiding fields (10 kV/cm). Intensity of methyl/ethyl bromide in the focused molecular beam increases seven/four times more than in the unfocused one, respectively. After UV photodissociation, the same light serving in [2+1] REMPI detection scheme, the spin-excited bromine atom fragment, Br [$^2P_{1/2}$] (as denoted Br*), was ionized at 234.021 nm (via 5p $^2S_{1/2}$ ← 4p $^2P_{1/2}$). The ion packet was slowly expanded through TOF acceleration region, extracted to TOF drift tube. Then its central segment (30 ns width) was observed with the slice imaging apparatus, which enables us to directly measure the speed and angular distributions of photofragment atoms. Fig. 1 exemplifies observed images of Br* fragment atom from isotropic (free-rotated/non-oriented) and oriented methyl bromide. The left image displays the nearly symmetrical arcs across the horizontal axis, in sharp contrast with asymmetrical intensity between upper and lower arcs on the right. Akin to methyl bromide, the kinetic energy release of Br* fragments from ethyl bromide reproduces the previous one [1]. The sliced image from oriented parents at the dissociation laser polarization angle 45° implies the vector correlation among the transition dipole moment **μ**, its fragment velocity **v**, and the diploe moment **d** of parent bromide nearly along C-Br bond axis [2], which reveals the direction of the transition dipole moment of both bromides to the first predissociation state. The detail of our examines will be shown in presentation.

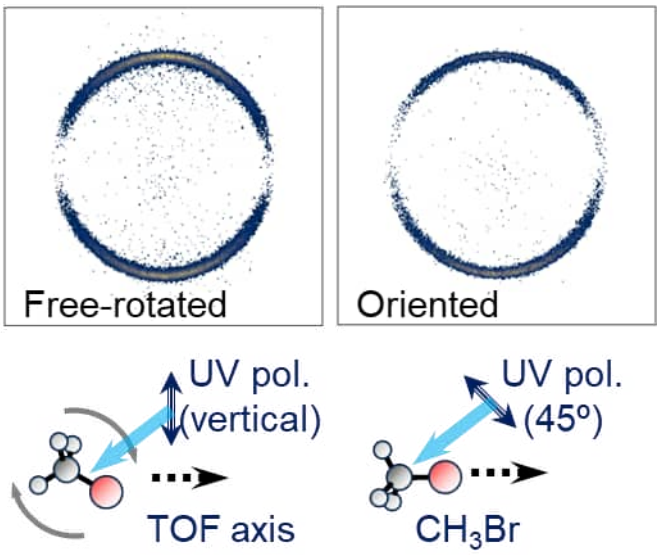

Fig. 1 Sliced images of spin- excited Br (Br*) fragment atom from free-rotated methyl bromide (left) and oriented one along TOF axis (right).

References

[1] J. Chem. Phys. **130**, 034304 (2009); https://doi.org/10.1063/1.3058730.
[2] Phys. Chem. Chem. Phys. **21**, 14164 (2019); https://doi.org/10.1039/c8cp04270e.

1P05 Suppression of twisted intermediate formation in uracil by C6 methylation

(Kyoto University) Aki, Yoshino; Ghosh, Srijon; Obara, Yuki; Suzuki, Toshinori

Pyrimidine nucleobases in aqueous environments undergo ultrafast internal conversion (IC) from the excited state (S_1) to the ground state (S_0). Recent computational and experimental studies have revealed that (1) IC induces *cis-trans* isomerization of the C5=C6 bond, generating a twisted intermediate (TI) in S_0;[1-3] (2) the TI mediates a hydration reaction with solvent water;[1-3] and (3) TI formation is suppressed by C5 methylation.[3] The suppression arises from steric hindrance between the bulky methyl group and the hydration shell, which inhibits pyramidalization around C5 and reduces momentum along the reaction coordinate at the point of non-adiabatic transition to S_0.[3]

Previously, we showed that C6 methylation does not significantly affect the IC dynamics of uracil.[4] This raises the question: does C6 methylation influence TI formation dynamics? In this study, we performed infrared transient absorption spectroscopy and photohydration measurements on 6-methyluracil (6-MU), 5,6-dimethyluracil (5,6-DMU), and 1,3-dimethyluracil (1,3-DMU), and found that 1,3-DMU does while 6-MU and 5,6-DMU do not form TI. Photohydration measurements revealed the photohydration quantum yield of 1.37×10^{-2} for 1,3-DMU, compared with 2.35×10^{-4} for 5,6-DMU and 2.85×10^{-4} for 6-MU, being consistent with TI formation yields.

These results indicate that the IC dynamics of 6-MU are very similar to those of uracil up to the non-adiabatic transition to S_0; however, the bifurcation into planar and twisted structures after non-adiabatic transition is strongly influenced by C6 methylation. Our findings provide new insights into substitution effects on the dynamics of nucleobases and their derivatives.

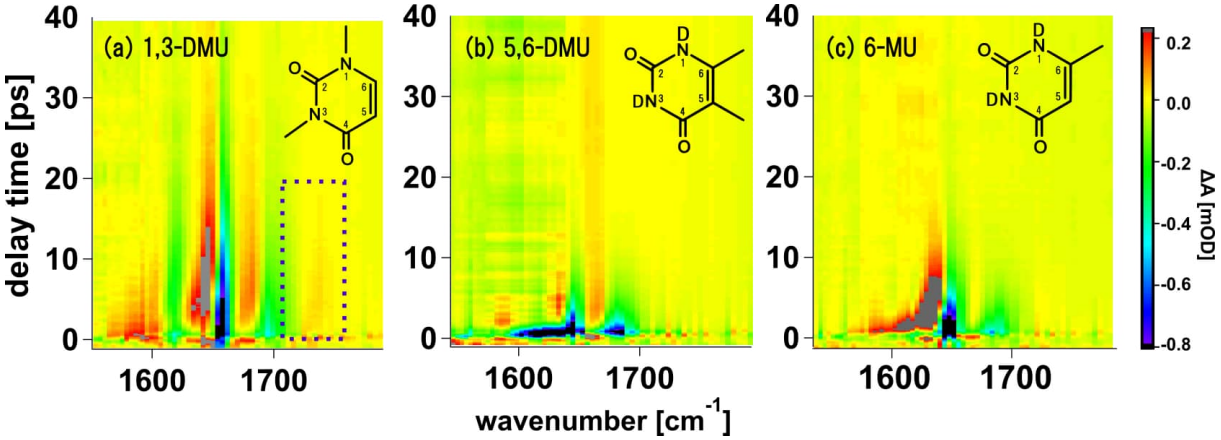

Figure 1 IR-TAS 2D color maps, where the vertical and horizontal axes represent the pump-probe delay time and wavenumber, respectively. 1,3-DMU shows a blue-shifted feature around 1720 cm^{-1}, whereas no corresponding feature is observed for 5,6-DMU or 6-MU.

Reference

[1] W. Park et al. *J. Phys. Chem. Lett.* **13**, 7072-7080 (2022).

[2] Y. Obara et al. *J. Am. Chem. Soc.* **147**, 15077-15087 (2025).

[3] S. Ghosh et al. *J. Am. Chem. Soc.*, in press, (2026).

[4] Orimo et al. *J. Phys. Chem. Lett.* **14**, 2758-2763(2023)

1P06 Theoretical study on C5 substituent effects on the excited-state relaxation dynamics of pyrimidine bases

([1]Hokkaido University) Yuto Kobayashi[1], Ryuto Kambara[1], Yusuke Minegishi[1], Satoi Wada[1] and Tetsuya Taketsugu[1]

[Introduction] Pyrimidine bases undergo ultrafast relaxation to the ground state after ultraviolet excitation. Upon excitation to the bright $^1\pi\pi^*$ state, these molecules undergo internal conversion involving the $^1n\pi^*$ state, accompanied by twisting of the C5=C6 bond. Such ultrafast excited-state relaxation has been considered an important factor related to the photostability of nucleic acid bases. Recently, extreme ultraviolet time-resolved photoelectron spectroscopy measurements for gas-phase uracil and thymine revealed that C5-substitution affects both the internal conversion quantum yield between the $^1\pi\pi^*$ and $^1n\pi^*$ states and the relaxation lifetime [1]. Uracil showed an internal conversion quantum yield of approximately 0.5 and a $^1\pi\pi^*$ lifetime of 17 fs, whereas thymine, the C5-methylated analogue, showed a strong preference for relaxation to the $^1n\pi^*$ state and a longer $^1\pi\pi^*$ lifetime of 39 fs. These differences suggest that the C5 substituent significantly alters the excited-state relaxation dynamics. In this study, we theoretically analyzed the C5 substituent effects responsible for this change.

[Methods] We first optimized the ground-state equilibrium structures of isolated uracil and thymine using DFT calculations (ωB97XD/cc-pVDZ). Starting from the Franck‐Condon structures, steepest-descent path calculations and geometry optimizations were then performed using TDDFT calculations to analyze how the C5 substituent changes the excited-state reaction pathways. In addition, we performed *ab initio* molecular dynamics (AIMD) simulations to investigate the relaxation dynamics after excitation to the $^1\pi\pi^*$ state. Nonadiabatic transition probabilities were evaluated using the Zhu-Nakamura global switching algorithm, and the MD simulations were performed with the in-house program package SPPR [2].

[Results and Discussion] The C5 substituent was found to change the shape of the potential energy surfaces and to induce clear differences in the reaction pathways after the $^1\pi\pi^*/^1n\pi^*$ intersection. In uracil, the molecule can reach the intersection with the ground state through barrierless twisting of the C5=C6 bond. In contrast, thymine has a stable structure on the $S_1(^1\pi\pi^*)$ state, denoted as $^1\pi\pi^*$-min, and an energy barrier exists before reaching the intersection with the ground state. Figure 1 shows the difference in the dynamical picture induced by the C5 substituent effects. The MD simulations also supported this difference. In the presentation, we will discuss differences in dynamics related to the experimentally observed differences in internal conversion quantum yields.

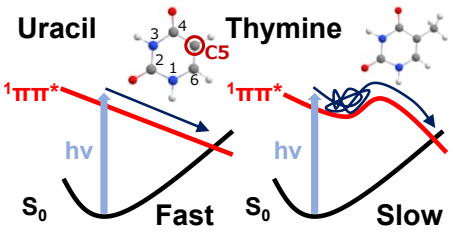

Fig. 1. Differences in the dynamical picture induced by C5 substitution.

[1] Y. Miura *et al.*, *J. Am. Chem. Soc.*, **145**, 3369 (2023).; N. Orimo *et al.*, *J. Phys. Chem. Lett.*, **14**, 2758 (2023).

[2] T. Tsutsumi *et al.*, *SPPR (a developmental version)*, Hokkaido University: Sapporo, Japan, (2022).

1P07 Observations of vibrational wavepackets of N_2 and N_2^+ generated in air plasma

([1]QST KPSI; [2]NTT BRL; [3]Nihon Univ.) ENDO, Tomoyuki[1]; MASHIKO, Hiroki[2]; SAKO, Tokuei[3]; OGURI, Katsuya[2]; ITAKURA, Ryuji[1]

Focusing intense laser pulses in air induces a variety of phenomena associated with molecular ionization and excitation, such as filamentation [1] and air lasing [2], enabling applications including remote sensing [3]. In this study, we investigate the vibrational motions of N_2 and N_2^+ simultaneously excited by sub-10 fs near-infrared (NIR) intense laser pulses in air, and discuss their excitation mechanisms through comparison with simulated vibrational wavepackets.

The output of a Ti:Sapphire laser system (800 nm, 1 kHz, 2mJ/pulse, 45 fs) is compressed by a pressure-gradient hollow core fiber (φ = 300 μm) flowing with Ar gas and chirped mirrors. The resulting sub-10 fs NIR laser pulse is split into two arms. One is used as pump pulses to ionize and excite N_2 molecules in air, while the other is introduced into a β-barium borate (BBO) crystal (8.5 μm thickness) to generate broadband ultraviolet (UV) probe pulses (λ = 355-435 nm). The pump and probe pulses are co-linearly focused in air using a parabolic mirror (f = 100 mm).

Figure 1(a) shows the difference spectra of the UV pulses with and without the NIR pump pulse. The UV spectrum exhibits temporal oscillations with a spectral tilt reflecting the chirp of the UV pulse. Slower oscillations around $\Delta t = 0$ are attributed to temporal modulation of the UV pulse induced by air plasma, whose transmissivity rapidly decreases. Faster oscillations at longer time delays are attributed to molecular vibrations. The Fourier-transformed spectra of Fig. 1 (a) are shown in Fig. 1 (b). Two peaks appear at 69.5 THz and 65 THz, corresponding to the vibrations of N_2 and N_2^+. The N_2^+ signal shows wavelength dependence reflecting the B-X transition. The excitation processes of the vibrational motions of N_2 and N_2^+ are further discussed through comparison with simulated vibrational wavepackets.

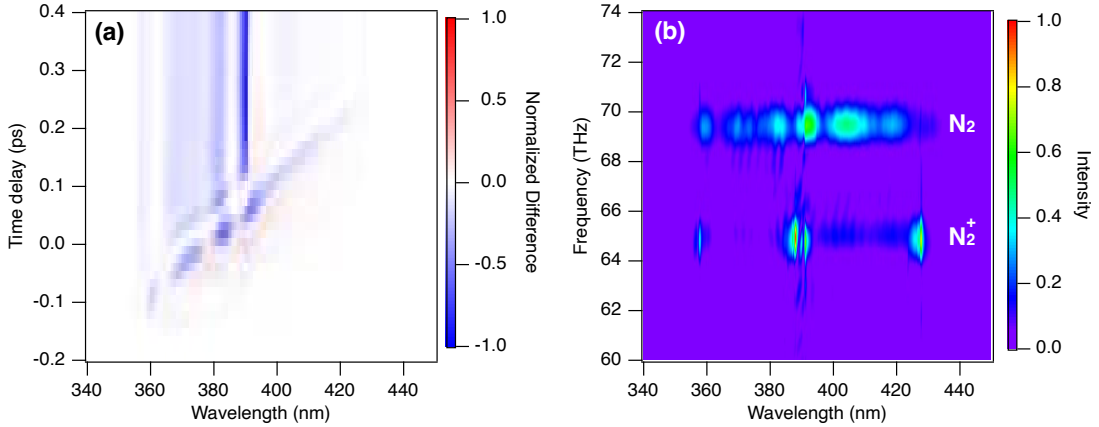

Fig. 1 (a) Difference spectra of the UV pulse with and without the NIR pump pulse as a function of time delay. (b) Fourier-transformed spectra of (a). Peaks at 69.5 THz and 65 THz correspond to vibration period of N_2 and N_2^+.

References

[1] S. Couairon and A. Mysyrowicz, Phys. Rep. **441**, 47 (2007).; M. Durand *et al*., Opt. Express **21**, 26836 (2013).
[2] A. Dogariu *et al*., Science **331**, 442 (2011).; T. Ando *et al*., Phys. Rev. Lett. **123**, 203201 (2019).
[3] J. Kasparian and J.-P. Wolf, Opt. Express **16**, 466 (2008).; X. Zhao *et al*., Opt. Lett. **45**, 3661 (2020).

1P08 Photoelectron circular dichroism of epichlorohydrin in near-infrared intense laser fields studied by electron-ion coincidence momentum imaging

([1]Grad. Sc. Sci, Nagoya U.; [2] RCMS, Nagoya U.)
Ogawa, Kazumi[1]; Kuroda, Runa[1]; Matsuda, Akitaka[1]; Hishikawa, Akiyoshi[1,2]

Photoionization of chiral molecules by circularly polarized light results in an asymmetry in the photoelectron angular distribution along the light propagation direction. This forward-backward asymmetry, known as photoelectron circular dichroism (PECD), was first demonstrated in single-photon and multiphoton ionization, and has since been observed in tunnel ionization in intense laser fields (10^{13}-10^{14} W/cm^2). The recent study on methyloxirane (MOX, C_3H_6O) suggested that tunnel PECD reflects the character of ionizing molecular orbital [2]. In this study, we measured the tunnel PECD of (*S*)-epichlorohydrin (ECH, C_3H_5OCl), in which a hydrogen atom in the methyl group of (*R*)-MOX is replaced by a chlorine atom, to clarify the role of the molecular orbital and geometrical structure in tunnel PECD (Fig. 1).

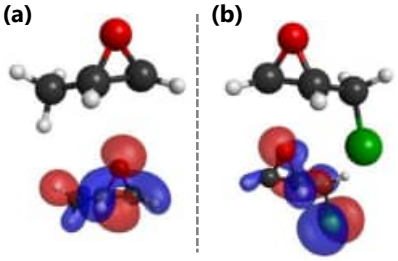

Figure 1. The structure and HOMO of (a) (*S*)-MOX and (b) (*S*)-ECH

The output of Yb:KGW laser system (1035 nm, 35 fs, 50 kHz) was converted into circularly polarized laser pulses. They were focused by a concave mirror onto the (*S*)-ECH gas beam in the cold target recoil frame ion momentum spectrometer (COLTRIMS) chamber. The fragment ions and photoelectrons were accelerated toward two separate position sensitive detectors by a static electric and magnetic field and detected in coincidence. The momenta $\boldsymbol{p} = (p_x, p_y, p_z)$ of each particle was calculated from the time of flight (t) and the detected positions (x, y).

The three-dimensional momentum distribution of photoelectrons emitted in a circularly polarized laser field exhibited a torus-like shape (Fig. 2). PECD is defined as $[Y_{LCP}(\boldsymbol{p})-Y_{RCP}(\boldsymbol{p})] / [Y_{LCP}(\boldsymbol{p})+Y_{RCP}(\boldsymbol{p})]$, where $Y_{LCP}(\boldsymbol{p})$ and $Y_{RCP}(\boldsymbol{p})$ represent the photoelectron momentum distributions obtained for left and right circularly polarized light, respectively, with $\boldsymbol{p}$ denoting the photoelectron momentum. The mass spectra were dominated by fragment ions with only a small contribution from the parent ion, which is attributed to significant photodissociation of the parent ion following the ionization. This implies that the fragment PECDs reflect that of the parent ion. For all fragment ions (CH_3^+, $C_2H_3^+$, CHO^+, CH_3O^+, $C_2H_2O^+$, CH_2Cl^+, $C_3H_5O^+$, $C_2H_3Cl^+$), PECD of photoelectrons recorded in coincidence exhibited a negative sign in the forward direction with respect to the laser propagation direction. Since both the (*S*)-ECH and (*S*)-MOX parent ions, which are produced by ionization from the HOMO [3,4], exhibited the same PECD sign, this suggests that tunnel PECD does not depend on the molecular geometry but rather reflects the molecular orbital character.

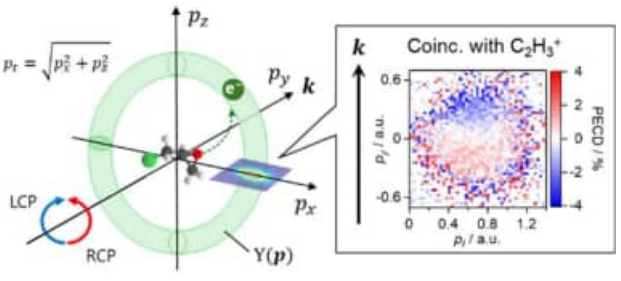

Figure 2. (Left) Schematic of torus-like momentum distributions of tunnel electrons in circular polarized intense laser fields. (Right) The PECD($\boldsymbol{p}$) image of $C_2H_3^+$ obtained at 4.8×10^{13} W/cm^2.

[1] M. H. M. Janssen *et al.*, Phys. Chem. Chem. Phys. **149**, 134301 (2018).
[2] R. Kuroda *et al.*, 40th Symposium on Chemical Kinetics and Dynamics, 2P07 (2025).
[3] S. Daly *et al.*, J. Chem. Phys. **134**, 064306 (2011).
[4] G. A. Garcia *et al.*, Phys. Chem. Chem. Phys. **16**, 16214 (2014).

1P09 Multimodal Energy Landscape Underlying Adhesive Interface Peeling

(Yamaguchi University) Koki Kubo and Yosuke Sumiya

1. Introduction

Adhesive bonding is widely used in various applications because it enables the integration of multiple materials and effective stress distribution, thereby enhancing mechanical durability and increasing design flexibility. However, the molecular origin of adhesion remains unclear due to the difficulty of directly observing interfaces. Adhesion strength depends on loading directions, and various adhesion tests have been proposed. In peel test, one of the principal tests, adhesive interface is progressively detached from an edge (Fig. 1a). Theoretical framework for estimating the adhesion strength has not yet been established, and the underlying molecular mechanisms remain poorly understood[1]. In this study, we develop a theoretical framework based on density functional theory (DFT) to analyze the peel process at adhesive interfaces and apply it to an epoxy resin/alumina interface.

2. Computational Procedure

As shown in Fig. 1b, epoxy resin **1** was treated as a fragment model **2**, and **2** was adsorbed on the alumina surface. Stable adsorption structures were obtained by DFT optimization, following molecular dynamics (MD) sampling. All DFT calculations were performed VASP code with the PBE functional, cutoff energy of 500 eV, and D3BJ dispersion correction.

The peel process of **2** was analyzed based on two modes, A and B, shown in Fig. 1c. Their dissociation energy curves were shown in Fig. 1d. Mode A describes detachment initiated at the terminal region of the interface, whereas mode B targets the more central region. Furthermore, the energy was decomposed into electronic and dispersion contributions.

3. Results and Discussion

As shown in Fig. 1d, mode A exhibits a two-step energy change: (i) breaking of interfacial interactions near the force point, followed by (ii) the upward pulling of **2**. Mode B corresponds to a process in which **2** is dragged from the edge, leading to sharp energy fluctuations. This feature is consistent with the stick–slip behavior observed during actual peeling[2]. This behavior correlates well with the E_{DFT} curve indicated by blue line, suggesting that it originates from the repeated breaking and reformation of interfacial interactions involving charge transfer.

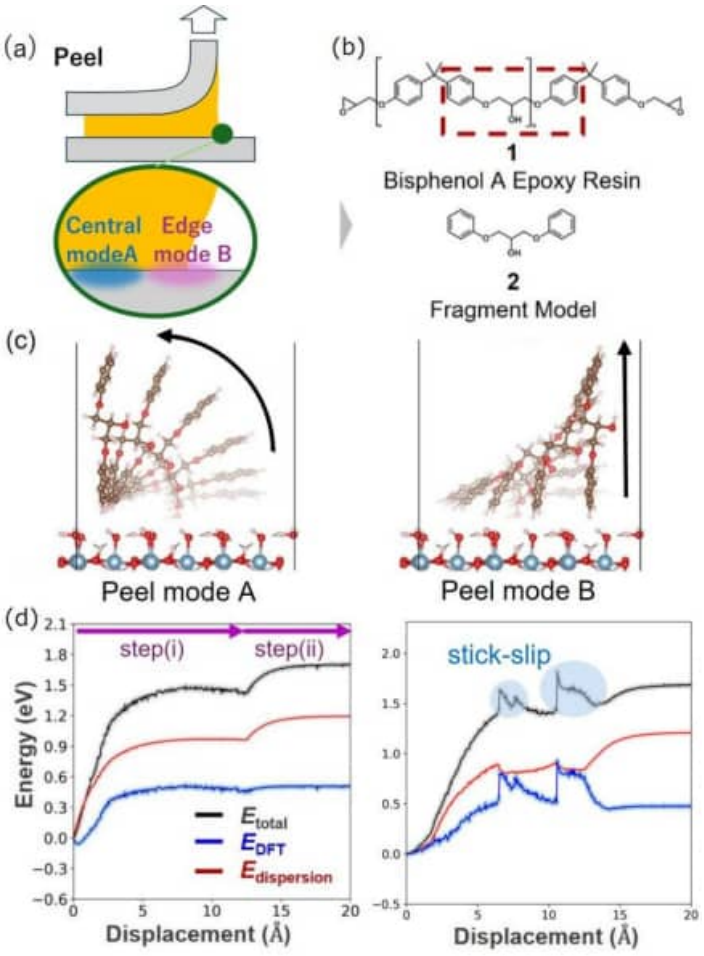

Fig. 1. (a) Peel test. (b) Structures of epoxy resin. (c) Peel mode A and B. (d) Energy curves for mode A and B.

References

[1] Y. Sumiya, *et al*., *ACS Omega* 7, 17393 (2022). [2] M.-J. Dalbe, *et al*., *J. Phys. Chem. C* 125, 23409 (2021).

1P10 Predicting Product Branching in Post-Transition State Bifurcation Reactions via Molecular Dynamics Simulations

([1]*Saitama University*, [2]*Tokyo Metropolitan University*)
Okamoto, Daichi[1]; Yamaki, Keita[1]; Hayashi, Daiki[1]; Nakagawa, Shota[1]; Matsubuchi, Hayato[1]; Sasaki, Yuki[1]; Takayanagi, Toshiyuki[1]; Murakami, Tatsuhiro[2]

In organic reactions yielding multiple products through distinct transition states, product selectivity is commonly estimated by transition state theory (TST). However, TST cannot describe branching fractions when reaction pathways bifurcate after traversing a single transition state (TS), a phenomenon known as post-transition state bifurcation (PTSB). In PTSB reactions, product selectivity is governed by nuclear dynamics in the bifurcation region, which is characterized by valley-ridge transition (VRT) points or valley-ridge inflection (VRI) manifolds. In this study, we aim to identify key physical descriptors governing branching behavior and develop a novel predictive model for estimating branching fractions. On-the-fly MD simulations and VRT searches were performed using AIQM2 [1] for 18 systems with varying tether structures in two types of intramolecular cycloaddition reactions shown in Fig. 1. Additionally, the resulting branching fractions were compared with predictions from our proposed model and existing predictive models, including VRA [2], dBond [3], and RMCF [4].

We propose a predictive model based on VRT location and post-VRT IRC maximum curvature in the R_2–R_3 distance space (Fig. 1). Outperforming existing models, it achieved a correlation coefficient of 0.921 across all 18 systems (Fig. 2). Benchmarking results of existing models revealed that RMCF performs better for early-VRT systems, where the VRT occurs near the TS, whereas dBond performs better for late-VRT systems, where the VRT occurs in the IRC shoulder region. These results demonstrate that our model is broadly applicable to a wide range of PTSB reactions.

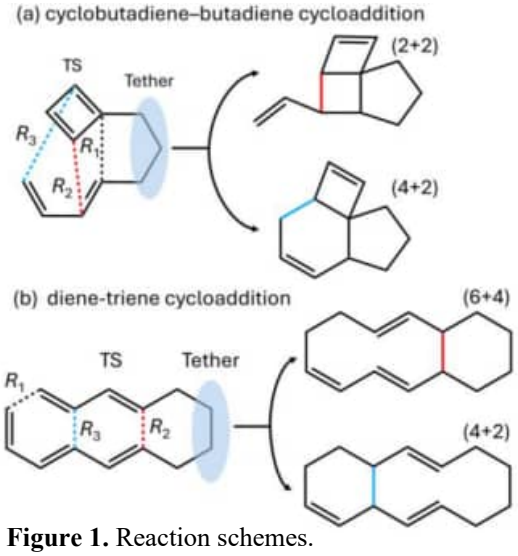

Figure 1. Reaction schemes.

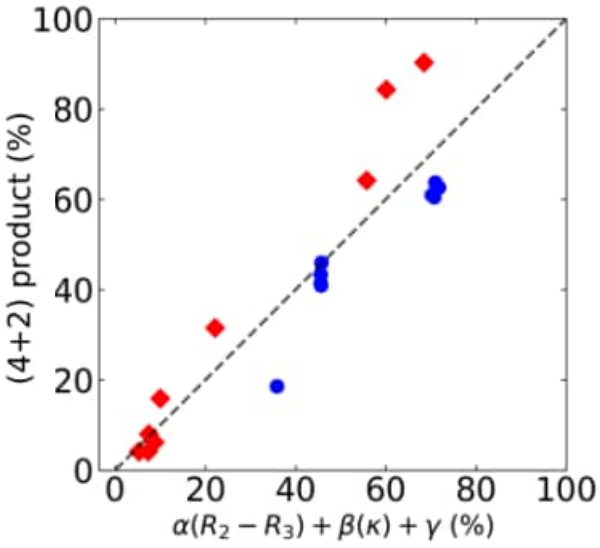

Figure 2. MD branching fraction vs. predicted fraction F from the two-parameter model $F = \alpha\Delta R + \beta\kappa + \gamma$, where ΔR and κ represent the VRT location and post-VRT maximum curvature, respectively.

[1] Y. Chen, P. O. Dral. *Chem. Sci*. **2025**, *16*, 15901.

[2] S. Lee, J. M. Goodman. *J. Am. Chem. Soc.* **2020**, *142*, 9210.

[3] C. Lam, K. N. Houk. *Pure Appl. Chem.* **2025**, *97*, 1135.

[4] P. Bharadwaz, M. Srnec *et al*., *Chem. Sci.* **2021**, *12*, 12682.

1P11

Robust High-Order Potential Energy Surface Derivatives from Chebyshev Polynomial Representations for Phase-Space Chemical Dynamics

U. Umer[1,*], J. Li[2], R. Staub[1], K. Yagi[3], T. Taketsugu[1,4], T. Komatsuzaki[1,2,*]
[1] WPI-ICReDD, Hokkaido University, Japan
[2] Research Institute for Electronic Science, Hokkaido University, Japan
[3] Department of Chemistry, University of Tsukuba, Japan
[4] Department of Chemistry, Faculty of Science, Hokkaido University, Japan

Reaction mechanisms are typically described on the potential energy surface (PES), but this framework becomes inadequate for complex dynamical regimes, where transition state theory (TST) breaks down. A phase-space (PS) formulation provides a rigorous alternative. This framework critically depends on numerically stable estimation of higher-order (HO) derivatives of the potential energy surface (PES); however, any convergence uncertainty in electronic-structure calculation is amplified at HO, degrading PS structures and the dynamical predictions.

Here, we introduce a Chebyshev polynomial-based framework for stable and systematically controlled evaluation of HO derivatives from PES data. Figure 1 uses the HCN isomerization system as a benchmark to assess HO derivative accuracy. Finite-difference (FD) results (orange) exhibit a high-variance in relative error, with high sensitivity to discretization, reflecting numerical instability when increasing order. In contrast, Chebyshev approach (purple) concentrates error distribution around zero with suppressed tail events, indicating substantially improved numerical stability. This reduction in variance persists under finer grid resolution, demonstrating weak sensitivity to discretization with consistent convergence behavior. The results indicate that Chebyshev differentiation significantly stabilizes HO derivative evaluation by suppressing error amplification inherent to FD schemes.

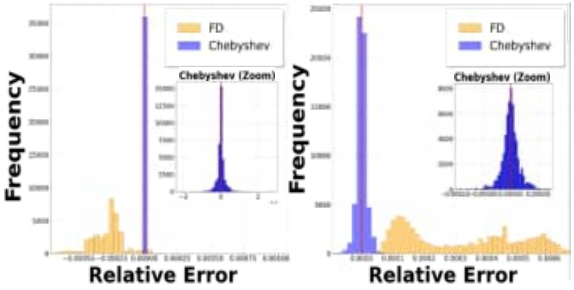

Figure 1: FD vs Chebyshev relative error for HCN isomerization reaction. Relative errors in fourth-order derivatives (left) and fifth-order derivatives (right), defined as $\partial^n V / \partial x_{i_1} \cdots \partial x_{i_n}$, with $n = 4, 5$ and $x_i \in \{x, y, z\}$, including all diagonal and mixed components.

In the left panel of Figure 2, Chebyshev 4th order derivatives computed on DFT data show pronounced scatter, structured deviations, and mode-specific inconsistencies relative to FD DFT references. In turn, in the right panel, a neural network potential (NNP) trained on the same DFT data is used as the PES. Applying Chebyshev differentiation to this surface yields derivatives that closely follow the parity line and agree with reference values as well as NNP. This indicates that HO differentiation amplifies SCF convergence errors for a set of molecular configurations prepared along normal mode 2 on the PES. It was almost impossible to identify the existance of ill-converged SCF configurations among various set only using standard FD approached. The agreement confirms that the Chebyshev spectral method as a numerical scheme to compute HOs of PES is accurate and robust, and that the main limitation originates from the raw DFT data rather than the numerical scheme. Our analysis shows Chebyshev method is not just more accurate, it is also a diagnostic tool for electronic structure calculations.

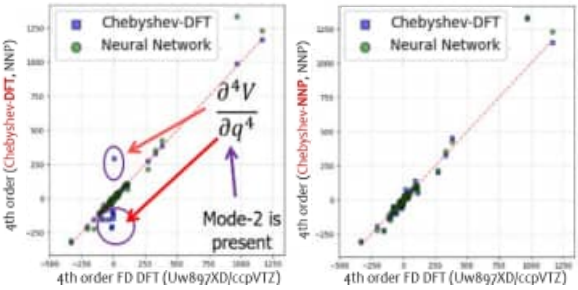

Figure 2: HO derivatives parity plots at saddle for H_2CO, including all 4th order diagonal and mixed (non-diagonal) components of normal mode.

1P12 Development of a fluctuation-assisted molecular dynamics method for the efficient sampling of chemical reactions

([1]Grad. Sch. Adv. Sci. Eng., Waseda Univ., [2]WISE, Waseda Univ.)
Sei Tsukamura[1], Yoshifumi Nishimura[2], and Hiromi Nakai[1,2]

In molecular dynamics (MD) simulations, observing statistically rare chemical reactions within limited system sizes and time scales is difficult. While the nanoreactor MD (NMD) method [1] efficiently promotes chemical reactions via periodic volume changes in the reactor, it inherently causes significant increases in temperature and pressure. In this study, we developed a novel approach, the fluctuation-assisted MD (FMD) method [2], to accelerate chemical reactions under significantly milder conditions.

In the NMD method, as shown in Fig. 1(a), the movement range of chemical species is confined by a boundary wall potential V_{NMD}, which promotes chemical reactions by increasing the collision frequency among the species. In the proposed FMD method, an additional potential $V_{\mathrm{FMD}}(r, t)$ with a time-dependent force constant $k(t)$ is introduced.

$$V_{\mathrm{FMD}}(r,t) = \frac{mr^2}{2}k(t) \qquad (1)$$

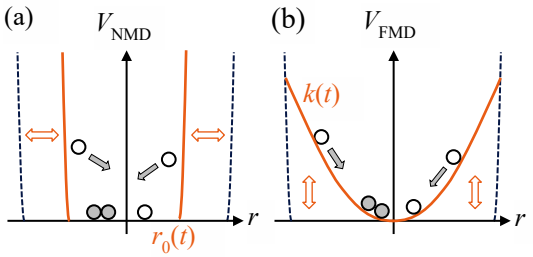

Fig. 1. Schematic diagram of the (a) NMD method and (b) FMD method. The variation of the additional potential shown in orange causes species (white circles) to cluster into the central radial region, triggering chemical reactions (black circles).

where r denotes the radial coordinate of an atom, t is time, and m is the atomic mass. As illustrated in Fig. 1(b), V_{FMD} causes the chemical species to aggregate toward the center to generate pseudo-concentration fluctuations, thereby accelerating chemical reactions by enhancing the collision frequency.

The FMD method was validated by targeting the acetylene (C_2H_2) polymerization reaction. Fig. 2 shows the time evolution of the number of C_2H_2 molecules and the temperature for the MD, NMD, and FMD methods. As shown in Fig. 2(a), the FMD method exhibited an acceleration effect in the consumption of C_2H_2 comparable to that of the NMD method. Furthermore, as illustrated in Fig. 2(b), the temperature increases in the FMD method were smaller than those in the NMD method. These results confirm that the FMD method promotes chemical reactions to a degree comparable to the NMD method but under significantly milder conditions.

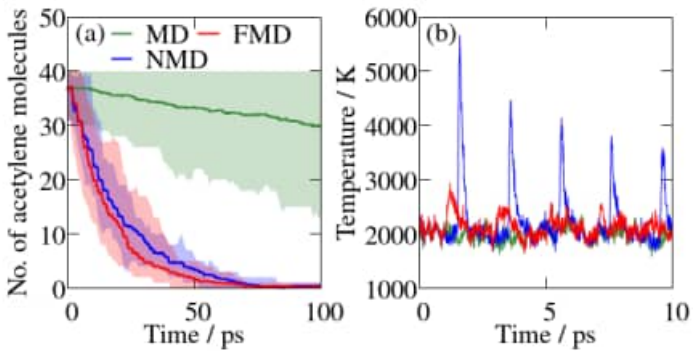

Fig. 2. (a) Time evolution of the number of C_2H_2 molecules. The lines represent the average values of 10 trajectories, and shaded areas indicate the minimum and maximum values. (b) Time evolution of temperature during the first 10 ps in trajectory No. 1 obtained from simulations at 2000 K.

[1] L.-P. Wang, A. Titov, R. McGibbon, F. Liu, V. S. Pande, and T. J. Martínez, *Nat. Chem.*, **6**, 1044 (2014). [2] S. Tsukamura, Y. Nishimura, and H. Nakai, *J. Phys. Chem. Lett.*, **17**, 3102 (2026).

1P13 Dynamical Effects Beyond Kinetic Analysis Based on Reaction Path Networks: An Ab Initio Molecular Dynamics Study

(Hokkaido Univ.) Soei Takizawa, Takuro Tsutsumi, Yuriko Ono, Kazuki Sada, Tetsuya Taketsugu

Understanding chemical reactions requires a reaction-path perspective. A representative concept of reaction paths is the intrinsic reaction coordinate (IRC). The IRC is defined as the minimum-energy path connecting a reactant and a product through a transition-state structure, providing a physically intuitive description of an elementary reaction process. Recent advances in the Global Reaction Route Mapping (GRRM) program have enabled exhaustive exploration of IRCs. The application of transition state theory to each elementary process in the reaction path network constructed by GRRM has facilitated kinetic simulations on experimentally relevant timescales[1] and kinetics-based navigation,[2] which guided the exploration of reaction pathways toward kinetically important elementary processes.

Although kinetic analysis is a simple yet powerful approach, actual chemical reactions do not proceed solely according to the activation barriers along IRCs. For example, non-IRC processes,[3] in which trajectories deviate from IRCs, and IRC-jumps, in which trajectories switch to another IRC after deviation, have been reported. These phenomena are known to be influenced by the effects of nuclear momenta, namely dynamical effects arising from translational, rotational, and vibrational motions. However, direct quantitative comparisons between such dynamical effects and kinetic analyses on global reaction path networks remain limited.

In this study, we performed kinetic analysis based on Rice–Ramsperger–Kassel–Marcus (RRKM) theory and population analysis of *ab initio* molecular dynamics (AIMD) trajectories over the reaction path network. AIMD simulations can explicitly incorporate dynamical effects, but their high computational cost has been a major limitation. By selecting the Au_5 cluster,[4] which has low activation barriers, as the target system, AIMD simulations on the same sub-nanosecond timescale as the kinetic analysis became feasible. In this presentation, we compare kinetic and dynamical analyses and identify where and how the AIMD populations deviate from the RRKM-based kinetic prediction, thereby clarifying the role of dynamical effects.

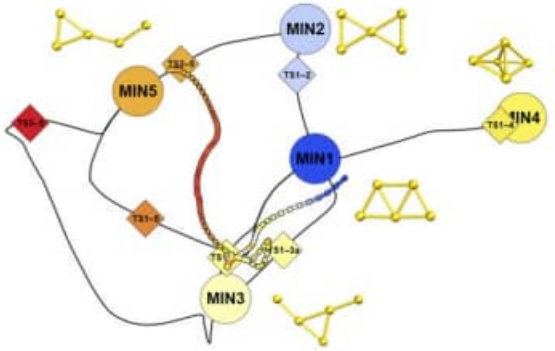

Figure 1. Reaction path network and non-IRC trajectory of the Au_5 cluster.[4]

[1] T. Mita *et al.*, *J. Am. Chem. Soc.*, **2022**, 144, 50, 22985.
[2] Y. Sumiya, S. Maeda, Chem. Lett., **2020**, 49, 5, 553.
[3] L. Sun, K. Song, W. L. Hase, *Science*, **2002**, 296, 875.
[4] T. Tsutsumi, Y. Ono, T. Taketsugu, *Chem. Commun.*, **2021**, 57, 11734.

1P14 ChemOntology: A Reusable Explicit Chemical Ontology-Based Method to Expedite Reaction Path Searches

(Institute for Chemical Reaction Design and Discovery (WPI-ICReDD), Hokkaido University, Kita 21 Nishi 10, Kita-ku, Sapporo, Hokkaido 001-0021, Japan) Pinku Nath

ChemOntology is a computational framework developed to extract and apply chemical knowledge from reaction intermediates generated during automated reaction path searches. By integrating chemical and geometric knowledge generated using chemical ontology and topology, ChemOntology identifies chemically relevant reaction paths and geometries to guide the reaction path search. Combined with an automated reaction path search method, Artificial Force Induced Reaction (AFIR) and applied to the Heck reaction, the ChemOntology-AFIR approach efficiently identified all key intermediates and elementary steps, including major and side products, even in high-energy regions where conventional AFIR need much larger computational efforts for extensive conformational sampling. This knowledge-driven approach significantly reduces computational costs by eliminating chemically irrelevant paths and structures. ChemOntology relies on three main inputs: the reaction setup, chemically informed assumptions encoded as Elementary Reaction Process Ontologies (ERPOs), and a set of reaction rules. Together, these enable efficient use of extracted knowledge to accelerate reaction exploration. Unlike machine learning models, it requires no training on data sets and is broadly applicable to a wide range of organometallic systems, offering a robust tool for mechanistic analysis and rational catalyst design, especially in systems where human insight remains indispensable.

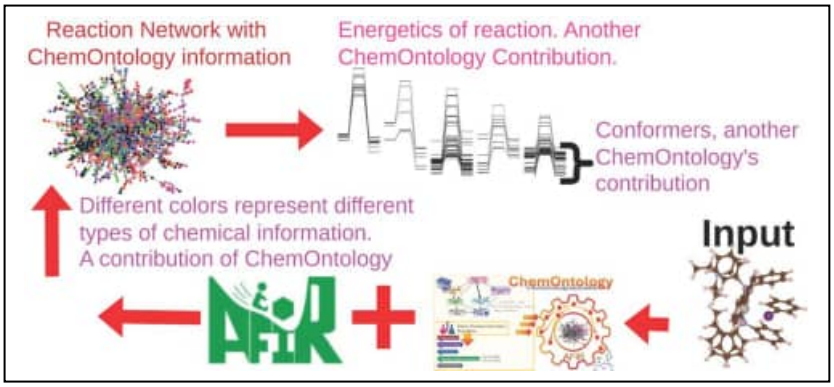

1P15 Analysis of the Product Branching Boundary Determining Reaction-Path Bifurcation

([1]Grad. Sch. Chem. Sci. Eng., Hokkaido Univ., [2]Fac. Sci., Hokkaido Univ., [3]Institute for Quantum Chemical Exploration, [4]WPI-ICReDD, Hokkaido Univ.)
Jidai Suzuki[1], Tatsuhiro Nakanishi[1], Ryuto Kambara[1], Yuriko Ono[2,3], Tetsuya Taketsugu[2,4]

[Introduction] For an elementary reaction, the reaction pathway connecting reactants and products via a transition state (TS) is defined as the intrinsic reaction coordinate (IRC). The IRC does not necessarily trace the bottom of a potential energy valley in the directions perpendicular to the path. In certain regions along the path, the IRC can change from a valley to a ridge, making the path unstable. As illustrated in Fig. 1a, on a potential energy surface (PES) that is symmetric with respect to the IRC, the IRC reaches the second TS via a valley-ridge inflection (VRI) point, at which the gradient vector is orthogonal to a normal-mode vector associated with a zero eigenvalue. By contrast, on the asymmetric PES shown in Fig. 1b, the IRC does not pass through the VRI point; instead, it bends sharply near the second TS and proceeds to the product on the left-hand side. In such a case, the valley-ridge transition (VRT) point, where the character of IRC changes from valley to ridge, has been identified on the IRC by diagonalizing the mass-weighted Hessian matrix with the IRC direction projected out, and the corresponding path bifurcation has been discussed. In this study, we aimed to gain insight into the product bifurcation boundary separating the two products. To this end, we identified VRI points in a reaction system with an asymmetric potential energy surface and performed an analysis based on Reaction Space Projector (ReSPer) [2].

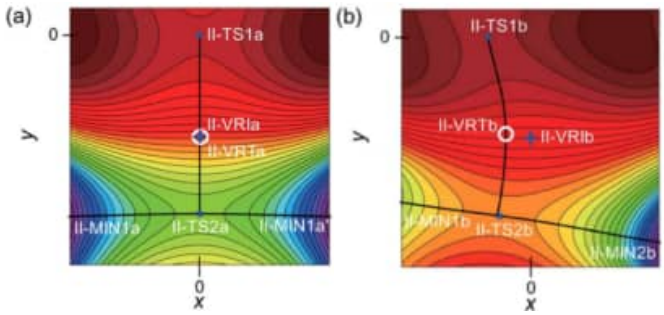

Fig. 1. Schematic illustrations of reaction-path bifurcation on two-dimensional model potentials: (a) a symmetric case; (b) an asymmetric case [1].

[Results and Discussion] For the reaction between α-bromoacetophenone and OH^-, which exhibits post-transition-state bifurcation, we calculated the IRC at the B3LYP/6-31+G* level and identified the VRT by projected vibrational analysis (Fig. 2). A quasi-VRI point was identified by displacing structures on the IRC along the VRT mode, thereby clarifying the geometrical characteristics of the PES around the product branching boundary that governs reaction path bifurcation. Because the product changes with the substituent in this reaction, IRCs obtained for different substituents were projected onto a common reaction space using ReSPer, and the behavior at the bifurcation boundary was analyzed.

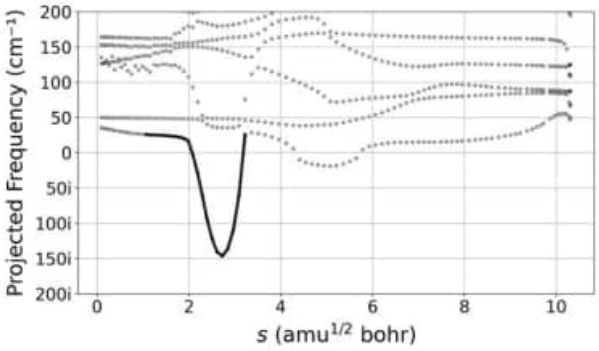

Fig. 2. Changes in the frequencies of the projected vibrational modes along the IRC. The thick line indicates the vibrational mode responsible for the VRT.

[References]

[1] S. Maeda, Y. Harabuchi, Y. Ono, T. Taketsugu, K. Morokuma, *Int. J. Quant. Chem.*, **115**, 258 (2015).
[2] **J. Suzuki**, T. Nakanishi, R. Kambara, Y. Ono, T. Tsutsumi, and T. Taketsugu, *submitted*.

1P16 Merged-beam experiment on a low-energy ion-neutral reaction study

(Department of Physics, Rikkyo University) S. Dhongade, H. Tamaru, R. Ota, LT Ballantyne, T Matsuzaki, S. Yabuki, Y. Nakano
(ELSI, Institute of Science Tokyo) A. Nakayama

Ion–neutral reactions are recognized as key elementary processes in gas-phase astrochemistry because they can proceed efficiently at low temperatures, often without activation barriers. Recent astronomical observations suggest that non-thermal processes, such as reactions under high UV irradiation, may significantly influence molecular abundances. To understand the non-thermal chemical evolution of molecular species, it is essential to investigate these reactions with respect to their collision velocity and internal quantum state.

To this end, we have been developing a merged-beam apparatus coupled with a tunable laser spectroscopy setup (Fig. 1). Using this setup, we have pursued studies of the internal-state population distribution of molecular ion beams using N_2O^+, which we have investigated in previous studies [1] at the cryogenic ion storage ring RICE [2]. In addition, a newly developed two-dimensional beam-profile tomography system [3] is expected to enable the determination of absolute reaction cross sections through accurate measurement of the beam-overlap integral. We have also developed a laser-induced metal-plasma light source that provides pulsed FUV radiation in the 120–250 nm range for this purpose [4]. In this presentation, we will report the current commissioning status of the merged-beam experiment and discuss its prospects for state-selective studies of ion–neutral reactions.

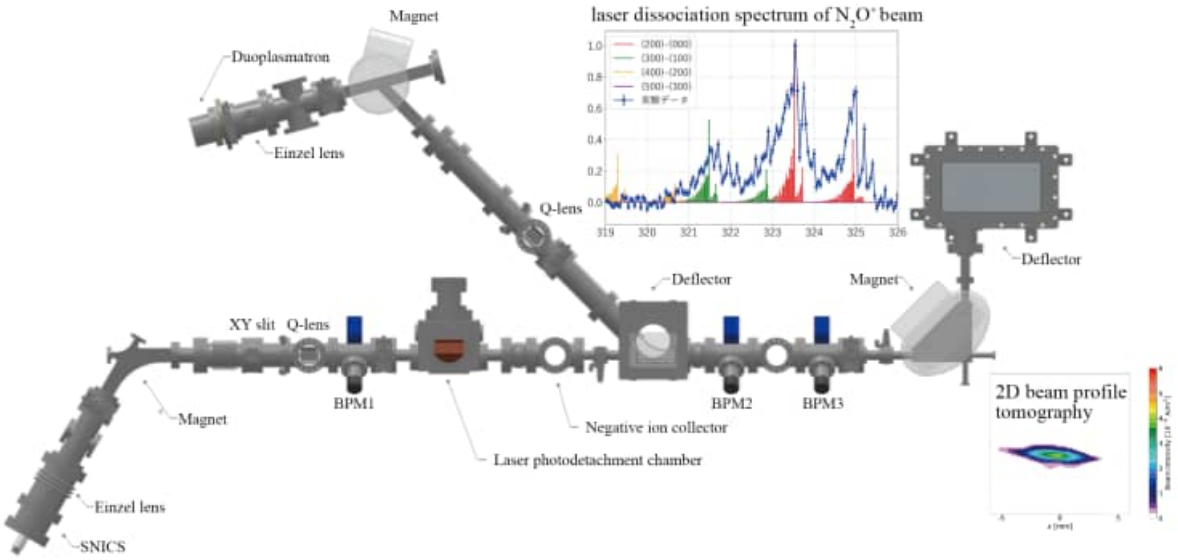

Figure 1. Experimental setup for the merged-beam experiment.

Reference:
[1]. "Fermi resonance in the radiative vibrational cooling dynamics of N2O+", S. Harayama, S. Kuma, N. Kimura, K. C. Chartkunchand, M. Baba, T. Murakami, T. Takayanagi, K. Yagi, T. Yamaguchi, Y. Nakano, and T. Azuma, Phys. Rev. A 111, 032803 (2025)
[2]. "解説:極低温静電型イオン蓄積リングの開発と冷却分子イオンの物理", 中野祐司, 榎本嘉範, 東俊行, 日本物理学会誌 77, 346 (2022)
[3]. "High-resolution computed tomography of two-dimensional beam profile using dual-axis rotating wire", R. Ota, N. Nakajima, R. Takemasa, H. Tamaru, Y. Shiina, Y. Nakano, Rev. Sci. Instr. 96, 093301 (2025)
[4]. "Generation of collimated far-ultraviolet (FUV) light using the laser-produced metal plasma", H. Ohnishi, S. Tamaki, Y. Shiina, Y. Nakano, J. Appl. Phys. 134, 013103 (2023)

1P17 Entropic advantage and induction-mediated polarization in the adsorption of cyclic oligomers on fullerene surfaces

Arima, Sota[1]; Yamamoto, Takuya[2]; Sato, Shin-ichiro[2]
([1]Grad. School Chem. Sci. Eng., Hokkaido Univ., [2]Div. Appl. Chem., Fac. Eng., Hokkaido Univ.)

Various studies are being conducted on fullerene C_{60} for biomedical applications such as drug delivery systems (DDS). However, as C_{60} aggregates and precipitates in water, it must be stabilized and dispersed for use within the body. Yamamoto and colleagues from our laboratory have succeeded in stabilizing the dispersion of gold nanoparticles and other particles even under high-temperature and physiological conditions through the physical adsorption of cyclic polyethylene glycol (c-PEG), a representative biocompatible polymer (Y. Wang, et al., *Nat. Commun.* **11**, 6089 (2020)). This suggests that the topology of the polymer plays an important role in its adsorption onto the surface.

Furthermore, we have successfully stabilized the dispersion of C_{60} nanoparticles using Pluronic L64, a block copolymer of polypropylene glycol (PPG) and PEG (Y. Wang, S. Arima et al., *Macromol. Rapid Commun.*, **47**, no. 5 (2026): e00586). In this study, quantum chemical calculations were performed on complexes formed between C_{60} and oligoethylene glycol $(EG)_n$, oligopropylene glycol $(PG)_n$, and the block oligomer $(EG)_{n/2}$-$(PG)_{n/2}$, in order to analyze the molecular-level mechanism by which Pluronic L64 adsorbs onto the C_{60} surface. Furthermore, to verify the topological effects of oligomers, comparisons were made between linear and cyclic forms. Gaussian 16 was used for the calculations, and DFT was employed for the calculation theory. The functional and basis set were set to PBE0-D3/6-31+G(d,p), using Grimme's dispersion correction. For geometry optimization, we first used 3-21G to improve efficiency and subsequently employed 6-31+G(d,p). The Counter Poise (CP) method and the Symmetry Adapted Perturbation Theory (SAPT) method were used to calculate the interaction electron energy. Thermodynamic parameters, such as the change in free energy due to adsorption, were determined using standard vibration calculations.

Figure 1 shows the optimized structures, charge distributions and dipole moments of C_{60}/*l*-$(EG)_6$ and C_{60}/*c*-$(EG)_6$. *l*-$(EG)_6$ curved to encapsulate C_{60}, whilst *c*-$(EG)_6$ adsorbed onto C_{60} with virtually no change in structure. In terms of interaction electron energy calculated using the CP method and the SAPT method, the linear chain was found to be more favorable for adsorption. In terms of free energy changes, however, the cyclic structure proved to be more favorable for adsorption. The entropy term $-T\Delta S$ was smaller for the cyclic structure. Furthermore, a topological effect was observed whereby the induced force increased in a ring-like pattern under the SAPT method. In the linear form, the dipole moment is parallel to the C_{60} surface, whereas in the cyclic form, it is oriented from the C_{60} surface towards the oligomer, and its magnitude is greater than that of the linear form. These results suggest that cyclic oligomers exhibit the following two topological effects in their adsorption onto the C_{60} surface: (1) The ring structure suppresses the entropy loss associated with adsorption, making adsorption thermodynamically favorable. (2) The dipole moments on the surface of C_{60} nanoparticles align cooperatively from the surface towards the oligomers, strengthening interactions with water molecules and thereby improving solubility.

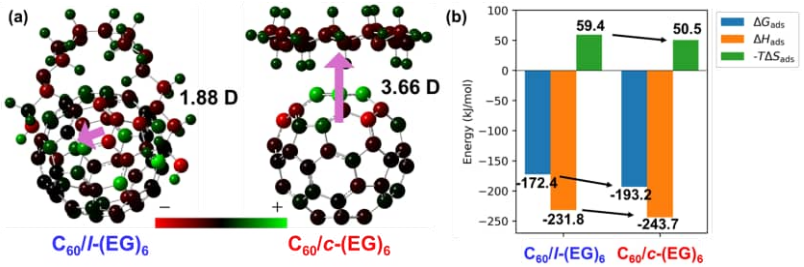

Figure 1 (a) Optimized structure, charge distribution and dipole moment of C_{60}/$(EG)_6$. (b) Thermodynamic parameters of C_{60}/$(EG)_6$.

1P18 Surface reactions of sulfur-bearing molecules with hydrogen atoms on amorphous solid water

([1]Hokkaido University, [2]Leiden University, [3]University of Gothenburg, [4]IFF-CSIC) Nguyen T.[1,2], Oba, Y.[1], Sameera, W.M.C.[1,3], Molpeceres, G.[4], Watanabe, N.[1]

Sulfur (S) is a crucial element that plays a key role in chemical evolution in space. Approximately 30 S-bearing species have been detected in the interstellar medium (ISM). However, their observed total abundance of S-bearing molecules remains considerably lower than the expected cosmic abundance of S [1]. Hence, it has been considered that there should be hidden S-source(s), typically denoted as "missing sulfur" somewhere in the ISM.

Although most S-bearing species have been detected so far in the gas phase, it is widely accepted that physicochemical processes on interstellar icy grains play an important role in their formation. This implies that surface processes might also be relevant to the source(s) of missing sulfur in the ISM. To understand deeply the formation processes of S-bearing molecules found in the ISM, we experimentally and computationally studied the surface reactions of hydrogen atoms with carbonyl sulfide (OCS), methyl mercaptan (CH_3SH), sulfur dioxide (SO_2), and carbon disulfide (CS_2) on amorphous solid water (ASW) at temperatures as low as 10 K. Reactions were monitored using a Fourier-transform infrared spectrometer and a quadrupole mass spectrometer. Also, possible reaction pathways were searched by quantum-chemical calculations.

Among the possible entrance channels for the reaction of CH_3SH with H atoms on ASW, an H-atom addition to the S atom should be the main path due to the lowest barrier (0.05 eV), which results in the formation of CH_3 and H_2S ($CH_3SH + H \rightarrow CH_3 + H_2S$). The formed CH_3 radicals would react with additional H atoms to yield CH_4. We have experimentally confirmed the formation of H_2S and CH_4 after the reaction of solid CH_3SH with H atoms, showing a good consistency between experiments and calculations. Although CH_4 and H_2S can be produced from another reaction ($CH_3SH + H \rightarrow CH_4 + HS$) and a following reaction ($HS + H \rightarrow H_2S$), it would not proceed even by tunneling due to the very high barrier (0.86 eV). We also confirmed that H-abstraction reactions ($CH_3SH + H \rightarrow CH_2SH + H_2$ or $CH_3S + H_2$) took place under the same experimental conditions. Experimental and computational results of other S-bearing molecules will be shown in the presentation, demonstrating that S-bearing species are converted to H_2S by reactions with H atoms, and the formed H_2S was easily desorbed into the gas phase by reactive desorption [2].

References

[1] Wakelam, V. et al 2004 Astron. Astrophys. 413, 609

[2] Oba, Y. et al 2018 Nature Astron. 4, 781

1P19 Towards the Observation of Gas-Phase Vibrational Polaritons via Transmission Spectroscopy

([1]Grad. Sch. Integr. Sci. Technol., Shizuoka Univ., [2]Dept. Chem., Fac. Sci., Shizuoka Univ.)
MIYASHITA Kaichi[1], MITSUKAWA Eiyu[1], MATSUMOTO Yoshiteru[2]

Vibrational strong coupling (VSC) is a strong light-matter interaction in an optical cavity. The optical cavity (length L) enables an electromagnetic (EM) wave with wavelength $\lambda_{EM} = 2L/n$ (n: positive integer) to be confined. Matching a molecular vibrational frequency to the cavity mode frequency ($f = c / \lambda_{EM}$, c: the speed of light) results in vibrational polaritons (VPs), hybrid states of light and matter. Recently, VPs have attracted attention as unique states that enable alteration of chemical reaction kinetics and branching in condensed phases [1][2]. Understanding the reaction mechanism under VSC requires detailed information about the potential energy surface along the reaction coordinate. However, significant solvents prevent us from obtaining high-resolution spectroscopic data for PES investigation. Thus, we aim to produce and observe gas-phase VPs as an optimal system in the absence of solvents. Using gaseous CO_2, we challenge the observation of the Rabi splitting due to VPs in an optical cavity.

The optical cavity consists of two gold-plate mirrors (R~90%), mounted in our homemade gas cell. The cavity is kinetically controlled by piezoelectric actuators and has a mirror distance of about 11 μm. Injecting an IR laser pulse (YAG pumped OPO/A) into the cavity results in a cavity transmission spectrum that consists of cavity modes characterized by a free spectral range.

Fig. 1 shows the absorption profile of the CO_2 anti-symmetric stretch. Tuning the cavity mode to the maximum of the R-branch at 2365 cm^{-1} yields no transmitted laser intensity even in the vacuum cell. This results from the loss of the IR output due to CO_2 in the air before injecting into the cavity. To avoid loss of the laser source, we adjust the cavity mode to 2400 cm^{-1}, the higher-wavenumber side of the R-branch. The black and red traces in Fig. 1 show the cavity transmission spectra observed under vacuum and 1atm of CO_2 in the gas cell, respectively. The red trace exhibits asymmetric two peaks at 2390 and 2420 cm^{-1}, resembling Rabi splitting, although differing from the simulated spectrum. The incoherence between experiment and simulation is now under consideration. In the poster presentation, we will report the updated transmission spectra measured using an improved apparatus that completely evacuates CO_2, except within the cavity.

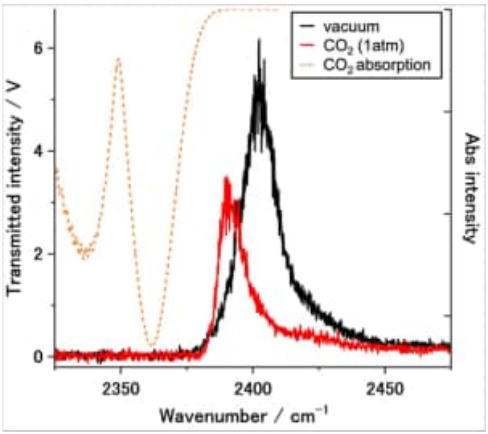

Fig. 1. Cavity transmission spectra under vacuum and 1atm of CO_2

[1] Ebbesen, *Acc. Chem. Res.*, **49**, 2403-2412 (2016).
[2] Hirai *et al.*, *Chem. Rev.* **123**, 8099-8126 (2023).

1P20 Physical Adsorption and Conformational Changes of Figure-Eight Poly(ethylene glycol) on Gold Nanosheet Surfaces: A Molecular Dynamics Study

([1]Hokkaido University) Kobayashi, Takuto[1]; Arima, Souta[1]; Yamamoto, Takuya[1]; Sato, Shin-ichiro[1]

[Introduction]

Poly(ethylene glycol) (PEG) is widely used for surface modification of gold nanomaterials due to its hydrophilicity and biocompatibility. Recently, polymer topology has emerged as an important factor influencing interfacial behavior. Figure-eight PEG (Fig. 1), consisting of two interconnected loops, is expected to exhibit adsorption behavior distinct from that of conventional architectures. In this study, we investigate its physical adsorption and conformational changes on gold nanosheet surfaces using molecular dynamics simulations.

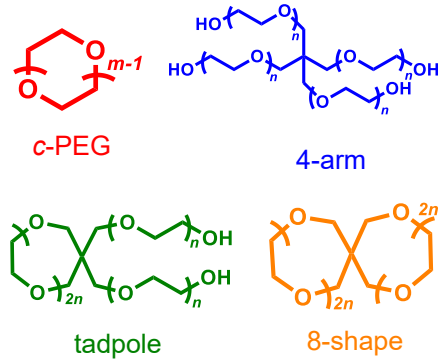

Fig.1 PEGs with different topologies.

[Computational]

A figure-eight poly(ethylene glycol) (PEG) molecule was placed near a gold nanosheet modeled as an Au(111) slab and solvated with explicit water under periodic boundary conditions. All-atom molecular dynamics simulations were performed in the NPT ensemble at 300 K and 1 atm. After equilibration, production runs were carried out to examine the adsorption behavior. Structural properties were analyzed using the center-of-mass distance from the surface, the number of surface contacts, and the radius of gyration. Conformational anisotropy was evaluated using the asphericity parameter derived from the gyration tensor.

[Results and discussion]

Figure 2 compares the distributions of the asphericity parameter for four polymer topologies: 4-arm, cyclic PEG (c-PEG), tadpole, and figure-eight PEG. In the bulk state, the figure-eight PEG exhibits a distribution centered around a spherical conformation, indicating a relatively isotropic structure. In contrast, the other three topologies show distributions biased toward prolate conformations. This tendency is particularly pronounced for 4-arm and c-PEG, while the tadpole topology shows a moderate shift toward the spherical region. Upon adsorption onto the gold nanosheet surface, distinct topology-dependent changes are observed. For 4-arm and c-PEG, the prolate component increases after adsorption, suggesting that these polymers adopt more elongated conformations on the surface. In contrast, the tadpole topology shows a decrease in the prolate component, indicating a shift toward more compact or isotropic conformations. Notably, the figure-eight PEG exhibits minimal change in its asphericity distribution before and after adsorption, suggesting that its conformational characteristics are largely preserved upon adsorption. This behavior may be attributed to its topological constraint, which stabilizes a near-spherical structure even at the interface.

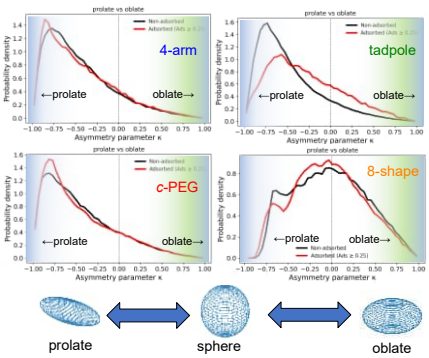

Fig. 2 Asphericity parameters before and after adsorption for four topologies

1P21 Molecular Dynamics Simulation of the Rotational Relaxation Time of an Aptamer-Based Fluorescent Molecular Sensor in Aqueous Solution

([1]Hokkaido University) Hashimoto Kohei[1], Arima Sota[1], Tokeshi Manabu[1], Yamamoto Takuya[1], Sato Shinichiro[1]

Noncompetitive fluorescence polarization aptamer assay (NC-FPAA) is a rapid and convenient method for quantifying target proteins based on fluorescence polarization, with promising applications in medical diagnostics such as virus detection. In a previous experimental study using four dye-labeled aptamers (Figure 1), Cy5-labeled aptamers exhibited significantly higher degree of polarization than those labeled with other dyes. In general, fluorescence polarization is governed by molecular rotational motion, which depends on molecular size and fluorescence lifetime; however, no essential differences in these properties have been reported among the dyes used in this study.

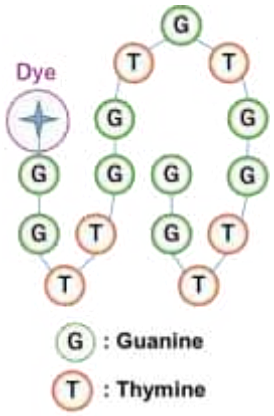

Figure 1. Dye-labeled aptamer

In this work, molecular dynamics (MD) simulations were performed to investigate the rotational relaxation behavior and conformational dynamics of dye-labeled aptamers, aiming to elucidate the origin of the anomalously high degree of polarization observed for Cy5. Two dyes, Cy5 and Dylight 650 (Dylight), were examined for isolated dye molecules and dye-labeled aptamers in aqueous solution. All simulations were carried out using GROMACS 2020.6 with the GAFF force field and AM1-BCC charges. The simulation times were 10 ns for dye-labeled aptamers, 50 ns for dye molecules, and 200 ns for an aptamer.

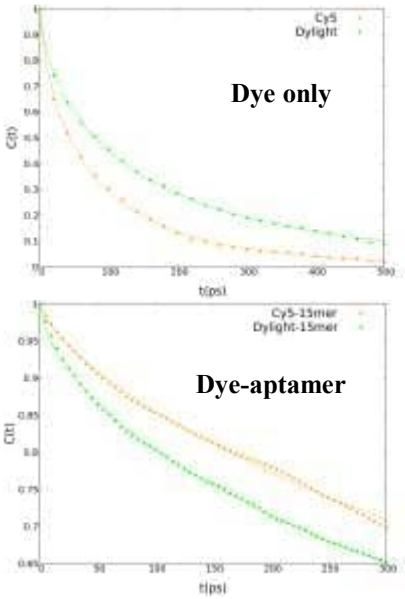

Figure. 2 Rotational autocorrelation functions for dye only (upper) and dye-aptamer (15mer) complexes. Orange curves for Cy5 and Green curves for Dylight.

Rotational relaxation times were evaluated from rotational autocorrelation functions derived from MD trajectories. By fitting the exponential decay region of the autocorrelation functions, relaxation times were obtained for the entire complex, the dye moiety, and the aptamer moiety (Figure 2). The rotational relaxation times of isolated dyes was 74 ps for Cy5 and 140 ps for Dylight. In contrast, in the dye-aptamer complexes, the rotational relaxation times were significantly longer for Cy5 (459 ps) than for Dylight (273 ps), showing a clear reversal of the trend observed for the isolated dyes. The rotational relaxation times in the complexes are consistent with the experimentally observed fluorescence polarization, where the Cy5-labeled aptamer exhibits higher degree of polarization.

1P23 Theoretical prediction of atomic diffusion energy at the ice surface under cryogenic conditions using the kinetic MC method.

([1]Tokyo Metropolitan University) Taniguchi, Riko[1]; Nakatani, Kaho[1]; Nakatani, Naoki[1]

[Introduction]

In chemical evolution on interstellar dust grains, diffusion is an important process that determines reaction efficiency and selectivity. Computational work on surface diffusion is conducted using the kinetic Monte Carlo (kMC) method [1], which is widely used for tracking phenomena with long timescales. However, since its time step depends on the rate constants, an extremely large time step can occur at cryogenic temperatures, leading to a loss of the molecular picture. In this research, we developed the finite-time kMC method to capture molecular dynamics during the diffusion of atoms on interstellar dust grains at cryogenic temperatures.

[Method]

The finite-time kMC (FT-kMC) algorithm that we developed limits the time step by incorporating self-transitions, whereas the conventional kMC always moves an adsorbent to the next site. We select the event using a uniform random number $u_1 = (0, 1]$ under the probability $p_{\mathrm{self}}(t_{\mathrm{max}}) = \exp(-k_{\mathrm{total}} t_{\mathrm{max}})$ in which the transition does not occur during the time period t_{max}. If the transition occurs, we select an event in the same way as the BKL algorithm [1]. After that, sampling the time step (Δt) between $(0, t_{\mathrm{max}}]$ by the following equation using another uniform random number $u_2 = (0, 1]$.

$$\Delta t = -\frac{\ln[(1-u_2)\exp(-k_{\mathrm{total}} t_{\mathrm{max}}) + u_2]}{k_{\mathrm{total}}}$$

[Results & Discussions]

To compare with conventional kMC, we first performed a benchmark simulation using a grid model, in which activation energies (20-600K) and adsorption energies (100-900K) were randomly assigned to mimic an ASW surface. For example, when $t_{\mathrm{max}} = \ln 2 / k_{\mathrm{total}}$ ($p_{\mathrm{self}} = 0.5$), we found a significant difference in diffusion pathways (Fig.1). Consequently, the FT-kMC method captures true physics, particularly at extremely low temperatures.

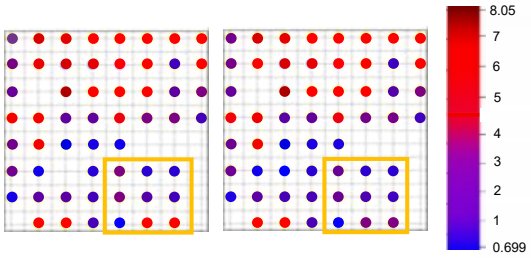

Fig.1 the diffusion path by conventional kMC(left) and FT-kMC(right). The colors displayed correspond to the number of walkers. ($\log_{10}$ scale)

[References]

[1] Mie Andersen; Chiara Panosetti; Karsten Reuter, “A Practical Guide to Surface Kinetic Monte Carlo Simulations”, *Front. Chem.*, **2019**, *7* ,202

1P24 Conformational Constraints in Ni Complexes for Tuning H_2 Production and Oxidation: A DFT-Based Ligand Design Study

([1]Hokkaido University, [2]Ubon Ratchathani University) Hadsadee, S.[1], Ratanasak, M.[1], Naweephattana, P.[1], Morita, S.[1], Miyazaki, R.[1], Iida, K.[1], Nakayama, A.[1], Jungsuttiwong, S.[2], Hasegawa, J.[1]

$[Ni(P^R{}_2N^{R'}{}_2)_2]$ complexes (Fig. 1) catalyze H_2 production or oxidation depending on the nature of the two bidentate P_2N_2 ligands. Ligand design plays a crucial role in determining the reaction direction and catalytic properties. In this study, density functional theory (DFT) calculations were performed to analyze the structural and energetic properties of Ni complexes with (R, R′) = (H, H), (Me, Me), (Cy, Me), (^{t}Bu, Me), (CF_3, H), and (NH_2, H).

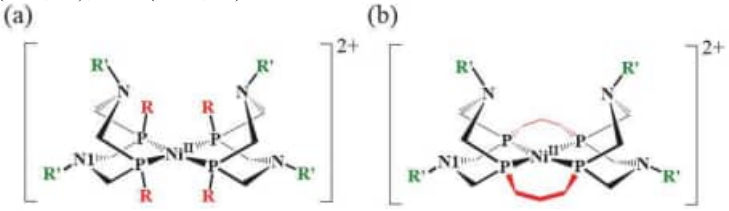

Fig. 1 (a) Structure of Ni-diphosphine complexes $[Ni(P^R{}_2N^{R'}{}_2)_2]^{2+}$ with substituents R and R′ at the phosphorus and nitrogen atoms, respectively. (b) A tetradentate [m3, Me] complex, in which the $-(CH_2)_3-$ unit connects P_1 to P_3 and P_2 to P_4.

Based on the structural features, relative stabilities of the Ni^{II} and Ni^0 complexes, and their energy profiles, these Ni complexes were classified into three groups, I–III (Fig. 2). In group I, the reaction is slightly exothermic toward H_2 production. In group II, the presence of ^{t}Bu and CF_3 groups introduces steric hindrance, forcing the Ni complexes into a tetrahedral conformation. This geometric constraint destabilizes the product state in the Ni^{II} oxidation state, shifting the thermodynamics toward H_2 oxidation. Conversely, destabilizing the reactant state in the Ni^0 oxidation state can be achieved using a tetradentate ligand in which the two bidentate P_2N_2 ligands are connected by trimethylene, $-(CH_2)_3-$, units at the P atoms. This ligand, classified as group III, maintains a square planar conformation, rendering H_2 production highly exothermic. These findings align with experimental observations of similar complexes and underscore the importance of ligand geometry and substituent effects.

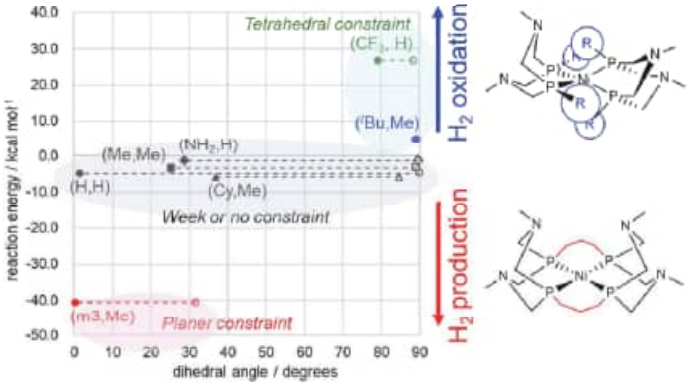

Fig. 2 Ligand design for H_2 oxidation/production activity of Ni complex via tuning dihedral angle. Tetrahedral constraint leads to H_2 oxidation while square-planer constraint switches to H_2 production.

1P25 Electron Momentum Spectroscopy Study of the Intramolecular Hydrogen Bond in Acetylacetone

([1]Institute of Science Tokyo, [2]Tohoku Univ., [3]Keio Univ.) F. Mohri[1], T. Sato[1], M. Takahashi[2], Y. Ohshima[1], M. Yamazaki[1,3]

[Introduction] Electron momentum spectroscopy (EMS) is a high-energy electron-impact ionization technique performed under electron Compton scattering conditions [1]. It provides direct access to orbital-specific electron momentum distributions, which reflect shape of molecular orbitals in momentum space. In this study, EMS was applied to acetylacetone (AcAc), a prototypical molecule having an intramolecular hydrogen bond and large-amplitude vibrational motion associated with proton transfer between the two oxygen atoms [2]. The measured momentum distributions were compared with theoretical calculations to investigate the relationship between the electron distribution and the characteristic vibrations associated to the intermolecular hydrogen bond in AcAc [3].

[Experiment] EMS experiments were performed using a high-sensitivity EMS spectrometer [4]. A thermionic electron beam with energies of 610 eV (or 1210 eV) was crossed with an effusive AcAc molecular beam. Ionized and inelastically-scattered electrons at 45° ± 1.0° were energy-dispersed by a spherical analyzer and detected by a two-dimensional delay-line position-sensitive detector. The binding energy and initial momentum of the target electron were determined from the measured energies and momenta of the two outgoing electrons with the help of conservation laws of energy and momentum.

[Result and Discussion] Figure 1 compares observed and theoretical electron momentum distributions for the (a) 13th and (b) 14th molecular orbitals, both of which have bonding character of the intramolecular hydrogen bond. Hence, these orbitals are expected to be sensitive to structural changes associated with the proton motion. The theoretical momentum distributions were scaled so that their intensities at the local maximum around 0.9 a.u. matched the corresponding intensity of the experimental data. Fig. 1 demonstrates that the experimental distributions lie in between the theoretical results calculated at the equilibrium (EQ) and transition (TS) structures for the proton transfer reaction, indicating significant contribution from the TS structure. The effect of the structural change along the proton-transfer coordinate on the molecular orbital shape was considered in the calculated results labeled with PT (proton transfer). Although the PT results show better agreement with the experimental results than the EQ and TS calculation, there still remains a significant deviation from the observation.

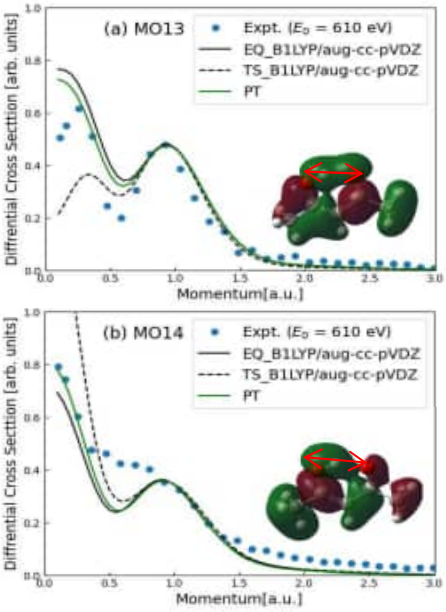

Fig. 1 Comparison of electron momentum distribution for the (a)MO13 (b)MO14 of AcAc between experiment and theory

[1] E. Weigold and I. E. McCarthy, Electron Momentum Spectroscopy (Kluwer Academic/Plenum Publishers, New York, 1999).
[2] Y.-C. Chou, *J. Mol. Spectrosc.* **263**, 34–43 (2010).
[3] J. Dean *et al. J. Phys. Chem. B* **126**, 3551-3562 (2022).
[4] T. Sato *et al. J. Chem. Phys*. **163**, 114301 (2025).

1P26 Electrochemical Behavior of BiF3-Based Electrodes in Liquid Electrolyte for Fluoride Shuttle Batteries

Pakpoom Athikaphana[a], Nicha Tabtimtong[a,b], Pattanapon Kaisook[a,b], Yumiko Imai[a], Tadashi Ueda[a], Arthit Neramittagapong[b,c], Sutasinee Neramittagapong[b,c], and Taketoshi Minato [a,d,*]

[a]Institute for Molecular Science, National Institutes of Natural Sciences, 38 Nishigonaka, Myodaiji, Okazaki, Aichi 444-8585, Japan

[b]Department of Chemical Engineering, Faculty of Engineering, Khon Kaen University, Khon Kaen 40002, Thailand

[c]Research Center for Environmental and Hazardous Substance Management, Khon Kaen University, Khon Kaen 40002, Thailand

[d]Core for Spin Life Sciences, Okazaki Collaborative Platform, National Institutes of Natural Sciences, Okazaki, Aichi 444-8585, Japan

*Corresponding author: minato@ims.ac.jp

Abstract

Fluoride shuttle batteries (FSBs) are promising candidates for next-generation energy storage because of their high theoretical energy density derived from reversible metal fluoride conversion reactions[1-3]. Nevertheless, the practical realization of liquid-electrolyte FSBs is still limited by poor fluoride availability and sluggish electrode kinetics. In this study, electrolytes such as $NaBF_4$ and KPF_6 were preliminarily explored for their ability to support reversible electrochemical reactions in a BiF_3-based electrode system. Galvanostatic charge-discharge measurements revealed reversible cycling behavior during the first three cycles. The electrode delivered discharge capacities of approximately 100-150 mAh g^{-1}, while the corresponding charge capacities were around 70-95 mAh g^{-1}. The observed voltage profiles exhibited characteristic discharge and charge regions, indicating that the $NaBF_4$-containing electrolyte can facilitate fluoride transfer and partially sustain the BiF_3/Bi conversion reaction. Although capacity fading was observed upon cycling, the results confirm the feasibility of this electrolyte system for fluoride-based electrochemical storage. Overall, these preliminary findings indicate that $NaBF_4$ is a promising electrolyte component for liquid-electrolyte fluoride shuttle batteries. This work provides an initial basis for further investigation into electrolyte design, reaction mechanism, and interfacial stabilization for improved reversible fluoride storage.

References

[1] Hiroaki Konishi *et al.*, *J. Electrochem. Soc.* **164**, A3702-A3708 (2017), [2] Keiji Shimoda *et al.*, *J. Electroanal. Chem.* **895**, 115508 (2021), [3] Nicha Tabtimtong *et al.*, *ACS Appl. Energy Mater.* **9**, 3690−3696 (2026).

Acknowledgements

The thank Shinako Iki and Kaho Hirano (Institute for Molecular Science) for experimental support. This research was supported by the grant of OML Project by the National Institutes of Natural Sciences (NINS program No, OML032301). A part of this work was conducted at the Institute for Molecular Science, supported by the Advanced Research Infrastructure for Materials and Nanotechnology in Japan (JPMXP1225MS1021, JPMXP1225MS0005, JPMXP1225MS3005) of the Ministry of Education, Culture, Sports, Science and Technology (MEXT), Japan.

1P27 Polar-molecule trajectory simulations for cluster isolation using a Stark deflector

(Institute of Science Tokyo)
Yutaro Miwa, Mellisa Ardelia, Masaaki Nakamura, and Yasuhiro Ohshima

[Introduction] Molecules possessing a permanent dipole moment experience a force in an inhomogeneous electric field. In this study, we improve the accuracy of trajectory simulations by comparing simulated trajectories with experimental deflection profiles of ammonia molecules, of which only specific quantum states are populated under ultracold conditions.

[Method] A molecular beam was generated in vacuum by supersonic expansion and introduced into a Stark deflector through a skimmer, where molecules in specific quantum states were deflected under an applied voltage. After the deflector, the beam was irradiated by ns-laser pulse to induce REMPI, and the resultant ions were analyzed by TOF mass spectrometry, enabling state-selective signal detection. In trajectory simulations, the force on a molecule was evaluated as the product of the gradient of the Stark energy with respect to the electric field strength and the spatial gradient of the electric field. Spatial profiles comparable to the experiment were obtained by accounting for the initial position distribution, emission angle, ionization region, and quantum states not subject to the field.

[Results and Discussion] The spatial profiles of ammonia molecules obtained by scanning the laser irradiation position [1], together with trajectory simulation results, are shown in Fig. 1. The nozzle conditions were determined with reference to experiments without an applied deflector voltage. The agreement of peak positions under all voltage conditions indicates that the simulations successfully reproduce the experimental deflection behavior, confirming their validity. Building on this, we next consider the benzene dimer [2], which, unlike other cluster sizes, possesses a permanent dipole moment and is expected to be spatially separable using a deflector. Trajectory simulations were performed to evaluate this feasibility, and the results are shown in Fig. 2. By accounting for rotational-state populations under ultracold conditions and the corresponding Stark energies, spatial profiles were obtained, demonstrating that the benzene dimer can be separated in the present setup. Future work will validate these results experimentally and aim to achieve spatial separation.

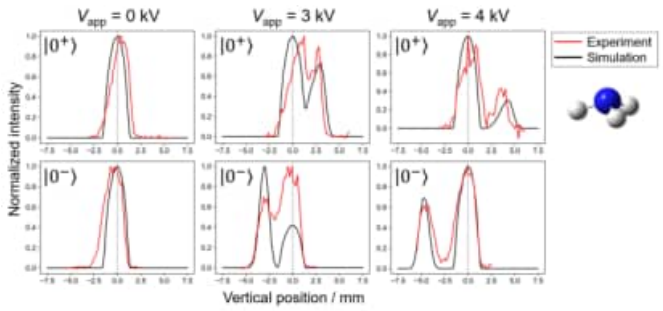

Fig. 1. Spatial profiles of NH_3

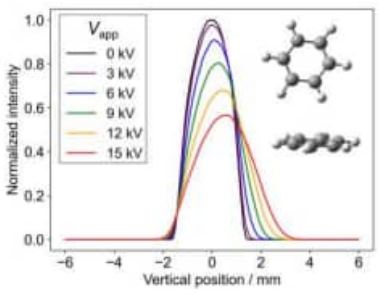

Fig. 2. Simulated spatial profiles of $(Bz)_2$

[1] M. Ardelia, K. Ueno, R. Saida, M. Nakamura, and Y. Ohshima, *The 19th Annual Meeting of Japan Society for Molecular Science*, 1P006 (2025).

[2] M. Schnell, U. Erlekam, P. R. Bunker, G. von Helden, J.-U. Grabow, G. Meijer, and A. van der Avoird, *Phys. Chem. Chem. Phys*., **15**, 10207−10223 (2013).

1P28 Photochemical Reaction of Methylene Blue and Ascorbic Acid

([1]Tokyo University of Science) Suzuki, Takahiro[1]; Ie, Kanon[1]; Kimura, Takayoshi[1]; Inoue, Masayuki[1]

A novel photochromic system was developed in which leucomethylene blue (LMB), generated by reducing methylene blue (MB) with L-ascorbic acid (AsA), is oxidized by molecular oxygen upon irradiation with 405 nm blue-violet light, producing a reversible colorless-to-blue transition. In the dark, the blue solution gradually returns to a colorless state as MB is reduced back to LMB by AsA. This light-driven redox cycle provides a simple platform for investigating photoinduced electron-transfer processes. [1)]

In this study, we investigated the electrochemical response of this system under light irradiation. Chronoamperometry (CA) was performed at fixed potentials to monitor current changes during light ON/OFF switching. The photoinduced current change was defined as $\Delta j = j_{ON} - j_{OFF}$, where j_{ON} and j_{OFF} are the current densities under irradiation and in the dark, respectively. The potential dependence of Δj was then evaluated to clarify how light-induced perturbation of the MB/LMB redox equilibrium appears as a photocurrent response.The redox properties of MB were characterized by cyclic voltammetry (CV) and differential pulse voltammetry (DPV). MB showed a formal potential of $E_{1/2}$ = 103 ± 1 mV (n = 3) in CV and an oxidation peak potential of E_p = 94.9 ± 0.03 mV (n = 3) in DPV, confirming that the MB/LMB redox couple is active near +100 mV. Representative CA traces are shown in **Fig. 1**. When 405 nm light was switched ON and OFF during CA measurements from 0 to 200 mV, clear current changes were observed depending on the applied potential. As shown in **Fig. 2**, Δj increased with increasing potential and changed sign from negative to positive between 50 and 100 mV. This sign reversal indicates that the dominant photoelectrochemical response switches from cathodic to anodic near the redox potential of the MB/LMB couple. Thus, Δj–E analysis revealed that light irradiation has the clearest electrochemical effect around the $E_{1/2}$ and E_p region of MB. These results demonstrate that CA monitoring of light ON/OFF responses is a useful approach for identifying the potential region where photoinduced redox changes in the MB–AsA–O_2 system are most sensitively detected.

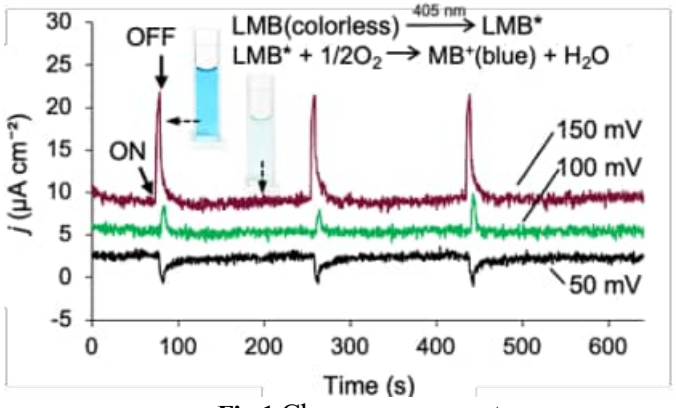

Fig.1 Chronoamperometry

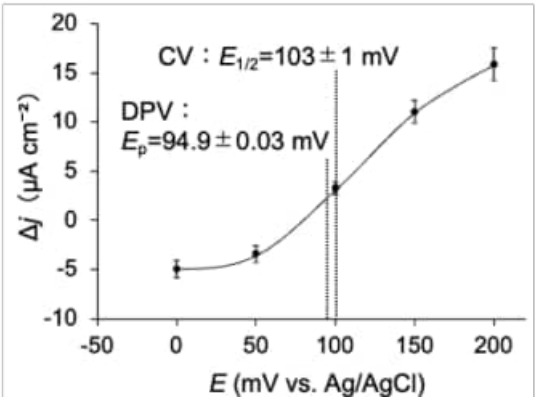

Fig.2 Δj–E (n=9)

1) T. Suzuki, F. Nakamura, K. Ie, M. Fujii, M. Inoue, *RSC Adv.* **2024**,*14*, 39708-39714.

2P01 Photodissociation dynamics of *N,N*-dimethylformamide: Generation of highly vibrational excited HCO

(Hiroshima University) M. Karino, R. Shinohara, K. Inoue, K. Yamasaki, H. Kohguchi

Nitrogen compounds (amines and amides) are essential building blocks of biomolecules. Amine photochemistry is dominated by the N-centered Rydberg and σ^* orbitals, whereas the delocalized π^* orbital between the N and CO is the key factor in amide photochemistry. The planar-to-nonplanar structural change following electron promotion to the π^* orbital is expected to significantly affect the photoexcitation with the Franck–Condon (FC) activation [1-3] and the photodissociation dynamics of the $\pi\pi^*$ state. The energetically congested electronic structure consisted of multiple excited states (Rydberg-type, valence-type, and their mixed-type) has hindered a detailed understanding of amide photochemistry. In this study, we performed the state-selective measurements of the CH_3 and HCO products from 223 – 245 nm photolysis of *N,N*-dimethylformamide (DMF, $(CH_3)_2N(CO)H$) to investigate $\pi\pi^*$ state dynamics.

The LIF spectrum of the HCO fragment indicated the generation of quasi-bound resonance state above the dissociation threshold (5070 cm^{-1}) (Fig. 1). The dissociation wavelength dependence of the intensity of the $2_2^0 3_1^0$ band revealed the generation of the HCO(v_1 = 0, v_2 = 2, v_3 = 1) state spreads across the 223–245 nm photolysis region (Fig. 2).

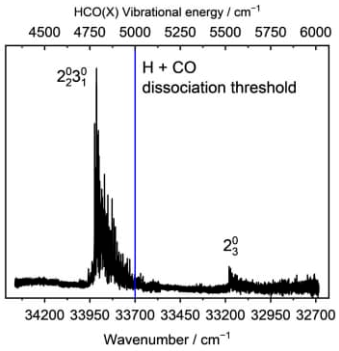

Fig. 1 LIF spectrum of the HCO fragment in the dissociation threshold region.

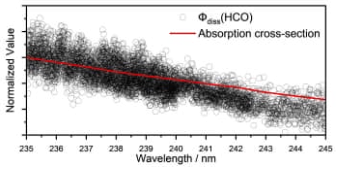

Fig. 2 Photofragment excitation spectra of HCO in the longer photolysis wavelength region

The formation of HCO(0, 2, 1) energetically limits the HCO(X) + $N(CH_3)_2$(X) pairs in the electronic ground states. The $n\pi^*$ state theoretically predicted to be located near 220 nm is adiabatically correlated with the HCO(X) + $N(CH_3)_2$(X) product asymptote, whereas theoretical calculations have revealed that the $n\pi^*$ state possesses an energy barrier arising from an avoided crossing. Consequently, the formation of highly vibrationally excited HCO should be inhibited in this channel. Population transfer between the $\pi\pi^*$ and $n\pi^*$ states is facilitated by the non-planar geometry with symmetry-breaking. The results indicates the significant contribution of the twisting of the amide framework in the photoinitiated $\pi\pi^*$ state, which extends in the wavelength region longer than 240 nm. The generation mechanism of the highly vibrationally excited HCO intermediate over the dissociation threshold is also explained based on the non-planarization of the amide plane.

References

[1] H. D. Hunt and W. T. Simpson *J. Am. Chem. Soc.* **75,** 4540 (1953).
[2] M. Eckert-Maksic *et al. J. Phys. Chem.* **113,** 12582 (2009).
[3] M. Dennis *et al. Phys. Chem. Chem. Phys.* **24,** 28343 (2022).

2P02 High-Resolution Laser Spectroscopy of the $S_1 \leftarrow S_0$ transition of Fluorene: Perturbation analysis in the S_1 state

(Kobe University) KASAHARA Shunji, MINIK Luke, KURODA Shinji

High-resolution laser spectroscopy is a powerful tool for studying the structure and dynamics of excited polyatomic molecules in detail and unambiguously. High-resolution and high-accuracy of the spectral lines enable to observe rotationally-resolved electronic transition and to find out the excited state dynamics through the fairly deviation of the spectral line position, intensity anomaly and the change of the spectral linewidth. In this study, we have observed the rotationally-resolved high-resolution fluorescence excitation spectra of the $S_1 \leftarrow S_0$ transition of fluorene. In the past, the transitions to the lower vibrational levels in the S_1 state were measured by Yi *et al*. [1]. They reported that the $0^0_0 + 204$ cm^{-1} band could not be assigned for large *J*' region.

A collimated molecular beam was obtained by expanding of fluorene vapor with Ar gas through a pulsed nozzle into the vacuum chamber and collimated by using a skimmer (ϕ 2 mm) and slit (0.5 mm). Sub-Doppler fluorescence excitation spectra were measured by crossing a single-mode UV laser beam (Coherent CR699-29 with SpectraPhysics WavetrainSC) perpendicular to a collimated molecular beam. Absolute wavenumber was calibrated with accuracy 0.0002 cm^{-1} by measuring the Doppler-free saturation spectrum of iodine and a fringe pattern of the stabilized etalon.

High-resolution electronic spectra were observed for the $S_1 \leftarrow S_0$ transition of fluorene. The typical linewidth was 25 MHz and the rotational temperature was 15 K. Several vibronic bands from the 0^0_0 band to $0^0_0 + 1228$ cm^{-1} band were measured in the region of 33770-35005 cm^{-1}, and their molecular constants were determined with high accuracy. For the $0^0_0 + 204$ cm^{-1} band, the observed high-resolution spectrum is shown in Fig. 1. We found the local energy shift centered at around *J*'=21 level (Fig.2) and it may be originating from the perturbation with the other vibronic levels in the excited state. We also estimated the molecular constants of the perturbing levels by using the spectral simulation program Pgopher [2].

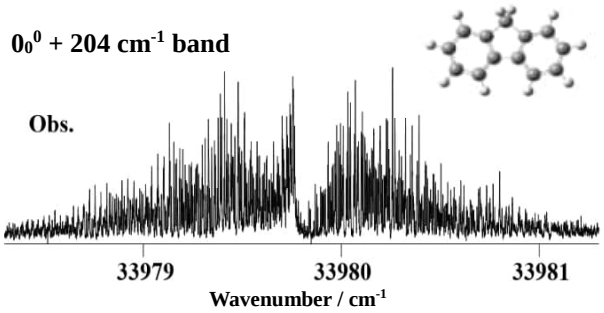

Fig. 1. Observed spectrum of $0^0_0 + 204$ cm^{-1} band.

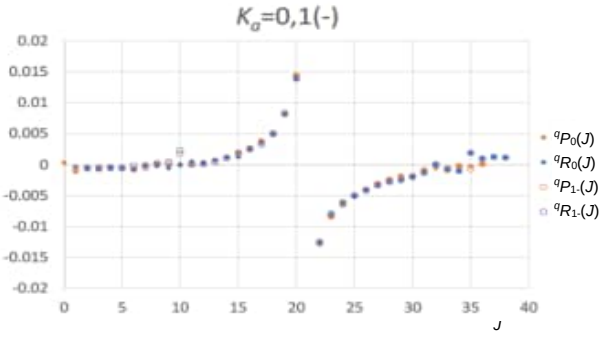

Fig. 2. Energy shift diagram of the $0^0_0 + 204$ cm^{-1} band (only for $K_a = 0$)

[1] J. T. Yi, L. Alvarez-Valtierra, and D. W. Pratt, J. Chem. Phys. **124**, 244302 (2006).

[2] C.M.Western,J.Quant Spectrosc. Radiat. Transf. 186, 221 (2017).

2P03 Photoelectron Circular Dichroism in Chiral Molecules using 21.7 eV HHG light

([1]Department of Applied Physics, Hokkaido University, [2]IMRAM, Tohoku University)
Shuhei Matano [1], Ryunosuke Oshima [1], Shinichiro Minemoto [2], Taro Sekikawa [1]

Chirality plays an important role in reaction selectivity in biological processes. Circular dichroism (CD) in photoabsorption is a well-established method for distinguishing enantiomers. However, the relative difference in absorption coefficients between opposite enantiomers is typically on the order of 10^{-4}, making it challenging to observe chiral-sensitive dynamics. In contrast, the angular distribution of photoelectrons emitted from chiral molecules exhibits a much larger forward-backward asymmetry, often by two orders of magnitude. This phenomenon, known as photoelectron circular dichroism (PECD), provides a promising approach for probing the dynamics of reacting chiral molecules and for understanding enantiomer-dependent reaction processes.

In this study, we develop a PECD measurement system based on high-harmonic extreme-ultraviolet pulses to probe the electronic states of chiral molecules. High harmonics enable direct access not only to excited states but also to valence electronic states. In particular, lower-lying molecular orbitals are sensitive to molecular structure and therefore expected to provide valuable information on chiral dynamics. Thus, PECD measurements using high-harmonic pulses offer a unique opportunity to investigate molecular chirality through electronic-structure-sensitive observables.

High-harmonic pulses were generated by focusing the second harmonic of Ti:sapphire laser pulses into Ar gas. The 7th harmonic of the 400 nm pulse, corresponding to a photon energy of 21.7 eV, was selected using SiC/Mg multilayer mirrors. The linear polarization of the 7th harmonic was then converted into circular polarization using a phase retarder consisting of three SiC mirrors. The circularly polarized 21.7 eV pulses were used for velocity-map imaging (VMI) of photoelectrons, allowing us to observe their angular distributions.

Figure 1(a) shows the PECD images of α-phellandrene, a chiral molecule. The photoelectron intensity exhibits a clear asymmetry along the laser propagation direction, demonstrating the observation of PECD. To obtain the energy dependence of the asymmetry, the photoelectron images were integrated over the radial direction to construct the photoelectron spectra. As shown in Fig. 1(b), the forward-backward asymmetry changes sign between 10 and 14 eV. This suggests that PECD mainly comes from lower-lying molecular orbitals.

1(a)

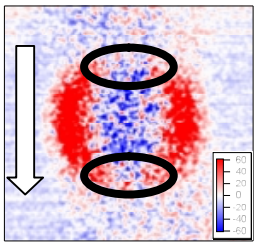

1(b)

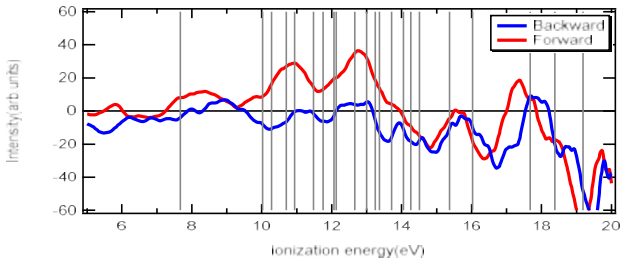

Figure 1.(a) Difference image obtained by subtracting the photoelectron image recorded with right circularly polarized light from that recorded with left circularly polarized light. The upper and lower parts correspond to the backward and forward emission directions, respectively.

(b) PECD spectrum of α-phellandrene. The vertical gray lines indicate the calculated ionization energies of α-phellandrene.

2P04 Unimolecular decomposition of highly excited C_2H_4: Trajectory calculations of product branching

([1]AIST, [2]NYCU) Matsugi, Akira[1]; Matsui, Hiroyuki[2]

The unimolecular decomposition of highly excited ethylene proceeds with molecular or atomic hydrogen elimination channels as follows:

$C_2H_4^* \rightarrow C_2H_2 + H_2$ or $H_2CC + H_2$ (a)

$C_2H_4^* \rightarrow C_2H_3 + H$ or $C_2H_2 + 2H$ (b)

There have been significant discrepancies in the reported product branching fractions from dissociation of $C_2H_4^*$ generated either by photoexcitation or by chemical activation through the self-reaction of methylene (CH_2) radicals. The VUV photodissociation experiments of C_2H_4 consistently reported that both channels (a) and (b) are competitive.[1] On the other hand, shock tube experiments gave much lower value, $\phi_b \approx 0.15$, in the decomposition of chemically activated C_2H_4 formed in the $CH_2 + CH_2$ recombination reaction.[2,3] This is an unexpected contrast because the photoexcitation and recombination are expected to produce C_2H_4 with similar internal energies, and the product branching in both cases is expected to occur on the same, ground-energy potential energy surface, possibly following an internal conversion and intersystem crossing process.

In this study, to investigate possible non-statistical effects, classical trajectory calculations were performed on the ground-state potential energy surface for vibrationally excited and chemically activated C_2H_4.[3] The trajectories were propagated on the full-dimensional, permutationally invariant potential energy surface constructed based on CASPT2-F12/cc-pVTZ-F12 calculations. The calculations gave $\phi_b = 0.6$–0.7 for both vibrational excitation and chemical activation, which is close to those reported in photodissociation experiments but is significantly higher than those observed in the $CH_2 + CH_2$ reaction. Selective excitation of certain vibrational modes of C_2H_4 suggested moderate non-statistical behavior that could potentially affect product branching, but its magnitude was insufficient to quantitatively account for the observed discrepancies. The origin of these discrepancies remains unsolved at present. Potential roles of coupling between the ground- and excited-state dynamics in the product branching are discussed.

[1] S.-H. Lee, Y. T. Lee, and X. Yang, *J. Chem. Phys.* 120 (2004) 10983.

[2] S. Bauerle, M. Klatt, and H. G. Wagner, *Ber. Bunsenges. Phys. Chem.* 99 (1995) 870.

[3] A. Matsugi, T.-C. Chen, H. Matsui, N.-S. Wang, and Y.-P. Lee, *J. Phys. Chem. A* 130 (2026) 2830.

2P05 Simulation of post-ionization population inversion in CO_2^+ in an ultrashort intense laser pulse

([1]School of Science, The University of Tokyo, [2]iTHEMS, RIKEN, [3]I-ALFA, The University of Tokyo) Huang, Siwei[1]; Lötstedt, Erik[2]; Yamanouchi, Kaoru[1,3]

1. Introduction

When CO_2^+ is irradiated with ultrashort intense mid-IR laser pulses at ~1300 nm, unidirectional emission at ~340 nm originating from the $\tilde{A}^2\Pi_u - \tilde{X}^2\Pi_g$ emission of CO_2^+ is generated [1]. To reveal the mechanism of the population transfer processes among the electronics states of CO_2^+ in an ultrashort laser field, resulting in the lasing type emission, we simulate the population transfer dynamics among the four lowest electronic states of CO_2^+ in an intense ultrashort laser pulse (λ = 300−1300 nm) and predict the emission spectrum of CO_2^+ based on the vibronic population differences and the oscillator strengths of the electronic transitions among the four lowest electronic states.

2. Methods

Assuming that CO_2^+ created at the peak of an ultrashort laser pulse keeps linear geometry, we calculate the time-dependent populations in the vibrational levels in the four lowest electronic states of CO_2^+ by solving the time-dependent Schrödinger equation,

$$i\hbar\frac{\partial}{\partial t}\psi(r_1,r_2,t) = \left(\boldsymbol{T}(r_1,r_2) + \boldsymbol{V}(r_1,r_2) + E(t)\left(\cos\theta\,\boldsymbol{D}_{\parallel}(r_1,r_2) + \sin\theta\,\boldsymbol{D}_{\perp}(r_1,r_2)\right)\right)\psi(r_1,r_2,t),$$

where $\psi(r_1,r_2,t)$ is the time-dependent vibronic wave packet, r_1 and r_2 are the two C-O distances, $\boldsymbol{T}(r_1,r_2)$ is the kinetic energy operator, $\boldsymbol{V}(r_1,r_2)$ represents the potential energy operator, θ is the alignment angle between the O-C-O molecular axis and the laser polarization direction, $\boldsymbol{D}_{\parallel}(r_1,r_2)$ and $\boldsymbol{D}_{\perp}(r_1,r_2)$ refer respectively to the parallel and perpendicular components of the transition dipole moment, and $E(t)$ is the linearly polarized laser field with a Gaussian envelope whose FWHM is Δt = 28 fs. The potential energy surfaces of the four electronic states and the transition dipole moments among them are obtained by the CASSCF (11e,9o) method with the aug-cc-pVTZ basis set in Molpro [2].

3. Results and Discussion

The population in the $\tilde{C}^2\Sigma_g^+(0,0)$ state becomes the largest at 406 nm, suggesting that the two-photon $\tilde{C}^2\Sigma_g^+ - \tilde{X}^2\Pi_g$ transition contributes to the $\tilde{C}^2\Sigma_g^+ - \tilde{A}^2\Pi_u$ and $\tilde{C}^2\Sigma_g^+ - \tilde{B}^2\Sigma_u^+$ population inversions. Figure 1 shows the time evolution of the populations in the six most occupied vibrational levels in the four electronically excited states of CO_2^+ exposed to a laser pulse (λ = 406 nm, Δt = 28 fs) at the laser field intensity of I = 3.5×10^{14} W/cm^2 and θ = 45°. The population is first transferred to the $\tilde{A}^2\Pi_u$ and $\tilde{B}^2\Sigma_u^+$ states, and then, to the $\tilde{C}^2\Sigma_g^+$ state, suggesting that the two-photon excitation proceeds in a stepwise manner from the $\tilde{X}^2\Pi_g(0,0)$ state via the intermediate $\tilde{A}^2\Pi_u$ and $\tilde{B}^2\Sigma_u^+$ states. After the light-molecule interaction period, the $\tilde{C}^2\Sigma_g^+ - \tilde{A}^2\Pi_u$ and $\tilde{C}^2\Sigma_g^+ - \tilde{B}^2\Sigma_u^+$ population inversions are achieved. The resultant emission spectrum is calculated as $f_{ij}(\omega_{ij}) \times \Delta p_{ij}$ using the oscillator strength $f_{ij}(\omega_{ij})$ at the angular frequency ω_{ij} between the i-th and j-th vibronic states at ω_{ij} and the final population difference Δp_{ij}. It is revealed that the $\tilde{C}^2\Sigma_g^+(0,0) \rightarrow \tilde{B}^2\Sigma_u^+(0,0)$ emission at 750 nm and the $\tilde{C}^2\Sigma_g^+(0,0) \rightarrow \tilde{B}^2\Sigma_u^+(1,0)$ emission at 827 nm are ideal candidates for the lasing lines of CO_2^+.

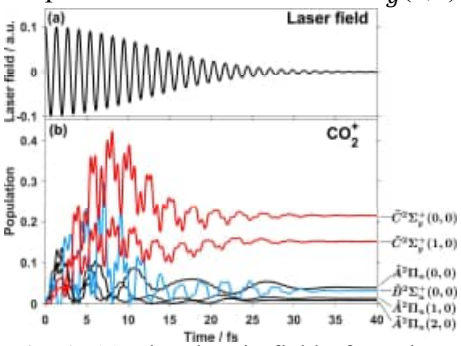

Fig. 1. (a) The electric field of an ultrashort intense laser pulse (λ = 406 nm, Δt = 28 fs, I = 3.5×10^{14} W/cm^2). **(b)** Time-dependent populations of CO_2^+ in the six vibronic states during the interaction with the laser field **(a)** at θ = 45°.

References

[1] W. Chu et al., *EPL*, **97**, 64004 (2012).

[2] H. -J. Werner, et al., *J. Chem. Phys.* **152**, 144107-1–24 (2020).

2P06 Relaxation dynamics via the S_1 state of Ag_3^- probed by time-resolved photoelectron imaging

(Kyushu University) Y. Kusaba, Y. Aoki, Y. Suzuki, Y. Ushiki, M. Shimizu, Y. Toyama, A. Terasaki, T. Horio

Time-resolved photoelectron spectroscopy (TRPES) [1] and imaging (TRPEI) [2] enable the exploration of photoinduced dynamics in molecules, clusters, and their anionic species. The application of TRPES to metal cluster anions was demonstrated by Ganteför et al. in 1998, where dissociation dynamics of photoexcited gold trimer anions were probed with femtosecond (fs) time resolution [3]. At that time, however, the data acquisition rate in TRPES experiments was typically limited to several tens of Hz, making it rather difficult to obtain a large number of time-dependent photoelectron spectra. Recently, our group has developed an anion photoelectron imaging setup capable of simultaneously measuring photoelectron kinetic energy and angular distributions with ultrahigh efficiency [4,5]. In the present work, we apply this setup to TRPEI to investigate the relaxation dynamics via the $S_1(^1\Sigma_u^+)$ state of silver trimer anion, Ag_3^-.

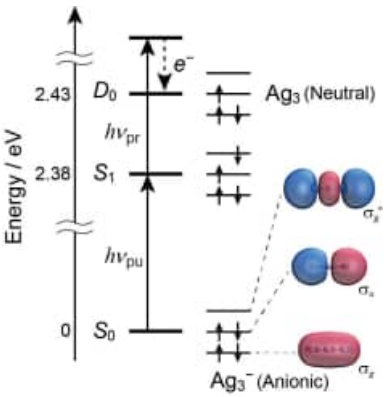

Fig. 1 Excitation scheme for probing the relaxation dynamics of the S_1 state of Ag_3^-.

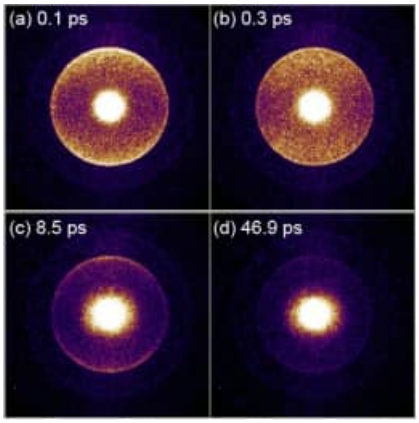

Fig. 2 Photoelectron 2D projections for Ag_3^- obtained at the pump-probe delay time of (a) 0.1, (b) 0.3, (c) 8.5, and (d) 46.9 ps.

Size-selected Ag_3^- anions were generated using a magnetron sputtering cluster ion source combined with a quadrupole mass filter. The continuous ion beam was converted into a pulsed (bunched) beam using a potential switch synchronized with tunable fs pulses from an optical parametric amplifier, pumped by an Yb:KGW regenerative amplifier operating at a repetition rate of 100 kHz. The bunched Ag_3^- anions were directed into a velocity-map imaging electrode assembly, where they were irradiated with visible fs pulses at 520 nm (2.38 eV) to induce the $S_1(^1\Sigma_u^+) \leftarrow S_0(^1\Sigma_g^+)$ transition [6]. The relaxation dynamics of the $S_1(^1\Sigma_u^+)$ transient state were probed by single-photon detachment using time-delayed fs pulses at 1030 nm (1.20 eV) (see Fig. 1 for the excitation scheme). Two-dimensional (2D) projections of photoelectron distributions were recorded using an event-based vision sensor, while systematically varying the pump-probe delay time, Δt. Our setup enables ultrafast (< 1 min.) acquisition of a photoelectron 2D projection at each delay time, significantly reducing the experimental workload in TRPEI measurements for anions. Figures 2(a)-(d) show representative 2D projections obtained at Δt = 0.1, 0.3, 8.5, and 46.9 ps, demonstrating that the sub-picosecond dynamics of photoexcited Ag_3^- anions were successfully captured. Discussion on the relaxation mechanism will be presented in the poster session.

【References】

[1] A. Stolow et al., *Chem. Rev.* **104**, 1719 (2004). [2] T. Suzuki, *Annu. Rev. Phys. Chem.* **57**, 555 (2006). [3] G. Ganteför et al., *J. Electron Spectrosc. Relat. Phenom.* **88-91**, 35 (1998). [4] T. Horio et al., *Rev. Sci. Instrum.* **93**, 083302 (2022). [5] T. Horio et al., *J. Chem. Phys.* **162**, 026101 (2025). [6] S. Kawamura et al., *J. Phys. Chem. A* **127**, 6063 (2023).

2P07 Microsolvation effects on photodissociation dynamics of the hemibonded $(H_2S)_2^+$ ioncore

(Tohoku University) Shioura Mitsuaki, Koshiba Takumi, Kanno Manabu, Misaizu Fuminori, Fujii Asuka

A hemibond is a non-classical covalent bond that forms between a radical and a neutral species. In H_2S radical cation clusters, $(H_2S)_n^+$, a hemibonded ioncore $(H_2S)_2^+$ is formed, which is solvated by H_2S molecules via hydrogen bonds [1,2]. These clusters exhibit a σ-σ* transition of the hemibond in the UV to visible region, which would induce direct dissociation of the ioncore. However, the photodissociation dynamics of the microsolvated ioncore remains poorly understood. In this study, we performed photofragment ion imaging experiments for $(H_2S)_n^+$ (n = 2-3) to investigate the photodissociation dynamics of the hemibonded $(H_2S)_2^+$ ioncore and its microsolvation effects.

The $(H_2S)_n^+$ radical cation clusters were generated by supersonic expansion of a 5:95 H_2S/Ar gas mixture, followed by electron impact ionization. Using a time-of-flight mass spectrometer equipped with a double linear reflectron [3], size-selected clusters were irradiated with linearly polarized laser light at 355 nm. Photofragments were detected as an image using a position-sensitive detector. We observed angular distributions and recoil velocities using the pBASEX method.

For $(H_2S)_2^+$, H_2S^+ was the primary photofragment. The corresponding image (**Fig. 1a**) is elongated along the laser polarization direction ***E***, suggesting that the dissociation axis is parallel to the transition dipole moment μ. This feature is consistent with the σ-σ* transition, and thus the photodissociation of $(H_2S)_2^+$ can be explained by the direct dissociation.

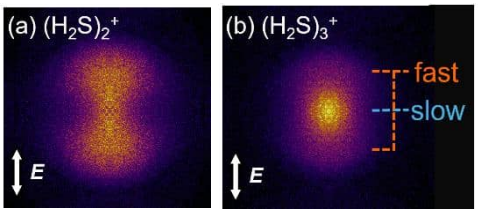

Fig. 1 Observed images of photofragments of (a) $(H_2S)_2^+$ and (b) $(H_2S)_3^+$

For $(H_2S)_3^+$, both H_2S^+ and H_3S^+ were observed as photofragments with nearly equal intensities. **Figure 1b** shows the image obtained from the detection of both H_2S^+ and H_3S^+, as the mass resolution was insufficient to distinguish between these fragments. The image consists of two components. A fast component is elongated along the ***E*** direction. Furthermore, its image size is similar to that of n = 2, indicating that their translational energy distributions are nearly identical. This implies that the H_2S^+ fragment is generated via direct dissociation, and that the solvent H_2S molecule has a negligible effect on this direct dissociation process of $(H_2S)_3^+$ (**Fig. 2a**). On the other hand, a slow component is isotropic and can be assigned to the H_3S^+ fragment, implying that a different process competes with the direct dissociation leading to H_2S^+. To obtain a more detailed picture of the generation of H_3S^+, we performed molecular dynamics simulations. The results reveal that H_3S^+ originates from proton transfer to the solvent H_2S accompanied by direct dissociation (**Fig. 2b**).

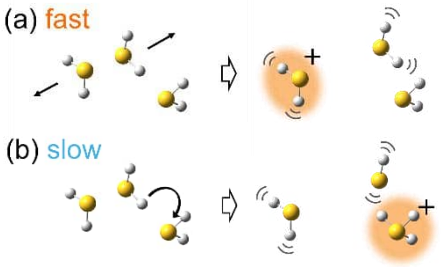

Fig. 2 Primary photodissociation processes of (a) fast and (b) slow components of $(H_2S)_3^+$

[1] D. Wang *et al.*, *Chem. Sci.* **8**, 2667 (2017). [2] M. Shioura *et al.*, *Phys. Chem. Chem. Phys.* **28**, 262 (2026).
[3] K. Okutsu *et al.*, *Rev. Sci. Instrum.* **88**, 053105 (2017).

2P08 High-resolution laser spectroscopy of the A-X transition of $^{14}NO_2$ radical

([1]Faculty of Science, Fukuoka University, [2]Faculty of Science, Kobe University, [3]Center for Life Photonic Innovation, Kobe University)
Tada, Kohei[1]; Misono, Masatoshi[1]; Yoshizawa, Takumi[2]; Kishigami, Ko[2]; Kasahara, Shunji[3]

Nitrogen dioxide (NO_2) is a prototypical open-shell molecule for investigating intramolecular interactions, such as vibronic and spin-orbit interactions, in polyatomic molecules. NO_2 exhibits broad absorption bands extending from the near-infrared to the ultraviolet region, primarily arising from electronic transitions from the ground X $^2A_1$ state to the first excited A $^2B_2$ state.

We have recorded hyperfine-resolved high-resolution fluorescence excitation spectra of $^{14}NO_2$ in the 16218 cm^{-1} band and 16320 cm^{-1} band, by crossing a jet-cooled molecular beam with a single-mode ring dye laser beam at right angles. Unambiguous rotational assignments were obtained based on ground state combination differences among the hyperfine levels using the latest HITRAN database [1]. For the 16218 cm^{-1} band, the dark C $^2A_2$ (v = 0) state lies close in energy to the upper $^2B_2$ vibronic state of this band [2]. Several anomalies were identified in this band, which are interpreted in terms of spin-orbit coupling between the $^2B_2$ and C $^2A_2$ (v = 0) states. The effective molecular constants for both states were determined. In the 16320 cm^{-1} band, multiple vibronic states overlap, as previously reported [3], and we determined the molecular constants for the individual states.

We recorded rotationally-resolved, Doppler-limited absorption spectra of $^{14}NO_2$ in the 12658 cm^{-1} band, by using a room-temperature gas cell and a single-mode Ti:sapphire laser. The upper $^2B_2$ state has been assigned to the A $^2B_2$ (0, 4, 0) vibronic state [4]. One of the advantages of cell spectroscopy is the ability to observe rotational lines with higher rotational quantum numbers, thereby enabling more reliable determination of molecular constants than in low-temperature experiments. Rotational assignments were obtained by referring to the previous studies [5, 6] and by using ground state combination differences. The effective molecular constants for the upper A $^2B_2$ (0, 4, 0) state were determined. These results provide a spectroscopic basis for future gas-cell Doppler-free studies in this energy region.

References

[1] I.E. Gordon, L.S. Rothman, et al., J. Quant. Spectrosc. Radiat. Transfer **353**, 109807 (2026).
[2] K. Aoki, K. Hoshina, and K. Shibuya, J. Chem. Phys. **105**, 2228 (1996).
[3] H. Nagai, K. Shibuya, and K. Obi, J. Chem. Phys. **93**, 7656 (1990).
[4] E. Leonardi and C. Petrongolo, J. Chem. Phys. **106**, 10066 (1997).
[5] C.A. Biesheuvel, J. Bulthuis, M.H.M. Janssen, S. Stolte, and J.G. Snijders, J. Chem. Phys. **109**, 9701 (1998).
[6] C.A. Biesheuvel, J. Bulthuis, M.H.M. Janssen, S. Stolte, and J.G. Snijders, J. Chem. Phys. **112**, 3633 (2000).

2P09 An analysis of charge migration in the McLafferty rearrangement utilizing natural reaction orbital method

([1]Grad. Sch. Chem. Sci. Eng., Hokkaido Univ., [2]Grad. Nanobio., Yokohama City Univ., [3]Dep. Chem., Fac. Sci., Hokkaido Univ., [4]WPI-ICReDD, Hokkaido Univ.)
Tatsuhiro Nakanishi,[1] Mitsuo Takayama,[2] and Tetsuya Taketsugu[3,4]

McLafferty rearrangement is a reaction widely used in mass spectrometry and plays a crucial role in the structural analysis of organic compounds. It is known that, in the McLafferty rearrangement, different fragment ions are formed through either a charge retention (CR) or a charge migration (CM) process (Fig. 1). Recently, the reaction mechanism has been studied using femtosecond time-resolved measurements, *ab initio* molecular dynamics, and the GRRM program [1,2]. However, the details of the charge and spin redistributions that lead to the formation of different fragment ions remain unclear. In this study, we theoretically investigated the charge migration process in the McLafferty rearrangement using the natural reaction orbital (NRO) method [3], which visualizes electron flow accompanying structural changes in molecules.

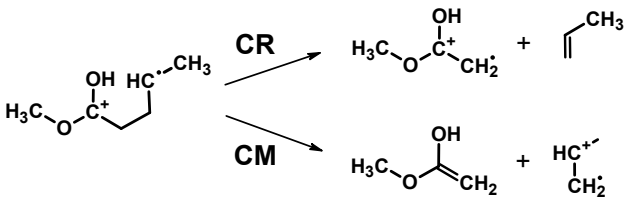

Fig. 1. Two processes of the McLafferty rearrangement.

First, we calculated the intrinsic reaction coordinate (IRC) from the transition state reported in the previous study [2]. Then, natural population analysis was carried out for each structure along the IRC. The results showed that spin transfer occurs in two regions. In the former region, spin transfer from Cγ to Cα occurs together with Cα-Cβ bond cleavage. In the latter region, spin transfer from Cγ to Cβ occurs together with charge transfer from the enol moiety to the propene moiety. In this latter region, NRO analysis was performed to visualize the electron flow accompanying the charge transfer. Figure 2 shows the results of the NRO analysis. In the figure, electron density decreases in the cyan region and increases in the yellow region, indicating electron flow from propene to enol. This electron flow corresponds to charge migration in the opposite direction, because electron flow is opposite to positive-charge migration. Based on these results, the mechanisms leading to the formation of different fragment ions are as follows. In the CR process, the system deviates from the IRC and cleaves into two fragments before charge transfer occurs. In contrast, in the CM process, the system follows the IRC, and charge transfer occurs along the pathway [4].

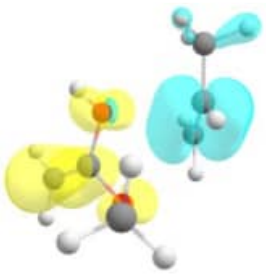

Fig. 2. Electron flow in the McLafferty rearrangement.

[1] J. Stamm et al., *J. Phys. Chem. Lett.*, **14**, 10088 (2023).

[2] M. Takayama, M. Hashimoto, K. Ohshimo, F. Misaizu, M. Ubukata, and K. Nagatomo, *PCCP*, **27**, 261 (2025).

[3] S. Ebisawa, M. Hasebe, T. Tsutsumi, T. Tsuneda, and T. Taketsugu, *PCCP*, **24**, 3532 (2022).

[4] **T. Nakanishi**, T. Taketsugu, and M. Takayama, submitted.

2P10 Theoretical Design of Unactivated Arene Conversion Reactions Using Triazene Compounds

([1]Yamaguchi University, [2]Chiba Institute of Technology) Ayana Nagano[1], Shusuke Kokubu[2], Kazuhito Yamakawa[2], Ryosuke Haraguchi[2], Yosuke Sumiya[1]

1. Introduction

Recently, increasing attention has been directed towards the reaction development initiated by the (3+2) cycloaddition of the 1,3-diazazonia allene (DAAA) cation **1**, generated from triazene compounds, with unsaturated bonds of unactivated arenes **2** and simple alkenes **3** (Scheme 1) [1-3]. These reactions proceed under catalyst-free and mild conditions; however, certain substrates exhibit low reactivity and/or selectivity, necessitating a comprehensive understanding of the reaction scope. Furthermore, although the DAAA cation is prone to decomposition, its decomposition mechanism remains unclear. In this study, we systematically investigate the reactivity and selectivity of the (3+2) cycloaddition of the DAAA cation with various functionalized arenes, as well as the decomposition mechanism of the DAAA cation using global reaction route mapping (GRRM) program [4]. All electronic state calculations are done at the ωB97X-D/def2-SV(P) level using Gaussian 16 program.

2. Results

We estimated the activation free energy for the reaction between the DAAA cation **1** of R_1 = Ph, Dipp (2,6-diisopropylphenyl) and arenes **2** bearing various functional groups at R_2, and investigated the reactivity and selectivity based on the ratio of rate constants obtained by transition state theory. As a result, we found that introducing an electron-donating functional group into arene **2** enhances reactivity, while introducing a functional group with a conjugated structure into arene **2** improves selectivity. As for the DAAA cation decomposition, a four-step mechanism was identified, in which the reaction of two DAAA cations yields two diazonium salts and an azo compound (Scheme 2). Further details regarding the mechanism and activation energy will be presented.

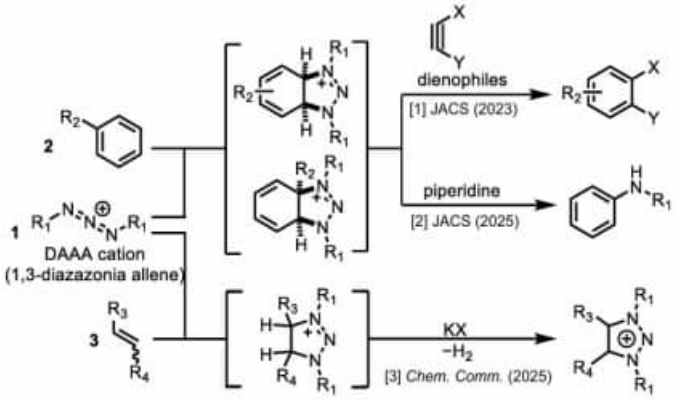

Scheme 1. Reaction examples by a (3+2) cycloaddition reaction using triazene.

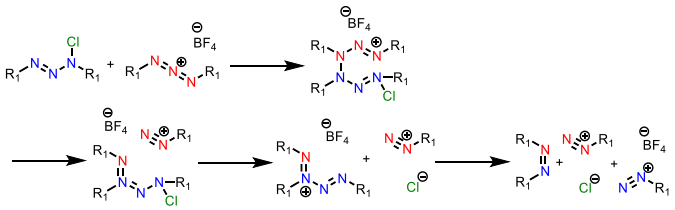

Scheme 2. Decomposition reaction of the DAAA cation.

[1] S. Pradhan, *et al*., *J. Am. Chem. Soc*., **145**, 12214 (2023). [2] S. Pradhan, *et al*., *J. Am. Chem. Soc*., **147**, 27731 (2025). [3] K. Yamakawa, *et al*., *Chem. Comm*., **61**, 8387 (2025). [4] S. Maeda, *et al*., *J. Comput. Chem*., **39**, 233 (2018).

2P11 Theoretical study on the thermal dissociation reaction of 3-methylaminopropylamine

(Meijo Univ.) KANNO Nozomu

3-methylaminopropylamine (MAPA, $CH_3NHCH_2CH_2CH_2NH_2$) is a candidate low-toxicity alternative fuel used as a spacecraft hypergolic bipropellant.[1] In the present study, the thermal dissociation reactions of MAPA have been investigated using quantum chemical calculations and microcanonical variational transition state theory (μVTST) combined with master-equation analysis.

The optimized structures and energies of the reactant and products were obtained at the CBS-QB3 level of theory. Microcanonical rate coefficients, $k(E)$, were evaluated on the basis of μVTST. The minimum-energy paths for the μVTST calculations were traced by partial geometry optimizations at the MRCISD+Q/aug-cc-pVTZ//CASPT2(2e, 2o)/cc-pVDZ level of theory. Product-specific rate coefficients were evaluated by solving the steady-state unimolecular master equation.

The overall energy diagram for the singlet ground-state MAPA dissociation reactions is shown in Figure 1. In general, the C/N–C bond dissociation energies (BDEs) are lower than the C/N–H BDEs. For the C/N–H dissociation channels, the pathways leading to α-amino-alkyl radical formation show lower energies due to SOMO delocalization arising from orbital interaction with the lone-pair orbital on the adjacent N atom.

Figure 2 shows the high-pressure limiting rate coefficients for the MAPA dissociation reactions. Consistent with the trend of BDEs, the dominant reaction pathways were found to be the C/N–C bond-fission channels, followed by the α-amino-alkyl radical and H-atom formation channels. At 1 atm in N_2 diluent, the calculated rate coefficients would reach their high-pressure limit below 1000 K.

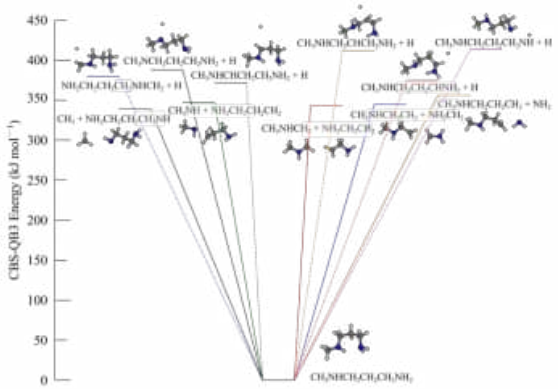

Fig. 1 PES of the MAPA dissociation reactions calculated at the CBS-QB3 level of theory.

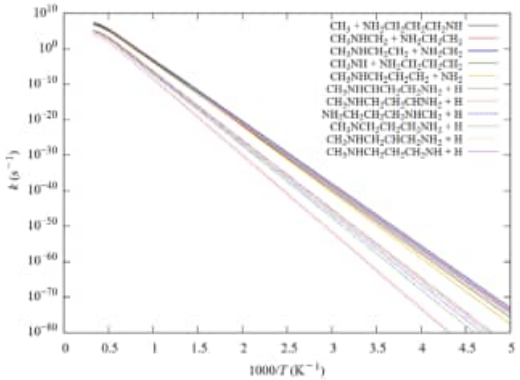

Fig. 2 Arrhenius plots of the high-pressure limiting rate coefficients for MAPA dissociation reactions.

References:

1. Hatai, K. and Nagata, T., *Aerospace*, **2022**, *9*, 129.

2P12 What Underlies the Woodward-Hoffmann rules? A Reaction Analysis Based on Orbital Energies

([1]Grad. Sch. Chem. Sci. Eng., Hokkaido Univ., [2]WPI-ICReDD, Hokkaido Univ., [3]Fac. Sci., Hokkaido Univ., [4]Grad. Sch. System Informatics, Kobe Univ.) Masaya Tsuruta,[1] Tsuyoshi Mita,[2] Tetsuya Taketsugu,[2,3] and Takao Tsuneda[2,4]

[Introduction] The Woodward-Hoffmann (WH) rules [1] constitute a theory that explains the mechanisms of pericyclic reactions based on frontier orbitals and orbital symmetry correlation diagrams. In recent years, however, the existence of reaction systems that do not obey the WH rules and the critical role of non-frontier orbitals have been reported [2,3]. Nevertheless, many aspects remain unclear regarding the detailed mechanisms by which non-frontier orbitals drive reactions, as well as the physical significance of orbital phase continuity. Therefore, in this study, we attempted to elucidate these unresolved issues using Reactive Orbital Energy Theory (ROET) [4], an electronic theory that focuses on the energy changes of individual molecular orbitals. In addition to providing a theoretical foundation for the curved arrows used in organic electron theory [5], ROET has demonstrated that the Hellmann-Feynman force exerted by identified reactive orbitals acts as a driving force on atomic nuclei [6]. By employing this approach, we aim to provide a new interpretation of pericyclic reactions beyond the conventional orbital-symmetry frameworks.

[Calculation Methods] In this study, we investigated the thermal conrotatory ring-closing reaction of 1,3,5-hexatriene as a WH-rule-forbidden reaction system. The analysis was conducted using intrinsic reaction coordinate (IRC) calculations and orbital tracking (ωB97X-D/cc-pVDZ for IRC calculations and ωB97X-D/cc-pVTZ for orbital tracking).

[Results and Discussion] The analysis revealed a HOMO-LUMO crossing in the vicinity of the transition state (TS). This crossing is directly linked to the activation barrier, suggesting that the Hellmann-Feynman force arising from the reactive orbital energy acts in the direction opposite to the reaction progress after the crossing and thereby increases the barrier. During the presentation, we will report detailed data, including changes in reactive orbitals, as well as additional examples of reaction systems that do not conform to the WH rules.

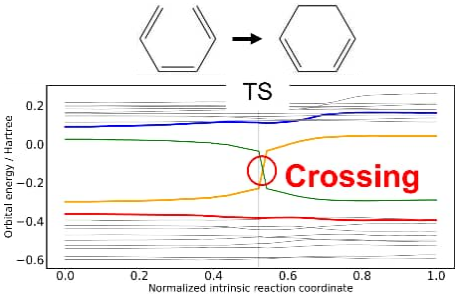

Fig. Orbital tracking diagram for the thermally forbidden cyclization of 1,3,5-hexatriene.

[References]

[1] R. B. Woodward, *et al.*, *J. Am. Chem. Soc.,* **87**, 395 (1965). [2] G. A. Kukier, *et al.*, *J. Am. Chem. Soc.*, **143**, 21694 (2021). [3] Q. Zhou, *et al.*, *J. Org. Chem.*, **89**, 1018 (2024). [4] T. Tsuneda, *et al.*, *J. Comput. Chem.* **35**, 1093 (2014). [5] T. Tsuneda, *et al.*, *J. Comput. Chem.,* **44**, 93 (2023). [6] T. Tsuneda, *et al.*, *Comm. Chem.*, **8**, 158 (2025).

2P13 Quantifying the Contribution of Nonreactive Modes to Reaction Dynamics in Phase Space: Analytical Prediction of the Passage Time τ near a Saddle Point

([1]Hokkaido University, [2]AIST) Kurahashi Ryo[1], Li Jizhou[1], Tanaka Ryoichi[1], Umer Umair[1], Nagahata Yutaka[1], Mizuno Yuta[2], Komatsuzaki Tamiki[1]

Transition state theory (TST) describes reaction rates as flux through a dividing surface, but real molecular systems often exhibit nonstatistical behaviors for which thermodynamic laws alone are insufficient and dynamical effects are essential. Examples include mode-selective reactivity and non-RRKM behavior arising from incomplete intramolecular vibrational energy redistribution (IVR). Understanding such reactions requires a trajectory-based dynamical approach. Even in such a trajectory-based formulation, however, a reliable framework requires a dividing surface free from recrossing—the long-standing difficulty in TST in which trajectories cross the dividing surface multiple times before being "captured" in the product state.

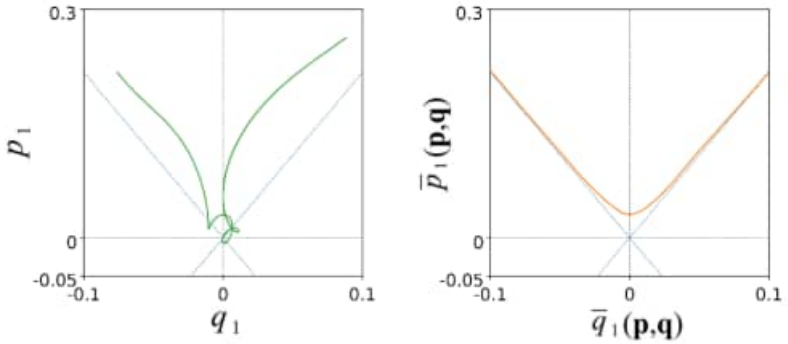

Fig. 1. Phase portrait of the reactive mode for a representative trajectory near the HCN⇌CNH saddle, in normal-mode coordinates (left) and NF coordinates (right). The LCPT transformation yields pure hyperbolic motion.

Lie canonical perturbation theory (LCPT) provides such a framework: by transforming the Hamiltonian near a first-order saddle into a normal form (NF) that depends only on conserved action variables $\bar{\mathbf{J}}$, it yields a recrossing-free dividing surface in phase space. $\bar{\mathbf{J}}$ are the classical-mechanical measures of vibrational excitation in each mode. In NF coordinates, the reactive mode $\bar{q}_1(\mathbf{p},\mathbf{q})$ decouples from the bath modes and undergoes pure hyperbolic motion (Fig. 1), making it possible in the phase-space picture to define a passage time for an individual trajectory—an object that has no natural counterpart in configuration-space TST. We define the local passage time τ as the time the trajectory spends within the symmetric domain $|\bar{q}_1(\mathbf{p},\mathbf{q})| \le L$ around the saddle.

What is less obvious is that τ admits a closed-form analytical expression,

$$\tau(\bar{\mathbf{J}}(\mathbf{p},\mathbf{q});L) = \frac{2\tanh^{-1}\left[\left(1+\frac{2|\bar{J}_1(\mathbf{p},\mathbf{q})|}{|\omega_1|L^2}\right)^{-\frac{1}{2}}\right]}{|\bar{\omega}_1(\bar{\mathbf{J}}(\mathbf{p},\mathbf{q}))|}$$

determined entirely by the initial action variables, with no trajectory integration required. Here $\bar{\omega}_1(\bar{\mathbf{J}})$ is the renormalized reactive-mode frequency, purely imaginary because the local potential is hyperbolic. The bath-mode actions enter τ exclusively through $|\bar{\omega}_1(\bar{\mathbf{J}}(\mathbf{p},\mathbf{q}))|$. This effect is entirely absent in the harmonic frame, where harmonic fundamental ω_1 is a fixed constant carrying no information about bath-mode excitation.

Applied to the HCN⇌CNH isomerization, τ agrees with direct trajectory calculations to high accuracy. Bath-mode excitation suppresses the reaction by reducing $|\bar{\omega}_1(\bar{\mathbf{J}})|$, with mode-resolved differences traceable to the nonlinear coupling coefficients of the NF Hamiltonian. The framework extends NF beyond reaction discrimination to a predictive, analytical description of mode-selective and nonstatistical reaction dynamics.

2P14

Development of a quadratic convergence two-point search algorithm using the Dynamical NEB method

([1]Tokyo Metropolitan University) [1]Kanazawa Ryosuke, [1]Nakatani Naoki, [1]Nakatani Kaho

Introduction

The NEB (Nudged Elastic Band) method[1] is widely used for reaction route analysis, particularly for transition state search in solid and/or surface reactions. A key feature is that the NEB method requires only the 1st derivatives of each image, in which forces parallel to the reaction route are replaced by spring forces. Though this projection preserves the interval between two images, the Hessian of the elastic band is no longer Hermitian (e.g., the 2nd derivative is discontinuous). As a result, an effective quadratic-convergence algorithm, such as the quasi-Newton method, is not applicable to optimize images, so the NEB calculation requires a large number of steps to find the optimal reaction route. In this study, we developed the mechanical NEB method (mNEB), in which no projection is used to account for image forces, thereby keeping the Hessian well-conditioned, and demonstrated it using efficient quadratic search algorithms.

Method

In the mNEB method, variable force constants are set for each image pair so that they have equivalent intervals along a model potential function. For instance, we chose a model potential function of the form (Fig. 1).

$$V(x) = \left(E_a - \frac{E_f}{2}\right)e^{-8x^2} + \frac{E_f}{1+e^{-16x}} \qquad (1)$$

where E_a is the estimated activation energy, and E_f is the reaction energy. Note that force constants are recursively determined from the low-energy side.

Result

We performed benchmark calculations for 24 gas-phase molecular reactions in the Baker list[2], using the HF/3-21G method. To compare with energy-weighted NEB (EW-NEB)[3], we examined the spring constants 0.97-9.72 eV/Å for the EW-NEB, and 1.0 eV/Å at the low-energy image for the mNEB. Initial geometries were generated using the IDPP method[4], and we optimized images using the quasi-Newton method with the L-BFGS algorithm to estimate the approximate Hessian. As shown in Table 1, mNEB demonstrated superior performance to EW-NEB in terms of robustness and fastness. This is the result of not destroying the Hessian.

Table 1: Comparison of the number of force evaluations required to converge when pathways using EW-NEB and mNEB. The median was calculated by treating non-converged cases as infinite, while the mean was calculated using only converged cases for both methods.

	CI-NEB	mNEB
Success rate	79	100
median	1062	430
average	1461	514

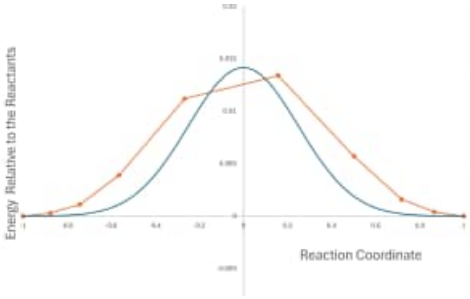

Figure 1: The shape of the estimated PES (blue) as expressed by Equation 1, and the layout of the simulation results (orrange) obtained by calculating the mNEB using the spring constants derived from estimated PES.

References: [1] H. Jónsson et al., *Class. Quantum Dyn. Condens. Phase Simul.*, 385 (1998). [2] J. Baker et al., *J. Comput. Chem.*, **17**, 888 (1996). [3] V. Ásgeirsson et al., *J. Chem. Theory Comput.*, **17**, 4929 (2021). [4] S. Smidstrup et al., *J. Chem. Phys.*, **140**, 214106 (2014).

2P15 Electronic Driving Factors in Outer-Sphere Electron Transfer Reactions: A Reactive Orbital Energy Theory Analysis

([1] Grad. School Chem. Sci. Eng., Hokkaido Univ., [2] Fac. Sci., Hokkaido Univ.,
[3] WPI-ICReDD, Hokkaido Univ., [4] Grad School of System Informatics, Kobe Univ.)
Daisuke Yamada[1], Masaya Tsuruta[1], Tetsuya Taketsugu[2,3], Takao Tsuneda[3,4]

[Introduction]

Outer-sphere electron transfer reactions proceed without the direct formation or cleavage of chemical bonds between reactants, maintaining their coordination spheres intact. Marcus theory effectively explains electron transfer kinetics via solvent reorganization[1], but lacks a microscopic understanding of the driving electron movement.

Reactive Orbital Energy Theory (ROET) is a novel electronic theory of reactions that quantitatively analyzes the e lectron movement driving a reaction based on the orbital energy changes of occupied and unoccupied orbitals, quantitatively determined by long-range corrected (LC) DFT[2]. It has been shown that the orbital energy gradient of the occupied reactive orbital (ORO), which is most stabilized during the reaction process, provides the maximum electrostatic force acting on the atomic nuclei along the reaction direction[3]. Furthermore, changes in the ORO indicate that electron movement, which closely aligns with the curly arrows used in organic electron theory, acts as the driving factor of the reaction[4].

This study aims to reinterpret outer-sphere electron transfer reactions in aqueous metal complexes from the perspective of reactive electronic theory using ROET analysis.

[Results and Discussion]

The following outer-sphere electron transfer reaction in an aqueous solution was examined as the target reaction:
$[Fe(CN)_6]^{3-}+[Ru(NH_3)_6]^{2+}\rightarrow[Fe(CN)_6]^{4-}+[Ru(NH_3)_6]^{3+}$

We obtained the respective stable structures for the two electronic states corresponding to the reactant and product of the electron transfer reaction, and generated an interpolated path connecting them. Next, we traced the more stable electronic state at each structural point and performed the ROET analysis.

Analysis of the orbital energy changes by ROET revealed that the quasi-degeneracy of the d orbitals (t_{2g}) of the Ru complex is lifted by the electron transfer, splitting them into a stabilized occupied orbital and a destabilized virtual orbital. As a result, the stabilized occupied d orbital was identified as the ORO, demonstrating that this d-orbital splitting is the driving factor of this electron transfer reaction (Fig.). Details, including the effects of solvent water molecules, will be reported during the presentation.

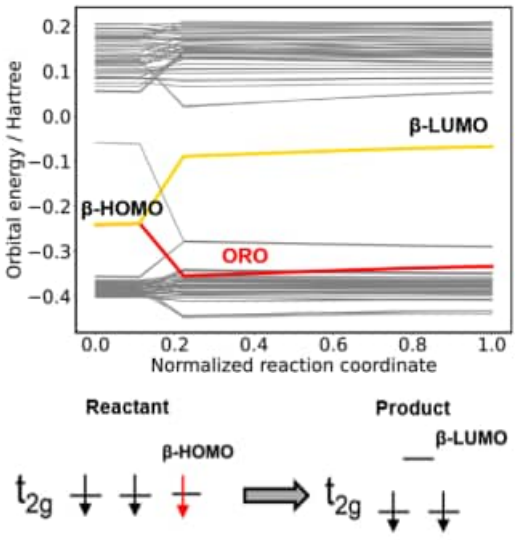

Fig. Energy profile of the β orbitals in the charge-transfer reaction and the corresponding d-orbital splitting pattern of the Ru β orbitals.

【References】

[1] R. A. Marcus, *J. Chem. Phys.*, **1956**, 24, 966.
[2] T. Tsuneda, R. K. Singh, *J. Comput. Chem.*, **2014**, 35, 1093–1100.
[3] T. Tsuneda, T. Taketsugu, *Comm. Chem.*, **2025**, 8, 158(1-7).
[4] T. Tsuneda *et al.*, *J. Comput. Chem.*, **2023**, 44, 93–104.

2P16 Heavy atom tunneling reactions on interstellar icy grain analogs

([1]Hokkaido University, [2]Hiroshima University, [3]IFF CSIC) M. Tsuge,[1,2] G. Molpeceres,[3] N.-E. Sie,[1] and N. Watanabe[1]

Chemical reactions on interstellar icy dust grains are essential for the formation of complex organic molecules (COMs). While quantum mechanical tunneling of hydrogen atoms is widely recognized as a dominant reaction mechanism at low temperatures (~10 K), tunneling reactions involving heavier atoms have been largely neglected in astrochemical reaction networks, despite their well-established significance in low-temperature organic chemistry.

Here, we present experimental evidence that atomic carbon undergoes heavy-atom tunneling mediated reactions on realistic interstellar ice analogs, including amorphous solid water (ASW) and solid carbon monoxide (CO) [1,2]. Using an in situ detection method combining photostimulated desorption combined and resonance-enhanced multiphoton ionization techniques, we show that carbon atoms initially physisorbed on ASW transform into chemisorbed states through a temperature-independent process, consistent with quantum tunneling. This transformation from physisorption to chemisorption states demonstrates that a fraction of carbon atoms are not instantaneously chemisorbed, contrary to conventional astrochemical assumptions.

Extending these studies to solid CO, we find that deposited atomic carbon reacts with CO molecules to form the CCO radical at cryogenic temperatures (≤10 K) via a non-thermal process. The absence of temperature dependence in the reaction kinetics strongly suggests the involvement of tunneling phenomena. Furthermore, subsequent reactions such as CCO + CO → C_3O_2 are inferred to proceed non-thermally as well. We propose that these non-thermal reactions are facilitated by the reorientation of CO molecules within the solid, which is plausibly enabled by quantum tunneling as recently demonstrated experimentally [3].

Together, these results indicate that heavy-atom tunneling involves not only reactive atoms but also the rearrangement of surrounding ice constituents, activating otherwise inaccessible reaction pathways. Heavy-atom tunneling-assisted chemistry on icy grains thus defines a previously overlooked regime of interstellar surface reactions that promotes early C–C bond formation and unsaturated carbon-chain growth. Incorporating such processes into astrochemical models is expected to significantly revise our understanding of carbon chemistry in translucent molecular clouds and protoplanetary disks.

In this presentation, we summarize experimentally identified carbon-driven reaction systems on icy grain analogs and discuss future experimental strategies for decisive verification of heavy-atom tunneling reactions in interstellar environments.

References

[1] Tsuge, M. et al., Nature Astronomy 7, 1362–1371 (2023).

[2] Tsuge, M. et al., Astrophys. J. 993, 177 (2025).

[3] Choudhury, A. et al., Nature 612, 691–696 (2022).

2P17 Molecular orbital signatures in photoelectron circular dichroism of oxirane derivatives studied by a tunnel ionization theory

([1]Grad. Sc. Sci, Nagoya U.; [2] RCMS, Nagoya U.)
Kuroda, Runa[1]; Ogawa, Kazumi[1]; Uchida, Tomohide[1]; Nishimura, Koya[1]; Matsuda, Akitaka[1]; Hishikawa, Akiyoshi[1,2]

[Introduction] Photoionization of a chiral molecule by circularly polarized light exhibits a forward-backward asymmetry in the photoelectron angular distribution along the light propagation direction. The effect, known as photoelectron circular dichroism (PECD), was first demonstrated in single-photon ionization and recently extended to tunnel ionization in intense laser fields (10^{13}–10^{14} W/cm^2) [1]. Our recent studies on (*S*)-methyloxirane (MOX, C_3H_6O) and (*S*)-epichlorohydrin (ECH, C_3H_5OCl) by electron-ion coincidence momentum imaging have revealed that they share the same sign of PECD, despite the fact that these two species have mirror-image structures around the chiral center (Fig. 1(a)). Here we study the tunnel PECD of (*S*)-MOX and (*S*)-ECH with a tunnel ionization theory to clarify the role of the phase structure of the ionizing molecular orbitals as well as the effect of molecular orientation on tunnel PECD.

[Methods] Molecular orbital calculations were performed at the RHF/aug-cc-pVQZ level using the GAMESS package [2]. The highest-occupied molecular orbital (HOMO) wavefunctions, Ψ, thus obtained (Fig. 1 (b)) were expanded by short-range potential wavefunctions at r = 12-20 a.u. to derive the structure factors, which were used to evaluate the probability current density $\mathbf{j}(\mathbf{p},\Psi)$, with $\mathbf{p}$ being the photoelectron momentum, for tunnel ionization calculation by the PPT theory [3]. The ratio of the net photoelectron current along the laser propagation direction y-axis $j_y(p,\Psi)$, to the total photoelectron current $j_r(p,\Psi)$, is employed as a measure of PECD [4].

[Results and Discussion] Fig. 1(d) shows the $j_y(p, \Psi)$ / $j_r(p, \Psi)$ ratio calculated for the HOMO of randomly oriented (*S*)-MOX and (*S*)-ECH in a left-handed circularly polarized field (LCP) at 4.8 × 10^{13} W/cm^2. The calculated results show clear PECD effects, which remain even after the molecular orientation averaging. The calculated PECD shows the same sign for both molecules as observed experimentally [5, 6]. The orientation-resolved PECD shows that the phase structure of HOMO in the asymptotic tunneling region far from the nuclei (see Fig. 1(c)) governs the tunnel PECD. These results suggest that the molecular orbital character, particularly its helicity, determines the sign and magnitude of PECD, rather than the local structure at the chiral center in the tunnel ionization regime.

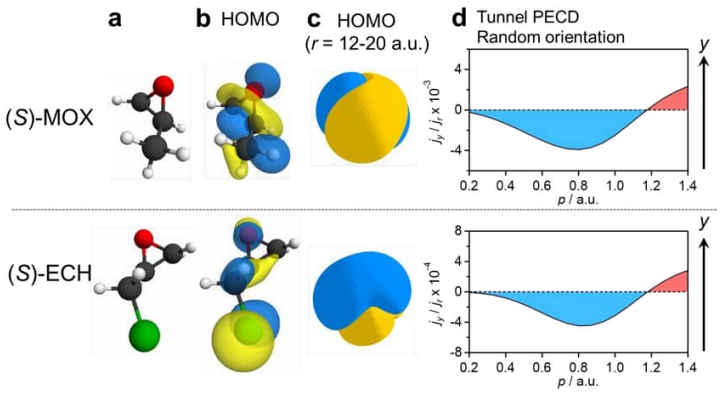

Fig. 1 (a) Geometrical structures, (b) HOMOs, and (c) the HOMO wavefunctions at r = 12-20 a.u. of (*S*)-MOX and (*S*)-ECH. (d) The ratio of $j_y(p, \Psi)$ to $j_r(p, \Psi)$ for the HOMOs of randomly oriented (*S*)-MOX and (*S*)-ECH an LCP at 4.8 × 10^{13} W/cm^2.

[1] K. Fehre *et al.*, J. Phys. Chem. A **123**, 30, 6491 (2019). [2] M. W. Schmidt *et al.*, J. Comput. Chem. 14, 1347 (1993). [3] A. M. Perelomov, V. S. Popov, M. V. Terent'ev, Sov. Phys. JETP **23**, 924 (1966). [4] A. F. Ordonez *et al.*, Phys. Chem. Chem. Phys. **24**, 5720 (2022). [5] R. Kuroda *et al.*, 40th SCKD, 2P07 (2025). [6] K. Ogawa *et al.*, 41th SCKD, 1P08 (2026).

2P18 Experimental determination of N-atom surface diffusion activation energy based on the decay of surface number density due to diffusive recombination reactions

([1]Institute of Low Temperature Science, Hokkaido University,
[2]Graduate School of Advanced Science and Engineering, Hiroshima University)
Endo, Tamaki[1]; Tsuge, Masashi[1,2]; Watanabe, Naoki[1]

In space, chemical evolution from atoms and simple molecules to complex molecules begins in very cold (~10 K) regions, so-called interstellar molecular cloud, which is the birthplace of stars and planets. In these environments, chemical reactions in the gas phase are generally inefficient, whereas surface reactions on icy dust grains remain effective even at temperatures around 10 K mainly because the surface acts as the third body of reactions. In the present study, we focus on the behaviors of nitrogen (N) atoms on the ice surface, as nitrogen is a key constituent of prebiotic molecules in space. However, the surface chemistry of N atoms on icy dust grains—regarded as the initial stage of chemical evolution of elemental N in molecular clouds—remains poorly understood [1]. One of the important initial pathways of N atoms on ice dust is the recombination reaction forming N_2 molecules, whereas the gas phase recombination of N atoms hardly occurs. On the ice dust, the surface can acts as a heat sink to dissipate excess energy of reactions. We experimentally approach the surface diffusion of N atoms on ice leading to recombination.

To detect trace amounts of N atoms on amorphous solid water (ASW), namely ice dust analog, the PSD-REMPI method (a combination of photo-stimulated desorption and resonance-enhanced multiphoton ionization techniques) was employed [2]. Using this method, N atoms on the ASW were photo-desorbed by a weak nano-second laser at 532 nm and selectively ionized by the REMPI laser. The ions, thus desorbed, were detected by a time-of-flight mass spectrometer. The signal intensity is considered to be proportional to the surface number density of N atoms at the time of measurement.

Nitrogen atoms were deposited onto ASW at 27–31 K for 200 s, and the signal intensities were tracked as a function of delay time, t_{delay}, between the termination of deposition and PSD-laser injection at each temperature. We observed the decrease in signal intensities as t_{delay} increased, meaning that N atoms were progressively lost during delay period. The consumption of surface N atoms should be attributed to the diffusive recombination reactions since the monoatomic desorption is expected to be activated at higher temperatures. Therefore, the rate equation for the surface number density of N atoms, $[\mathrm{N}]_{(t)}$, after the termination of N-atom supply is expressed by the following rate equation:

$$\frac{d[\mathrm{N}]_t}{dt} = -2k_{\mathrm{rxn}}[\mathrm{N}]_t{}^2, \quad (1)$$

, where k_{rxn} is the rate constant of diffusive recombination reaction. Assuming that the recombination of N atoms is barrierless, the rate determining step of the reaction is surface diffusion; thus, k_{rxn} can be expressed by the rate constant of surface diffusion k_{sd}. Then, the integration of Equation 1 gives

$$\frac{[\mathrm{N}]_0}{[\mathrm{N}]_t} = 2k_{\mathrm{sd}}[\mathrm{N}]_0 t + 1, \quad (2)$$

where $[\mathrm{N}]_0$ is the initial density at $t_{\mathrm{delay}} = 0$. By fitting the experimental decay data with Equation (2), we determined k_{sd} at each temperature. Finally, by following the Arrhenius law, we derived the activation energy for the N-atom surface diffusion to be 1060 ± 90 K.

References

[1] Öberg, K. I., & Bergin, E. A. (2021). *Phys. Rep., 893*, 1-48.

[2] Tsuge, M., & Watanabe, N. (2023). *Proc. Jpn. Acad., Ser. B, 99 (4)*, 103-130.

2P19 Dynamical electronic structure change of metal oxide surface with oxygen defects under electric current revealed by first-principles computational method

(ICAT, Hokkaido Univ.) Shunsuke Toyama, Kenji Iida, Jun-ya Hasegawa.

[Introduction] Heterogeneous catalysts under electric currents are attracting increasing attention because recent experimental studies have shown that electric currents enhance reactivity.[1,2] However, the role of electric currents in catalysis remains unclear. Therefore, a deeper understanding of electrically conductive surfaces is required. In this study, we investigate the effect of hydrogen adsorption on the electronic structure of a TiO_2(101) surface with oxygen defects under an electric current.

[Method] Geometry optimization was performed using Quantum Espresso. A TiO_2 slab model with oxygen defects was constructed by removing all two-coordinated oxygen atoms from the outermost surface. The H-atom adsorption structure was then optimized. These TiO_2 models exhibit electrical conductivity because oxygen defects generate gap states near the Fermi level. Using the optimized structures, electron dynamics under an external electric field was simulated with the SALMON program,[3] where the period of the electric field was set to 80 fs.

[Result] Figure 1 shows the time-dependent energy changes under electric currents. The energy increases as electrons accelerate, followed by a decrease after 40 fs due to deceleration. Initially, the H-adsorbed model (red) exhibits a smaller energy change than the H-free model (blue); this is due to the difference in electric current magnitude. Nevertheless, the H-adsorbed model gains energy more rapidly over time, leading to a larger energy change than that of the H-free model after 60 fs.

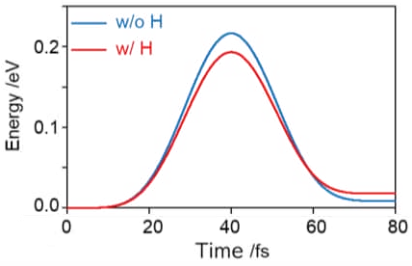

Fig. 1 Time dependent energy change of TiO_2 models (blue) without and (red) with an H-adsorbate.

Figure 2 shows the spatial distribution of electronic transitions near the Fermi level for the H-adsorbed model. Electronic transitions proceed from blue-green to yellow distributions. At 40 fs (Figure 2(a,b)), electrons transfer from the outermost TiO_2 surface to the inner region. By 80 fs (Figure 2(c,d)), electrons migrate toward the surface Ti-atom to which the H atom is adsorbed; this is attributed to the electronic structure change in the Ti atom due to H-adsorption. We elucidated how H-adsorption influences the electronic structure change of an oxygen-deficient TiO_2 surface under electric currents.

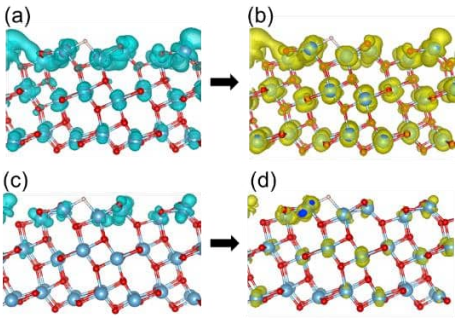

Fig. 2 Spatial distribution of electronic transitions at (a,b) 40 fs and (c,d) 80 fs.

[References] [1] E. B. Ledesma, et al., ChemCatChem 2024, 16, e202301110. [2] J. Zhang, et al., Angew. Int. Ed. 2023, 62, e202300744. [3] M. Noda, et al., Comp. Phys. Comm. 2019, 235, 356-365.

2P20 Comparison of HCl dissociation behaviors on hexagonal (I_h) and amorphous ice clusters accounting for nuclear quantum effects

([1]*Saitama University*, [2]*Tokyo Metropolitan University*)
Sasaki, Yuki[1]; Ueno, Hinami[1]; Takayanagi, Toshiyuki[1]; Murakami, Tatsuhiro[2]

HCl ionic dissociation on water ice surface is critical for stratospheric ozone depletion and interstellar chemistry [1]. Nuclear quantum effects are known to enhance this process on amorphous ice [2], but structural influences are yet to be fully elucidated. To address this, we compare the dissociation dynamics on amorphous and hexagonal (I_h) crystalline clusters.

Using classical MD and ring-polymer MD (RPMD) based on on-the-fly GFN2-xTB [3] with optimized parameters, a total of 120 trajectories were calculated at T = 100 K for (a) and (b) clusters with different structures shown in Fig.1.

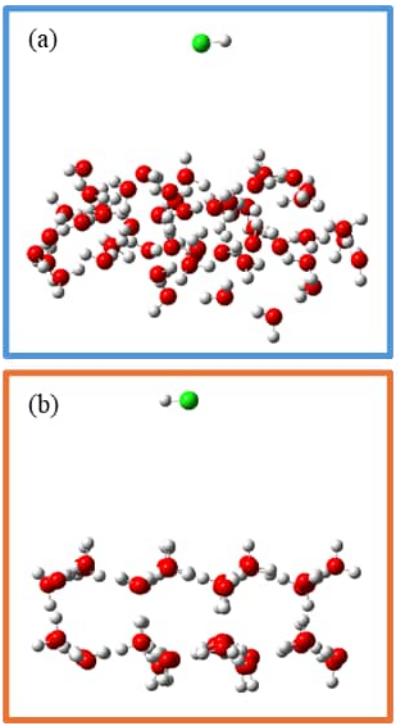

Figure1. Snapshots of the ice cluster models: (a) amorphous (n=49) and (b) hexagonal (I_h) (n=48).

The RPMD simulations showed a higher frequency of HCl dissociation on the hexagonal (I_h) (116 trajectories, 96.7%) compared to the amorphous (76 trajectories, 63.3%). This reactivity stems from a specific local arrangement of two H and one O atoms, free from the hydrogen-bond network, which stabilizes the proton-accepting site and the Cl^-. As shown in Fig. 2, the coordination number (CN) of Cl distributions for the hexagonal (I_h) clusters are shifted toward higher values compared to the amorphous. Furthermore, both systems exhibit a temporal shift toward even larger CNs, suggesting that the evolution of such highly coordinated environments promotes dissociation.

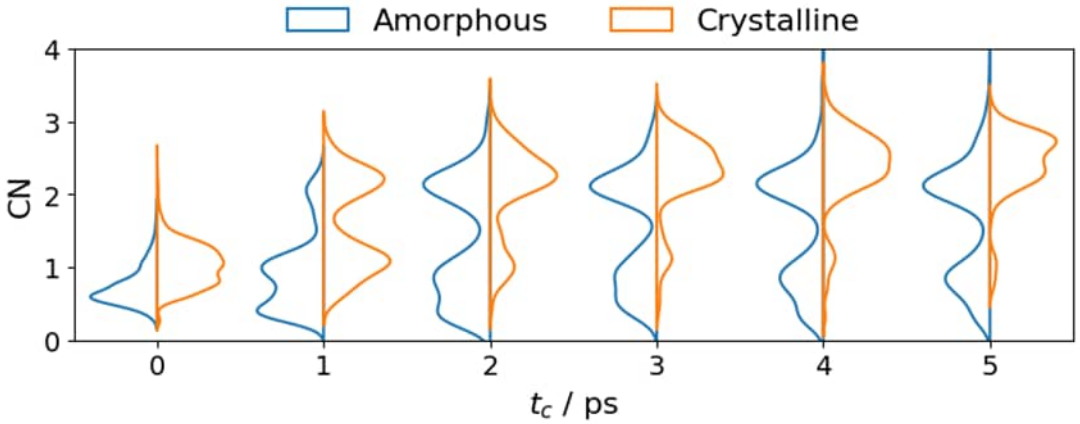

Figure2. Time-evolved violin plots of the coordination number (CN) of Cl excluding the HCl hydrogen for amorphous (blue) and hexagonal (I_h) (orange, labeled as "Crystalline") in RPMD.

References

[1] S. Solomon *et al.*, *Nature* **321**, 755 (1986).
[2] T. Murakami *et al.*, *Molecules* **30**, 442 (2025).
[3] C. Bannwarth *et al.*, J. *Chem. Theory Comput.* **15**, 1652 (2019).

2P21 Reactions between low-energy CH_3^+ ions with a methanol solid surface at low temperatures

([1]RIKEN Nishina Center, [2]ILTS, Hokkaido Univ.)
Yoichi Nakai[1], Hiroshi Hidaka[2], Naoki Watanabe[2]

Although the temperature inside of interstellar molecular clouds is extremely low, at approximately 10 K, it is known that a wide variety of molecules exists there. These molecules are thought to form through various reaction pathways, starting with reactions involving simple molecules containing atoms or ionic species. Understanding these reaction processes is also closely linked for elucidating the physical and chemical properties of interstellar matter. Ion-molecule reactions are considered the most important mechanism in the gas phase of molecular evolution. However, these reactions alone cannot account for the abundance of even relatively common molecules such as hydrogen, water, and methanol. Therefore, neutral reactions involving radicals on the surfaces of icy grains are also recognized as essential. In particular, the importance of hydrogen-atom addition reactions has been experimentally demonstrated at low temperatures below approximately 20 K [1]. On the other hand, since radicals heavier than hydrogen atoms exhibit extremely slow thermal diffusion at temperatures below 20 K, it is also believed that non-thermal diffusion of radicals driven by the heat of preceding reactions and photodissociation of precursors, as well as high-temperature environments associated with star formation in molecular clouds, play significant roles [2].

Over the past decade or so, theoretical calculations using computational chemistry methods have proposed a different type of molecule formation via the reactions between low-energy ions and the surface of amorphous ice [3, 4]. To verify these theoretical predictions, we developed a new experimental apparatus employing a surface molecular detection method known as reactive scattering ion spectrometry (also known as the ion pickup method) [5]. Using this apparatus, we investigated the formation of methanol molecules via the reaction of CH_3^+ with the surface of amorphous solid water at extremely low temperatures [6]. Recently, we have been conducting experiments on the reaction between CH_3^+ and the methanol solid surface to investigate reactions involving methanol formed on ice particles. To the best of our knowledge, there are no theoretical predictions regarding this reaction. The experiments using methanol with natural isotope abundance suggest the formation of formaldehyde and dimethyl ether (or ethanol). We also have been performing experiments using isotope labeling to investigate the origin of constituent atoms in the reaction products.

References

[1] N. Watanabe and A. Kouchi, Prog. Surf. Sci. **83**, 439 (2008)
[2] A. Iguchi et al., Astrophys. J. **998**, 249 (2026).
[3] D.E. Woon, Astrophys. J **728**, 44 (2011); D.E. Woon, Acc. Chem. Res., **54**, 490 (2021).
[4] N. Inostroza-Pino et al., A&A **650**, A169 (2021).
[5] H. Kang, Bull. Korean Chem. Soc. **32**, 389 (2011); A. Ishibashi et al., Astrophys. J. Lett. **921**, L13 (2021).
[6] Y. Nakai et al., ApJ **953**, 162 (2023).

2P22 Development of a new apparatus for atomic momentum spectroscopy at the world's highest incident electron energy

([1]IMRAM, Tohoku university, [2]Institut für Kernphysik, Universität Frankfurt, [3]RoentDek Handels GmbH) S. Kanaya[1], S. Minemoto[1], O. Jagutzki[2,3], M. Takahashi[1]

Intramolecular atomic motion has long been attracting interest of physicists and chemists for its relationship to the reactivity and functionality of molecules. To directly observe this atomic motion, atomic momentum spectroscopy (AMS) has been proposed [1], which would measure momentum of a constituent nucleus in a molecule by using electron-nucleus Compton scattering. In recent years, we have developed AMS as a new molecular spectroscopy method through a series of attempts, including construction of a highly-sensitive AMS apparatus [2], development of data analysis protocol [3] to extract and quantum chemistry-based AMS theory [3,4] to predict Compton profile due only to intramolecular atomic motion. We have then started to systematically study how intramolecular atomic motion of the same nuclear species depends upon the difference in the chemical environment [5,6]. However, the target species of the study are limited to the lightest nucleus H, partly due to lack of the mass resolution that originates in the use of an insufficiently high incident electron energy (2 keV). To bring breakthrough to this awkward situation, a new apparatus using a higher energy (6 keV) has independently been constructed [7], however, it has revealed that 6 keV is not enough for measuring intrinsic Compton profile of the C atom in CH_4 properly due to non-fulfillment of the high momentum transfer limit [8]. Clearly, a further higher energy is required to bring out the true strength of AMS.

Under the situations mentioned above, we are now developing a new AMS apparatus using 10 keV incident electron energy that has never been employed. Briefly, it measures energy loss of backscattered electrons created by the collision of a 10 keV incident electron with a gaseous target molecule in an effusive beam. Here the incident 10 keV electron beam is generated using a LaB6 filament to minimize the energy spread of the beam. The energy and angular distribution of backscattered electrons emerging at a scattering angle of 135 degrees are analyzed with a spherical analyzer after being decelerated with a ratio of 100. The electrons having passed through the analyzer are then detected with a position sensitive detector, customized for this experimental setup. Electron trajectory simulations indicate that the overall mass resolution of this spectrometer is more than 16 under the 10 keV conditions, so one may expect that AMS can properly be extended to much heavier target species such as the C and O atoms.

References

[1] M. Vos, 2001 Phys. Rev. A 65 012703.
[2] M. Yamazaki, M. Hosono, Y. Tang, and M. Takahashi, 2017 *Rev. Sci. Instrum.* **88**, 063103.
[3] Y. Tachibana, Y. Onitsuka, H. Kono, and M. Takahashi, 2022 *Phys. Rev. A* **105**, 052813.
[4] S. Kanaya, Y. Onitsuka, N. Watanabe, H. Kono, and M. Takahashi, 2025 *Phys. Chem. Chem. Phys.* **27**, 2453.
[5] D. B. Jones, S. Kanaya, Y. Onitsuka, and M. Takahashi, 2026 *J. Phys. Chem. Lett.* **17**, 166.
[6] S. Minemoto, S. Kanaya, T. Sugai, D. B. Jones, and M. Takahashi, 2026 SCKD symposium, 2A4.
[7] S. Sakaguchi, T. Kodama, H. Konishi, M. Takahashi, Y. Ohshima, and M. Yamazaki, 2025 MolSci meeting, 2A02.
[8] Onitsuka, Y. Tachibana, and M. Takahashi, 2022 *Phys. Chem. Chem. Phys.* 24, 19716.

2P23 Methanol formation via CH_3 + OH reaction with transient diffusion on amorphous solid water at low temperatures

([1]Hokkaido Univ., [2]UEC, [3]U Tokyo, [4]Hiroshima Univ.) H. Hidaka[1], A. Iguchi[2], A. Ishibashi[3], M. Tsuge[4], Y. Oba[1], N. Watanabe[1]

Chemical reactions on amorphous solid water (ASW) surfaces at low temperatures are important for understanding molecular evolution in interstellar molecular clouds. At temperatures as low as 10 K, non-energetic surface reactions are mainly driven by hydrogen atoms, since only hydrogen atoms can thermally diffuse on the surface. Recently, association reactions between radicals on ASW surfaces have been reported even at temperatures where thermal diffusion of radicals is inefficient [1,2]. These reactions are thought to proceed via transient diffusion mechanism, in which part of the energy released during radical formation temporarily enhances radical mobility. This suggests that complex molecules can form through chain reactions even under extremely low temperature conditions. In this study, we investigated methanol formation through the chain reactions $CH_4 + OH \rightarrow CH_3 + H_2O$ and $CH_3 + OH \rightarrow CH_3OH$, as methanol is an important precursor of more complex organic molecules in space.

To examine this process under astrochemically relevant conditions, experiments were performed at very low reactant coverages. We employed the highly sensitive Cs^+ pickup method, which enables mass spectroscopic detection of trace adsorbates on ASW surface [1]. Surface species (X) are detected as ionic complexes (Cs^+-X) after irradiation with a low energy Cs^+ beam. Figure 1 shows the pickup mass spectra of (a) photolyzed ASW and (b) photolyzed ASW after CH_4 deposition at 10 K. Signals corresponding to CH_3 (148 u) and CH_3OH (165 u) were observed only after CH_4 deposition. These results indicate that CH_3OH is formed via the CH_3 + OH reaction, since the direct reaction of CH_4 + OH → CH_3OH + H is highly endothermic (+58.8 kJ/mol) [3].

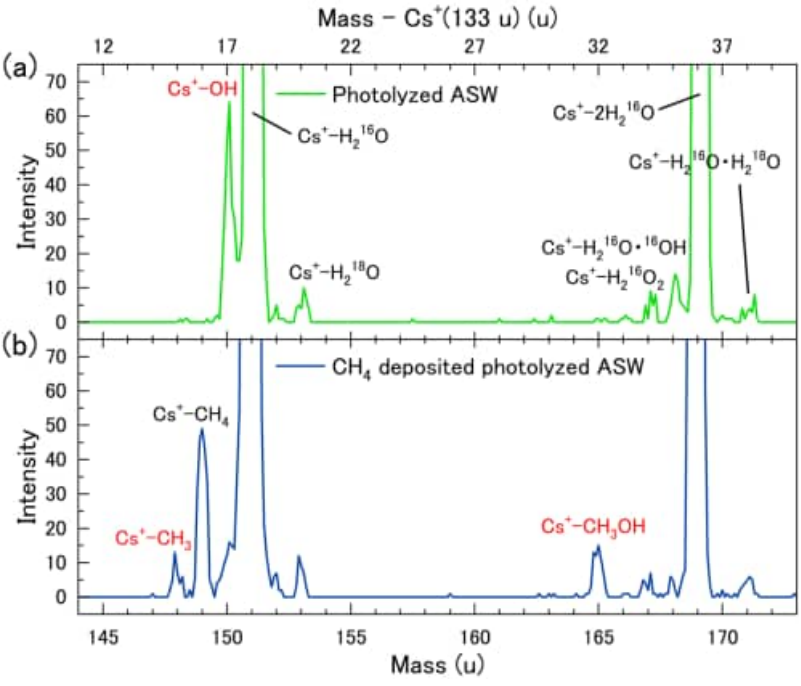

Figure 1: The pickup mass spectra for (a) photolyzed ASW and (b) CH_4 deposited on photolyzed ASW. The coverage of CH_4 is 0.17.

References

[1] A. Ishibashi, H. Hidaka, Y. Oba, A. Kouchi, & N. Watanabe, 2021, ApJL 921, L13.

[2] A. Ishibashi, G. Molpeceres, H. Hidaka, Y. Oba, T. Lamberts, & N. Watanabe, 2024, ApJ 976, 162.

[3] C. Tao & J. Li, 2022, Comput. Theor. Chem. 1217, 113906.

2P24 Kinetic analysis of luminol chemiluminescence in dimethyl sulfoxide driven by dissolved oxygen under a nitrogen atmosphere

([1]Graduate School of Science, Tokyo University of Science, [2]Tokyo University of Science)
[1]Kanon Ie, [2]Takahiro Suzuki, [2]Masayuki Inoue

The chemiluminescent reaction of luminol in dimethyl sulfoxide (DMSO) uses dissolved oxygen as an oxidizing agent and is characterized by its ability to realize repeatable luminescence[1](Fig.1). In this study, we aimed to quantitatively understand the luminescent behavior in this reaction system. To this end, we investigated the effects of basic conditions, alkali metal ions and oxygen supply conditions.

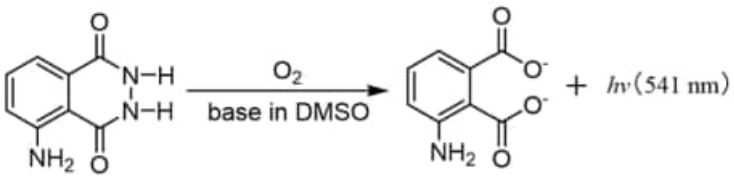

Figure 1 Reaction mechanism of the luminol oxidation reaction

First, to standardize the basic conditions, the concentration of the alcoholic hydroxide was adjusted to 1.5 mol L^{-1} and the luminescence behavior was compared in reaction systems using various alkali metal hydroxides. All measurements were performed under a nitrogen atmosphere to minimize the influence of oxygen supplied from the gas-liquid interface. The results confirmed a tendency for the luminous intensity to increase as the radius of the alkali metal ions increased. These results suggest that metal ions may influence the solvation structure and reaction field, thereby contributing to the luminescence properties.

Furthermore, under these conditions, luminescence decay attributable solely to dissolved oxygen was successfully monitored. A rate constant of k = 0.247 s^{-1} was obtained for the RbOH system (Fig. 2). In contrast, it was difficult to monitor the decay behavior via luminescence measurements in systems using NaOH and KOH. For these systems, we plan to analyze the temporal evolution in luminescent species using fluorescence spectroscopy.

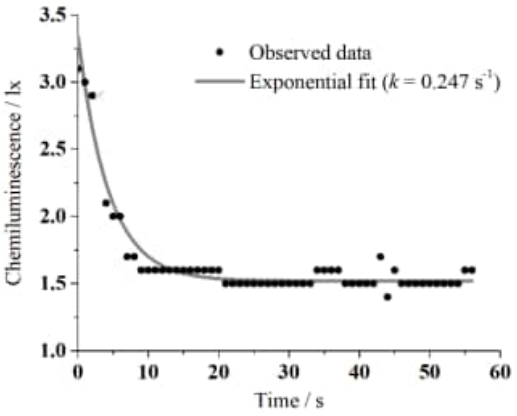

Figure 2 Luminescence decay of the luminol oxidation reaction with exponential fitting

In summary, this study identified the factors governing the luminescence behavior of the luminol reaction in dimethyl sulfoxide (DMSO) and clarified the effects of metal ions and oxygen supply conditions by making comparisons under standardized conditions. This research will provide a useful foundation for improving the reproducibility and comparability of luminescence phenomena, offering insights that contribute to our understanding of the reaction mechanism.

1. Kanon Ie, Takahiro Suzuki, and Masayuki Inoue, *J. Chem. Educ.* **2025**, *102*, 3743-3747.

2P25 Development and Application of a Conformational Analysis Method Combining MD Simulation and Ion Mobility Mass Spectrometry

(Fac Sci., Hokkaido Univ.[1], WPI-ICReDD, Hokkaido Univ.[2], Fac. Pharm Sci., Tokushima Bunri Univ.[3], Fac. Eng., Hokkaido Univ.[4]) Keisuke Tashiro[1], Yuki Ide[2], Tetsuya Taketsugu[1,2], Kazuaki Ohara[3], Kentaro Yamaguchi[3], Masato Kobayashi[1,2], Yasuhide Inokuma[2,4]

Ion mobility-mass spectrometry (IM-MS) is a powerful technique that enables the structural analysis of medium-to-large molecules by *m/z* and the collision cross section (CCS), a physical quantity derived from ion arrival time distributions. Despite its potential, the scope of structural characterization via IM-MS has been limited due to the lack of a versatile simulation methodology that accurately correlates CCS with three-dimensional molecular structures. In this study, we developed a computational scheme designed to reproduce shifts in CCS distributions resulting from subtle conformational changes. This approach enables efficient CCS calculations for snapshots obtained from molecular dynamics (MD) simulations, allowing for direct correlation with experimental data. Figure 1 illustrates the conformation determination of polyketone–Na^+ complexes using the proposed scheme. The CCS distributions obtained from MD simulations successfully reproduced experimental IM-MS profiles. Principal component analysis (PCA) further revealed a distinct cluster where the Na^+ is coordinated by 5–6 oxygen atoms, including the terminal carbonyl oxygen O1. The scheme also captured multimodal CCS profiles for long-chain polyketones, identifying the specific conformations corresponding to each peak.[1]

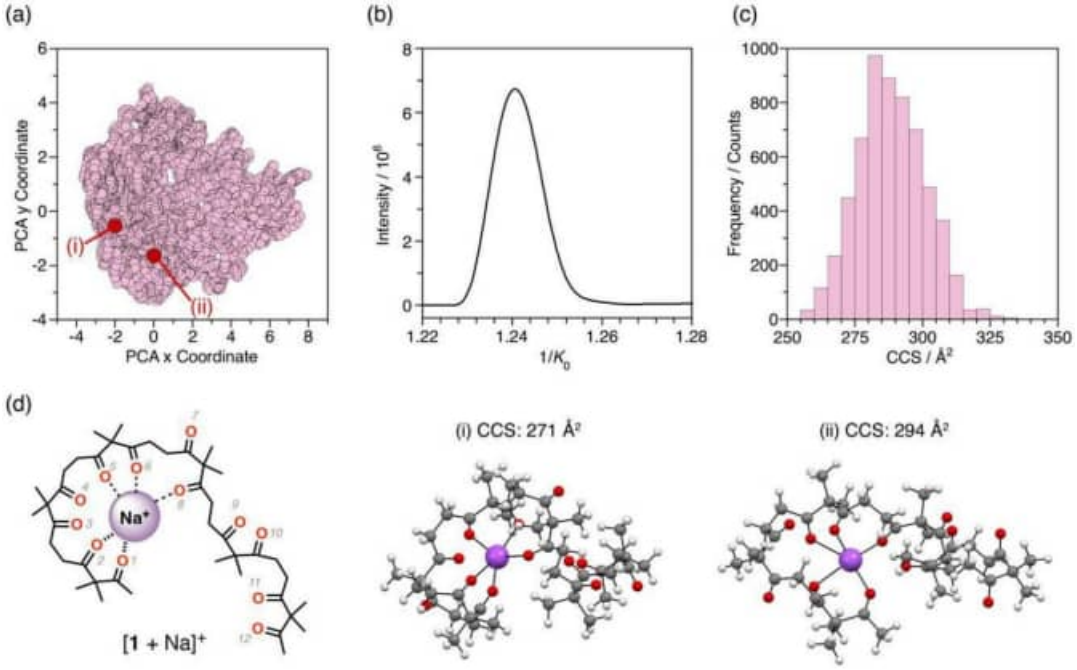

Figure 1. (a) Structural distribution of organic oligomer–cation complexes in a two-dimensional space defined by the first and second principal components (PC1 and PC2) obtained from PCA. **(b)** Experimentally observed IM-MS spectra. **(c)** CCS distributions derived from MD simulations. **(d)** Representative binding sites of the organic oligomer–cation complex identified through computational analysis.

[1] K. Tashiro, *et al*. *Adv. Theory Simul.*, **2024**, *7* (11), 2400691.

2P26 Development of Fourier Transform Three-Color Excitation Action Spectroscopy for Model-Free Analysis of Photo-Stationary States

(KOBE University) YAMASHITA, Sayaka; INOUE, Rinka; FUKUDA, Kai; WADA, Akihide

Multicolor, multistep reaction processes involving photoexcitation, de-excitation, and relaxation are important for solar-driven reactions, such as photosynthesis and photocatalytic reactions [1,2]. In order to understand such complex photochemical reaction processes, conventional monochromatic pump-probe measurement is insufficient because of its monochromatic single step excitation feature. One effective approach is to investigate reaction pathways under photostationary conditions that include multistep and multicolor process, referred to as higher-order and/or cross-terms of photoexcitation. In our laboratory, methods for evaluating reactions including higher-order and cross terms have been developed. In this method, the action spectrum obtained from Fourier transforms of the interferogram acquired using multiple modulated pump beams. The existence of higher order terms and cross terms are evaluated by the appearance of peak at corresponding frequencies. In this study, we developed an experimental system to obtain insights into higher-order and cross terms, including their phases, under three-color excitation.

In the experiment, the sample was excited by three-color laser beams (wavelength of 375nm,405nm, and 532nm), each modulated as cos waves at different frequencies. To observe the photo-stationary state, the modulation frequencies of ~0.01 Hz, which are much slower than the sample response (~2 s^{-1}), were adopted. Changes in the photo-stationary state were monitored as an interferogram of the absorbance change of the probe beam (wavelength of 405nm). The interferogram was Fourier-transformed to obtain an action spectrum after the data treatment of symmetrization and replication. A p-amino azobenzene (AAB) solved in methanol (0.5mM) was used as the sample. AAB exists as trans and cis isomers. The trans isomer absorbs 375 nm and 405 nm light, whereas the cis isomer additionally 532 nm.

The action spectrum is shown in Fig. 1. The frequencies (ω_1, ω_2, ω_3) correspond to excitation at 405 nm, 532 nm, and 375 nm, respectively. Signals at the fundamental frequencies ω_1, ω_2, and ω_3, originating from single-step excitation processes, are observed. Furthermore, both the intensity and phase information of higher-order and cross terms arising from multistep photoexcitation processes are obtained. The analysis of these results will be presented in the poster.

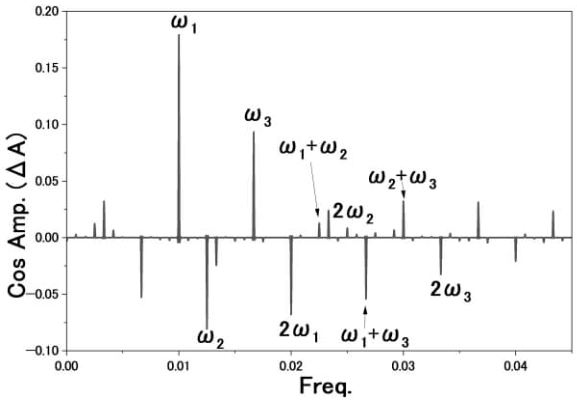

Fig.1 Action Spectrum

[1]B. Kok, B. Forbush and M. McGloin, *Photochemistry and Photobiology*, **11**, 457-&(1970).

[2]P. Joliot, G. Barbieri and R. Chabaud, , *Photochemistry and Photobiology*, **10**, 309-&(1969)

2P27 Vibrational states and transition intensities based on variational vibrational theory

([1]Hokkaido Univ., [2]Eötvös Loránd Univ.) Ayaki Sunaga[1,2]

[Introduction]

Methanol is a prototype molecule that includes a single large-amplitude motion (LAM) associated with torsional motion of the CH_3 unit and is attractive as a tracer for investigating the chemical and physical environments in the universe. LAM has been a challenging problem in molecular spectroscopy because it cannot be described by the harmonic-oscillator approximation. The development of a vibrational theory that can describe the torsional motion is encouraged.

[Method]

We obtained vibrational states of methanol by variationally solving the Schrödinger equation for nuclear motion GENIUSH-Smolyak method [1] was employed for vibrational computations. We developed vibrational coordinate systems that minimize the coupling between vibrational and torsional motions by defining normal coordinates based on the minimum-energy path on the PES along the torsional angle [2]. The geometry sampling for developing the methanol PES was performed using the Robosurfer code [3].

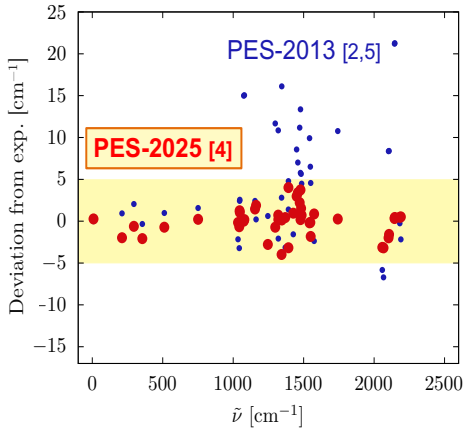

Fig. 1. Deviation of experiment and theoretical values (up to 2500 cm^{-1}) obtained using PES-2013 [2,5] and PES-2025 [4] for vibrational energies of methanol.

[Result]

Our vibrational computation using a newly developed PES (PES-2025 [4]) agrees with the experiment within a maximum deviation of 5 cm^{-1} (**Fig. 1**). The agreement is improved compared with the one using an early-reported PES (PES-2013 [5]). The calculated IR spectra show strong peaks for the torsional excited state ($\tau = 4$) and mixing states around 2930 cm^{-1} (**Fig. 2**). This can be attributed to the mixing with the fundamental CO stretch and CH symmetric stretch modes, respectively.

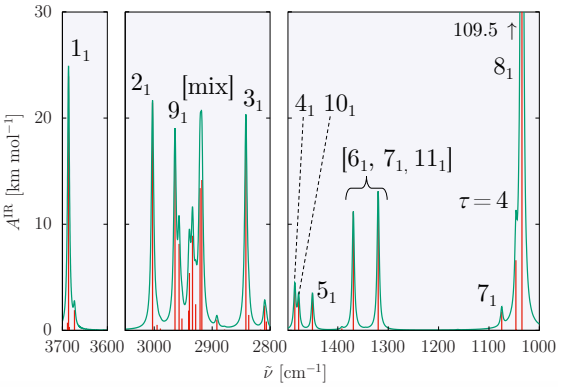

Fig. 2. Calculated IR spectra of methanol [6]. X_n refers to the X^{th} vibrational mode (e.g., $X = 1$ corresponds to the OH stretch) at the n^{th} excited state. [mix] refers to strongly mixing states. $\tau = 4$ refers to the 4th excited state of torsional motion.

[Reference]

[1] G. Avila and E. Mátyus, J. Chem. Phys. **150**, 174107 (2019). [1] A. Sunaga, G. Avila, and E. Mátyus, J. Chem. Theory Comput. **20**, 8100 (2024). [3] T. Győri and G. Czakó, J. Chem. Theory Comput. **16**, 51 (2020). [4] A. Sunaga, T. Győri, G. Czakó, and E. Mátyus, J. Chem. Phys. **163**, 064101 (2025). [5] C. Qu and J. M. Bowman, Mol. Phys. **111**, 1964 (2013). [6] A. Sunaga, A. Bartók, and E. Mátyus, Phys. Chem. Chem. Phys., accepted.

3P01 Substituent Effects on Electrocyclic Reactions: Ultrafast Ring-Opening of α-Phellandrene Stimulated by Impulsively Excited Molecular Vibrations

Zhiyi, Zhou[1]; Kenichiro, Saita[2]; Yusuke, Minegishi[3]; Tetsuya, Taketsugu[4,5]; Taro, Sekikawa[1]
([1]Appl. Phys., Eng., Hokkaido Univ., [2]Nanobiosci., Yokohama City Univ., [3]Chem. Sci. Eng., Hokkaido Univ., [4]Chem., Sci., Hokkaido Univ., [5]WPI-ICReDD, Hokkaido Univ.)

Since the ring-opening of cyclic hydrocarbons can introduce specific functionalities into molecules, studying their electronic dynamics provides essential insights into the photochemical mechanisms of complex biomolecules. In this study, we investigate the ring-opening dynamics of (−)-α-phellandrene (αPH), which shares the same cyclic backbone as cyclohexadiene but is substituted with a methyl and an isopropyl group at diagonal positions. It therefore represents an intermediate structural complexity between simple model systems and more complex hydrocarbons. Time-resolved photoelectron spectroscopy utilizing high-harmonic-generated EUV pulses was used to monitor the ultrafast dynamics of αPH, supported by quantum chemical calculations. The molecule was excited to Rydberg states via two-photon absorption of the 3.1-eV pulses and probed with EUV pulses, allowing access to deeper molecular orbitals (MOs). In addition to the relaxation of the excited state and time-dependent MO evolution, the spectrogram shows periodic splitting of signals from HOMO−1 and HOMO−2 after ultrafast relaxation to the ground state (S_0). This observation provides evidence for a previously unreported stepwise ring-opening mechanism that occurs entirely in the S_0 state.

Upon photoexcitation, the system undergoes rapid nonadiabatic relaxation to the S_0 state, where the impulsive redistribution of excess energy stimulates a limited set of coherent intramolecular vibrational modes, manifesting as vibrational wavepackets. Because of the relatively high barrier at the first transition state, most wavepackets remain trapped in high-lying vibrational levels of the S_0 potential rather than overcoming it ballistically, with only a fraction surmounting the barrier during each oscillation cycle. Consequently, most αPH undergo periodic structural distortions driven by this persistent coherent vibrational motion, while the ring-opened products accumulate incrementally. Born–Oppenheimer molecular dynamics (BOMD) simulations identify an out-of-plane wagging mode that facilitates both conformational interconversion and subsequent ring opening. The agreement between its frequency and the experimentally observed spectral splitting provides strong evidence that this mode plays a key role in driving the stepwise ring-opening phenomenon in the S_0 state. Detailed information is available in Ref. 1.

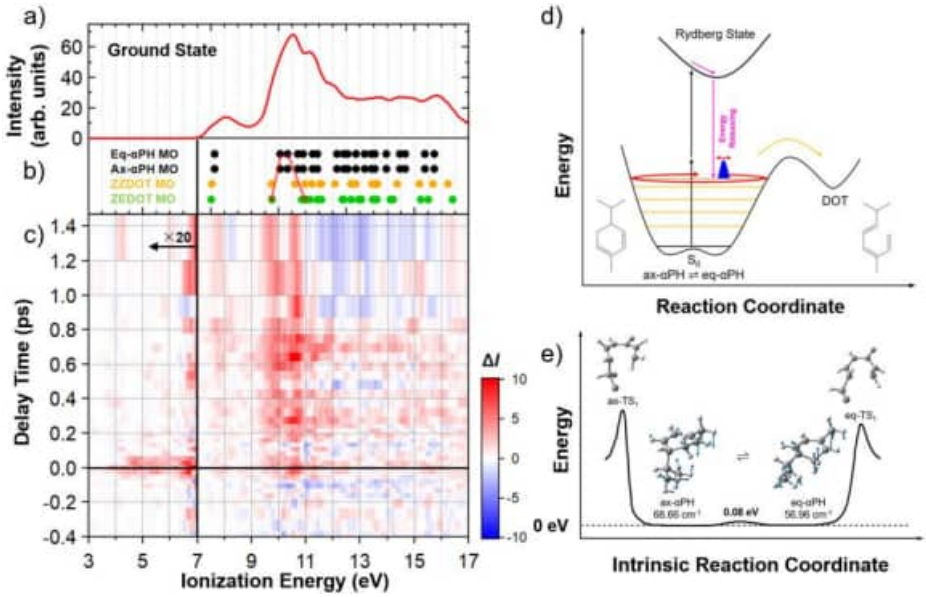

Figure 1. (a) Photoelectron spectrum of the ground state αPH. (b) Absolute values of MO energies for eq- and ax-αPH, tZt-Z-DOT, and tZt-E-DOT. (c) Difference photoelectron spectrogram of αPH with signal intensities of <7.0 eV amplified 20 times. (d) Schematic diagram of the ring-opening process of αPH upon photoexcitation to Rydberg states. (e) Out-of-plane wagging vibrational modes facilitate isomerization between eq- and ax-αPH.

[Reference] [1] Z. Zhou et al., *J. Phys. Chem. A*, **129**, 8733–8743 (2025).

3P02 Photochemical reaction of pyrene with CCl_4 in alcohols

(Kobe City College of Technology)
WATANABE, Akihiro; KANEMURA, Sakura; NARUO, Nanami

Photochemical reactions are fascinating because the interaction between light and molecules can lead to unexpected reactions. Among these, reactions that form excited complexes are particularly interesting because of how potential energies interact in subsequent reactions. Aromatic compounds are known to be easily excited by ultraviolet light. In our laboratory, irradiating anthracene and carbon tetrachloride with an ultraviolet laser revealed broad emission peaks, and it was found that the rate constant for the photochemical reaction of anthracene depends on the dielectric constant of the solvent[(1)]. Since aromatic compounds are electron-donating, n-π* charge-transfer complexes (CT) are expected as products. In this study, pyrene was used to determine the reaction rate constant of the photochemical reaction with carbon tetrachloride and to investigate the reaction mechanism.

Experiments were carried out using pyrene and carbon tetrachloride in various polar solvents under batch conditions. The solvents used were primary alcohols (methanol, ethanol, 1-propanol, ... etc.). Pyrene was excited with OPO laser (317 nm) irradiation and observed the emission spectra. We also determined the reaction rate constant from the attenuation of the emission peak of pyrene and compared it with the electrical properties of the solvent. The attenuation of the pyrene peak is affected by CT, so this is removed by deconvolution.

Figure 1 shows the change in the emission spectrum. As the irradiation time increases, the peak thought to be related to CT on the longer wavelength side increases. Although there is a peak originating from pyrene at 374 nm, the emission of CT greatly influences the measurement of its time evolution. Therefore, by also measuring the time evolution at 395 and 580 nm, the pyrene-derived decrease peak was obtained. The reaction rate obtained from these results shows a positive correlation with the dielectric constant of the solvent (Figure 2), which is consistent with the assumed mechanism of charge transfer complex formation.

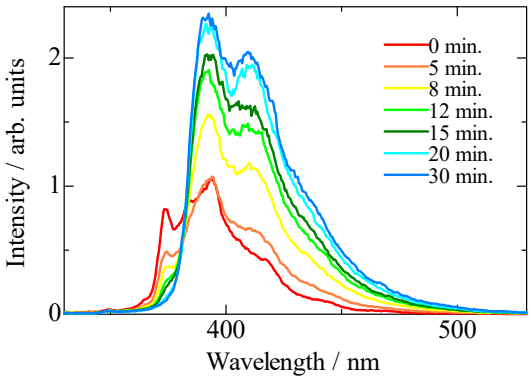

Figure 1. The emission spectra of pyrene with 317 nm photoexcitation. The pyrene concentration is 1.0×10^{-5} mol/L, and carbon tetrachloride is added at 7.0×10^{-3} mol/L in

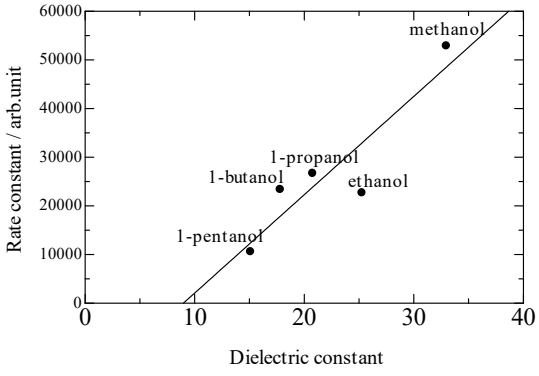

Figure 2. Relationship between reaction rate constant and dielectric constant of photochemical reaction between pyrene and carbon tetrachloride. The names of the solvents used are shown in the figure.

(1) A. Watanabe and Y. Hamada 40th Symposium on Chemical Kinetics and Dynamics Book of Abstracts, 2025, 2P15.

3P03 Ion pair dissociation of carbon dioxide following absorption of a vacuum ultraviolet photon

([1]Sophia University) Akiko Oda[1], Isao H. Suzuki[1], Takeshi Odagiri[1]

There is increasing interest in reactions involving negative ions in the field of planetary physics [1]. Ion-pair dissociations are recognized as a significant source of negative ions in the upper atmosphere [2]. In the present study, the dynamics of the ion-pair photodissociation ($AB + h\nu \rightarrow AB^* \rightarrow A^+ + B^-$) of carbon dioxide have been investigated by the measurement of kinetic energy and angular distributions of fragment negative ions by using an imaging technique in conjunction with synchrotron radiation. Absolute values of cross sections for the processes have also been obtained.

The experiments were carried out at BL20A of the Photon Factory, KEK. The storage ring was operated in Hybrid-fill mode, consisting of an isolated high current bunch and a series of low current bunches. The time structure of the synchrotron radiation was used for detection of the time-of-flight of negative ions. Fragment negative ions formed in the interaction region were accelerated by using velocity-map-imaging electrode system towards a delay line position sensitive detector. The initial velocity components of the ions were constructed from their arrival time and position on the detector surface.

The O^- fragments were observed in the photon energy range of 20 to 35 eV. Figure 1 shows an image plot of kinetic energy (KE) distributions of O^- as a function of incident photon energy. Each KE distribution has been normalized so that the total counts sum to 1. In the photon energy range of 21 to 26 eV, an increase in KE was observed with increasing photon energy, which is well reproduced by a kinematical prediction that the O^- is formed through the two-body dissociation into $CO^+(A^2\Pi) + O^-(\,^2P)$. In the higher photon energy range from 27 to 33 eV, where the cross sections for the O^- formation are large, the observed KE are well accounted for by interpretation of the three-body dissociation into $C^+(\,^2P) + O(\,^3P) + O^-(\,^2P)$.

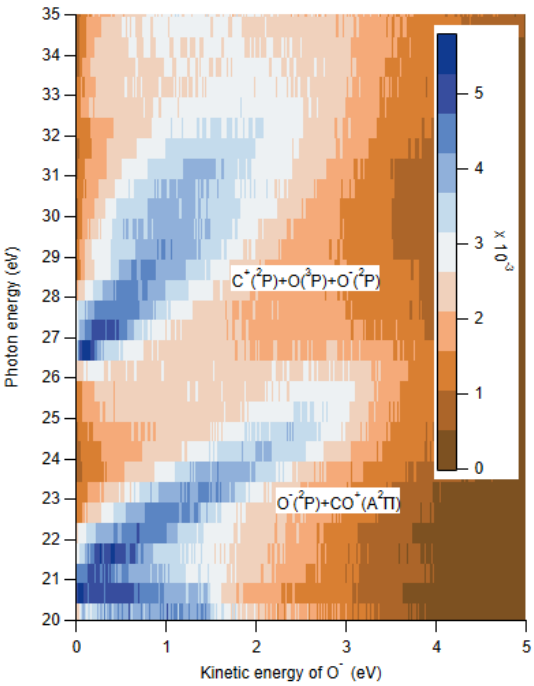

Fig 1 An image plot of kinetic energy (KE) distribution of O^- from CO_2 as a function of incident photon energy. Each KE distribution has been normalized so that the total counts sum to 1.

[1] V Vuitton *et al*. *Planet Space Sci.* **57**, 1558 (2009)

[2] E Szymańska *et al*. *Phys. Chem. Chem. Phys.* **16**, 3425 (2014)

3P04 Rotational excitation of NO in an intense femtosecond laser field carrying orbital angular momentum

(Graduate School of Arts and Sciences, UTokyo, Komaba Institute for Science, UTokyo)
Shinichi Fukahori and Hirokazu Hasegawa

When molecular rotation is excited by the interaction with photons, angular momentum is transferred from the photons to the molecule. For example, when NO is irradiated with an intense femtosecond laser field, rotational excitation occurs nonresonantly by Raman transition. The selection rule of the total angular momentum J of NO is $|\Delta J| \leq 2$ [1,2] in a single Raman transition because the angular momentum of a photon included in the conventional laser light is $1\hbar$, which is spin angular momentum, and two photons interact with NO. Orbital angular momentum (OAM) of laser beam can be controlled based on its spatial phase [3]. However, effects of the OAM of the laser beam on the rotational excitation of molecules have not been evaluated. In the present study, we examined rotational excitation of NO in an intense femtosecond laser field carrying nonzero OAM.

A femtosecond laser pulse (790 nm, 100 fs, 15 mJ, 10 Hz, linear pol.) was split into the pump pulse for rotational excitation and the probe pulse for ionization. The OAM of the pump beam was set to be $4\hbar$ by a LCOS-SLM, and the probe pulse was delayed by 20 ns from the pump pulse. The two pulses were focused on the supersonic molecular beam of NO diluted in Ne (0.1%, 0.25 MPa) in a vacuum chamber. After 15 ns delayed from the pump pulse, a tunable UV nanosecond laser pulse which was obtained as the second harmonics of the output from the dye laser (452.78-452.52 nm, 6 ns, 0.3 mJ, 10 Hz, linear pol.) was also focused on NO. When the UV wavelength is resonant to the rotational line of the A-X(0,0) band of NO [2], ionization of NO by the probe pulse is enhanced. We recorded the rotationally resolved excitation spectrum as the NO^+ yield as a function of the UV wavelength.

Figures 1(a) and 1(b) show the excitation spectrum recorded when NO is not irradiated with the pump pulse and the differences between the spectra obtained with the pump pulse and those without the pump pulse, respectively. In Fig. 1(b), the probe position dependence is shown, and the spatial profile of the pump beam at the focal spot is shown in Fig. 1(c). When the probe beam is focused on the circumference of the circle of the focused pump beam, the peaks at $J \leq 2.5$ decrease while the peaks at $J \geq 3.5$ increase, meaning that NO is rotationally excited on the circumference. We found that, when the probe beam is focused at the spatial center of the circle of focused pump beam, the extent of the rotational excitation of NO is weaker than that on the circumference.

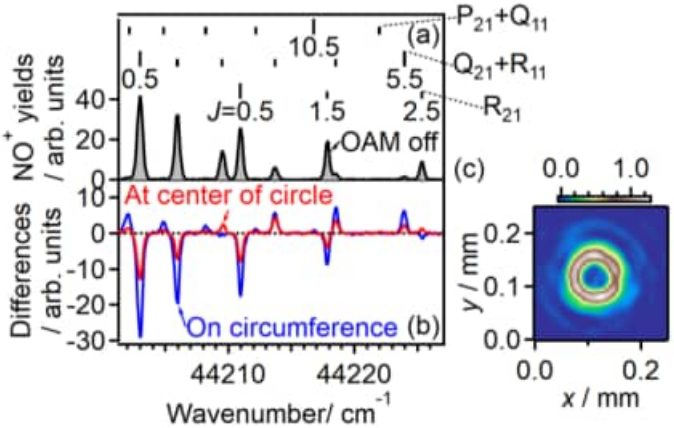

Fig. 1. (a) Rotationally resolved electronic excitation spectrum of NO without the pump pulse. (b) Difference spectra when the probe beam is focused on the circumference (blue) and at the center of the circle (red) of the focused pump beam. (c) Spatial profile of the pump beam at the focus.

References

[1] Y. Ohshima and H. Hasegawa, *Int. Rev. Phys. Chem.* **29**, 619 (2010).
[2] H. Hasegawa and Y. Ohshima, *Phys. Rev. A* **74**, 061401 (2006).
[3] L. Allen, M. W. Beijersbergen, R. J. C. Spreeuw and J. P. Woerdman, *Phys. Rev. A* **45**, 8185 (1992).

3P05 Photodissociation pathways of O_4^+ leading to singlet oxygen $O_2(a\ ^1\Delta_g)$ and $O_2(b\ ^1\Sigma_g^+)$ studied by mass-analyzed ion imaging

([1]Graduate School of Science, Tohoku Univ., [2]Hokkaido Univ. of Education) Watabe Yu[1], Koshiba Takumi[1], Ito Yuri[1], Kanno Manabu[1], Ohshimo Keijiro[2], Misaizu Fuminori[1]

[Introduction] An atmospheric species, O_4^+, exhibits broad photodissociation bands over the UV-visible spectral region [1], producing triplet ($X\ ^3\Sigma_g^-$) or singlet ($a\ ^1\Delta_g$, $b\ ^1\Sigma_g^+$) O_2 fragments. We recently reported that simple adiabatic dissociation producing $O_2^+(X\ ^2\Pi_g) + O_2(b\ ^1\Sigma_g^+)$ proceeds on a single excited state in the UV (< 400 nm) photoexcitation [2]. In contrast, photodissociation in the visible region is more complex, owing to the presence of several excited states (B^2A_u, C^2A_u, and D^2A_u) that correlate with $O_2^+(X\ ^2\Pi_g) + O_2(a\ ^1\Delta_g)$ or $O_2^+(X\ ^2\Pi_g) + O_2(b\ ^1\Sigma_g^+)$, as shown in Fig. 1 (a). To investigate the dissociation pathways from these states, we performed photofragment-ion imaging experiments for the visible photodissociation of O_4^+.

[Method] Oxygen cluster cations, $(O_2)_n^+$, were produced by supersonic expansion of an O_2/Ar (50%) gas mixture, followed by electron impact ionization. The O_4^+ ion was mass-selected using a homemade linear-type tandem reflectron time-of-flight mass spectrometer [3] and irradiated with a tunable pulsed laser (448 or 473 nm). The O_2^+ photofragment ion was detected as a two-dimensional image, and the sliced image of the distribution was reconstructed from the observed image using the pBASEX method.

[Results and Discussion] Figure 1 (b) shows sliced images of the photofragment distributions. At 448 nm, the distribution consists of two anisotropic components split along the electric vector ***E*** of the laser. The inner component is attributed to the D^2A_u state, while the outer component arises from the B^2A_u and C^2A_u states. This is because the D^2A_u state correlates with electronically excited singlet oxygen ($b\ ^1\Sigma_g^+$), resulting in lower translational energy than those from the B^2A_u and C^2A_u states.

At 473 nm, the inner component is significantly diminished despite the small energy difference (0.15 eV) between the two excitation wavelengths. As shown in Fig. 1 (a), the O_2-O_2^+ distance in the D^2A_u state is elongated at 473 nm, whereas those in the B^2A_u and C^2A_u states change slightly. Thus, at 473 nm, the D^2A_u state should lie outside the Franck-Condon region, and this is likely reflected in the experimental observation of the disappearance of the inner component.

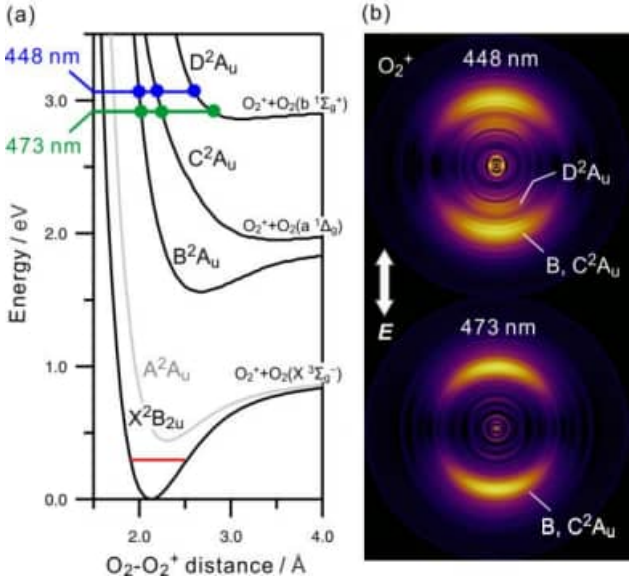

Fig. 1 (a) Potential energy curves calculated by SA-CASSCF(15, 12)/aug-cc-pVTZ. (b) Sliced images of the O_2^+ fragment distributions.

[References]

[1] G. P. Smith *et al.*, *J. Chem. Phys.* **69**, 5393 (1978).
[2] Y. Watabe *et al.*, *J. Chem. Phys.* **163**, 024301 (2025).
[3] K. Okutsu *et al.*, *Rev. Sci. Instrum.* **88**, 053105 (2017).

3P06 Mechanism of the delayed fragmentation of ethanol molecules upon VUV photoionization

([1]Kyoto University, [2]Institute for Molecular Science, [3]Sokendai) T. Nakao[1], T. Kaneyasu[2,3], T. Yanagawaya[1], H. Iwayama[2], T. Majima[1]

Polyatomic molecular ions sometimes fragment on the microsecond timescale via long-lived metastable intermediates [1]. Delayed fragmentation from ethanol has been recognized in mass spectrometry for more than half a century, yet the mechanism for singly charged intermediates remains unclear—largely because previous studies neither controlled the parent-ion excitation energy nor detected the neutral counterparts of fragment ions. Here, we overcome both limitations by combining vacuum-ultraviolet (VUV) photoionization at selected photon energies with ion–neutral coincidence detection.

Monochromatic VUV photons of 13.0–23.0 eV (BL7B, UVSOR) ionized an effusive ethanol target. A time-of-flight (TOF) mass spectrometer recorded fragments in list mode. Delayed-fragmentation channels were then identified through ion–neutral coincidences, where the neutral fragment becomes detectable by inheriting the parent-ion velocity prior to dissociation.

Two-dimensional TOF correlation maps revealed four delayed-fragmentation channels: (1) $C_2H_5O^+ \rightarrow CHO^+ + CH_4$, (2) $C_2H_5O^+ \rightarrow C_2H_3^+ + H_2O$, (3) $C_2H_5O^+ \rightarrow H_3O^+ + C_2H_2$, and (4) $C_2H_3O^+ \rightarrow CH_3^+ + CO$. In channels (1)–(3), ionized ethanol molecules undergo prompt loss of a hydrogen atom to form metastable $C_2H_5O^+$ ions, which subsequently dissociate with sub-microsecond delays; channel (4) corresponds to delayed fragmentation of $C_2H_3O^+$ formed via the prompt loss of three hydrogens. The threshold energy for delayed fragmentation, E_{th}, was determined for each channel (Fig. 1(a)). The E_{th} values lie only a few eV above the vertical ionization potential (10.6 eV) and are in close agreement with reaction barrier heights computed on the ground electronic state [2]. Above 15 eV, the $1/t$ decay of channel (3) (Fig. 1(b)) indicates dissociation from a broad internal-energy distribution—evidence of thermal fragmentation from vibrationally excited states of $C_2H_5O^+$ rather than from specific metastable electronically excited states.

[1] T. Nakao *et al.*, Eur. Phys. J. Spec. Top. (*in press*). https://doi.org/10.1140/epjs/s11734-026-02253-7

[2] T. Nakao *et al.*, *submitted.*

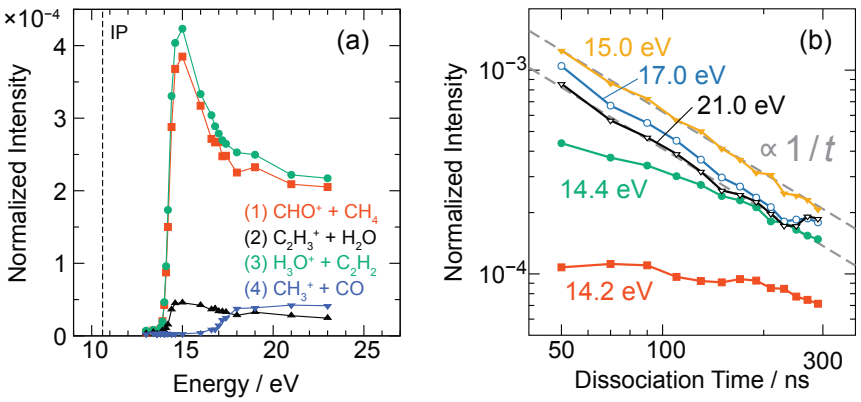

Figure 1. (a) Photon-energy dependence of the normalized intensities of the four delayed-fragmentation channels. (b) Decay profiles of channel (3) at selected photon energies; the dashed lines indicate $1/t$.

3P07 The relationship between photon energy and two translational energy components of the CH_3 fragment in photodissociation of $Zn(CH_3)_2$

(Hiroshima University) Morimoto Takumi, Okuda Yuuka, Haze Misato, Kohguchi Hiroshi

Dialkyl metal complexes ($M(CH_3)_2$: M = Hg, Cd, Zn) exhibit strong dissociative absorption bands in the ultraviolet region, which undergo photodissociation with single and double bond cleavages.[1] The two product pathways that generate the coordinatively unsaturated MCH3 complex and the atomic metal (M) fragments have not been experimentally distinguished, perhaps because of the comparably strong absorption of the parent and the MCH3 radical, hindering detailed understanding of the reaction mechanism. Distinct reaction mechanisms can be disentangled by analyzing differences in the recoil velocity distributions of products arising from competing reaction pathways. In this study, we investigated the photodissociation dynamics of $Zn(CH_3)_2$ using ion-imaging across a range of photolysis wavelengths to distinguish the individual product pathways.

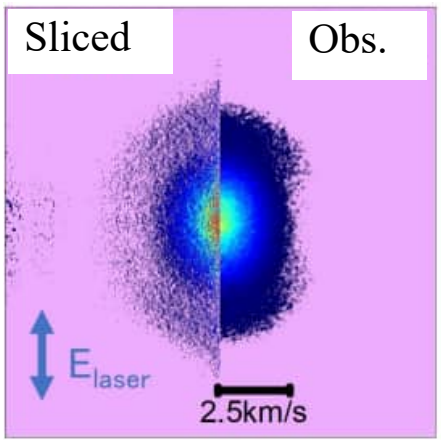

Fig. 1 State-resolved scattering image of the CH_3 fragments in the $Zn(CH_3)_2$ photodissociation exhibiting the fast and slow components

The observed scattering image of the CH_3 fragments state-selectively measured for the vibrational excited states (v_{CH} = 1, v_2 = 1) with the REMPI detection scheme exhibited two velocity components (Fig. 1). We extended our measurements to various photolysis wavelengths with the photolysis (pump) laser power, especially to examine the generation origin of the faster CH_3 components. Our careful measurements of the power dependence of the pump laser excluded the two-photon photolysis that produces the fast and anisotropic components. Meanwhile, the photolysis wavelength dependence indicated a relative increase of the fast components (Fig. 2). Two possible interpretations could explain these observed results, as well as the absence of the fast CH_3 pathway in the v = 0 state. One is the participation of the first (S_1) and second (S_2) excited states in the $Zn(CH_3)_2$ photodissociation with different portions over the 215 – 240 nm region. Another is the onset of secondary photodissociation of the CH_3Zn intermediate at the longer wavelengths.

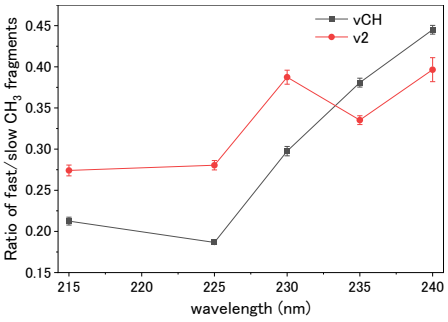

Fig. 2 The ratio of two translational energy components of the CH_3 fragments with respect to the photolysis wavelength.

Reference:

[1] S. J. C. Irvine *et al*, *J. Electrochem. Soc.* **132**, 968–972 (1985).

3P08 Solvent effects on the ground and first excited states of aniline

(Kyushu Univ.) Kazuhiko Ohashi

Solvatochromic shift is the displacement of a spectrum of a solute when it is dissolved in a solvent. Our goal here is to understand the solvatochromic shifts in absorption and emission spectra of aniline ($C_6H_5NH_2$) in various solutions. As a first step toward this goal, we study 1:1 complexes of aniline and a variety of solvent molecules. DFT and TD-DFT calculations are performed for the ground (S_0) and the first excited (S_1) states of such aniline–solvent 1:1 complexes.

Shown at the bottom of Fig. 1 are the optimized geometries for three isomers of the aniline–H_2O complex. In the N-bound isomer, which is most stable in the S_0 state, an H_2O molecule is hydrogen-bonded to the nitrogen atom of aniline. In the H-bound isomer, an H_2O molecule is bound to one of the amino hydrogen atoms of aniline. In the π-bound isomer, an H_2O molecule is attached on the phenyl ring. Subsequently, geometry optimization is carried out in the S_1 state, starting from the S_0 minimum; the results are shown at the top of Fig. 1. The respective minimum is obtained for each of the H- and π-bound isomer. However, no minimum is found for the N-bound isomer; the optimization ends up with the π-bound isomer. All attempts starting from other initial geometries fail to find a minimum corresponding to the N-bound isomer. The H-bound isomer bocomes most stable in the S_1 state; the hydrogen bond is strengthened on the S_1←S_0 excitation from 5 to 11 kJ/mol.

For each isomer, TD-DFT calculations are performed at the S_0 minimum for predicting the S_1←S_0 vertical transition energies and oscillator strengths. The S_1←S_0 transition (absorption) of the N-bound isomer is up shifted (+1152 cm^{-1}), whereas those of the H- and π-bound isomers are down shifted (–470 and –179 cm^{-1}, respectively) from that of the bare aniline. Then the calculations are carried out at the S_1 minimum for gaining information on the S_1→S_0 transition (emission). The transitions of the H- and π-bound isomers are down shifted (–525 and –1004 cm^{-1}, respectively), while that of the unstable N-bound geometry is up shifted (+399 cm^{-1}) from that of the bare aniline.

The points are: (1) the most stable N-bound isomer in the S_0 state shows the largest solvent shift and (2) the corresponding isomer is not stable in the S_1 state and exhibits only a smaller solvent shift. Model structures for aniline in solutions are constructed from MD simulations and used for analyzing the solvatochromic shifts in absorption [1] and emission spectra.

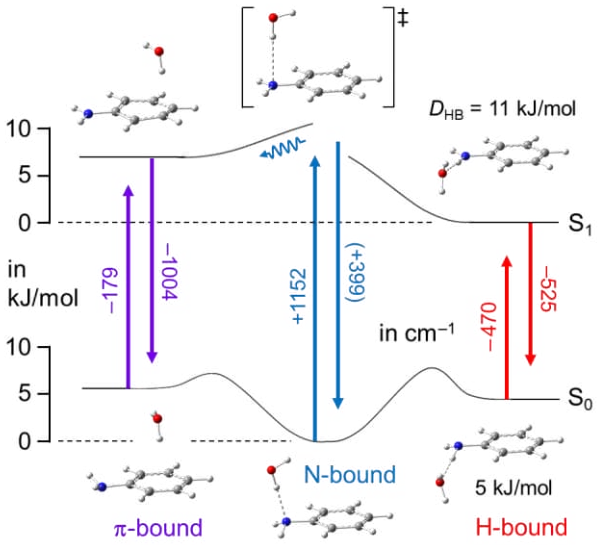

Fig. 1. Optimized geometries in the S_0 and S_1 states of the aniline–H_2O complex embedded in polarizable continuum. Barrier heights are not to scale.

[1] J. Mol. Liq. 436 (2025) 128243.

3P09 Mechanochemical Reaction Path Analysis of Polymer Chain Cleavage

([1]Yamaguchi Univ.) Mori, Itsuki[1]; Sumiya, Yosuke[1]

1. Introduction

Polymeric materials are lightweight and versatile, making them indispensable in modern society. Adhesive polymers are used in automobile manufacturing, construction, and biomedical engineering. Improving the performance of adhesives requires not only enhancing their adhesion strength but also understanding their degradation mechanisms. Under ideal adhesion, degradation is predominantly governed by cohesive failure involving polymer chain scissions, which is regarded as a mechanochemical reaction induced by external forces[1].

Recent theoretical studies have shown that external forces can deform the potential energy surface (PES) **(Fig.1(a))**[2]. Force-induced reactions can be investigated using the artificial force-induced reaction (AFIR) method[3]. The force-modified energy (E^{FM}) is formulated as follows:

$$E^{\mathrm{FM}}(\mathbf{Q}) = E(\mathbf{Q}) - F_{\mathrm{EX}} \frac{\sum_{i\in L}\sum_{j\in R}\omega_{ij} r_{ij}}{\sum_{i\in L}\sum_{j\in R}\omega_{ij}}$$

where an external force F_{EX} is applied to terminal groups L and R. By exploring the E^{FM} surface, force-coupled transition state (TS) structures for chain scission can be identified. This framework was applied to epoxy resin, one of the most widely used adhesives. As target systems, (1) a single polymer chain and (2) an entangled two-chain system were constructed: (1) a fragmented epoxy resin (FER1) shown in **Fig. 1(b)**, and (2) a two-chain system connected by two virtual carbon-chain linkers ($\mathrm{FER2}^{Cn}\times\mathrm{FER2}^{Cn}$) shown in **Fig. 1(c)**. In the (2) system, the effect of polymer chain entanglement on cohesive failure was investigated. Electronic state calculations were performed at UωB97X-D/Def2-SV(P) level.

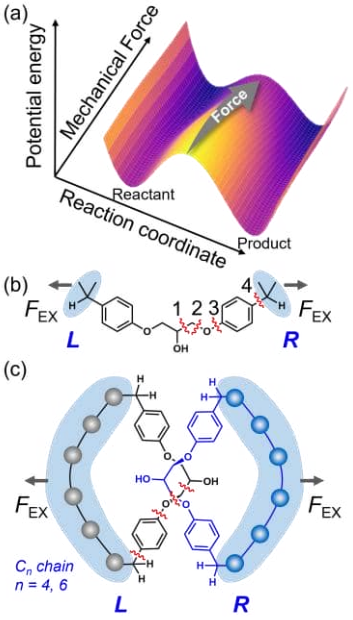

Fig. 1. (a) Modification of PES by external forces. (b) Fragmented epoxy resin (FER1). (c) Entangled chain model ($\mathrm{FER2}^{Cn}\times\mathrm{FER2}^{Cn}$).

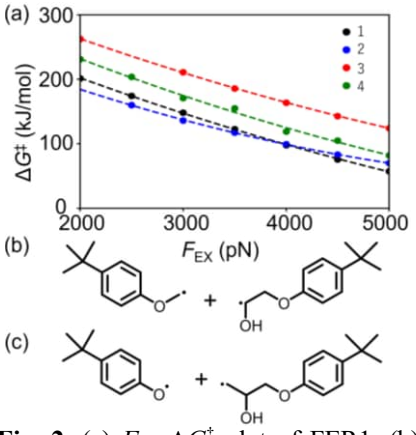

Fig. 2. (a) F_{EX}-$\Delta G^{\ddagger}$ plot of FER1. (b) and (c) Chemical structures showing C.C and C-O bond cleavage, respectively.

2. Results

Fig. 2(a) shows the change in activation free energy $\Delta G^{\ddagger}$ at each cleavage site for FER1 when F_{EX} was varied from 2000 to 5000 pN. An increase in F_{EX} leads to $\Delta G^{\ddagger}$ decrease, indicating that the polymer chain becomes more susceptible to scission. In addition, the preferential cleavage site shifts from a C-C bond (site 1) to a C–O bond (site 2) **(Fig. 2(b), (c))**. In $\mathrm{FER2}^{Cn}\times\mathrm{FER2}^{Cn}$, the $\Delta G^{\ddagger}$ for chain scission becomes smaller than that of the FER1 due to strain energy of the polymer chains.

[1] Y. Tsuji, *Langmuir*, **40**, 7479 (2024). [2] G. Subramanian, *et al.*, *J. Chem. Phys.*, **143**, 134109 (2015).
[3] J. Jiang, *et al.*, *J. Am. Chem. Soc.*, **147**, 32502 (2025).

3P10 Elucidation of the Mechanism of Bifurcation Control in Enzymatic Reactions Based on the Reaction Space Projector Method

(Hokkaido University) Qu, Lihao; Tsutsumi, Takuro; Ono, Yuriko; Taketsugu, Tetsuya

[Introduction] Diterpenes are biomolecules that exhibit diverse physiological activities. Miltiradiene, a representative diterpene, has been studied using reaction path analysis and *ab initio* molecular dynamics (AIMD) simulations in an isolated system. The previous study revealed that reactions from a reactant compound to the miltiradiene precursor involve sequential dynamical branching via post-transition-state bifurcations (PTSBs) (Fig. 1a).[1] These findings indicate that PTSB can lead to byproduct formation in the absence of enzymes. In contrast, biosynthetic reactions yield the miltiradiene precursor, implying that enzymes play a crucial role in suppressing such bifurcations. However, the molecular mechanism by which enzymes regulate PTSBs remains unclear.

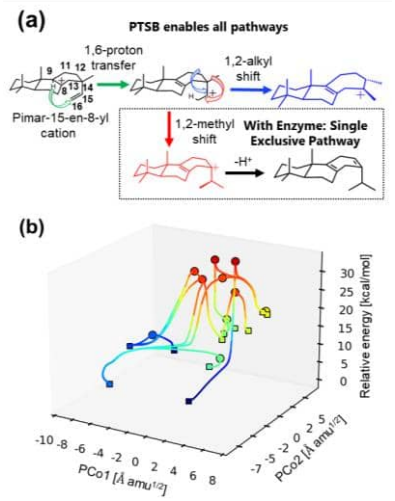

Figure 1. (a) Reaction scheme. (b) Potential energy landscape of the isolated system constructed by the ReSPer-AO method. EQs, TSs, and IRCs are denoted as square, circles, and curved lines, respectively.

To address this issue, we employ the Reaction Space Projector (ReSPer) method, which constructs a low-dimensional reaction space from high-dimensional structural data using a dimensionality reduction technique.[2] The method has been further accelerated by incorporating combinatorial optimization theory (the AO method).[3] In this study, we investigate the mechanism of enzymatic PTSB suppression by combining reaction path analyses and AIMD simulations for isolated, aqueous, and enzyme cluster systems, followed by the ReSPer-AO analysis.

[Results and Discussion] Following previous work on the isolated system,[1] we constructed a reaction path network for the aqueous phase. In addition, an enzyme cluster model was developed for the key reaction pathway leading to precursor formation. AIMD simulations revealed that PTSB occurs more frequently in the isolated system than in the aqueous system, whereas it is suppressed in the enzyme model, resulting in the selective formation of the primary product. Visualization of the potential energy landscape using ReSPer-AO revealed a cluster of transition states with similar energies in the region associated with PTSB (Fig. 1b). Furthermore, projection of AIMD trajectories onto this space showed that structural changes after passing the transition state are restricted in the enzyme model, thereby suppressing PTSB. The detailed mechanism of enzyme-mediated PTSB suppression will be discussed.

[1] Y. J. Hong, D. J. Tantillo, *Nat. Chem.*, **6**, 104, (2014).

[2] T. Tsutsumi, Y. Ono, and T. Taketsugu, *Chem. Commun.* (Feature Article), **57**, 11734, (2021).

[3] L. Qu, T. Tsutsumi, Y. Ono, T. Taketsugu, *J. Chem. Theory Comput.*, **20**, 10931, (2024).

3P11 Accelerating the Mechanistic Study of Triarylborane Catalysts through Virtual Borane

Ken Hirose[1], Satoshi Maeda[1,2], Wataru Matsuoka[1,2] ([1]Hokkaido University, [2]WPI-ICReDD)

Lewis acid catalysis plays an important role in organic synthesis. Triarylboranes (BAr_3) are widely used as Lewis acid catalysts because of their strong Lewis acidity and high chemical stability. Their electronic and steric properties can be tuned by modifying the aryl substituents, enabling control over catalytic reactivity and selectivity. However, the optimization of these properties has traditionally relied heavily on experimental trial-and-error approaches. Even in computational catalyst design, it is generally necessary to compare individual catalysts one by one, making it difficult to directly extract the key factors governing their reactivity.

To address this issue, our group previously developed the virtual ligand (VL) method for phosphine ligands in transition-metal catalysis (Matsuoka W., *et al.*, *ACS Catal.* **2024**, *14*, 16297–16312.). A VL is a mathematical model that reproduces the electronic and steric properties of phosphine ligands in quantum chemical calculations. In addition, we extended this concept to BAr_3 catalysts and establish a virtual borane (VB) model (Hirose K., *et al.*, *J Comput. Chem.* **2025**, *46*, e70285.). In this study, we applied a VB to extract the essential electronic and steric factors determining reactivity without explicitly comparing individual catalysts by performing virtual borane-assisted screening (VBAS), namely parameter screening in the VB space.

We applied VBAS to the BAr_3-catalyzed cycloaddition of tropone with 1,1-diethoxyethene (Li, P.; Yamamoto, H. *J. Am. Chem. Soc.* **2009**, *131*, 16628–16629.). This reaction is known to yield different products depending on the BAr_3 catalyst. First, based on a previous study (Sakata, K. *et al. ACS Omega* **2023**, *8*, 30410–30420.), we demonstrated that a VB parameterized for $B(C_6F_5)_3$ quantitatively reproduces the reaction pathway of the corresponding real $B(C_6F_5)_3$. We then applied VBAS to two competing transition states determining product selectivity. The results revealed that selectivity depends not only on electronic effects but also on steric effects arising from substituent repulsion. Thus, a VB enables the quantitative visualization of electronic and steric effects in parameter space, providing mechanistic insight into BAr_3-catalyzed reactions.

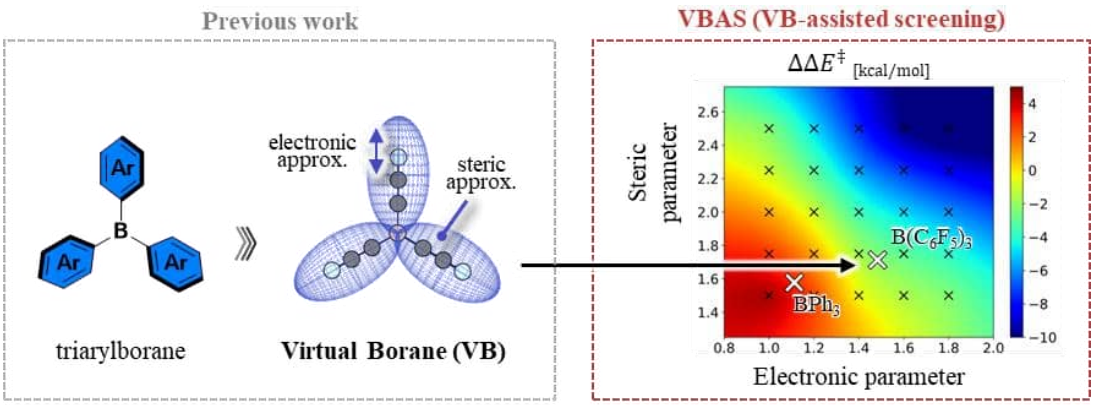

Fig. 1. Schematic of Virtual Borane-assisted screening (VBAS).

3P12 Mechanistic Study on the Degradation of Aliphatic Amines for CO_2 Capture Using Systematic Reaction Path Exploration

([1]Yamaguchi University) Toma Shunta[1], Yosuke Sumiya[1]

1. Introduction

Amine absorption liquids are attracting attention as an effective means of carbon dioxide capture. However, as amine compounds decompose under various environmental conditions, their lifespan remains a challenge. For TMBDA (**1**), a typical amine compound, degradation mechanisms involving protonation (Scheme 1) and oxidative radical reactions (Scheme 2), as shown in Fig. 1, have been proposed [1]. However, their detailed mechanisms and the dominant paths remain unclear. In this study, we thus applied the Artificial Force-Induced Reaction (AFIR) method [2], implemented in the Global Reaction Route Exploration (GRRM) program, to typical aliphatic amines to systematically investigate the degradation reaction pathways. Electronic structure calculations were performed at the ωB97X-D/def2-SV(P) level.

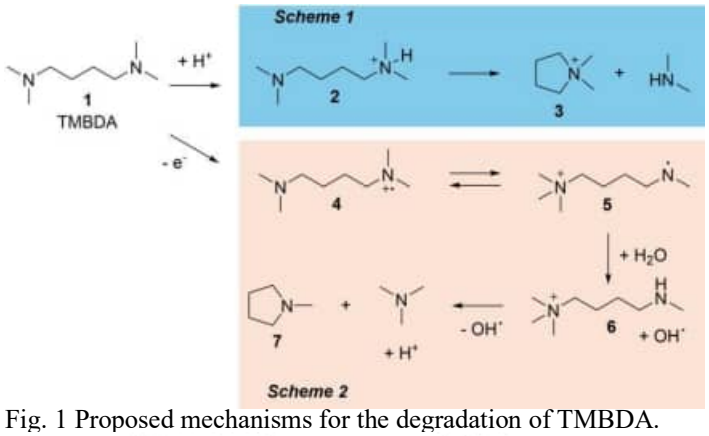

Fig. 1 Proposed mechanisms for the degradation of TMBDA.

2. Results and Discussion

The activation free energies ($\Delta G^{\ddagger}$) in Schemes 1 and 2 were very high. The $\Delta G^{\ddagger}$ for the reaction (**2**→**3**), in which a dimethylamine is released from protonated TMBDA, was 194.3 kJ/mol. The $\Delta G^{\ddagger}$ for the reaction (**4**→**5**), in which a methyl group is transferred, was 251.6 kJ/mol. These reactions do not proceed at the experimental temperature of 140 °C [1]. It was thus suggested that amine degradation proceeds via different mechanisms.

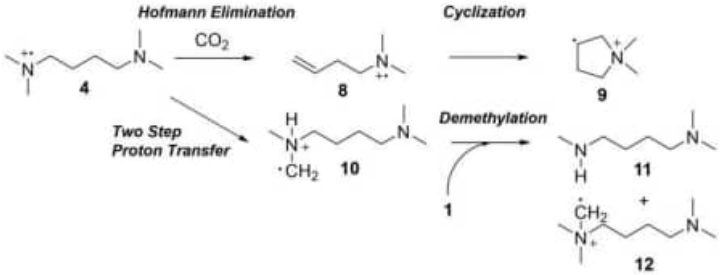

Fig. 2 The obtained mechanisms.

Further reaction path exploration revealed the demethylation reaction (**1**+**10**→**11**+**12**) initiated by the α-hydrogen proton transfer (**4**→**10**), with $\Delta G^{\ddagger}$ of 136.2 kJ/mol (Fig. 2, bottom). Under conditions of high carbon dioxide concentration, a two-step Hofmann-type elimination (**4**→**8**) proceeds easily, followed by the cyclization (**8**→**9**) with $\Delta G^{\ddagger}$ of 74.3 kJ/mol (Fig. 2, top). These results suggest that different reactions proceed depending on the carbon dioxide concentration. Furthermore, the dominant mechanism varied depending on the carbon chain length of the amine. Details of these findings, along molecular design guidelines for suppressing decomposition, will be presented.

[1] H. Lepaumier, et al., *Ind. Eng. Chem. Res.* 2009, 48, 9061.

[2] S. Maeda, et al., *J. Comput. Chem*. 2018, 39, 233.

3P13 Machine-learning extraction of reaction coordinates and transition states in phase space

Noda, Takuto[1]; Md. Al Mehedi, Hasan[2]; Li, Jizhou[2]; Komatsuzaki, Tamiki[1,2,3]
([1]CSE, Hokkaido University, [2]RIES, Hokkaido University, [3]WPI-ICReDD, Hokkaido University)

Chemical reaction dynamics is fundamentally governed by phase-space structures, whereas many data-driven studies have focused primarily on configuration-space descriptions. In chemical physics, Lie canonical perturbation theory (LCPT) provides a rigorous framework for identifying reactive modes and constructing dividing surfaces near a saddle point. However, LCPT generally requires an analytically tractable Hamiltonian, and its practical application becomes increasingly difficult for larger systems. This motivates the development of machine-learning approaches that retain the phase-space viewpoint while reducing the dependence on explicit analytic constructions.

In this study, we investigate a deep-learning framework for extracting reactive coordinate in the neighborhood of a saddle point by using both reaction outcomes and phase-space consistency as supervisory information. The objective is not simply trajectory classification, but the construction of a representation in which the local reactive structure becomes more explicit. As a benchmark system, we consider the Müller–Brown potential, whose reaction dynamics near the saddle region can be analyzed in a physically-transparent manner. Initial conditions are sampled on a fixed energy shell near the saddle, and reactive or nonreactive labels are assigned by basin shooting of momentum-reversal pairs. This setup makes it possible to relate the learned representation directly to local phase-space organization.

The present results indicate that the proposed framework yields a phase-space representation in which the boundary between reactive and nonreactive trajectories becomes visible near the saddle region. Although the current formulation is not yet sufficient for a complete Hamiltonian description in transformed coordinates, the analysis suggests that momentum information plays an essential role in identifying reactive structure. At the same time, the study clarifies an open issue for future development: how to define or compute the momentum associated with newly introduced coordinates while preserving time-reversal symmetry. These results suggest that machine-learning methods informed by phase-space dynamics may provide a useful route toward data-driven reactive coordinate that is more closely connected to chemical-physics concepts such as reactive mode and dividing surfaces.

3P14 Exploring Valley-Ridge Inflection Regions in Post-Transition State Bifurcation Reactions

(1*Saitama University*, 2*Tokyo Metropolitan University*) Yamaki, Keita[1]; Okamoto, Daichi[1]; Hayashi, Daiki[1]; Nakagawa, Shoto[1]; Matsubuchi, Hayato[1]; Sasaki, Yuki[1]; Takayanagi, Toshiyuki[1]; Murakami, Tatsuhiro[2]

Reactions in which multiple distinct product channels originate from the same transition state (TS, near an index-1 saddle point) are called post-transition state bifurcation (PTSB) reactions. Predicting and controlling the product branching ratios of the PTSB reactions is a fundamental challenge in theoretical chemistry. While the branching ratios can be estimated to some extent from the structure and momentum at the TS, such simple predictions break down when the reaction path length from the TS to the bifurcation point is long. Consequently, characterization of the bifurcation point is crucial both for predicting selectivity and for elucidating the underlying reaction mechanism.

In essence, a bifurcation point can be defined as a specific point, namely, VRT (valley-ridge transition) or VRI (valley-ridge inflection), on a potential energy surface (PES) where the topography changes from a stable "valley" into an unstable "ridge". The VRT point and VRI points are commonly used as indicators for bifurcation region[1]. A VRT is typically identified through vibrational analysis along the intrinsic reaction coordinate (IRC), but several issues have been reported with this approach [2, 3]: (1) the IRC is inherently a non-branching path, (2) it is not necessarily the minimum energy path, and (3) a VRT does not always lie on the IRC. For this reason, identifying "VRI manifolds" which intrinsically characterizes the bifurcation is highly valuable.

In this study, we investigated the PTSB reactions in asymmetric organic molecular systems, as shown in Figure 1. We implemented a direct VRI search algorithm based on the method of Ref. [4] and successfully identified points on VRI manifolds. By systematically varying the tether connecting the two reactive moieties, we found that the positions of the VRT and VRI shift significantly. These shifts in position correlate strongly with the product branching fractions obtained from molecular dynamics (MD) simulations. In this presentation, we will describe the technical implementation of the algorithm, discuss how the relative positions of VRT and VRI govern the branching mechanism, and present in detail the mathematical properties and theorems of VRI that form the basis of this research.

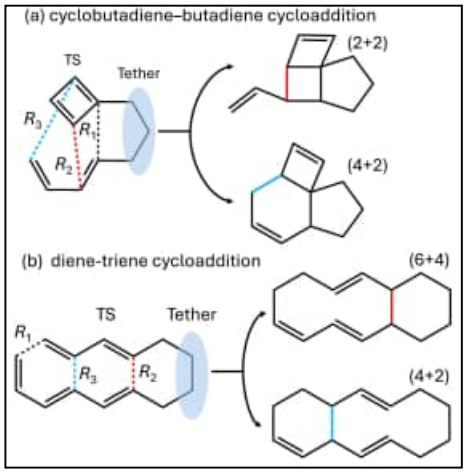

Figure. 1. Reaction schemes

References
[1] J. M. Bofill, W. Quapp. *J. Math. Chem*. **2013**, *51*, 1099.
[2] W. Quapp, G. H. H. Chuang, J. M. Bofill. *Theor. Chem. Acc.* **2025**, *144*, 67.
[3] W. Quapp. *J. Chem. Phys*. **2015**, *143*, 177101.
[4] B. Schmidt, W. Quapp. *Theor. Chem. Acc*. **2013**, *132*, 1305.

3P15 Machine Learning-based Multi-objective Optimization of reaction condition of ^{211}At Astatination Reactions

(Hokkaido University[1], National Institute of Advanced Industrial Science and Technology[2]) T. Kitano[1], Y. Mizuno[2, 1], A. Mukaimine[1], S. Hashiba[1], K. Nakajima[1], K. Tabata[1], M. Ogawa[1], T. Komatsuazaki[1]

We develop an informatics-driven framework to optimize reaction conditions for nucleophilic ^{211}At-astatination [1]. This reaction produces ^{211}At-labeled compounds with potential use in nuclear medicine, but also generates byproducts. Because separation is constrained in clinical settings, conditions must be identified that simultaneously maximize the yield of the desired product and suppress byproduct formation. This naturally leads to a multi-objective optimization problem.

The framework iterates the following procedure. (1) An Extra Trees Regressor [2] is trained on available data to predict the yields of the main product and byproducts, together with their uncertainties. (2) each candidate condition, an optimistic estimate is computed using the upper confidence bound (UCB) for the main product and the lower confidence bound (LCB) for byproducts. (3) A scalar satisfaction score is then calculated from these estimates and predefined aspiration levels [3]. (4) The top-ranked conditions are clustered (k-means, k= 10), and one representative from each cluster is selected to ensure diversity. (5) The selected conditions are experimentally evaluated.

The effectiveness of the approach is validated through both experiments and simulations. In particular, we show that the algorithm reaches the target aspiration levels within a comparable number of iterations across different initial samplings. Because the number of feasible experiments is limited, we additionally employ a noise-inclusive data generator constructed from real data. Starting from multiple random initial datasets, the algorithm sequentially proposes new conditions, and their outcomes are evaluated using this generator.

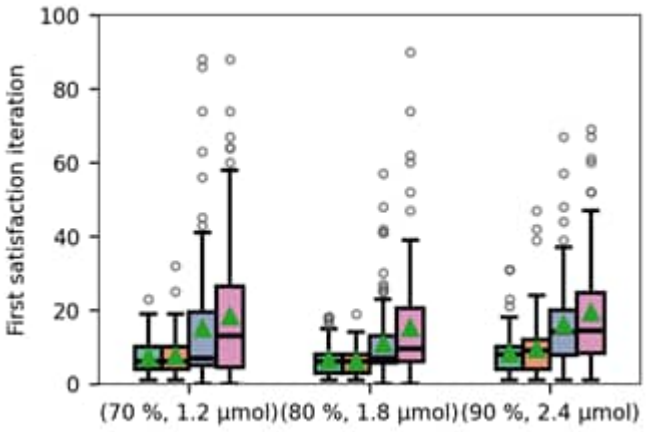

Figure 1 Distribution of iterations to first satisfy the aspiration criteria for different targets. Colors: green (proposed, with clustering), orange (proposed, without clustering), blue (MOTPE, with clustering), purple (MOTPE, without clustering).

We simulated how quickly our algorithm, and a conventional method (MOTPE) can identify conditions that satisfy the aspiration criteria under multiple target settings (Fig. 1). The proposed method with clustering generally requires fewer iterations to reach the aspiration criteria compared to the other approaches, indicating improved efficiency in the search process.

[1] K. Matsuoka *et al. Org Biomol Chem*, vol. 19, no. 25, pp. 5525–5528, 2021.
[2] P. Geurts, D. Ernst, and L. Wehenkel, Mach Learn, vol. 63, pp. 3–42, 2006.
[3] H. Nakayama and Y. Sawaragi, IFAC Proceedings Volumes, vol. 17, no. 2, pp. 1345–1350, Jul. 1984.
[4] Y. Ozaki *et al*. *Proceedings of the 2020 genetic and evolutionary computation conference*. 2020.

3P16 Can Reactive Species Be Spontaneously Formed at the Air−Water Interface of Microdroplets? A Spray Ionization Mass Spectrometry Investigation

Kei Kurokawa, Naoki Numadate, Shinichi Enami

[Introduction]

Water microdroplets and the air-water interface (AWI) are unique media, which can increase rate constants and open unique reaction pathways for some reactions. Recently, there have been reports that reactive species such as hydroxyl radical[1], hydrated electron (e_{aq}^-)[2], and ozone anion[3] are spontaneously formed at the AWI of microdroplets. However, the spontaneous formation of reactive species from unactivated water microdroplets is questioned.[4][5]

In this study, we focus on e_{aq}^- and quantitatively examine whether e_{aq}^- is spontaneously formed by using spray ionization mass spectrometry (SIMS), combined with the use of glutathione disulfide (GSSG) as a scavenger of e_{aq}^-. GSSG reacts with e_{aq}^- to form glutathione anion (GS^-).[6]

$$GSSG + e_{aq}^- \rightarrow GSSG^{\bullet -}$$

$$GSSG^{\bullet -} \rightarrow GS^{\bullet} + GS^-$$

The rate constant of the first step of reaction is sufficiently large, i.e., $3.7 \times 10^9\ M^{-1}\ s^{-1}$. GSSG and other e_{aq}^- scavengers are used to derive the yield of spontaneously formed e_{aq}^- from water microdroplets.

[Experiments]

Aqueous GSSG solution was introduced into the SIMS chamber as microdroplets by a stainless nebulizer. Negative ion mass spectral signals of GSSG and GSH at the AWI of microdroplets were then detected using a time-of-flight mass spectrometry (Agilent 6230 Accurate-Mass TOF LC/MS) and a quadrupole mass spectrometry (Agilent 6130 Quadrupole LC/MS System).

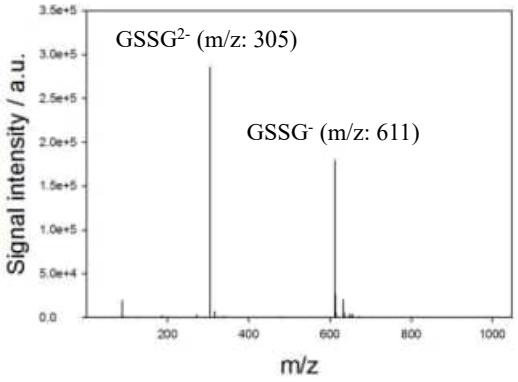

Figure 1. Negative ion mass spectrum obtained from water microdroplets containing 100 μM GSSG.

[Results]

In the negative ion mass spectrum of aqueous GSSG microdroplets, the prominent peaks of GSSG, for example, m/z: 305 ($GSSG^{2-}$) or m/z: 611 ($GSSG^-$), were observed as shown in Figure 1. However, the peaks of GSH such as m/z 306 (GS^-)[7] were below detection limit. Separate experiments using a standard GSH solution enabled us to derive the upper limit of spontaneously formed e_{aq}^- from microdroplets under the present experimental conditions. The data obtained from experiments using different e_{aq}^- scavengers will also be discussed.

[Reference]

[1] Lee et al., *PNAS*, **2019**, 116, 19294 [2] Chen et al., *Angew. Chem. Int. Edt*. **2025**, 64, 368 e202424662

[3] Meng et al., *J. AM. Chem. Soc*. **2025**, 147, 23399 [4] Enami *J. Phys. Chem. Lett*. 2025, 16, 11604

[5] Chen and Willams, *Angew. Chem. Int. Ed*. **2024**, 63 (51), No. e202407433

[6] Hofstetter et al., *Chem. Res. Toxicol*. **2010**, 23, 1596 [7] Enami et al, *J. Phys. Chem. Lett.* **2015**, 6, 3935-3943

3P17 Transient diffusion of radicals induced by surface reactions at 10 K

(Hokkaido Univ.) Atsuki Ishibashi, Hiroshi Hidaka, Arisa Iguchi, Naoki Watanabe

In interstellar molecular clouds, various molecules are formed despite environments of ultra-high vacuum and low temperature (~10 K), which are generally unfavorable for chemical reactions. In such conditions, the surfaces of ice particles floating in the clouds play a pivotal role in molecular formation; reactions proceed efficiently as atoms and molecules are accumulated on the cryogenic surface and heat of reaction can dissipate into the surface. In many cases, the surface reactions are rate-limited by the diffusion of the reactants. It is known that reactions involving H atoms, which are capable of thermal diffusion even at 10 K, are particularly important for molecular formation (relatively simple molecules such as H_2O, CH_4, NH_3, and CH_3OH) in these regions [1]. On the other hand, the synthesis of more complex molecules requires reactions between "heavy radicals" such as CH_3O, CH_3, and NH_2. However, at the temperatures as low as 10 K, thermal diffusion of these heavy radicals is generally negligible. Therefore, for the formation of complex organic molecules under such cold conditions, non-thermal radical association processes are essential. In this study, we focus on the phenomenon of “non-thermal transient diffusion,” in which radicals generated by surface reactions migrate over a specific distance during dissipating their reaction heat to the surface prior to thermalization. To clarify the transient diffusion is challenging with conventional methods like infrared spectroscopy. To address this, we employed a newly developed, highly sensitive surface analysis technique [2, 3].

In our experiments, by investigating the chemical reactions between radicals generated at spatially well-separated sites, we obtained evidence of transient diffusion and information regarding the diffusion distance. Four types of molecules, (1) CO, (2) CH_3OH, (3) CH_4, and (4) NH_3, were deposited on ice with trace amount of OH radicals (up to 0.01 ML) at 10 K, respectively. If the reactant radicals, (1) HOCO, (2) CH_3O and CH_2OH, (3) CH_3, and (4) NH_2, that can be formed by “primary reactions” as below, CO + OH, CH_3OH + OH, CH_4 + OH, and NH_3 + OH, respectively, transiently diffuse to encounter another OH radical, “secondary reactions” may occur (see Figure). Since both reactant radicals and OH are immobile via thermal diffusion at 10 K, the occurrence of secondary reactions under these experimental conditions provides evidence that these processes are driven by transient diffusion. Therefore, analyzing these products provides information on transient diffusion.

Reference
1. Hama & Watanabe 2013, Chem. Rev. 113, 8783.
2. Ishiabshi et al., Astrophys. J. Lett. 921, L13 (2021).
3. Kang, Bull. Korean Chem. Soc. 32, 389 (2011).

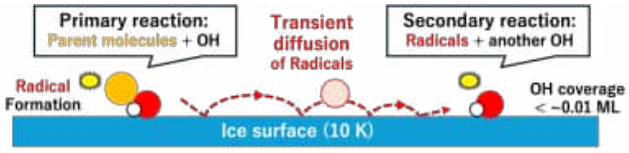

Figure. Experimental scheme for investigating surface transient diffusion using sequential radical reactions as a probe.

3P18 Theoretical investigation of the structure and electronic properties of N_2O adsorbed on an Ir_{20} cluster.

([1]Hokkaido University, [2]AIST) Nino Uchiyama[1], Tetsuya Taketsugu[1], Satoshi Hinokuma[2], Takeshi Iwasa[1]

[Introduction] Catalytic decomposition of nitrous oxide (N_2O) is important because of its high global warming potential. Among various catalysts, iridium catalysts exhibit high activity for N_2O decomposition[1)], but the reaction mechanism remains unclear. To gain insights into the reaction mechanism of N_2O decomposition on Ir nanoparticle catalysts, we performed a first-principles investigation of N_2O adsorbed on a tetrahedral Ir_{20} cluster.

[Methods] Thirty structures with different N_2O adsorption sites and orientations were optimized, and their vibrational and electronic properties were analyzed. Quantum chemistry calculations were carried out using TURBOMOLE at the RI-B3LYP-D3/def-SV(P) level.

[Results and Discussion] We obtained 21 molecular adsorption structures and 9 dissociative adsorption structures. The molecular adsorption structures of N_2O on the Ir_{20} cluster were classified into seven types based on their adsorption modes. Three representative structures, one linear adsorption structure (**1a**) and two bent adsorption structures (**1b, 1c**) are shown in Figure 1.

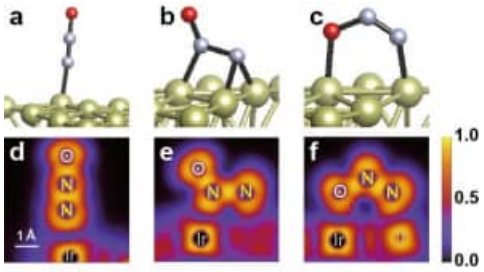

Figure 1. N_2O adsorbed structures and ELF.

Negligible charge transfer between N_2O and Ir_{20} was observed for **1a**, whereas substantial electron transfer from Ir to N_2O was found for **1b** and **1c** via back-donation[2)]. The electron localization function (ELF)[3)], shown in Figures 1d–f, indicates that the regions with high ELF values in **1b** and **1c** extend toward the Ir cluster, suggesting the formation of chemical bonds between N_2O and Ir. In contrast, the low ELF value between N and Ir in **1a** indicates physisorption. Compared with the ELF of **1a**, the distributions around the N–N bond in **1b** and the N–O bond in **1c** are narrower, suggesting weaker N-N and N-O bonds in adsorbed N_2O than in the free molecule.

By comparing the calculated IR spectra with the experimental data, the peaks in the 1200–1800 cm^{-1} range, which were previously attributed to byproducts[1)], can instead be assigned to the bent N_2O species. Furthermore, as shown in Figure 2, the N–N stretching mode in **1b** and the N–O stretching mode in **1c** exhibit the largest redshifts among the seven adsorption structures, respectively. These large redshifts strongly suggest that **1b** is an intermediate leading to N–N bond dissociation, whereas **1c** is an intermediate leading to N–O bond dissociation. Future work will focus on identifying the reaction pathways and transition states for N_2O decomposition on Ir_{20}.

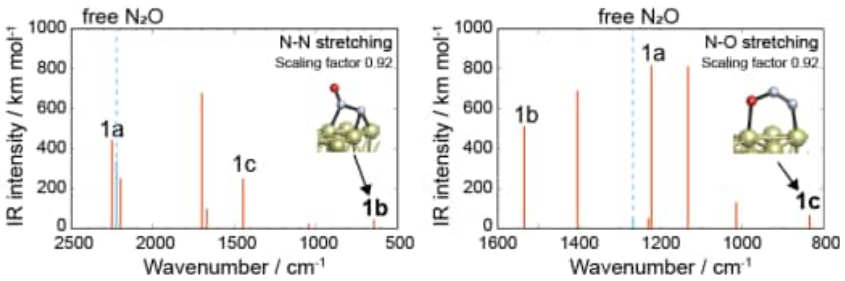

Figure 2. IR peaks of N-N or N-O stretching nodes.

[References]

1) S. Hinokuma, T. Iwasa, et al., *Catal. Commun.*, **149**, 106208 (2021).

2) R. Hoffmann. *Rev. Mod. Phys.*, **60**, 601 (1988).

3) A. Savin, et al., *Angew. Chem. Int. Ed. Engl.*, **36**, 1808-1832 (1997).

3P19 A near-edge x-ray absorption fine structure study of products in ice film by monochromic soft x-ray irradiation

(1:TIRI, 2:Ibaraki Univ., 3:JAEA, 4:QST) S. Nakagawa[1], Y. Obata[2], Y. Baba[3], A. Yokoya[2,4]

Photo- and Auger- electrons are emitted when materials are irradiated with soft X-rays. Interaction of electrons induces ionization and super-excitation of molecules to produce activated species, such as cations, secondary electrons, and radicals. In liquid water, the thermalization lengths of electrons with initial energies below several hundred eV have been estimated to be less than 10 nm.[1)] Then, the concentration of activated species produced by soft X-rays and ejected electrons will be extremely high in a narrower region. The higher concentration will induce the loss of products because of recombination of activated species. The yield of products will be affected by energies of soft X-rays and ejected electrons. In this study, the relative yield of OH in ice film by irradiation of soft X-rays whose energies were 1000- and 1600-eV, was investigated using a near-edge x-ray fine structure (NEXAFS) technique.

Experiments were performed at Photon Factory on the BL-13B, which is the AppleII-type undulator beamline equipped with a plane grating monochromator (energy resolution of approximately 200 meV at 867 eV). The flux of circular polarized photons was controlled by the gap between the magnetic arrays of insertion devices. The irradiation and the NEXAFS measurements were conducted on a high vacuum chamber connected to the beamline. The total electron yield was measured by the micro-channel plates biased at 1.98 kV and the NEXAFS spectra were obtained as the ratio of the photocurrent. The ice films were deposited on a clean Au(111) surface mounted on a rotatable sample holder at 20 K by exposing H_2O vapor of $5x10^{-7}$ Torr for 100 sec. The thickness of the ice film was estimated to 20-30 nm.[2)] After irradiation, the NEXAFS measurements have been done. To eliminate the irradiation effect during the NEXAFS measurements, a fresh area was used for each irradiation.

The peak at 526 eV assigned as OH was observed after irradiation. The integrated intensities of OH relative to the O1s $\longrightarrow 4a_1$ transition of H_2O (535 eV) increased with the irradiation flux and saturated. Other products, O, HO_2, O_2 and H_2O_2 were also observed as same as the previous report[2)] by 1000-eV X-ray irradiation with higher flux. The yield of OH versus absorbed dose which is estimated by photon flux, irradiation time, photon energy and absorption efficiency, showed that OH was produced effectively by X-ray irradiation with 1600-eV than that with 1000-eV. The energies of photoelectrons from the O-*K* edge by X-ray irradiation with 1000- and 1600-eV are 460- and 1060-eV, respectively. The thermalization length of the former would be shorter than the latter.[1)] The concentration of activated species and mechanism of the OH production will be discussed.

This work was performed under the approval of the Photon Factory Program Advisory Committee (No. 2025G114). The authors thank Prof. Kenichi Ozawa for his help in experimental setup and his support during runs.

References: 1) R. Signorell, Phys. Rev. Lett., 124, 205501 (2020).

2) C. Laffon, et al., J. Chem. Phys., 125, 204714 (2006).

3P20 Nonlinear photocurrent generation in SiO_2 device by ω-2ω asymmetric strong laser fields

([1]Grad. Sc. Sci., Nagoya U.; [2]RCMS, Nagoya U.)
Hiroshi Kinoshita[1], Ryutaro Matsumoto [1], Mizuho Fushitani [1], Akiyoshi Hishikawa [1, 2]

[Introduction] Recent advances in laser technology allow us to generate light-field-driven photocurrents in homogeneous media by spatially asymmetric laser pulses. Compared with single-color carrier-envelope-phase (CEP) stabilized few-cycle lasers that have been widely used in previous researches [1], two-color phase-locked ω-2ω laser pulses offer pronounced field asymmetry and longer pulse durations [2], facilitating larger photocurrents. Despite these advantages of ω-2ω pulse, the application has been limited for small bandgap materials whose carriers are driven by one-photon absorption of 2ω laser pulse. In this work, we demonstrate nonlinear control of transient photocurrent in a wide bandgap material, SiO_2, using intense ω-2ω laser fields.

[Experimental] The output of Ti:Sapphire laser system (ω: 800 nm, 50 fs, 1 kHz) was partly converted to the second harmonic (2ω: 400 nm, 65 fs) by a β-BBO crystal to obtain ω-2ω laser pulses, The time delay and relative phase between the ω and 2ω pulses controlled by α-BBO crystal and a pair of wedge plate, the positions of the wedge plates was controlled by a stepping-motor stage for a coarse time delay, and by a voice coil stage to modulate the relative phase with a frequency of 16 Hz. The collinearly propagating ω and 2ω laser pulses were polarized in parallel each other by a dual wave plate and focused on a SiO_2 device between electrodes (Fig. 1 (a)). The generated photocurrent signals were detected by a boxcar integrator and a lock-in amplifier.

[Result and Discussion] Figure 1 (b) shows lock-in photocurrent signals as a function of the time delay. The transient photocurrent varied its flow direction in a periodic manner when the ω and 2ω laser pulses were temporally overlapped. The transient current signal oscillates with a period of 1.33 fs corresponding to the frequency of the 2ω laser at 400 nm. The maximum photocurrent amplitude 250 pA (Fig. 1 (c)) was achieved at 0.6 V/Å for ω, and 1.2 V/Å for 2ω, which are substantially smaller than 7.2 V/Å needed for a CEP stabilized pulse to generate to 20 pA [3]. The waveform dependent periodic photocurrent in SiO_2 using ω-2ω pulses can be explained by a theoretical model [4] based on electron acceleration by virtual transitions in multi-photon processes with asymmetric laser pulses.

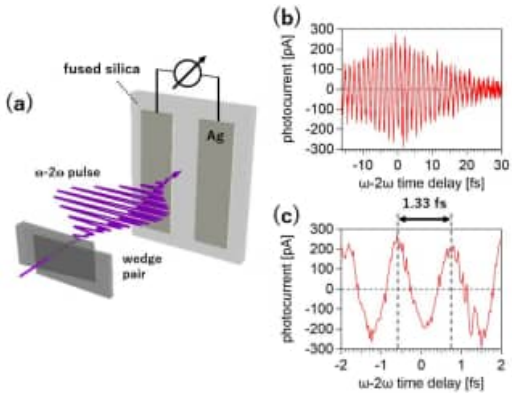

Figure 1. (a) Schematic experimental setup for photocurrent measurement. (b) Waveform dependent photocurrent of SiO_2 device as a function of the time delay between ω (0.6 V/Å) and 2ω (1.2 V/Å) laser pulses from -15 fs to 30 fs. (c) The same as (b), but from -2 fs to 2 fs.

[1] A. Schiffrin *et al., Nature*, **493**, 70 (2013). [2] C. Heide *et al., Nanophotonics*, **10**, 3701 (2021). [3] T. Paasch-Colberg, Doctoral dissertation, (Technische Universität München, 2014). [4] J. B. Khurgin *et al., J. Opt. Soc. Am. B,* **33**, C1 (2015).

3P21 Syntheses and evaluation of photocatalytic activities of the composites of antimony halide perovskites and graphitic carbon nitride

(Hosei Univ.,[1] Hosei Univ. Res. Cntr. Micro-Nano Technol.[2])
Akiyama,Sogo[1]; Iitaka,Fumiaki[1]; Kadota,Yusuke[1]; Mitsuke,Koichiro[1,2]; Ogata, Hironori[1,2]

Dimeric $Sb_2X_{10}^{4-}$ anion units in antimony halide perovskites $(C_5H_5NI)_4Sb_2X_{10}$ (X = Cl or Br) are formed by edge-sharing of two octahedral metal centers via two bridging halide ligands. Despite being highly confined pseudo-zero-dimensional systems, the $Sb_2X_{10}^{4-}$ units give rise to semiconductive band-gap energies because they create supramolecular networks involving large iodopyridinium cations [1]. Here, we have synthesized nanocomposite materials between $(C_5H_5NI)_4Sb_2X_{10}$ and graphitic carbon nitride g-C_3N_4 and then attempted to investigate their photocatalytic activities by applying them to degrade Rhodamine B under visible light irradiation.

The bulk synthesis of g-C_3N_4 was carried out through a thermal polycondensation using melamine $C_3H_6N_6$. Thus formed g-C_3N_4 was dissolved in water together with antimony oxide Sb_2O_3, and C_5H_4IN, followed by sonication, addition of concentrated hydrohalic acid HX, and hot-stirring. After letting the mixed solution sit for 24 hours we added pure water, separated the precipitate from the mixture, and dried the precipitate at 60 - 80 °C. This precipitate had included also the residues recovered from two times centrifuging the supernatant of the mixed solution. In what follows we will refer to this dried precipitate as unidentified nanocomposites NC1. For comparison we synthesized single crystals of the antimony halide perovskite by dissolving Sb_2O_3 and C_5H_4IN in HX at 50 – 80 °C. These single crystals have been identified to $(C_5H_5NI)_4Sb_2X_{10}$ from the powder X-ray diffraction (PXRD) analyses (see Fig.1 (c) for X = Br).

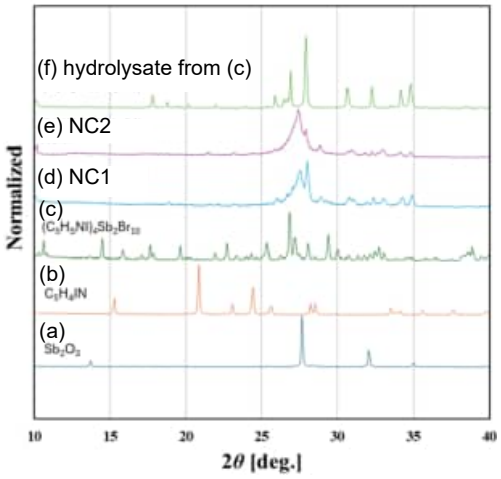

Fig.1. PXRD patterns of antimony bromide perovskites, raw materials, and nanocomposites.

Fig. 1 includes the PXRD patterns of (a) Sb_2O_3, (b) C_5H_4IN, (c) $(C_5H_5NI)_4Sb_2Br_{10}$, and (d) NC1. Trace (e) is due to the residue named NC2 that was retrieved from NC1 after the degradation experiment for Rhodamine B. Moreover, we dipped $(C_5H_5NI)_4Sb_2Br_{10}$ of (c) into water and obtained hydrolysate product that yields trace (f). Comparison between the patterns of (c), (d), and (f) implies that the antimony halide perovskites may rather decompose when they interact with H_2O. We constructed Tauc plots from photoabsorption spectra of the $(C_5H_5NI)_4Sb_2X_{10}$ single crystal. The slopes at the absorption edges exhibit involvement of indirect allowed transitions with the optical band gaps of E_g = 1.6 eV. The curves of the thermal gravimetric and differential thermal analysis (TG-DTA) reveal higher thermal stability for $(C_5H_5NI)_4Sb_2X_{10}$ than for traditional lead halide perovskites, such as NH_4PbX_3. The details of the degradation experiments for Rhodamine B will be explained at the venue.

[1] A.D. Nicholas et al., J. Phys. Chem. C, **2020**, *124*, 25686−25700.

3P22 Electron momentum spectroscopy of aniline: Towards molecular orbital imaging of the excited triplet state

([1]Science Tokyo, [2]Tohoku Univ., [3]Keio Univ.) T. Sato[1], Y. Mori[1], M. Takahashi[2], Y. Ohshima[1], M. Yamazaki[1,3]

[Introduction] In the triplet state, electrons with parallel spins cannot occupy the same region of space due to exchange interaction, resulting in a substantial change in electron distribution that governs molecular structure and chemical reactivity. Therefore, directly probing the electron distribution of the T_1 state is essential for understanding photochemical processes. One of the techniques capable of directly probing such electron distributions is electron momentum spectroscopy (EMS) [1]. In this study, we aim to observe the T_1 state of aniline (~200 ns [2]) using a highly sensitive EMS apparatus [3]. Here, we report results of EMS measurements on the ground state S_0 aniline and of theoretical calculations on S_0 and the excited states.

[Experiment and theoretical calculation] Briefly, an electron impact ionization of an aniline molecule in an effusive molecular beam was induced, and scattered and ionized electrons with a scattering angle of 45° ± 1.0° and azimuthal angle ranging over 15°–165° and 195°–345° were introduced into the spherical electron energy analyzer. In the calculations, electron momentum distributions for each Kohn-Sham orbital were obtained at the (U)B3LYP/aug-cc-pVDZ level, using the optimized geometries for the S_0, S_1, and T_1 states reported in the literature [4].

[Results and Discussion] Fig. 1 compares the experimental electron momentum distribution of the outermost orbital in the S_0 state with theoretical results, showing good agreement to each other. For comparison, the theoretical distributions for the S_1 and T_1 states are also included. It was found that the T_1 distribution differs significantly from the others, reflecting its characteristic electron distribution. In the triplet state, exchange interaction reduces π conjugation and induces σ character around the C–N bond, accompanied with the nitrogen atom being out of the ring plane [4]. This is manifested in the momentum distribution as an increased intensity near the momentum origin, which can be understood from the modification of the orbital shape shown in Fig. 2, reflecting increased σ-like contribution. Progress toward experiments on the excited state will also be reported in this presentation.

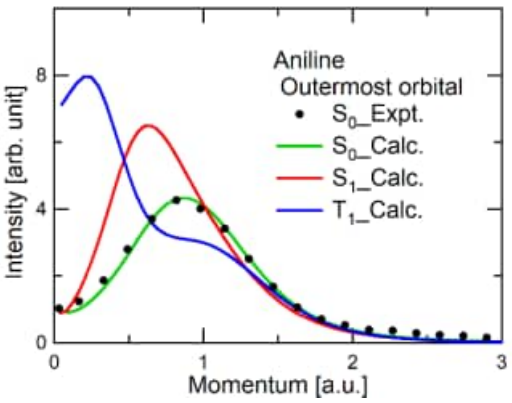

Fig. 1. Comparison of electron momentum distribution for outermost orbitals of aniline

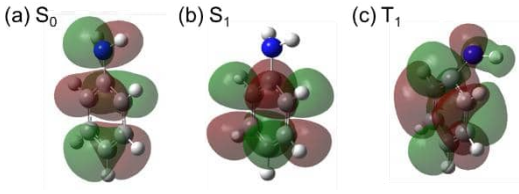

Fig. 2. The outermost orbital shapes of (a)S_0, (b)S_1, and (c)T_1 states

[1] M. Takahashi *Bull. Chem. Soc. Japan*. **82**, 751 (2009). [2] J. K. Knee and P. M. Johnson *J. Chem. Phys*. **80**, 13 (1984). [3] T. Sato *et al. J. Chem. Phys*. **163**, 114301 (2025). [4] X. J. Hou *et al. J. Phys. Chem. A* **109**, 10396 (2005).

3P23 Toward Time-Resolved Core-Level Spectroscopy Beyond Oxygen K-edge Using an Ultrashort Soft X-ray Light Source

(Kansai Institute for Photon Science, QST) ISHII, Nobuhisa; SUN, Hung-Wei; MARUYAMA, Momoko; ITAKURA Ryuji

Recent advances in fully coherent, laser-based SX sources enable direct access to ultrafast measurements of nuclear and electronic dynamics. This capability is particularly important in the water window region, where water is transparent between the carbon *K* edge at 280 eV and the oxygen *K* edge at 540 eV [1]. Time-resolved measurements using laser-based SX sources have demonstrated light-induced chemical reactions in the gas phase [2], real-time observation of electronic, vibrational, and rotational dynamics in nitric oxide [3], and femtosecond proton transfer in aqueous urea solutions [4]. These demonstrations rely on high-harmonic generation (HHG) driven by long-wavelength laser sources operating at central wavelengths of 1600-1700 nm. However, the photon flux decreases rapidly at higher energies, limiting its spectral coverage up to the nitrogen K-edge at 400 eV and the titanium L-edge at 450 eV.

To overcome this limitation, we have developed a high-power, femtosecond infrared light source (1700-2500 nm, 1.32 mJ, 19.5 fs, 5 kHz) based on optical parametric chirped-pulse amplification using a 1030-nm Yb:YAG thin-disk laser as a common source providing both pump and seed pulses. With this light source, we demonstrated the HHG extending up to 620 eV and performed x-ray absorption near edge structure (XANES) measurements of gaseous media across the entire water window [5].

In this presentation, we describe the development of a pump-probe setup in which a part of the fundamental laser at 2000 nm is used as a pump, while the remaining part drives soft x-ray HHG to serve as a probe, as illustrated in Fig. 1. Currently, 40% of the infrared output is used to ionize nitric oxide molecules, while the remaining 60% is used to generate the SX probe pulses. Details of the experimental setup and measurement results will be presented.

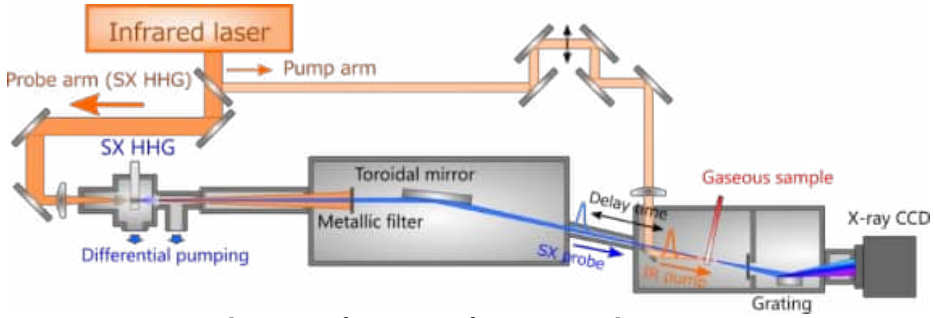

Fig. 1. Schematic of our setup for pump-probe measurements.

References

[1] N. Ishii, K. Kaneshima, K. Kitano, T. Kanai, S. Watanabe, and J. Itatani, Nature communications **5**, 3331 (2014).

[2] Y. Pertot *et al.*, Science **355**, 264 (2017).

[3] N. Saito *et al.*, Optica **6**, 1542 (2019).

[4] Y. Zhong *et al.*, Nature **619**, 749 (2023).

[5] N. Ishii, M. Maruyama, and R. Itakura, Opt. Lett. **51**, 456 (2026).

3P24 Distribution of ions at the air-water interface investigated by spray ionization mass spectrometry

(University of Tsukuba) Kento Kosugi, Naoki Numadate, Shinichi Enami

At the air-water interface, chemical species (i.e., molecules, ions, radicals) indicate unique reactivities compared with in the bulk-phase. For example, it has been experimentally demonstrated that the photochemical reaction of phenol becomes ultrafast at the air-water interface.[1] Another example is that the oxidation process of iodide anion by gas-phase ozone proceeds much faster at the air-water interface than expected in the bulk water phase.[2] In ambient atmospheric conditions, such interface-specific reactions are expected to occur on the air-water interface of aerosols, cloud droplets and sea surfaces, influencing on the atmospheric multiphase chemistry. The distribution of atmospherically relevant ions at the air-water interface is a key to understanding the mechanism of interface-specific reactions. However, the origin of why specific ions accumulate at the air-water interface still remains unclear.

In this study, we report the measurements of the relative number density of both inorganic/organic ions at the air-water interface at variable concentrations using an interface-selective spray ionization mass spectrometry (SIMS).[3] SIMS enables a selective measurement of ions at the air-water interface by a bag breakup mechanism as shown in Figure 1.

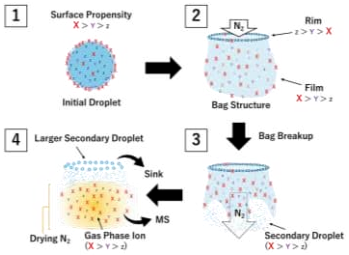

Fig. 1 The schematic illustration of a bag breakup mechanism.

Figure 2 shows the signal intensities derived from 10 nM sodium carboxylate (R_NCOONa, N =1~9) mixture solution as a function of carbon number N. Signal intensities of carboxylate increase as a function of N. This result implies that the abundance of carboxylate at the air-water interface has a positive size dependence. In addition, we measured the mass spectra of inorganic ions. Figure 3 shows relative surface propensity (RSP) of organic and inorganic ions as a function of Connolly solvent excluded volume (CSEV). RSP is calculated as the ratio of the signal intensity of each ion to that of the nonanoate ion. The observed larger CSEV dependence on RSP for inorganic ions than organic ions suggests the charged head-group affects the surface propensity more effectively than the hydrophobic alkyl group does.

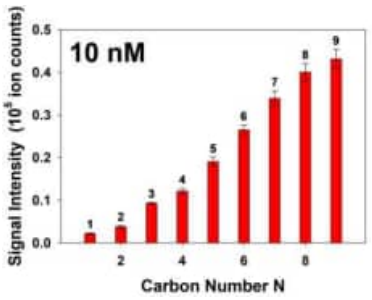

Fig. 2 Signal intensities of 10 nM sodium carboxylate (R_NCOONa, N =1~9) mixture solution as a function of carbon number N.

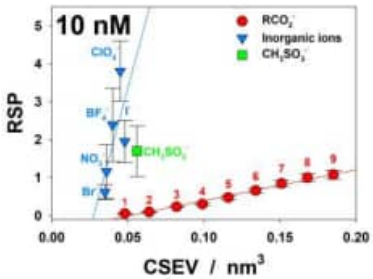

Fig. 3 Relative surface propensity of organic and inorganic ions determined by SIMS as a function of Connolly solvent excluded volume.

[1] Kusaka et al. *Nat. Chem.* **2021**, *13*, 306–311.

[2] Enami et al., *J. Phys. Chem. A* **2007**, *111*, 8749–8752.

[3] Enami et al., *J. Phys. Chem. A* **2016**, *120*, 9224−9234.

3P25 Synthesis and Optical Property of Eu doped Carbon Dots

(Kobe City College of Technology) Morihiko Hamada[1], Misaki Tanaka[1]
(Kobe University) Masaaki Fuki[2], Yasuhiro Kobori[2]

As a new class of carbon nanomaterials such as carbon dots (CDs), owing to their broad absorption and excitation wavelength (λ_{ex}) independent and -dependent photoluminescence (PL) emission as well as blight, stable, and ability of multimodal functionalization, have become promising materials for optical applications such as biological and optoelectronic devices.[1-4] In particular, CDs show the unique optical properties that λ_{ex} independent and -dependent PL components are denoted as PL(I) and PL(II).[1] In addition, CDs are possible to obtain unique properties when metal ions are doped in CDs, e.g., Hg^{2+}-sensing property by the introduction of Tb^{3+} and MRI contrast agent Gd^{3+}.[3,4] In this paper, we present the microwave-assisted synthesis and steady-state and time-resolved optical properties of Europium-doped ethylenediaminetetraacetic acid-based CDs (Eu-CDs).

Figure 1(a) shows the results of PL spectral shifts of Eu-CDs when λ_{ex} was shifted from 280 to 460 nm. Peaks of PL spectra were shifted from 450 to 540 nm as a function of shifts of λ_{ex}. In addition, PL of Eu^{3+} was also observed at 579, 592, and 615 nm. Therefore, we successfully synthesized Eu-CDs, because unreacted Eu^{3+} ions were removed by using dialysis. Figure 1(b) represents the results of PL lifetime measurement of CDs and Eu-CDs. PL lifetime of Eu-CDs shows decreased drastically that compared with PL lifetime of naked CDs. Thus, the decrease of PL lifetime of Eu-CDs means the excited energy transfer from CDs to doped Eu^{3+} was occurred. Interestingly, PL intensities of Eu^{3+} were changed at different λ_{ex} and Eu^{3+} didn't show PL in time-resolved PL spectra. These results indicate that the energy transfer bands from CDs to Eu^{3+} have selection rules.

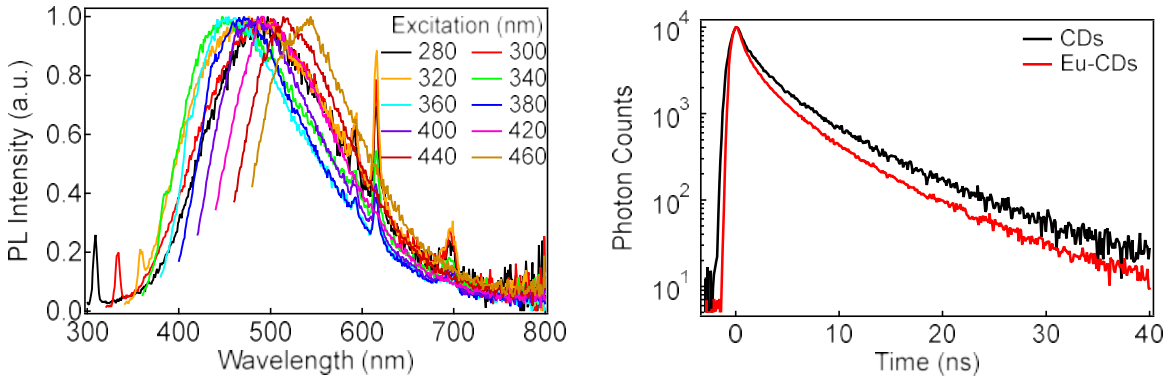

Figure 1. PL spectra of Eu-CDs in water (a) and PL decay profiles of CDs and Eu-CDs in water (b). CDs and Eu-CDs were excited at 403 nm ps laser and monitored the range from 520 to 560 nm.

References

[1] M. Hamada, *et al.*, *J. Phys. Chem. C* **2018**, *122*, 6463−6474.

[2] S. N. Baker and G. A. Baker, *Angew. Chem., Int. Ed.* **2010**, *49*, 6726−6744.

[3] T. K. Mondal, *et al.*, *ACS Omega*, **2018**, *3*, 11439–11446.

[4] N. Mauro, *et al.*, *ACS Appl. Nano Mater.* **2023**, *6*, 17206−17217.

3P26 A Systematic Exploration of Nonradiative Decay Paths in Carbo[*n*] Helicenes (*n* = 5-12): Role of Cyclization Paths

(Hokkaido Univ.) I. Kondo, Y. Harabuchi, S. Akiyama, Y. Nagata, S. Maeda

Carbo[*n*]helicenes are polycyclic aromatic hydrocarbons composed of ortho-fused benzene rings.[1,2] Because of their helical chirality, carbo[*n*]helicenes have been studied as promising molecular frameworks for luminescent materials. However, carbo[*n*]helicenes show low fluorescence quantum yields, and experimental studies have suggested triplet-mediated relaxation after photoexcitation.[1] For the rational design of helicene-based materials, it is important to understand the decay mechanisms.

In this study, we systematically investigated nonradiative decay paths of carbo[*n*]helicenes using automated searches for potential energy surface crossings. For [5]- and [6]helicenes, we compared the internal conversion path via S_1/S_0 conical intersections with the intersystem crossing path through the triplet manifold (**Fig. 1**). Cyclization-type crossings were found in both S_1/S_0 and T_1/S_0 regions. The 6-membered-ring path is energetically favorable in [5]helicene, whereas the 7-membered-ring path is more favorable in [6]helicene. SOC-based ISC rate constants at the S_1/T_i (i = 1 ~ 6) crossings agreed with experimental estimates,[1] supporting efficient access to the triplet manifold.

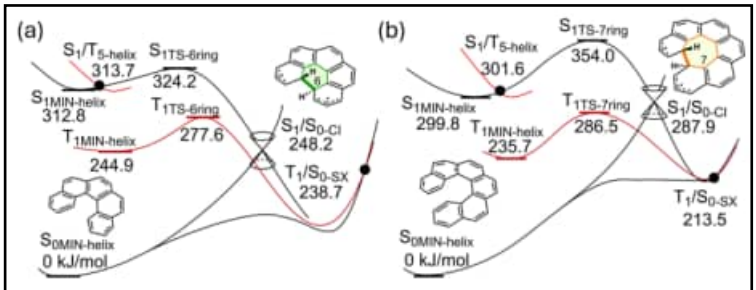

Fig. 1. Potential energy profiles at the B3LYP/Def2-SV(P) level for (a) [5]helicene and (b) [6]helicene. The energies are shown relative to $S_{0MIN\text{-}helix}$ in kJ mol^{-1}.

Based on the importance of triplet-mediated decay, we further examined T_1/S_0 decay paths in [7]–[12]helicenes. In addition to the 6-membered-ring and 7-membered-ring types, we identified outer-type crossings, where cyclization occurs between outer-side carbon atoms of the helix (**Fig. 2a**). Overall, the 6-membered-ring type is the most favorable for [5]- and [7]–[12]helicenes, whereas [6]helicene uniquely favors the 7-membered-ring type. The barrier for the outer-type path decreases with helicene size and becomes kinetically competitive in longer helicenes (**Fig. 2b**).

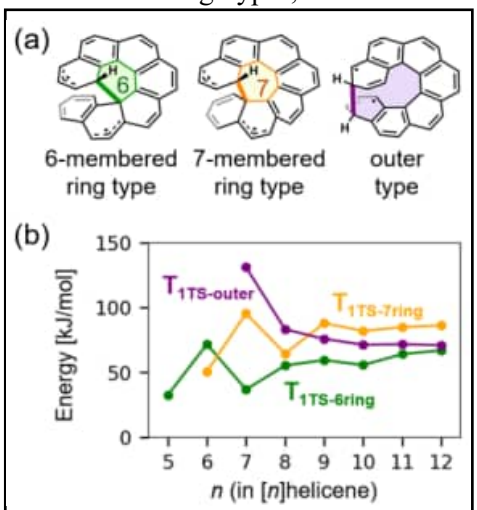

Fig. 2. (a) Three cyclization types identified for carbo[*n*]helicene. (b) Size dependence of the barrier heights of three cyclization types. Outer-type path becomes competitive in longer helicenes

These results show that larger helicenes have multiple kinetically competitive cyclization paths, making nonradiative decay more difficult to suppress by molecular modification. This trend suggests that [5]–[7]helicene frameworks may be more promising scaffolds for luminescent material design.

[1] M. Sapir *et al*., *Chem. Phys. Lett.*, **36**, 108 (1975).
[2] M. Gingras *et al*., *J. Phys. Chem. A*, **42**, 1007 (2013).

3P27 The rate rules for the reactions of Alkenes with OH

([1] Toyohashi Univ. Tech., [2] NIT, Hakodate College) Fushimi, Ryota[1,2]; Oguchi, Tatsuo[1]

Alkenes are not only important intermediates but also components of fuels for practical use in combustion. It is known that the reactions with hydroxyl radical (OH) initiate the decomposition of alkenes. Recently, rate measurements for some large alkenes were performed by our group in a wide temperature range. We confirmed that the OH addition reactions are dominant up to 700 K, and the pressure dependence of the rate coefficient (k) was found [1-3]. These results suggest that the major route of this reaction is

$$OH + R_1C(R_2) = C(R_3)R_4 \rightarrow R_1C(R_2)(OH)C(R_3)R_4, \qquad (1)$$

where R means alkyl groups that substitute a hydrogen atom in the ethylene ($CH_2=CH_2$). We also found a size-dependence of k(298 K) for several alkenes [3], however, it was unclear what factors it quantitatively depended on. Therefore, quantum chemical calculations were performed to investigate the correlation between k and the potential energy of the reaction in this study. Geometry optimization and vibrational frequency analysis were performed using hybrid density functional theory with Dunning's correlation consistent basis set (ωB97X-D/aug-cc-pVTZ). CBS-QB3 level calculations were also performed to compare the accuracy of energy and performance, and it was confirmed that the energy levels obtained from the calculations of both methods correlated very well, and the difference was only ~1 kJ/mol.

Three types of potential energy for each alkene obtained by calculation were used: 1) the recombination energy of the addition reaction, 2) the barrier height energy of the transition state before bond formation of (C=C)--OH, and 3) the association energy of the van der Waals complex located approximately 3.3 Å away from the C=C structure. were compared with the reaction rate constant. As a result, it was found that the van der Waals (vdW) complex energy was the best choice for correlation with k, shown in Figure 2. As the number of substituents increases, the stability of the vdW complex increases, and consequently, the reaction rate coefficient tends to increase as well. It suggests that vdW stability is one of the rate-determining factors.

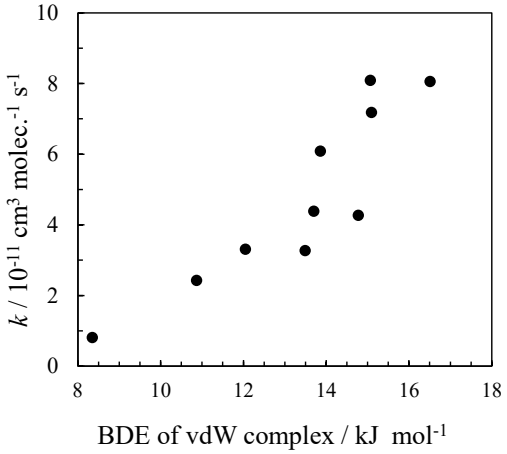

Fig. 1 Bond dissociation energy of Alkene-OH vdW complex.

References
[1] Fushimi *et al*., 38th Symposium on Chemical Kinetics and Dynamics, 2P02 (2023).
[2] Fushimi, Oguchi, 39th Symposium on Chemical Kinetics and Dynamics, 1P05 (2024).
[3] Fushimi, Oguchi, 40th Symposium on Chemical Kinetics and Dynamics, 3P18 (2025).

Author Index

mXnn for a speaker and mXnn for co-authors

A)

Adachi, Motoyasu 3A5
Aki, Yoshino 1P05
Akiyama, Seiji 3P26
Akiyama, Sogo 3P21
Allum, Felix 1A6
Ando, Masaya 3P15
Ando, Toshiaki 1A4
Aoki, Yuma 2P06
Arai, Yuto 1A7
Ardelia, Mellisa 1P27, **2A3**
Arima, Sota **1P17**, 1P21
Arima, Souta 1P20
Athikaphan, Pakpoom **1P26**
Awasthi, Kamlesh 3A4

B)

Baba, Yuji 3P19
Bai, Dong-Jie 3A4
Bllantyne, Lucius Thaine 1P16
Britton, Mathew 1A6
Brouard, Mark 1A6
Burt, Michael 1A6

C)

Che, Dock-Chil 1P04
Conti, Irene 1A1

D)

Dhongade, Siddhant **1P16**
Downes-Ward, Briony 1A6
Driver, Taran 1A6

E)

Enami, Shinichi 3P16, 3P24
Endo, Tamaki **2P18**
Endo, Tomoyuki **1P07**

F)

Forbes, Ruaridh 1A6
Fujii, Asuka 2P07
Fujita, Takatoshi 3A5
Fukahori, Shinichi **3P04**
Fuki, Masaaki 3P25
Fukuda, Kai 2P26
Fushimi, Ryota **3P27**
Fushitani, Mizuho **1A5**, 3P20

G)

Garavelli, Marco 1A1
Ghosh, Srijon 1A1, 1P05

H)

Hadsadee, S. 1P24
Hamada, Morihiko **3P25**
Harabuchi, Yu 3P26
Haraguchi, Ryosuke 2P10
Harries, James R. 1A6
Hasegawa, Hirokazu 3P04
Hasegawa, J. 1P24
Hasegawa, Jun-ya 2P19
Hashiba, Shinnichi 3P15
Hashigaya, Kasumi 1P02
Hashimoto, Kohei **1P21**
Hayashi, Daiki 1P10, 3P14
Haze, Misato 3P07

Heathcote, David 1A6
Hidaka, Hiroshi 2P21, **2P23**, 3P17
Hikosaka, Yasumasa 1A5
Hinokuma, Satoshi 3P18
Hirose, Ken **3P11**
Hishikawa, Akiyoshi **IL1**, 1A5, 1P02, 1P08, 2P17, 3P20
Hockett, Paul 1A6
Horio, Takuya **2P06**
Hsu, Hsin-Yun 3A4
Huang, Siwei **2P05**

I)

Ide, Yuki 2P25
Ie, Kanon 1P28, **2P24**
Iguchi, Arisa 2P23, 3P17
Iida, K. 1P24
Iida, Kenji 2P19
Iida, Keita 3P15
Iitaka, Fumiaki 3P21
Imai, Yumiko 1P26, 3A6
Inokuma, Yasuhide 2P25
Inoue, Kosuke 2P01
Inoue, Masayuki 1P28, 2P24
Inoue, Rinka 2P26
Inoue, Tomoya 3A3
Ishibashi, Atsuki 2P23, **3P17**
Ishii, Nobuhisa **3P23**
Ishizaki, Akihito **IL7**
Itakura, Ryuji 1P07, 3A5, 3P23
Ito, Yuri 3P05
Iwasa, Takeshi 3P18
Iwasaki, Atsushi 1A4
Iwayama, Hiroshi 1A6, 3P06

J)

Jagutzki, Ottmar 2P22
Jaiswal, Vishal Kumar 1A1
J. Howard, Andrew 1A6
Jifuku, Shuntaro 3A1
Jones, Darryl 2A4
Jungsuttiwong, S. 1P24

K)

Kadota, Yusuke 3P21
Kaisook, Pattanapon 1P26, 3A6
Kambara, Ryuto 1A7, **1P01**, 1P06, 1P15
Kanaya, Satoru 2A4, **2P22**
Kanazawa, Ryosuke **2P14**
Kanemura, Sakura 3P02
Kaneyasu, Tatsuo 3P06
Kanno, Manabu 2P07, 3P05
Kanno, Nozomu **2P11**
Karino, Momiji **2P01**
Kasahara, Shunji **2P02**, 2P08
Kawai, Akio **IL6**
Kawamata, Hiroshi **1P04**
Kimura, Mizuki 1P03
Kimura, Takayoshi 1P28
Kinoshita, Hiroshi **3P20**
Kishigami, Ko 2P08
Kitano, Tomoyuki 3P05
Kobayashi, Masato 2P25
Kobayashi, Takuto 1P20
Kobayashi, Yuto **1P06**
Kobori, Yasuhiro 3P25
Kokubu, Shusuke 2P10
Komatsuzaki, Tamiki 1P11, 2A1, 2P13, 3P13, 3P15
Kondo, Itsuki **3P26**
Koshiba, Takumi 2P07, 3P05
Kosugi, Kento **3P24**
Kubo, Koki **1P09**
Kumagai, Yoshiaki **1A6**

Kurahashi, Ryo **2P13**
Kuroda, Runa 1P08, 2P17
Kuroda, Shinji 2P02
Kurokawa, Kei **3P16**
Kusaba, Yuri 2P06

L)
Li, Jizhou 1P11, 2P13, 3P13
Liu, Yusong 1A6
Lötstedt, Erik 2P05
Lu, Bateer **1A8**

M)
Maeda, Satoshi 3P11, 3P26
Majima, Takuya **3A1**, **3P06**
Maruyama, Momoko 3P23
Mashiko, Hiroki 1P07
Matano, Shuhei **2P03**
Matsubuchi, Hayato 1A2, 1P10, 3P14
Matsuda, Akitaka **1P02**, 1P08, 2P17
Matsugi, Akira **2P04**
Matsui, Hiroyuki 2P04
Matsumoto, Ryutaro 3P20
Matsumoto, Yoshiteru 1P19
Matsuoka, Wataru 3P11
Matsuzaki, Taichi 1P16
Md. Al Mehedi, Hasan 3P13
Milĕsević, Dennis 1A6
Minato, Taketoshi 1P26, **3A6**
Minegishi, Yusuke 1A3, 1P06, 3P01
Minemoto, Shinichirou **2A4**, 2P03, 2P22
Minik, Luke 2P02
Minns, Russell 1A6
Misaizu, Fuminori 2P07
Misono, Masatoshi 2P08
Mita, Tsuyoshi 2P12
Mitsukawa, Eiyu 1P19
Mitsuke, Koichiro **3P21**
Miwa, Yutaro **1P27**
Miyashita, Kaichi **1P19**
Miyazaki, R. 1P24
Mizuno, Yuta 2P13, 3P15
Mohri, Fumiya **1P25**
Molpeceres, Germán 1P18, 2P16
Mori, Itsuki **3P09**
Mori, Yutori 3P22
Morimoto, Takumi **3P07**
Morita, S. 1P24
Mukaimine, Akari 3P15
Murakami, Tatsuhiro 1A2, 1P10, 2P20, 3A1, 3P14

N)
Nagahata, Yutaka **2A1**, 2P13
Nagano, Ayana **2P10**
Nagata, Yuuya 3P26
Nagaya, Kiyonobu 1A6
Nakagawa, Seiko 3P19
Nakagawa, Shota 1P10
Nakagawa, Shoto **1A2**, 3P14
Nakai, Hiromi 1P12
Nakai, Yoichi **2P21**, 3A2
Nakajima, Atsushi **3A3**
Nakajima, Kohei 3P15
Nakamoto, Kei-ichi 3A6
Nakamura, Masaaki 1P04, 1P27, 2A3
Nakanishi, Tatsuhiro 1P15, **2P09**
Nakano, Yuji 1P16
Nakao, Tomohiko 3P06
Nakatani, Kaho 1P23, 2P14
Nakatani, Naoki 1P23, 2P14
Nakayama, A. 1P24
Nakayama, Akifumi 1P16

Nanbu, Shinkoh 1P03
Naruo, Nanami 3P02
Nath, Pinku **1P14**
Naweephattana, P. **1P24**
Nenov, Artur 1A1
Neramittagapong, Arthit 1P26
Neramittagapong, Sutasinee 1P26
Nguyen, Thanh 1P18
Niozu, Akinobu 1A6
Nishi, Takanori 2A2
Nishimura, Koya 2P17
Nishimura, Yoshifumi 1P12
Niskanen, Johannes 1A6
Noda, Takuto **3P13**
Numadate, Naoki 3P16, 3P24

O)
Oba, Yasuhiro **1P18**, 2P23
Obara, Yuki 1A1, 1P05
Obata, Yui 3P19
Oda, Akiko **3P03**
Odagiri, Takeshi 3P03
Ogata, Hironori 3P21
Ogawa, Kazumi **1P08**, 2P17
Ogawa, Mikako 3P15
Oguchi, Tatsuo 3P27
Oguri, Katsuya 1P07
Ohara, Kazuaki 2P25
Ohashi, Kazuhiro **3P08**
Ohshima, Yasuhiro 1P25, 1P27, 2A3, 3P22
Ohshimo, Kenjiro 3P05
Ohta, Nobuhiro **3A4**
Okuda, Yuuka 3P07
Okamoto, Daichi **1P10**, 3P14
Okumura, Yuya 1P02
Ono, Yuriko 1P13, 1P15, 3P10
Orr-Ewing, Andrew 1A6
Oshima, Ryunosuke 2P03
Ota, Haruki 1A2
Ota, Rin 1P16
Otsuka, Sota 3A1
Owada, Shigeki 1A5

Q)
Qu, Lihao **3P10**

R)
Ratanasak, M. 1P24
Robertson, Patrick 1A6
Rolles, Daniel 1A6
Rudenko, Artem 1A6

S)
Sada, Kazuki 1P13
Saida, Ryota 2A3
Saita, Kenichiro 3P01
Saito, Manabu 3A1
Sako, Tokuei 1P07
Sameera, W. M. C. 1P18
Sasaki, Yuki 1P10, **2P20**, 3P14
Sato, Hazuki **1P03**
Sato, Shin-ichiro 1P17, **1P20**, 1P21
Sato, Takumi 1P25, **3P22**
Sekikawa, Taro 1A7, 1A8, 2P03, 3P01
Shimizu, Misaki 2P06
Shinohara, Ryo 2P01
Shioura, Mitsuaki **2P07**
Sie, Ni-En **3A2**, 2P16
Sims, Ian **IL5**
Staub, Ruben 1P11
Sugai, Takuma 2A4
Sumiya, Yosuke 1P09, 2P10, 3P09, 3P12

Sun, Hung-Wei 3P23
Sunaga, Ayaki **2P27**
Suzuki, Isao H. 3P03
Suzuki, Jidai **1P15**
Suzuki, Takahiro **1P28**, 2P24
Suzuki, Toshinori **1A1**, 1P05
Suzuki, Yuta 2P06

T)

Tabata, Koji 3P15
Tabtimtong, Nicha 1P26, 3A6
Tada, Kohei **2P08**
Taddei, Mario 1A1
Takahashi, Masahiko 1P25, 2A4, 2P22, 3P22
Takahashi, Satoshi **IL4**
Takayanagi, Toshiyuki 1A2, 1P10, 2P20, 3P14
Takayama, Mitsuo 2P09
Taketsugu, Tetsuya 1A3, 1A7, 1P01, 1P06, 1P11, 1P13, 1P15, 2P09, 2P12, 2P15, 2P25, 3P01, 3P10, 3P18
Takizawa, Soei **1P13**
Tamaru, Hiroya 1P16
Tanaka, Misaki 3P25
Tanaka, Ryoichi 2P13
Taniguchi, Riko **1P23**
Tashiro, Keisuke **2P25**
Tenaillon, Johan 3A6
Terasaki, Akira 2P06
Tiwari, Ashwani K. **IL2**
Toda, Mikito 2A1
Tokeshi, Manabu 1P21
Toma, Shunta **3P12**
Toyama, Shunsuke 2P19
Tsubouchi, Masaaki **3A5**
Tsuchida, Hidetsugu 3A1
Tsuneda, Takao 2P12, 2P15
Tsuge, Masashi **2P16**, 2P18, 2P23, 3A2
Tsukamura, Sei **1P12**
Tsuoka, Kazuki **2A2**
Tsuruta, Masaya **2P12**, 2P15
Tsutsumi, Takuro 1A3, 1P01, 1P13, 3P10
Toyama, Yuki 2P06

U)

Uchida, Tomohide 2P17
Uchiyama, Nino **3P18**
Ueda, Tadashi 1P26, 3A6
Ueno, Hinami 2P20
Ueno, Kazuki 2A3
Umer, Umair **1P11**, 2P13
Unwin, James 1A6
Ushiki, Yuta 2P06

V)

Vallance, Claire 1A6

W)

Wada, Akihide 2P26
Wada, Satoi **1A3**, 1A7, 1P06
Walmsley, Tiffany 1A6
Watabe, Yu **3P05**
Watanabe, Akihiro **3P02**
Watanabe, Naoki 1P18, 2P16, 2P18, 2P21, 2P23, 3A2, 3P17
Wei, Chun-Yen 3A4
W. L. Lee, Jason 1A6

Y)

Yabuki, Sorato 1P16
Yagi, Kiyoshi 1P11
Yamada, Daisuke **2P15**
Yamada, Kana **1A4**
Yamaguchi, Kentaro 2P25
Yamakawa, Kazuhiro 2P10

Yamaki, Keita 1P10, **3P14**
Yamamoto, Takuya 1P17, 1P20, 1P21
Yamanouchi, Kaoru 1A4, 2A2, 2P05
Yamasaki, Katsuyoshi 2P01
Yamashita, Sayaka **2P26**
Yamazaki, Masakazu 1P25, 3P22
Yanagawaya, Takuma 3P06
Yokoya, Akinari 3P19
Yoshizawa, Takumi 2P08

Z)
Zhou, Zhiyi **1A7**, **3P01**
Zhu, Chaoyuan **IL3**

第 41 回化学反応討論会実行委員会

SCKD41 Local Organizing Committee

委員長	渡部　直樹	(北大低温研)
副委員長	武次　徹也	(北大院理*)
委員	飯田　健二	(北大触媒研)
（50 音順）	岩佐　豪	(北大院理*)
	小林　正人	(北大院理*)
	小松崎　民樹	(北大電子研*)
	佐藤　信一郎	(北大院工)
	関川　太郎	(北大院工)
	柘植　雅士	(北大低温研/広島大院先進)
	堤　拓朗	(北大院理)
	長谷川　淳也	(北大触媒研*)
	原渕　祐	(北大 ICReDD)
	前田　理	(北大院理*)
	松岡　和	(北大 ICReDD)
	宮崎　玲	(北大触媒研)
	村上　正晃	(北大遺制研)
		*ICReDD 兼任

第 41 回化学反応討論会　講演要旨集

SCKD41 Book of Abstracts

発行日　2026 年 5 月 15 日

発行　第 41 回化学反応討論会実行委員会

代表　〒060-0819　札幌市北区北 19 条西 8 丁目

北海道大学低温科学研究所

渡部直樹